Absorptie van elektromagnetische straling in een menselijk lichaam afkomstig van mobiele toestellen en multipadblootstelling aan basisstationantennes

Electromagnetic Human-Body Absorption Due to Near-Field Exposure from Hand-Held Wireless Devices and Multi-Path Exposure from Base Station Antennas

Günter Vermeeren

Promotoren: prof. dr. ir. L. Martens, prof. dr. ir. W. Joseph
Proefschrift ingediend tot het behalen van de graad van
Doctor in de Ingenieurswetenschappen: Elektrotechniek

Vakgroep Informatietechnologie
Voorzitter: prof. dr. ir. D. De Zutter
Faculteit Ingenieurswetenschappen en Architectuur
Academiejaar 2012 - 2013

UNIVERSITEIT GENT

ISBN 978-90-8578-622-1
NUR 959
Wettelijk depot: D/2013/10.500/55

Universiteit Gent
Faculteit Ingenieurswetenschappen en Architectuur
Vakgroep Informatietechnologie

Promotoren: prof. dr. ir. Luc Martens
prof. dr. ir. Wout Joseph

Universiteit Gent
Faculteit Ingenieurswetenschappen en Architectuur

Vakgroep Informatietechnologie
Gaston Crommenlaan 8 bus 201, B-9050 Gent, België

Tel.: +32-9-331.49.00
Fax.: +32-9-331.48.99

Proefschrift tot het behalen van de graad van
Doctor in de Ingenieurswetenschappen:
Elektrotechniek
Academiejaar 2012-2013

Dankwoord

Met dit schrijven vul ik het laatste lege blad van mijn proefschrift. Dit dankwoord is met verve de minst wetenschappelijke tekst in dit proefschrift, maar daarvoor niet minder belangrijk. In tegendeel, een proefschrift is een bouwwerk waarin vele handen bijdragen om te slagen. En dus is een woord van dank zeker op zijn plaats.

In de eerste plaatst wil ik mijn promotoren, prof. Luc Martens en prof. Wout Joseph, bedanken dat ik mijn onderzoek heb mogen uitvoeren onder hun deskundige leiding in de inspirerende en dynamische omgeving van de Wireless & Cable onderzoeksgroep, in de mond "de WICA". Enerzijds, voor het aanbieden van de nodige tools, het delen van hun ervaringen en mij in contact te brengen met toonaangevende wetenschappers uit binnen- en buitenland. Maar ook voor de vele discussies, de kritische blik op mijn resultaten en teksten. Jullie zetten me steeds op weg om mijn onderzoek tot een goed einde te brengen daarbij ruimte latend voor creativiteit en eigen inbreng.

Ook wil ik alle collega's en ex-collega's bedanken voor de goede sfeer "op den bureau"en de praatjes in de gang of tijdens het eten. Deze waren niet altijd wetenschappelijk van aard, vaak interessant maar evenzeer niets vertellend. In het bijzonder wil ik Leen en Francis bedanken voor de praktische ondersteuning bij mijn onderzoek en de vele metingen die we samen hebben uitgevoerd in binnen- en buitenland. Ook wil ik Isabelle, onze secretaresse van de WICA groep, bedanken voor de administratie bij reizen, onkostenvergoedingen, etc. Verder wil ik ook Nobby bedanken voor de begeleiding tijdens de prille dagen - al eventjes geleden - van mijn onderzoek.

Mijn doctoraatsonderzoek werd uitgevoerd binnen het kader van verschillende Europese projecten zoals: BASEXPO, SARSYS-BWP, SEAWIND en LexNet. Daarnaast heb ik ook mogen meewerken aan kleinschalige projecten. Hierdoor kruisten veel wetenschappers en ingenieurs uit binnen- en buitenland mijn pad en verrijkten mij met hun kennis en ervaringen. In het bijzonder wil ik prof. Niels Kuster en zijn onderzoeksgroep IT'IS (Zurich, Zwitserland) bedanken voor de goede samenwerking. Andreas, Sven en Marie-Christine "many thanks!"voor de hulp bij de SEMCAD simulaties, de vruchtbare discussies tijdens de vele projectvergaderingen en de uitjes na het harde werken op conferenties en projectvergaderingen. Niels en Sven, ook bedankt dat ik de absorptiemetingen voor de walkietalkies in de IT'IS labo's heb mogen uitvoeren. Verder wil ik ook de groep van prof. Theodoros Samaras en zijn onderzoeksgroep van de Aristoteles Universiteit van Thessaloniki (Griekenland) bedanken. Zij hebben de blootstellingsmetingen

uitgevoerd in Griekenland (in het kader van het SEAWIND project) waarvoor ik in dit proefschrift de absorptie bepaald heb.

In het bijzonder wil ik ook mijn ouders bedanken voor alle kansen die ze mij gegeven hebben om mij te ontplooien zowel in mijn studies (industrieel ingenieur en burgerlijk ingenieur) als in mijn hobby's (de vele ritten van en naar het voetbal). Ik begrijp goed dat dit zeker niet evident is in een gezin met drie kinderen. En nog steeds staan jullie klaar om een handje toe te steken waar nodig en zo het drukke leven van jullie kinderen te ontlasten. Bedankt!

Ook wil ik de ouders van Sofie - moeke en vake - bedanken voor de steun en de hulp bij de opvang van de kindjes tijdens drukke periodes zoals het schrijven van een proefschrift, en de leuke vakanties in de Provence.

Ik wil ook al mijn vrienden bedanken voor het boeiend vullen van de agenda met weekendjes (Spermaliehoeve en Limburgs mooiste) etentjes, spelletjesnamiddagen, fietstochten en droppings. Op die manier zorgend voor een perfecte balans tussen ontspanning en werk.

En tot slot wil ik ook mijn drie schatjes bedanken. Sofie voor de niet aflatende steun en het begrip voor de weinige tijd tijdens het schrijven van mijn proefschrift. Mijn twee kleine rakkers die er wel vaak een boeltje van maken, maar met hun pretoogjes, maniertjes en kwajongensstreken, heel even, de kopzorgen verdrijven. Ik zie jullie graag!

Gent, Augustus 2013
Günter Vermeeren

Table of Contents

List of Figures

List of Tables

List of Acronyms

B

BR	Basic Restriction
BFD	Basic Field Distribution

C

CDF	Cumulative Distribution Function
CENELEC	European Committee for Electrotechnical Standardization

D

DAE	Data Acquisition Electronics
DECT	Digital Enhanced Cordless Telecommunications
DL	Downlink

E

EMF	Electromagnetic Fields
ETSI	European Telecommunications Standards Institute
ERP	Effective Radiated Power

F

FCC	Federal Communications Commission
FDTD	Finite-Difference Time-Domain method

FEM	Finite Elements Method
FM	Frequency Modulation
FRS	Family Radio Services

G

GPU	Graphical Processing Unit
GSM	Global System for Mobile Communications

H

HP	Half Plane

I

ICNIRP	International Commission on Non-Ionizing Radiation Protection
IEC	Innternational Electrotechnical Commission
IEEE	Institute of Electrical and Electronics Engineers

L

LOS	Line-Of-Sight

M

MRI	Magnetic Resonance Imaging
MTE	Mobile Terminal Equipment

N

NLOS	Non Line-Of-Sight

P

PCB	Printed Circuit Board
PEM	Personal Exposure Meter or exposimeter
PMR	Private Mobile Radio

R

RAM	Random Access Memory
RF	Radio Frequency
RL	Reference Level
RMS	Root-Mean-Square

S

SAM	Specific Anthropomorphic Mannequin
SAR	Specific Absorption Rate
SME	Statistical Multipath Exposure
SPC	System Performance Check

T

TE	Transverse Electric
TM	Transverse Magnetic

U

UMTS	Universal Mobile Telecommunications System

V

VNA	Vector Network Analyzer

W

wb	whole body

WiFi	Wireless Fidelity

Samenvatting
– Summary in Dutch –

De opkomst van draadloze communicatiesystemen wordt beinvloed door stijgende vraag naar informatie op iedere plaats en elk ogenblik. Toegankelijkheid, connectiviteit en mobiliteit zijn sleutelbegrippen in het ontwerp van mobiele netwerken. De architectuur van draadloze communicatiesystemen hangt af van de beoogde dienst die het network zal leveren. Omroepnetwerken verzorgen de draadloze uitzendingen van radio en televisie, mobiele telefoons verbinden met cellulaire netwerken voor spraak en datacommunicatie, en draadloze lokale netwerken verzorgen de verbinding voor laptops, tablets en smartphones. De toenemende vraag naar toestellen voor draadloze communicatie is duidelijk door het toenemend aanbod van mobiele toestellen op de markt zoals smartphones, laptops en tablets.

Sinds de opkomst van de GSM netwerken onstond de publieke bezorgdheid omtrent mogelijke schadelijke gezondheidseffecten door de blootstelling aan de radiofrequente elektromagnetische straling afkomstig van draadloze communicatiesystemen. Internationale organisaties zoals de International Commission on Non-Ionizing Radiation Protection (ICNIRP) en de Federal Communications Commission (FCC) hebben richtlijnen uitgevaardigd om de blootstelling aan elektromagnetische velden te beperken. Deze richtlijnen zijn gebaseerd op de huidige wetenschappelijke kennis omtrent mogelijke gezondheidseffecten. Regelgevende instanties baseren hun limieten op deze richtlijnen al dan niet in een meer stricte vorm.

Het wetenschappelijke onderzoek naar de blootstelling aan radiofrequente elektromagnetische velden (EMV) situeert zich hoofdzakelijk binnen drie domeinen: biologie, epidemiologie en dosimetrie. De bioloog onderzoekt de reacties van cellen en dieren (voornamelijk knaagdieren) bij blootstelling aan elektromagnetische velden. De epidemioloog zoekt verbanden tussen (schadelijke) gezondheidseffecten en bronnen van elektromagnetische straling. Dosimetrie is voornamelijk het domein van de ingenieur. Dosimetriestudies richten zich op de meting, karakterisering en modellering van de invallende velden op en de geinduceerde velden in het menselijke lichaam.

Het bepalen van de blootstelling hangt af van de afstand van de zender tot het lichaam. Mobiele toestellen worden gebruikt dicht bij het lichaam (in het nabije veld van de antenne) en vereisen een directe bepaling van de geïnduceerde velden of absorptie in het lichaam. Voor antennes op grote afstand van het lichaam (in het verre veld van de antenne) dient de bepaling van het invallende veld als eerste

schatting voor de geinduceerde absorptie. Dit proefschrift behandelt aspecten aangaande de dosimetrie voor mobiele toestellen dicht bij het lichaam en de multipad blootstelling aan de golven van basisstationantennes.

Het eerste deel van het proefschrift onderzoekt de dosimetrie van draadloze zenders die dicht bij het lichaam uitstralen. Hoofdstuk 2 onderzoekt de volumes gebruikt voor de uitmiddelling van de lokale absorptie in het lichaam. Blootstellingsrichtlijnen en -standaarden beperken de maximale absorptie in een volume dat 1 g of 10 g weefsel omvat. De ICNIRP richtlijn, waarop de Europese regelgeving is gebaseerd, definieert limieten voor de lokale absorptie maar legt niet vast welke vorm het volume moet aannemen waarover uitgemiddeld wordt. Standaarden bepalen dat de absorptie moet worden uitgemiddeld over een kubus. Hoofdstuk 2 evalueert het gebruik van kubussen voor de uitmiddeling en vergelijkt deze met het volume dat aanleiding geeft tot de maximale uitgemiddelde waarde voor de absorptie en met een sferisch volume. Uit de studie blijkt dat de kubus de laagste uitgemiddelde waarde (van de drie beschouwde volumes) oplevert en dat het sferische volume beter de waarde volgt, verkregen in het volume dat aanleiding geeft tot de maximale uitgemiddelde waarde. Dit komt omdat het sferische volume meer absorptiepunten ter hoogte van het lichaamsoppervlak in rekening brengt.

Dosimetriestudies spitsten zich voornamelijk toe op de blootstelling afkomstig van mobiele toestellen en basisstationantennes voor cellulaire netwerken. Met de studie van de walkie talkies willen we de aandacht richten op een toestel dat als alternatief kan dienen voor mobiele telefoons in het geval van korte afstandscommunicatie. De voordelen van walkie talkies zijn: het eenvoudige gebruik – één druk op de knop om een oproep te starten –, de goedkope aankoopprijs en de gratis communicatiekost. In Europa werken walkie talkies volgens de Private Mobile Radio standaard bij een frequentie van 446 MHz (PMR 446). Het onderzoek naar de blootstelling afkomstig van walkie talkies werd gedreven door de relatief lage frequentie van 446 MHz, het effectief uitgestraalde vermogen van 500 mW, het eenvoudige gebruik van walkie talkies voor kinderen en het beperkt aanbod aan studies over de blootstelling van walkie talkies. De volgende twee hoofdstukken in het proefschrift beschrijven het ontwerp van een walkie talkie model dat nodig is voor de bepaling van de absorptie in realistische hoofdmodellen.

In hoofdstuk 3 behandelt het ontwerp van walkie talkie modellen door reverse engineering van een commerciële walkie talkie. De modellen werden numeriek en experimenteel gevalideerd door de antennekarakteristieken en de nabije velden te vergelijken met deze van de echte walkie talkies. Daarnaast werd ook het effectief uitgestraalde vermogen van de walkie talkies gemeten. De walkie talkie modellen kunnen pas als vervanger van de echte toestellen gebruikt worden als ze op dezelfde manier uitstralen.

Het onderwerp van hoofdstuk 4 is de dosimetrie van de absorptie in het hoofd van een mens geïnduceerd door de elektromangetische velden van walkie talkies. De echte toestellen voldeden aan de limieten voor de lokale absorptie. Het walkie talkie model met omhulsel rond de spiraalvormige antenne schat goed de lokale absorptiewaarden van de echte walkie talkies indien herschaald wordt naar het magnetische nabije veld. Dit model werd gebruikt voor de numerieke studie naar

absorptie van de blootstelling aan walkie talkies in realistische mensmodellen. We toonden aan dat de veroudering van de lichaamsweefsels enkel een beperkte invloed hebben op de absorptie in het hoofd en dat het vlakke fantoom aanleiding geeft tot hogere SAR waarden dan het homogene specifiek anthropomorphisch mannequin (SAM) hoofdmodel voor de verticale positie van de walkie talkie voor de neus. Het SAM hoofd wordt gebruikt bij het testen of mobiele telefoons voldoet aan de limiet voor de lokale absorptie.

Het tweede deel van het proefschrift behandelt multipad blootstelling aan elektromagnetische velden afkomstig van basisstationantennes. De meeste dosimetriestudies modelleren de blootstelling aan verre velden als één enkel invallende vlakke golf al dan niet gecombineerd met een gereflecteerd vlakke golf. Propagerende elektromagnetische golven interageren met de omgeving (reflectie, breking en transmissie) waardoor meerdere propagatiepaden ontstaan die aanleiding geven tot een multipadblootstelling aan elektromagnetische velden. In een multipadomgeving varieert de blootstelling in tijd en plaats. De variatie van de blootstelling in een multipadomgeving resulteert in een grote veelheid aan absorptiewaarden en wordt gekwantificeerd door het vermelden van het interval waarbinnen de absorptiewaarden liggen of door samenvattende statistieken.

Hoofdstuk 5 onderzoekt de invloed van sterk reflecterende omgevingen op de absorptie in arbeiders die zich bevinden op korte afstand van een basisstationantenne voor frequenties van 300 MHz tot 5 GHz. Deze studie ondersteunde de onwikkeling van de IEC standaard 62232 over de methodes voor het bepalen van de blootstelling van de mens aan elektrische, magnetische en elektromagnetische velden. We vonden dat de lokale en totale lichaamsabsorptie in een sterk reflecterende omgeving en in de nabijheid van de basisstationantennes sterk varieerde (van -8.7 dB tot 8 dB) in vergelijking met de blootstelling in de vrije ruimte. Maar een omgeving die aanleiding geeft tot een maximale blootstelling kon niet worden bepaald. We toonden ook aan dat de ICNIRP referentieniveaus niet altijd verzekeren dat er wordt voldaan aan de basisrestricties in een sterk reflecterende omgeving en voor afstanden korter dan 10 m tot de basisstationantenne.

Hoofdstuk 6 bespreekt de ontwikkeling en validatie van een numerieke methode om snel de distributie van absorptiewaarden te bepalen in rotatiesymmetrische (bijvoorbeeld een sferoide) en realistische mensmodellen in een realistische, multipad omgeving. Deze methode draagt de naam statistische multipadblootstellingsmethode, in het Engels afgekort als SME. De SME methode bepaalt de totale lichaamsabsorptie in een multipadomgeving aan de hand van vooraf berekende totale velden op een gesloten oppervlak rond het mensmodel voor een beperkt aantal enkelvoudig invallende vlakke golven en de lineariteit van de Maxwell vergelijkingen. De totale velden voor de enkelvoudig invallende vlakke golven rond het lichaam worden vooraf berekend via 3D elektromagnetische simulaties. De SME methode versnelt de berekeningen met ten minste 45 % in vergelijking met een eindige differenties eindige elementen (FDTD) methode. De SME methode werd gevalideerd met 3D FDTD simulaties en vertoonde een nauwkeurigheid die afhankelijk is van het aantal vooraf berekende totale velden en die lager kan zijn dan 1 %. We vonden ook dat de totale lichaamsabsorptie voor multipadblootstelling de

maximale totale absorptie voor enkelvoudige invallende vlakke golven kan overschrijden. We stelden vast dat de ICNIRP referentieniveaus niet altijd verzekeren dat er wordt voldaan aan de basisrestricties in het geval van multipadblootstelling. De SME methode toonde ook aan dat de gemiddelde absorptie in een multipadomgeving kan bepaald worden door 100 verschillende blootstellingen. Echter, indien de volledige distributie aan absorptiewaarden gewenst is dan zijn minstens 4000 verschillende blootstellingen nodig. We hebben de SME methode ook toegepast voor de bepaling van de totale lichaamsabsorptie in een realistisch model van een 6-jarige jongen blootgesteld aan GSM downlink signalen bij een frequentie van 950 MHz in een stadsomgeving. We toonden aan dat de totale lichaamsabsorptie in realistische mensmodellen de totale lichaamsabsorptie in homogene sferische mensmodellen overschreed. De sferische modellen hadden dezelfde dielektrische eigenschappen als hoofdweefsel zoals vermeld in de IEC 62209 standaard. We hebben de SME methode ook toegepast om de totale lichaamsabsorptie te bepalen als gevolg van de blootstelling afkomstig van draadloze communicatiesystemen dat werd gemeten in vier binnenomgevingen (scholen, huizen, kinderdagverblijven en kantoren). De totale lichaamsabsorptie in deze binnenomgevingen voldeed aan de ICNIRP basisrestrictie voor de totale lichaamsabsorptie voor het algemeen publiek. We stelden ook vast dat in binnenomgevingen de absorptie geïnduceerd door bronnen aanwezig in de binnenomgeving groter kan worden dan de absorptie door buitenshuis bronnen en dit voornamelijk wanneer de binnenshuis bronnen worden benaderd.

Hoofdstuk 7 bestudeert de invloed van het lichaam op de afgelezen waarden van een persoonlijke blootstellingsmeter. Persoonlijke blootstellingsmeters worden frequent gebruikt in epidemiologische studies om de blootstelling van een persoon te registreren. De persoonlijke blootstellingsmeter wordt typisch op het lichaam gedragen en meet de blootstelling aan elektromagnetische velden in meerdere communicatiebanden gedurende een zekere tijd. Bij het gebruik van de blootstellingsmeter op het lichaam ontstaat er elektromagnetische koppeling tussen lichaam en blootstellingsmeter, en schermt het lichaam de blootstellingsmeter deels af van invallende elektromagnetische golven. Deze koppeling en afscherming zorgen voor een gewijzigde aflezing van de blootstellingswaarden op de persoonlijke blootstellingsmeter in vergelijking met een meting waarbij de persoonlijke blootstellingsmeter vrij wordt opgesteld. We gebruikten de SME methode, die in Hoofdstuk 6 werd ontwikkeld, om de invloed te onderzoeken van het lichaam op de aflezing van de persoonlijke blootstellingsmeter. We stelden vast dat de blootstellingsmeter wanneer gedragen op het lichaam de blootstelling aan invallende elektromagnetische velden gemiddeld met 3.4 dB onderschat.

Het laatste hoofdstuk van het proefschrift vat de besluiten van de studie samen en vermeld opportuniteiten voor toekomstig onderzoek die verder bouwen op dit proefschrift.

Summary

The advent of wireless communication systems was, and still is, driven by an ever increasing demand for information at any time and any place. Accessability, connectivity, and mobility are key aspects in the design of mobile networks. The architecture of wireless communication systems depend on the intended services it provides. Broadcasting networks are installed for radio and television broadcasting, mobile phones connect to cellular networks for their voice and data communication, and wireless local area networks provides wireless connectivity mainly for notebooks, tablets, and smartphones. The increasing demand for wireless communication devices is reflected in the exponential growth of mobile devices, such as smartphones, notebooks, tablets, etc.

Since the advent of the Global System for Mobile Communications (GSM) public concern rose with respect to possible adverse health effects from exposure to radio-frequency electromagnetic fields irradiated by wireless commnunication systems. International bodies, such as International Commission on Non-Ionizing Radiation Protection (ICNIRP) and the Federal Communications Commission (FCC), issued guidelines to limit exposure to electromagnetic fields based on current scientific knowledge. Regulatory bodies adopted these guidelines whether or not in a modified way.

The research on the exposure to radio-frequency (RF) electromagnetic fields (EMF) situates mainly in three research domains: biology, epidemiology, and dosimetry. A biologist investigates the responses of cells and living animals (such as rodents) to EMF exposure. An epidemiologist attempts to correlate (adverse) health effects to different sources of electromagnetic fields. The field of dosimetry is mainly populated by engineers. Studies on dosimetry aim at measuring, characterizing, and modelling the fields incident on and induced in the human body.

In exposure assessment a distinction is made depending on the distance of the wireless transmitter to the body. On the one hand, mobile devices are typically operated close to the human body (near field) and require a direct assessment of the induced fields or the absorption in the body. On the other hand, for antennas operating at large distances from the human body (far field) it is often sufficient to measure the incident electric fields as a first estimate of the induced absorption. This dissertation deals with the dosimetry for mobile devices operated close to the body and the multi-path exposure from base station antennas.

The first part of the dissertation focusses on the dosimetry of wireless transmitters operated in the proximity of the body. Chapter 2 investigates the averaging volumes for assessing the local absorption in the human body. International

guidelines and standards limit the maximum absorption (in terms of the specific absorption rate (SAR)) in a volume containing 1 g or 10 g of tissue. The ICNIRP guidelines, on which the European limits are based, define limits for the local absorption but do not specify the shape of the volume over which the absorption needs to be averaged. Standards mainly define a cubical averaging volume. Chapter 2 evaluates cubical averaging volumes against a worst-case and a spherical averaging volume. Peak local absorption always occur near the body surface. We observed that a cubical averaging volume yields lower averaged localized absorption values than the spherical averaging scheme because the spherical averaging scheme takes into account more absorption values at the surface of the body.

The vast amount of studies on dosimetry deals with the exposure due to mobile devices and base station antennas for cellular communication systems. With the case study of the walkie-talkie, we draw the attention to a device that gained interest as an alternative for cellular phones for short range communications. The advantages of walkie-talkies are their ease-of-use (push-to-talk), their cheap price, and their free-of-charge communication. In Europe, a walkie-talkie operates according to the Private Mobile Radio at 446 MHz (PMR 446) standard. The relative low frequency, the effective radiated power of 500 mW, the use of walkie-talkies by children, and the limited number of exposure studies for walkie-talkies attracted our attention to these devices. The next two chapters present the design of walkie-talkie models and investigated the absorption induced by walkie-talkies.

In chapter 3, we designed walkie-talkie models by reverse engineering of commercially available devices. The models were numerically and expirementally validated in free space against the real devices in terms of antenna characteristics and near-field behavior. In order to use the model as a substitute for real walkie-talkies, we do not only need a good physical representation of a walkie-talkie, but we also need the power typically transmitted by these devices. Therefore, the effective radiated powers of the commercial devices were measured.

The subject of chapter 4 is the dosimetry of the absorption in the human head induced by the electromagnetic fields of walkie-talkies. The commercial devices showed to be compliant with current absorption limits for the localized averaged SAR. The walkie-talkie model with coating around the antenna provides a good estimate for the local absorption values of the real walkie-talkie devices when rescaled to the magnetic near field. The model enabled the numerical study of the absorption of the fields induced by walkie-talkies in realistic human body models. We showed that the ageing of tissues only marginally influences the absorption in the head and that the flat phantom is conservative for heterogeneous head models and the homogeneous specific anthropomorphic mannequin (SAM) which is used for the compliance testing of mobile phones when the walkie-talkie is vertically positioned in front of the face.

The second part of the dissertation deals with the multi-path exposure to base station antennas. Until recently, most studies on far-field exposure assumed single incident plane-wave exposure or took into account one reflected plane wave. Travelling electromagnetic waves interact (reflection, refraction, and transmission) with the environment resulting in a multi-path exposure of people to radio-

frequency electromagnetic fields. In a multi-path environment, exposure varies in time and space resulting in a distribution of absorption values. The exposure in a multi-path environment can be quantified by specifying a range of exposures or by providing summary statistics on the exposure.

Chapter 5 investigates the influence of highly reflective environments on the absorption in a worker at short distances of a base station antenna in the frequency range of 300 MHz to 5 GHz. This study supported TC106 in the development of the standard IEC62232 on the methods for the assessment of electric, magnetic and electromagnetic field associated with human exposure. We found that the local and the whole-body absorption in a reflecting environment and at short distances from the base station antenna varied from -8.7 dB to 8 dB with respect to free space for the investigated configurations, but a worst-case environment could not be determined. We also showed that the ICNIRP reference levels are not always conservative with respect to the basic restrictions in a highly reflective environment and for distances below 10 m from the base station antenna.

In Chapter 6 we developed and validated a numerical method, called the statistical multipath exposure method or SME method, to determine quickly the distribution of the whole-body absorption in rotation symmetric (e.g., spheroid) and realistic human bodies in a realistic environment. The SME method assesses the whole-body absorption in a multipath environment from precomputed total fields on a closed surface around the human body for a limited number of single incident plane waves and the linearity of Maxwell's equations. The total fields are precomputed by full-wave electromagnetic solvers. This fast method accelerates the computations by at least 45 % compared to the finite-difference time-domain (FDTD) method. The SME method was validated with 3D full-wave FDTD computations. The uncertainty introduced by the presented method with respect to FDTD computations depend on the number of precomputed fields and can be as low as 1 %. We found that the whole-body absorption due to multipath exposure can exceed the whole-body absorption for worst-case single plane-wave exposure. We also found that the ICNIRP reference levels were not always compliant with the basic restrictions for multi-path exposure. The SME method was also used to determine the number of exposures needed for accurately assessing the summary statistics of the whole-body absorption in a realistic environment. We observed that the mean whole-body absorption can be estimated from about 100 exposures, while assessing accurately summary statistics requires at least 4000 exposures. We also applied the SME method for assessing the whole-body absorption in a realistic model of a 6-year-old boy exposed to the GSM downlink at 950 MHz and showed that the absorption in realistic human body models exceed the absorption in homogeneous prolate spheroid models with the dielectric properties of head tissue suggested in IEC62209 standard. We also applied the SME method to evaluate the whole-body absorption due to the exposure of wireless communication systems measured in four indoor environments (schools, homes, day nurseries, and offices). The whole-body absorption in these indoor environments showed to be compliant with the ICNIRP basic restriction for general public. We also observed that in indoor environments the absorption induced by indoor sources can become larger

than the values induced by outdoor sources, especially when the indoor wireless sources are approached.

Chapter 7 deals with the influence of the body on the exposimeter reading. Personal exposure meters or dosimeters are frequently employed in epidemiological studies to record the exposure of a person. The exposimeter is worn on the body and measures the exposure (i.e., the electric fields) in multiple frequency bands during a certain period of time. When the exposimeter is worn on the body, the coupling betweeen the body and the exposimeter, and the shadowing of the body change the exposimeter reading compared with a free-space measurement of the exposimeter. We used the SME method, developed in Chapter 6, to investigate the influence of the human body on the dosimeter reading. We found that the exposimeter worn on the body underestimates the incident field levels by 3.4 dB on average.

The last chapter of the dissertation summarizes the conclusions of the study and points out future research oppertunities based on the achievements presented in this dissertation.

1 Introduction

During the last decades, wireless communication systems became a part of daily life as humans want to communicate and retrieve information at any place, any time. A wide variety of wireless systems emerged each providing a wireless connection to the community for a certain service, inter alia, broadcasting systems, cellular communication systems, and local area networks. The architecture of wireless communication systems depends on the intended services it provides. Broadcasting networks are installed for radio and television broadcasting, mobile phones connect to cellular networks for voice and data communication with national and international coverage, and wireless local area networks provide wireless data connectivity to fixed wired access networks within a limited distance. The increasing demand for wireless communication devices is reflected in the exponential growth of mobile devices, such as smartphones, notebooks, tablets, etc.

The era of radio communications took off at the end of the 19th century with wireless telegraphy. Ever since, radio communications have influenced increasingly society as it evolved over time. In the beginning of the 20th century the deployment of radio broadcasting systems provided the first radio transmission service to the public on a large scale. Radio broadcasting was followed by television broadcasting in the 1960s. These broadcasting technologies became an important source of information for the public, however, it did not change to a large extent their way of living because people could not contribute easily to these services.

As opposed to broadcasting networks, the deployment of cellular communication networks at the end of the 20th century, such as the Global System for Mobile Communications (GSM), brought about a revolutionary change not only in wire-

less communications, but in the way we live. Cellular networks were not the first to provide voice communication between persons by means of radio-frequency (RF) electromagnetic waves. Walkie-talkies or two-way radios already enabled a wireless transmission of voice between two or more persons. But, these radio devices only provided wireless communication between humans over short distances because a direct wireless link was established between the radio transmitters operated by the users. Walkie-talkies were mainly used by local services, such as emergency services. Cellular networks were designed to overcome the distance limitation which is a characteristic for direct links between mobile devices and, thus, enabling people to communicate with each other irrespective of distance and the specific location. This required that the area being covered must be split up in cells. A base station antenna provided the wireless connection in each cell. The network behind the base station antennas provided the necessary intermediate to enable long distance communication. The only requirement to set up a call was that the mobile phone of the user should be within the range of an antenna (cell) to access the (backbone) network.

At about the same time, the worldwide web or the internet was invented. This worldwide network also grew exponentially as it brought data information right at the doorstep of everybody's home. Nowadays, wireless networks still evolve aiming at merging voice, video, and data services and allowing the user to access these services at any time without restricting his or her mobility. Wireless radio communication became one of the building blocks of modern society. As shown in Figure 1.1 mobile data traffic will continue to grow exponentially.

1.1 Exposure to radio-frequency electromagnetic fields

Although, transmission of electromagnetic waves already happened on a large scale by means of broadcasting networks for radio and television, it were mainly the cellular networks which made people conscious about possible health effects associated with the exposure to radio-frequency electromagnetic fields (EMF). As opposed to broadcasting systems, cellular networks require that (base station) antennas are installed all over the country. The proliferation of antennas in the environment raised the awareness of the people that they are exposed all day to radio-frequency electromagnetic fields. Moreover, the cellular networks also imply that radio transmitters (mobile devices) are operated close to the body on a large scale.

Despite the growing concern of possible adverse health effects associated to radio-frequency electromagnetic fields, wireless communication is very successful because it provides a degree of freedom to humans to communicate with each other. This is clearly illustrated in the continuously growing market of mobile communication devices.

This dissertation focusses on the local and whole-body exposure to radio-

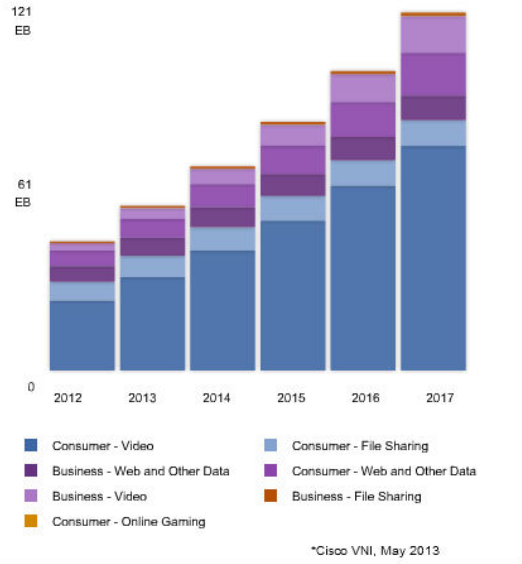

Figure 1.1: *Forecast of the data on mobile networks from 2012 to 2017 (source: Cisco VNI, 2013).*

frequency electromagnetic fields radiated by wireless communications systems and devices in the frequency range of 100 MHz to 6 GHz.

1.2 The role of the engineer in exposure assessment

The research on the exposure to radio-frequency electromagnetic fields situates mainly in three research domains: biology, epidemiology, and dosimetry. A biologist investigates the responses of cells and living animals (such as rodents) to EMF exposure. An epidemiologist attempts to correlate (adverse) health effects to different sources of electromagnetic fields. The field of dosimetry is mainly populated by engineers. Studies on dosimetry aim at measuring, characterizing, and modeling the fields incident on and induced in cells, animals or the human body. Engineers provide the necessary tools and methods to perform a sound assessment of the exposure and develop exposure systems used in animal studies and in-vitro studies.

In exposure assessment a distinction is made depending on the distance of the wireless transmitter to the body. On the one hand, mobile devices are typically operated close to the human body (near field) and require a direct assessment of the induced fields or the absorption in the body. On the other hand, for antennas

operating at large distances from the human body (far field) it is often sufficient to measure the incident electric fields as a first estimate of the induced absorption. This dissertation deals with the dosimetry for mobile devices operated close to the body and the multi-path exposure from base station antennas used in a cellular or wireless local area network.

1.3 The exposure metrics

The dissertation focuses on RF EMF with operating frequencies ranging from 100 MHz to 6 GHz. In this frequency range, several quantities are used to express exposure: incident electric field levels (E), incident magnetic field (H), incident power density (S) and specific absorption rate in the human body (SAR).

Electromagnetic fields radiated by antennas propagate in the environment. These propagating waves interact with the environment (reflection, scattering, attenuation, and diffraction). Electromagnetic waves that hit the body partly scatter at the surface of the body and penetrate in the body. Inside the body, the energy of the electromagnetic fields is absorbed (heating of body tissues) by the body tissue due to the electromagnetic losses of the body, which are expressed in terms of electrical conductivity. The basic quantity for dosimetry is the specific absorption rate (hereinafter denoted as SAR). SAR is defined as the rate at which electromagnetic energy is absorbed (transferred into heat) by the body per unit of mass:

$$SAR\left(r\right) = \frac{\sigma\left(r\right) E_{\mathrm{rms}}\left(r\right)^{2}}{\rho\left(r\right)} \tag{1.1}$$

with r the location in the body, $\mathrm{E_{rms}}$ the root-mean-square (RMS) electric field induced in the body (in V/m), σ the conductivity of the tissue (in S/m) in point r, and ρ the mass density (in kg/m^3).

Because it is impossible to measure the SAR inside the body of a living person, a large part of the research on dosimetry deals with investigating the relationship between the incident fields and the specific absorption rate for all kind of exposure situations. The specific absorption rate is a quantity that is related to short-term thermal effects of radio-frequency electromagnetic field exposure. It can also be used to evaluate long-term non-thermal effects (low level exposure) because it also relates to the induced incident fields.

1.4 Guidelines, standards, and regulations

In 1996, the World Health Organization (WHO) established the international EMF project. Within this project, the WHO evaluates scientific literature, identifies

knowledge gaps, and advises national authorities on the EMF radiation. The international EMF project of WHO works closely together with the International Commission on Non-Ionizing Radiation Protection (ICNIRP).

In 1998, ICNIRP issued guidelines for limiting exposure to time-varying electromagnetic fields. In the United States the recommendations to protect people from hazardous effects of RF electromagnetic fields were developed between 1982 and 1992 by several organizations, such as the American National Standards Institute (ANSI), the Institute of Electrical and Electronics Engineers, Inc. (IEEE), and the National Council on Radiation Protection and Measurements (NCRP) [1–4].

Exposure guidelines and standards define two limits to protect humans against adverse health effects from whole-body and partial-body RF EMF exposures because antennas can be operated close to or far from the body. At large distances from the antennas humans are exposed to the far fields of the antenna(s) (e.g., exposure to base station antennas). Wireless transmitters can also be close to the human body, e.g., mobile phones, walkie-talkies, laptops, access points for wireless local area networks and cordless telephony. In this case, humans are exposed to the near fields of these wireless devices. The exposure limits protect against whole-body and partial-body exposures caused by antennas at large and short distances to the body, respectively.

Exposure guidelines distinguish between occupational or controlled exposure and general public or uncontrolled exposure. Occupational exposure occurs when individuals are exposed in the course of performing their work [5]. This considers healthy adults who are informed about the EMF exposure and who can take measures if limits are exceeded. The ICNIRP exposure limits for occupational exposure are 5 times higher than those for the general public [5]. Limits for general public are lower because they take into account that age and health status differ from that of workers. For instance, children and elderly people are assumed to be more sensitive to EMF exposure.

1.4.1 Exposure limits by ICNIRP

In Europe, national exposure limits are mostly based on the ICNIRP guidelines. ICNIRP provides two classes of guidance: basic restrictions and reference levels. Basic restrictions (BR) are limits on the specific absorption rate that can be directly related to possible health effects. The SAR, however, can not be directly assessed in the human body. Therefore, reference levels (RL) on the incident electric fields are derived for practical exposure assessment and indicate if the basic restrictions are likely to be exceeded. As opposed to SAR, incident field strength can be easily measured. Table 1.1 and Table 1.2 list the basic restrictions and the reference levels for radio-frequency EMF in the frequency range of 100 MHz and 6 GHz issued by ICNIRP, respectively. ICNIRP specifies that the RMS electric and magnetic fields,

power density, and SAR need to be averaged over any 6 min period.

These limits are based on established adverse health effects taking into account a safety factor of 50 and 10 for general public and workers, respectively. Safety factors account for possible additional heath stress in severe environments and possible higher sensitivity to heat stress in certain population groups.

Studies showed that a whole-body temperature increase larger than 1 degree celcius can cause adverse health effects. This temperature increase was not reached for whole-body SAR levels below 4 W/kg and an exposure of up to 30 minutes. Taking into account the safety factors, the basic restrictions on the whole-body SAR are 0.08 W/kg and 0.4 W/kg for general public and occupational exposure, respectively.

To limit partial-body exposure, ICNIRP defines a basic restriction on the peak spatial-averaged SAR in 10 g. The basic restriction for partial-body exposure is based on cataract in a rabbit's eye, which occurred for a SAR level of 100 – 140 W/kg. Taking into account the safety factors, the basic restriction on the peak spatial-averaged SAR in 10 g of contiguous tissue equals 2 W/kg and 10 W/kg for general public and occupational exposure, respectively. The basic restrictions for the limbs are a factor 2 larger than for the head and the trunk because limbs do not contain vital organs.

Exposure characteristic	Whole-body averaged SAR (W/kg)	Localized SAR in 10 g (trunk and head) (W/kg)	Localized SAR in 10 g (limbs) (W/kg)
General public	0.08	2	4
Occupational	0.4	10	20

Table 1.1: *The ICNIRP basic restrictions for general public and occupational exposure.*

Frequency range	RMS electric field (V/m)	RMS magnetic field (A/m)	Equivalent plane-wave power density (W/m^2)
Occupational exposure			
100 MHz - 400 MHz	61	0.16	10
400 MHz - 2000 MHz	$3f^{1/2}$	$0.008f^{1/2}$	f/40
2 GHz - 6 GHz	137	0.36	50
General public exposure			
100 MHz - 400 MHz	28	0.073	2
400 MHz - 2 GHz	$1.375f^{1/2}$	$0.0037f^{1/2}$	f/200
2 GHz - 6 GHz	61	0.16	10

Table 1.2: *The ICNIRP reference levels (RL) for general public and occupational exposure for frequencies ranging from 100 MHz to 6 GHz. f is indicated in MHz.*

The limits specified by ICNIRP are recommended in the European Union [6].

1.4.2 Exposure limits recommended by FCC

In the US, Federal Communications Commission (FCC) adopted the NCRP's recommended Maximum Permissible Exposure limits for field strength and power density for the transmitters operating at frequencies of 300 kHz to 100 GHz in 1996. In addition, the FCC adopted the SAR limits for devices operating within close proximity to the body as specified within the ANSI/IEEE C95.1-1992 guidelines [1]. FCC specifies a limit on the partial-body absorption of 1.6 W/kg in 1 g of tissue. This limit is obtained by multiplying the whole-body limit of 0.08 W/kg with a factor of 20 because studies showed that the ratio of the peak local-averaged SAR in 1 g and the whole-body SAR could be as high as 20 [7].

In 2005, IEEE changed their recommendation on the peak local-averaged SAR from 1.6 W/kg in 10 g to 2 W/kg in 10 g of tissue. Although IEEE harmonized the values of the limits with ICNIRP guidelines, a lot of differences still exists. One of the differences between these two guidelines is the specified averaging volume: ICNIRP specifies a contiguous averaging volume whereas IEEE recommends a cubical averaging scheme. To date, FCC has not adopted to the new recommendation of IEEE and still uses an averaging volume of 1 g of tissue [8].

1.5 Exposure assessment

In exposure assessment, a distinction is made between worst-case and realistic exposure assessment. For compliance testing of the exposure with limits a worst-case approach is required to verify that it is unlikely that exposure limits will be exceeded. Compliance testing is performed before mobile phones are introduced on the market, before base station antennas are put into service, and in-situ to assess the cumulative exposure. Obviously, a worst-case approach largely overestimates the realistic exposure and is, thus, a bad estimator for realistic exposure. Realistic exposure is of interest in epidemiological studies which try to correlate health issues to long-term exposure to low-level, radio-frequency electromagnetic fields. Although a worst-case and a realistic approach differ in methodology, they both use the same measurement instrumentation except from the exposimeter (see page 9) which is solely used to assess realistic exposure. This section provides a brief overview on the instrumentation and tools used to assess the exposure of the human to RF EMF.

1.5.1 Averaging of the specific absorption rate and the fields as defined by standards

Standardization bodies, such as International Electro-technical Commission (IEC), European Committee for Electro-technical Standardization (CENELEC) and IEEE in the US, describe the measurement procedures for testing compliance of wireless

radio-frequency devices with exposure standards or guidelines. We will not discuss into detail these standards but of importance for this dissertation is how these standards specify the averaging of the specific absorption rate.

1.5.1.1 Averaging of specific absorption rate

The SAR is spatially averaged over the mass (M) of the averaging volume (V) and, hence, equals the ratio of the total absorbed power in the volume and the mass of the volume. The mass-averaged SAR ($\mathrm{SAR_M}$) is defined as follows [9]:

$$SAR_{\mathrm{M}} = \frac{1}{M}\int_R SAR\,(r)dm = \frac{1}{M}\int_R \sigma\,(r)\,E_{\mathrm{rms}}\,(r)^2 dV = \frac{P_{\mathrm{abs}}}{M} \qquad (1.2)$$

with R the region of the averaging volume.

The ICNIRP guidelines specify a contiguous volume for the local-averaged SAR in 10 g. This contiguous volume can have any shape and is not adopted by standards on measurement and numerical techniques. Instead, these standard specify cubical averaging volumes. To deal with air enclosures in the cubical averaging volumes – air enclosures occur at the surface of the body (see Figure 1.2) and the lumina inside the human body – a variety of cubical averaging schemes are defined in standards. These averaging volumes are discussed in more detail in Chapter 2.

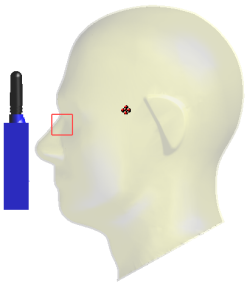

Figure 1.2: *The cubical averaging volume (red box) with air enclosures at the surface of the body.*

1.5.1.2 Averaging of incident fields

The ICNIRP guidelines specify that for compliance testing the RMS incident fields must be spatially averaged over the volume of the body. This is impractical as the volume of the body differs amongst the population. Therefore, standards define several averaging planes and lines of fixed size. As an example, Figure 1.3 shows the spatial-averaging grid as defined by IEC62232 [10].

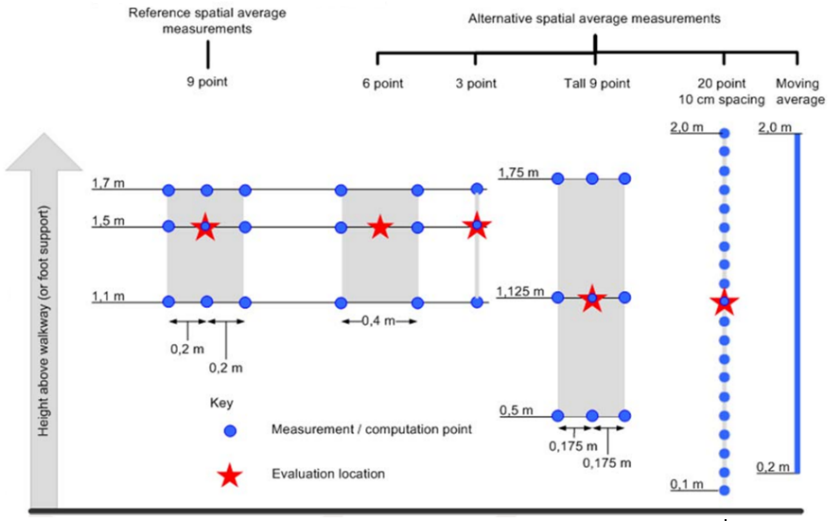

Figure 1.3: *The measurement grids defined by IEC for spatial averaging of the incident fields.*

1.5.2 Measurement techniques

1.5.2.1 Incident fields

Radio-frequency electromagnetic fields span a wide range of frequencies. Every communication technology operates in its designated frequency band. When measuring the exposure, we distinguish between broadband and narrowband measurements. Broadband measurements span a broad frequency band at once and are performed using a field meter and a broadband probe (see Figure 1.4). A single exposure value is obtained for the whole frequency range. Narrowband measurements are band-selective or frequency-selective measurements using a combination of an antenna (e.g., conical dipole or tri-axial isotropic antenna) and a spectrum analyzer. In case of narrowband measurements, an exposure value is obtained for each of the considered frequency bands. Frequency-selective measurements allow identifying the importance of a communication technology in the total exposure.

In epidemiological studies personal exposure meters (PEM), in short exposimeters, are used. Exposimeters are also narrowband devices that measure the exposure in multiple bands at the same time. Commercially available dosimeters are the EME Spy 120/121/140 (Satimo, Brest, France) (see Figure 1.5) and the ESM 140 (Maschek Elektronik, Bad Wrishofen, Germany). These devices are typically worn on the body of a person to assess the personal exposure to RF EMF. Exposimeters are easy to handle but require a measurement protocol [11, 12], have a limited dynamic range with a maximum value of typically 5 V/m, and suffer from

(a) (b)

Figure 1.4: *Instrumentation for assessing incident electric fields: (a) broadband probe and (b) narrowband setup.*

a large number of measurements below the detection limit of the device (non-detects). To handle these large numbers of non-detects in data analysis, Röösli et al. [13] propose the robust regression on order statistics (robust ROS) to determine summary statistics.

Figure 1.5: *The personal dosimeter (EME SPY 140, Satimo, Brest, France) used in epidemiological studies.*

1.5.2.2 Peak local-averaged SAR

Compliance testing of the far-field exposure of (base station) antennas can be determined by verifying compliance with the reference levels on the incident fields and are performed in-situ. For near-field exposure, compliance testing requires the direct assessment of the peak local-averaged SAR. The latter can only be performed in a laboratory in a well-defined environment and under well-defined ex-

posure conditions: the wireless devices are operated in a test-mode to ensure that they radiate at maximum power. The dosimetric measurement setup consists of a dosimetric probe connected to a data acquisition equipment (DAE), a robot, a measurement server, a computer or laptop for operating the measurement system, and a flat or a standardized head phantom (Specific Anthropomorphical Mannequinn or SAM) filled with tissue simulating liquid (see Figure 1.6). The wireless device is placed at short distance to the phantom (touch or 15 mm). Before an experimental SAR assessment, a system performance check is performed to verify that the measurement system operates within its boundaries. Standardized dipole antennas are used in a system performance check. The dipole is fed by an RF generator. The input power of the antennas is measured by a power meter via a directional coupler. This setup is also used for measuring the local absorption induced by the walkie-talkie model developed in Chapter 4. The setup is shown if Figure 1.6.

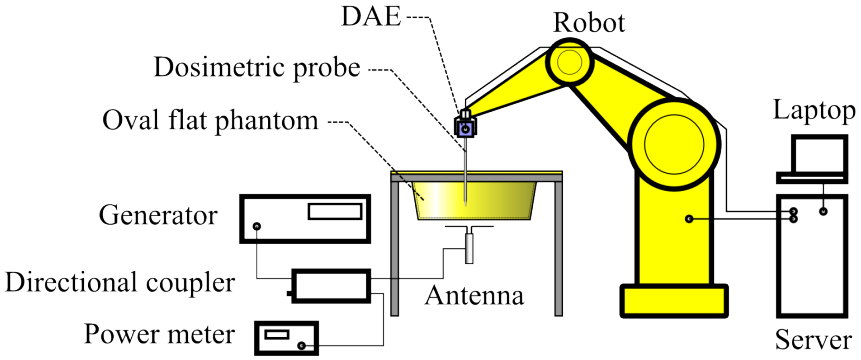

Figure 1.6: *The dosimetric measurement setup for compliance testing of mobile devices.*

A dosimetric probe consists of three perpendicular short-dipole antennas, recording the electric fields inside the tissue-simulating liquid. A dosimetric probe is a broadband probe with a large dynamic range. The calibration parameters of the probe depend on the frequency and the tissue used for the SAR assessment. The robot positions the probe inside the tissue-simulating liquid. The phantom and the tissue properties of the liquid are designed to provide a conservative estimate of the peak local-averaged SAR obtained in realistic human heads. Two phantoms exist for compliance testing: the Specific Anthropomorphic Mannequin (SAM) head and the oval flat phantom. The former is used for compliance testing of mobile phones operated next to the ear [14], the latter is used for compliance testing of body-worn, wearable, and portable devices operated in the proximity of the human body (such as the walkie-talkie) [15].

1.5.2.3 Whole-body averaged SAR

To assess a partial-body SAR, such as the local-averaged SAR in 1 g and 10 g, the knowledge of the SAR distribution is required. This distribution can only be assessed directly in the tissue. But, the total- or whole-body averaged SAR can be determined from the total absorbed power inside the body (see Eq. (1.2)) because mass averaging is used. As opposed to the local-averaged SAR, the total absorbed power in a body can be assessed from reflection measurements. For instance, reverberation chambers are used to measure the total absorbed power in (homogeneous) head phantoms.

Recently, Bamba et al. [16] developed a measurement methodology to assess in-situ the whole-body averaged SAR in closed environments.The whole-body averaged SAR can be assessed in closed environments (i.e., rooms) by measuring the reverberation time with and without people inside the room. From the difference in reverberation time, the whole-body SAR can be calculated [16]. This measurement methodology is based on room electromagnetics theory [17].

1.5.3 Numerical exposure assessment

Measuring the induced fields is impossible in a living human and we have to turn to numerical techniques for characterizing the SAR in a human body. This requires realistic models of humans and full-wave 3D electromagnetic solvers to compute the fields induced in the body.

Computational methods used for solving electromagnetic problems in the radio-frequency range of 100 MHz to 6 GHz are the Finite-Difference Time-Domain (FDTD) method, the Method-of-Moments, and the Finite Element Method (FEM). The FDTD method is an efficient method for computing electromagnetic fields because of its straightforward treatment of material inhomogeneities, such as the human body [18, 19]. The FDTD method solves the partial differential Maxwells equations in the time domain. The FDTD method requires a spatial and temporal discretization of the simulation domain and the simulation domain is terminated by absorbing boundary conditions to mimic the infinite free space. Nowadays, the availability of graphical processing units (GPU) and sufficient random-access-memory (RAM) allow the calculation of very complex electromagnetic problems.

The Method-of-Moments (MoM) is a frequency domain technique that is very successful in antenna design. The radiating and scattering structures are represented by equivalent currents, often surface currents. These currents are discretized into wire segments or surface patches. The interaction between the segments and patches are computed by using a Green function and solving a matrix equation [19]. The MoM does not require the termination of the simulation domain by means of absorbing boundary conditions and is very powerful to calculate the fields at any distance of an antenna. For dosimetric calculations, the MoM is of-

ten combined with the Finite Element Method (FEM) to compute the fields inside lossy dielectric bodies. This hybrid technique allows the assessment of the SAR in homogeneous bodies, but performs poorly with respect to the FDTD method for heterogeneous bodies.

Despite the advancement in computer hardware (GPUs, parallel computing, availability of RAM), it is sometimes necessary to combine the best of the FDTD and the MoM techniques in a hybrid method. In dosimetry, the hybrid methods are applied to electromagnetic problems where the antenna is at a large distance (a couple of meters) of the human body because the FDTD discretizes all the free space between the antenna and the body resulting in huge FDTD simulations. Typically, the MoM computes the incident fields on a closed surface around the human body (Huyghens' surface) [20]. Afterwards, the FDTD method calculates the electromagnetic fields induced in the heterogeneous body from the incident fields on the Huygens' surface. This hybrid approach reduces the FDTD simulation domain to the area around the human body because the body can be isolated from the antenna and the environment. This hybrid method requires that there is no capacitive coupling or conducting effects between, on the one hand, the human body and, on the other hand, the antenna and the environment.

1.5.3.1 Realistic human body models

A number of realistic heterogeneous body models are currently used for electromagnetic field simulations. These models are obtained from Magnetic Resonance Imaging (MRI), Computer Tomography (CT), and anatomical images. Data are represented by voxel images of thin slices of the body, and each voxel corresponds to a particular type of the body tissue. Currently a large data set of heterogeneous human body models are available and represent males and females of different age and different populations. The various electric parameters of the body tissues can be obtained (i.e., for required frequency band) from the 4-Cole-Cole Model described in [21]. Several human models are developed especially during the last decade. The Virtual Family (see Figure 1.7 and Virtual class room [22] are a family of magnetic resonance imaging (MRI) models. There are also the Japanese models (male and female model) [23]), Korean models [24, 25] Chinese adult models (male and female models [26]), Norman and Naomi models [27, 28], Zubal adult model [29] and Visible human model [30].

1.6 Main research contributions and outline

This dissertation dealt in the first part with the dosimetry of the SAR in the human body for wireless devices operated in front of the face for positions other than the ear position. In a second part the influence of the environment on the whole-body

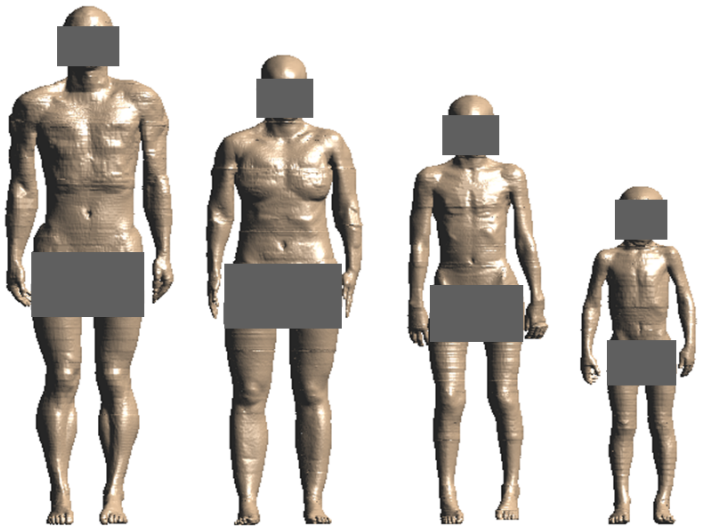

Figure 1.7: *The Virtual Family.*

averaged SAR is investigated in the near field as well as in the far field.

This chapter introduced briefly various aspects of exposure assessment for electromagnetic fields in the radio frequencies from 100 MHz to 6 GHz.

Chapter 2 describes the investigation of the averaging volumes for assessing the local absorption in the human body. International guidelines and standards for radio-frequency exposure limit the maximum local absorption (in terms of the specific absorption rate (SAR)) in a volume containing 1 g or 10 g of tissue. The ICNIRP guidelines, on which most European limits are based, define limits for the local absorption but do not specify the shape of the volume over which the absorption needs to be averaged. Standards mainly define a cubical averaging volume. Chapter 2 evaluates cubical averaging volumes that are defined in measurements standards against a worst-case and a spherical averaging volume. Peak local absorption always occurs near the body surface in homogeneous tissue. We observed that a cubical averaging volume yields lower local-averaged SAR values than the spherical averaging scheme because the spherical averaging scheme takes into account more absorption values at the surface of the body.

The vast amount of studies on dosimetry deals with the exposure due to mobile devices and base station antennas for cellular communication systems. With the case study of the walkie-talkie, we draw the attention to a device that gained interest as an alternative for cellular phones for short-range communications and as a toy. The advantages of walkie-talkies are their ease-of-use (push-to-talk), their cheap price, and their free-of-charge communication. In Europe, a walkie-talkie

operates according to the Private Mobile Radio at 446 MHz (PMR 446) standard. The relative low frequency, the effective radiated power of 500 mW, the use of walkie-talkies by children, and the limited number of exposure studies for walkie-talkies attracted our attention to these devices. The next two chapters present the design of walkie-talkie models and investigated the absorption induced by walkie-talkies. In Chapter 3, we designed walkie-talkie models by reverse engineering of commercially available devices. The models were numerically and experimentally validated in free space against the real devices in terms of antenna characteristics and near-field behavior. In order to use the model as a substitute for real walkie-talkies, we do not only need a good physical representation of a walkie-talkie, but we also need the power typically transmitted by these devices. Therefore, the effective radiated powers of the commercial devices were measured.

The subject of Chapter 4 is the dosimetry of the absorption in the human head induced by the electromagnetic fields of walkie-talkies. The commercial devices showed to be compliant with current absorption limits for the local-averaged SAR. The walkie-talkie model with coating around the antenna was validated and showed that it overestimates the local-averaged SAR of the real walkie-talkies in a dosimetric study. The model was used in the numerical study of the absorption of the fields induced by walkie-talkies in realistic human body models. We showed that the ageing only marginally influences the absorption in the head and that the flat phantom is conservative for heterogeneous head models and the homogeneous Specific Anthropomorphc Mannequin (which is used for the compliance testing of mobile phones) when the walkie-talkie is vertically positioned in front of the face.

The second part of the dissertation deals with the multi-path exposure to base station antennas. Until recently, most studies on far-field exposure assumed single incident plane-wave exposure or took into account only one reflected plane wave. Travelling electromagnetic waves interact (reflection, scattering, refraction, and transmission) with the environment resulting in a multi-path exposure of people to radio-frequency electromagnetic fields. In a multi-path environment, exposure varies in time and space resulting in a distribution of absorption values. The exposure in a multi-path environment can be quantified by specifying a range of exposure cases or by providing summary statistics on the exposure.

Chapter 5 investigates the influence of highly reflective environments on the absorption in a worker at short distances of a base station antenna in the frequency range of 300 MHz to 5 GHz. This study supported TC106 in the development of the standard IEC62232 on the methods for the assessment of electric, magnetic and electromagnetic field associated with human exposure. We found that the local and the whole-body absorption in a reflecting environment and at short distances from the base station antenna varied from -8.7 dB to 8 dB with respect to absorption in the free-space environment for the investigated configurations, but a worst-case environment could not be determined. We also showed that the ICNIRP reference

levels are not always conservative with respect to the basic restrictions in a highly reflective environment and for distances below 10 m from the base station antenna.

In Chapter 6 we developed and validated a numerical method, called the statistical multipath exposure method or SME method, to determine quickly the distribution of the whole-body absorption in rotation symmetric (e.g., spheroid) and realistic human bodies in a realistic environment. The SME method assesses the whole-body absorption in a multipath environment from precomputed total fields on a closed surface around the human body for a limited number of single incident plane waves and uses the linearity of Maxwell's equations. The total fields are precomputed by full-wave electromagnetic solvers. This fast method accelerates the computations by at least 45 % compared to the finite-difference time-domain (FDTD) method. The SME method was validated with 3D full-wave FDTD computations. The uncertainty introduced by the presented method with respect to FDTD computations depends on the number of precomputed fields and can be as low as 1 %. We found that the whole-body absorption due to multipath exposure can exceed the whole-body absorption for worst-case single plane-wave exposure. We also found that the ICNIRP reference levels were not always compliant with the basic restrictions for multipath exposure. The SME method was also used to determine the number of exposure cases needed for accurately assessing the summary statistics of the whole-body absorption in a realistic environment. We observed that the mean whole-body absorption can be estimated from about 100 exposure cases, while assessing accurately summary statistics requires at least 4000 exposure cases. We also applied the SME method for assessing the whole-body absorption in a realistic model of a 6-year-old boy exposed to the GSM downlink at 950 MHz and showed that the absorption in realistic human body models exceeds the absorption in homogeneous prolate spheroid models with the dielectric properties of head tissue suggested in IEC62209 standard. We applied the SME tool to evaluate the whole-body absorption due to the exposure of wireless communication systems measured in four indoor environments (schools, homes, day nurseries, and offices). The whole-body absorption in these indoor environments showed to be compliant with the ICNIRP basic restriction for general public. We also observed that in indoor environments the absorption induced by indoor sources can become larger than the values induced by outdoor sources, especially when the indoor wireless sources are approached.

Chapter 7 deals with the influence of the body on the exposimeter reading. Personal exposure meters or dosimeters are frequently employed in epidemiological studies to record the exposure of a person. The exposimeter is worn on the body and measures the exposure (i.e., the electric fields) in multiple frequency bands during a certain period of time. When the exposimeter is worn on the body, the coupling between the body and the exposimeter, and the shadowing of the body change the exposimeter reading compared with a free-space measurement of the

exposimeter. We used the SME method, developed in Chapter 6, to investigate the influence of the human body on the dosimeter reading. We found that the exposimeter worn on the body underestimates the incident field levels by 3.4 dB on average.

Finally, Chapter 8 concludes the dissertation by summarizing the major outcomes of the research performed within this dissertation and points out future research oppertunities based on the achievements presented in this dissertation.

1.7 Overview of publications

1.7.1 Publications in peer-reviewed journals

[1] Vermeeren G, Markakis I, Goeminne F, Samaras T, Martens L and Joseph W 2013 Spatial and temporal RF electromagnetic field exposure of children and adults in indoor micro environments in Belgium and Greece *Prog Biophys Mol Biol* Accepted for publication.

[2] Vermeeren G, Joseph W and Martens L 2013 Statistical multi-path exposure method for assessing the whole-body sar in a heterogeneous human body model in a realistic environment *Bioelectromagnetics* **34** 240–51.

[3] Vermeeren G, Gosselin MC, Kühn S, Kellerman V, Hadjem A, Gati A, Joseph W, Wiart J, Meyer F, Kuster N and Martens L 2010 The influence of the reflective environment on the absorption of a human male exposed to representative base station antennas from 300 MHz to 5 GHz *Physics in Medicine and Biology* **55** 5541–55.

[4] Vermeeren G, Joseph W, Olivier C and Martens L 2008 Statistical multi-path exposure of a human in a realistic electromagnetic environment *Health Physics* **94** 345–54.

[5] Vermeeren G, Joseph W and Martens L 2008 Whole-body SAR in spheroidal adult and child phantoms in realistic exposure environment *Electronics Letters* **44** 1–2.

[6] Vermeeren G, Rogier H, Olyslager F and De Zutter D 2002 Low-cost planar rectangular ring antenna for operation in HiperLAN band *Electronic Letters* **38** 208–9.

[7] Vermeeren G, Rogier H, Olyslager F and De Zutter D 2001 Simple low-cost planar antenna for indoor communication under the Bluetooth protocol *Electronic Letters* **37** 1153–4.

[8] Joseph W, Vermeeren G, Verloock L and Goeminne F 2012 In situ magnetic field exposure and ICNIRP-based safety distances for electronic article surveillance systems *Radiation Protection Dosimetry* **148 (4)** 420–7.

[9] Gosselin M, Vermeeren G, Kühn S, Kellerman V, Benkler S, Uusitupa T, Joseph W, Gati A, Wiart J, Meyer F, Martens L, Nojima T, Hikage T, Balzano Q, Christ A and Kuster N 2011 Estimation Formulas for the Specific Absorption Rate in Humans Exposed to Base-Station Antennas *IEEE Trans. Electromagn. Compat.* **53 (4)** 909–22.

[10] Joseph W, Vermeeren G, Verloock L and Martens L 2010 Estimation of whole-body SAR from electromagnetic fields using personal exposure meters *Bioelectromagnetics* **31 (4)** 286–95.

[11] Joseph W, Vermeeren G and Martens L 2007 Correction factor to be applied to the SAR in phantom models for occupational electromagnetic exposure *Microw. Opt. Technol. Lett.* **49 (3)** 652–5.

[12] Peyman A, Gabriel C, Grant EH, Vermeeren G and Martens L 2009 Variation of the dielectric properties of tissues with age: the effect on the values of SAR in children when exposed to walkie-talkie devices *Physics in Medicine and Biology* **54** 227–41.

[13] Joseph W, Vermeeren G, Verloock L, Heredia MM and Martens L 2008 Characterization of personal RF electromagnetic field exposure and actual absorption for the general public *Health Physics* **95** 317–30.

[14] Joseph Wout, Goeminne F, Verloock L, Vermeeren G and Martens L 2012 In situ occupational and general public exposure to VHF/UHF transmission for air traffic communication *Radiat. Prot. Dosim.* **151 (3)** 411–9.

[15] Joseph W, Goeminne F, Vermeeren G, Verloock L and Martens L 2012 In situ exposure to non-directional beacons for air traffic control *Bioelectromagnetics* **33 (3)** 274–7.

[16] Bamba A, Joseph W, Andersen JB, Tanghe E, Vermeeren G, Plets D, Nielsen J and Martens L 2012 Experimental assessment of specific absorption rate using room electromagnetics *IEEE Trans. Electromagn. Compat.* **54 (4)** 747–57

[17] Joseph W, Verloock L, Goeminne F, Vermeeren G and Martens L 2012 In situ LTE exposure of the general public: characterization and extrapolation *Bioelectromagnetics* **33 (6)** 466–75.

[18] Joseph W, Verloock L, Goeminne F, Vermeeren G and Martens L 2012 Assessment of RF exposures from emerging wireless communication technologies in different environments *Health Phys.* **102 (2)** 161–72.

[19] Joseph W, Pareit D, Vermeeren G, Naudts D, Verloock L, Martens L and Moerman I 2013 Determination of the duty cycle of WLAN for realistic radio frequency electromagnetic field exposure assessment *Prog. Biophys. Mol. Biol.* **111 (1)** p.30–6

[20] Joseph W, Frei P, Röösli M, Vermeeren G, Bolte J, Thuroczy G, Gajsek P, Trcek T, Mohler E, Juhasz P, Finta V and Martens L 2012 Between-country comparison of whole-body SAR from personal exposure data in urban areas *Bioelectromagnetics* **33 (8)** 682–94.

[21] Joseph W, Frei P, Röösli M, Thuroczy G, Gajsek P, Trcek T, Bolte J, Vermeeren G, Mohler E, Juhasz P, Finta V and Martens L 2010 Comparison of personal radio frequency electromagnetic field exposure in different urban areas across Europe *Environ. Res.* **110 (7)** 658–63.

[22] Joseph W, Verloock L, Goeminne F, Vermeeren G and Martens L 2010 Assessment of general public exposure to LTE and RF sources present in an urban environment *Bioelectromagnetics* **31 (7)** 576–9.

[23] Kurup D, Joseph W, Vermeeren G and Martens L 2012 In-body path loss model for homogeneous human tissues *IEEE Trans. Electromagn. Compat.* **54 (3)** 556–64.

[24] Kurup D, Joseph W, Tanghe E, Vermeeren G and Martens L 2011 Extraction of antenna gain from path loss model for in-body communication *Electron. Lett.* **47 (23)** 1262–3.

[25] Kurup D, Scarpello ML, Vermeeren G, Joseph W, Dhaenens K, Axisa F, Martens L, Vande Ginste D, Rogier H and Vanfleteren J 2011 In-body path loss models for implants in heterogeneous human tissues using implantable slot dipole conformal flexible antennas *EURASIP J. Wirel. Commun. Netw.* **51**.

[26] Kurup D, Joseph W, Vermeeren G and Martens L 2009 Path loss model for in-body communication in homogeneous human muscle tissue **Electron. Lett. 45 (9)** 453-U30.

[27] Verloock L, Joseph W, Vermeeren G and Martens L 2010 Procedure for assessment of general public exposure from Wlan in offices and in wireless sensor network testbed *Health Phys.* **98 (4)** 628–38

[28] Reusens E, Joseph W, Vermeeren G, Verloock L and Martens L 2010 WBAN transmission model for coils at 10.8 MHz in free space and near a flat conducting medium *IEEE Trans. Electromagn. Compat.* **52 (3)** 521–9.

[29] Reusens E, Joseph W, Latr B, Braem B, Vermeeren G, Tanghe E, Martens L, Moerman I and Blondia C 2009 Characterization of on-body communication channel and energy efficient topology design for wireless body area networks *IEEE T. Inf. Technol. Biomed.* **13 (6)** 933–45.

[30] Reusens E, Joseph W, Vermeeren G, Verloock L and Martens L 2008 Transmission model for coils near flat conducting medium simulating a Wireless Body Area Network at 10.8 MHz *Electron. Lett.* **44 (19)** 1115–6.

[31] Roelens L, Joseph W, Reusens E, Vermeeren G and Martens L 2008 Characterization of scattering parameters near a flat phantom for wireless body area networks *IEEE Trans. Electromagn. Compat.* **50 (1)** 185–93.

[32] Roelens L, Van den Bulcke S, Joseph W, Vermeeren G and Martens L 2006 Path loss model for wireless narrowband communication above flat phantom *Electron. Lett.* **42 (1)** 10–1.

[33] Scarpello ML, Kurup D, Rogier H, Vande Ginste D, Axisa F, Vanfleteren J, Joseph W, Martens L, Vermeeren G 2011 Design of an implantable slot dipole conformal flexible antenna for biomedical applications *IEEE Trans. Antennas Propag.* **59 (10)** 3556–64.

1.7.2 Publications in conference proceedings

[1] Vermeeren G, Goeminne F, Joseph W and Martens L 2013 Statistical whole-body averaged SAR in indoor microenvironments by cellular communication and indoor signals *BioEM2013 — Joint Meeting of The Bioelectromagnetics Society and the European BioElectromagnetics Association, Thessaloniki, Greece, 10-14 June 2013*.

[2] Vermeeren G, Goeminne F, Joseph W and Martens L 2012 Measurement of the electromagnetic field exposure in indoor environments by spectrum analyzer and exposimeters *The Bioelectromagnetics Society 34th Annual Meeting Abstract Collection - Complete Collection, Brisbane, Australia, 17-22 June 2012* 291–293.

[3] Vermeeren G, Joseph W and Martens L 2012 Whole-body absorption in heterogeneous adult and child human body model in realistic environments *7th ICNIRP NIR Workshop, Edinburgh, UK, 9-11 May 2012*.

[4] Vermeeren G, Joseph W and Martens L 2011 Statistical multi-path exposure tool for realistic human body models *The Bioelectromagnetics Society 33th Annual Meeting Abstract Collection — Platform Sessions, Hallifax, Canada, 12-17 June 2011*.

[5] Vermeeren G, Joseph W and Martens L 2011 Measurement of the duty cycle of WLAN in different environments *The Bioelectromagnetics Society 33th Annual Meeting Abstract Collection —Session PB, Hallifax, Canada, 12-17 June 2011*.

[6] Vermeeren G, Markakis I, Joseph W, Samaras T and Martens L 2011 Measurement of the time-evolution of the exposure to electromagnetic fields by exposimeters *The Bioelectromagnetics Society 33th Annual Meeting Abstract Collection — Session PA, Hallifax, Canada, 12-17 June 2011* PA-119.

[7] Vermeeren G, Joseph W and Martens L 2010 Influence of the body on exposimeter reading *The Bioelectromagnetics Society 33th Annual Meeting Abstract Collection, Seoul, Korea, 14-18 June 2010*.

[8] Vermeeren G, Gosselin MC, Kühn S, Joseph W, Martens L and Kuster N 2009 Influence of a Reflective Environment on the Absorption of a Human Male Exposed to Representative Base Station Antennas from 300 MHz to 5 GHz *BioEM2009 — Joint Meeting of the Bioelectromagnetics Society and the European BioElectromagnetics Association, Davos, Switzerland, 14-19 June, 2009* P-31.

[9] Vermeeren G, Joseph W and Martens L 2008 Whole-body SAR in spheroidal adult and child phantoms in a realistic exposure environment *Abstracts for the 30th Bioelectromagnetics Society Annual Meeting, San Diego, California, 8-12 June, 2008*.

[10] Vermeeren G, Joseph W, Olivier C and Martens L 2007 Statistical multipath exposure of a human in a realistic electromagnetic environment *The Bioelectromagnetics Society 29th Annual Meeting Abstract Collection, Kanazawa, Japan, 10-15 June, 2007* 249–52.

[11] Vermeeren G, Olivier C, Joseph W and Martens L 2007 Statistical model of the electromagnetic fields in a realistic environment *The Bioelectromagnetics Society 29th Annual Meeting Abstract Collection, Kanazawa, Japan, 10-15 June, 2007* P-24, 288–90.

[12] Vermeeren G, Joseph W, Martens L, Preiner P, Cecil S, Mitrevski N, Neubauer G, Kühn S and Kuster N 2007 Influence of a perfectly conducting ground on the whole-body SAR *Book of Abstracts of the 8th International Congress of the European BioElectromagnetics Association*.

[13] Vermeeren G, Joseph W and Martens L 2006 Assessment of the SAR in the SAM Head Phantom for a PMR446 Radio Held in Four Typical Positions Close to the Head *The Bioelectromagnetics Society 28th Annual Meeting, Cancún, Mexico, 11-15 June, 2006* 42–5.

[14] Vermeeren G and Martens L 2005 Assessment of the SAR for a Walkie-talkie Setup *BioEM2005 — A joint meeting of The Bioelectromagnetics Society and The European BioElectromagnetics Association — Abstract Collection, Dublin, Ireland* 487–8.

[15] Vermeeren G and Martens L 2004 Comparison of Averaging Volumes Used for Averaging of Local SAR *Twenty-Sixth Annual Meeting, Washington, DC 20008, US, 20–40 June, 2004* 143–5.

[16] Vermeeren G and Martens L 2004 Interaction of wireless devices with the body *5th FTW PhD Symposium* Interactive Poster Session, Paper 128.

[17] Thielens A, Vermeeren G, Joseph W and Martens L 2012 Influence of the incident angle of single plane-waves on the organ specific averaged SAR at 950 MHz *34th Annual Meeting of the Bioelectromagnetics Society, Proceedings* 286–9.

[18] Joseph W, Verloock L, Goeminne F, Vermeeren G and Martens L 2012 LTE exposure assessment and extrapolation *34th Annual Meeting of the Bioelectromagnetics Society, Proceedings* 14–6

[19] Joseph W, Goeminne F, Vermeeren G, Verloock L and Martens L 2012 Exposure to air traffic control systems *34th Annual Meeting of the Bioelectromagnetics Society, Proceedings* 16–8.

[20] Bamba A, Joseph W, Vermeeren G, Tanghe E and Martens L 2012 Validation of the experimental whole-body SAR assessment method in a complex indoor environment *34th Annual Meeting of the Bioelectromagnetics Society, Proceedings* 320–2.

[21] Bamba A, Joseph W, Vermeeren G, Tanghe E and Martens L 2012 The DMC contribution in the human absorption in an indoor environment *6th European Conference on Antennas and Propagation, Proceedings IEEE* 460–2.

[22] Bamba A, Tanghe E, Joseph W, Vermeeren G, Plets D and Martens L 2012 Theory for exposure prediction in an indoor environment due to UWB systems *IEEE Antennas and Propagation Society International Symposium*.

[23] Kurup D, Joseph W, Tanghe E, Vermeeren G and Martens L 2012 Antenna independent path loss model for in-body communication in homogeneous tissue *6th European Conference on Antennas and Propagation, Proceedings IEEE* 3375–7.

[24] Thielens A, Vermeeren G, Joseph W and Martens L 2012 Organ specific averaged SAR for the central nervous system *7th International Workshop on Non-Ionizing Radiation, Abstracts*.

[25] Thielens A, Vermeeren G, Kurup D, Joseph W and Martens Luc 2012 Compliance boundaries for LTE base station antennas at 2600 MHz *6th European Conference on Antennas and Propagation, Proceedings (IEEE)* 889–2.

[26] Thielens A, Vermeeren G, Kurup D, Joseph W, Martens L 2012 Organ specific averaged SAR near multiple-frequency base station antennas *34th Annual Meeting of the Bioelectromagnetics Society, Proceedings* 289–91.

[27] Thielens A, Vermeeren G, Joseph W and Martens L 2011 Organ specific averaged SAR in a realistic environment at 950 MHz **33nd annual meeting of the Bioelectromagnetics Society, Abstracts** 1–2.

[28] Joseph W, Verloock L, Goeminne F, Vermeeren G and Martens L 2011 General public exposure to LTE in an urban environment *10th international congress of the European BioElectromagnetics Assocation, Proceedings* European BioElectromagnetics Assocation (EBEA).

[29] Joseph W, Frei P, Röösli M, Thuroczy G, Gajsek P, Trcek T, Bolte J, Vermeeren G, Mohler E, Juhasz P, Finta V and Martens L 2011 Personal radio frequency exposure comparison among five countries in urban areas *10th international congress of the European BioElectromagnetics Assocation, Proceedings*.

[30] Bamba A, Andersen JB, Joseph W, Plets D, Tanghe E, Vermeeren G, Nielsen JO and Martens L 2011 Experimental specific energy absorption rate assessment from absorption cross section measurement for far-field exposure at 2-3 GHz *Proceedings of 33nd annual meeting of the Bioelectromagnetics Society*.

[31] Joseph W, Verloock L, Vermeeren G, Goeminne F and Martens L 2011 Assessment of field exposure by electronic article surveillance systems *33nd annual meeting of the Bioelectromagnetics Society, Proceedings*.

[32] Bamba A, Joseph W, Plets D, Tanghe E, Vermeeren G, Martens L, Andersen JB and Nielsen JO 2011 Assessment of reverberation time by two measurement systems for room electromagnetics analysis *IEEE Antennas Propag. Soc., Int. Symp.* 3106–9.

[33] Gosselin MC, Kellerman V, Vermeeren G, Benkler S, Kühn S, Hadjem A, Gati A, Joseph W, Wong MF, Wiart J, Meyer F, Martens L and Kuster N 2009 Hybrid SAR analysis of various human models in front of base station antennas in the frequency range from 300 MHz to 5000 MHz **BioEM, Abstract collection**.

[34] Kuster N, Kühn S, Pedersen G, Samaras T, Vermeeren G, Martens L and Andersen JB 2011 Exposure from WiFi: levels of exposure, challenges in exposure assessment and compliance testing *33nd annual meeting of the Bioelectromagnetics Society, Abstracts* 1–2.

[35] Martens L, Kurup D, Joseph W and Vermeeren G 2011 In-body path loss model for homogeneous and heterogeneous human tissues *XXX URSI general assembly and scientific symposium of the international union of radio science, Proceedings* 1–4.

[36] Joseph W, Verloock L, Goeminne F, Vermeeren G and Martens L 2010 Assessment of mobile WiMAX exposure in an urban environment *EMF Bordeaux event: programme* European BioElectromagnetics Association (EBEA). 55–6.

[37] Joseph W, Verloock L, Vermeeren G and Martens L 2010 General public exposure due to electromagnetic fields of new wireless technologies in different environments *32nd annual meeting of the Bioelectromagnetics Society, Abstracts*.

[38] Joseph W, Verloock L, Vermeeren G and Martens L 2010 Accurate assessment of WLAN exposure in a wireless sensor testbed *32nd annual meeting of the Bioelectromagnetics Society, Abstracts*.

[39] Kurup D, Joseph W, Vermeeren G and Martens Luc 2010 In-body path loss model for homogeneous human muscle, brain, fat and skin *Proceedings of the fourth European Conference on Antennas and Propagation. IEEE*.

[40] Kurup D, Joseph W, Vermeeren G, Martens L, Scarpello ML, Vande Ginste D and Rogier H 2010 Simulation of path loss between biocompatible antennas embedded in homogeneous human tissues and comparison of their specific absorption rate *IEEE Antennas and Propagation Society International Symposium*.

[41] Joseph W, Vermeeren G and Martens L 2009 Calculation of whole-body SAR from exposimeter measurements for different phantoms *BioEM, Abstract collection*.

[42] Kurup D, Joseph W, Vermeeren G and Martens Luc 2009 Simulation of the path loss between insulated dipoles embedded in homogeneous human muscle tissue *2009 IEEE Antennas and Propagation Society international symposium and USNC/URSI National Radio Science meeting, vols 1-6* 1808–11.

[43] Joseph W, Vermeeren G, Verloock L, Heredia MM and Martens L 2008 Personal RF electromagnetic field exposure and relation with actual absorption for general public *The Bioelectromagnetics Society 30th annual meeting abstract collection* 165–8.

[44] Reusens E, Joseph W, Vermeeren G, Kurup D and Martens L 2008 Real human body measurements, model, and simulations of a 2.45 GHz wireless body area

network communication channel *5th International Summer School and Symposium on Medical Devices and Biosensors (IEEE)* 149–52.

[45] Neubauer G, Preiner P, Cecil S, Vermeeren G, Joseph W, Martens L, Kühn S and Kuster N 2007 Averaging methods for reliable measurements *29th Annual Meeting of the Bioelectromagnetics Society, 29th, Abstract book* 333–4.

[46] Preiner P, Cecil S, Mitrevski N, Rusu B, Neubauer G, Vermeeren G, Joseph W, Martens L, Kühn S and Kuster N 2007 Radio frequency averaging methods *Book of Abstracts of the 8th International Congress of the European BioElectromagnetics Association*.

[47] Reusens E, Joseph W, Vermeeren G and Martens L 2007 On-body measurements and characterization of wireless communication channel for arm and torso of human *4th International Workshop on Wearable and Implantable Body Sensor Networks (BSN)* 264–9.

[48] Reusens E, Joseph W, Vermeeren G, Martens L, Latre B, Moerman I, Braem B and Blondia C 2007 Path loss models for wireless communication channel along arm and torso: measurements and simulations *IEEE Ant. Propagat. Soc. Int. Sym. 2007* 336–9.

[49] Neubauer G, Cecil S, Preiner P, Mitrevski N, Vermeeren G, Joseph W, Martens L, Kühn S and Kuster N 2006 The relation between SAR and the electromagnetic field distribution for heterogeneous exposure conditions *Proceedings of the European Conference on Antennas and Propagation (EUCAP 2006)*.

[50] Martens L and Vermeeren G 2006 Dosimetric evaluation for walkie-talkies used by children (invited abstract) *Abstract Book of the FGF-Workshop 'Do Children Represent a Special Sensitive Group for EMF-Exposure'?* 30–30.

[51] Martens L and Vermeeren G 2005 Electromagnetic dosimetry of the SAR for a walkie-talkie set-up *Proceedings of the XXVIIIth General Assembly of International Union Radio Science (URSI)*.

[52] Latre B, Vermeeren G, Martens L and Demeester P 2004 Networking and propagation issues in body area networks *Proceedings of the 11th Symposium on Communications and Vehicular Technology in the Benelux, SCVT 2004*.

References

[1] FCC. Available from: http://www.fcc.gov/encyclopedia/radio-frequency-safety.

[2] ANSI. *American National Standard for Safety Levels with Respect to Human Exposure to Radio Frequency Electromagnetic Fields, 300 kHz to 300 GHz (ANSI C95.1)*, 1982.

[3] IEEE. *IEEE Standard for Safety Levels with Respect to Human Exposure to Radio Frequency Electromagnetic Fields, 3 kHz to 300 GHz (IEEE C95.1-1991)*, 1992.

[4] NCRP. *Biological effects and exposure criteria for radiofrequency electromagnetic fields*, 1986.

[5] ICNIRP. *Guidelines for limiting exposure to time-varying electric, magnetic, and electromagnetic fields (up to 300 GHz)*. Health Physics, 4:494–522, 1998.

[6] The Council of the European Union. *COUNCIL RECOMMENDATION of 12 July 1999 on the limitation of exposure of the general public to electromagnetic fields (0 Hz to 300 GHz) (1999/519/EC)*. Official Journal of the European Communities, L199:59–70, 1999.

[7] J. C. Lin. *Safety Standards for Human Exposure to Radio Frequency Radiation and Their Biological Rationale*. IEEE Microwave Magazine, (December):22–6, December 2003.

[8] J. Lin. *A New IEEE Standard for Safety Levels with Respect to Human Exposure to Radio-Frequency Radiation*. IEEE Antennas Propag. Mag., 48(1):157–9, 2006.

[9] IEEE. *IEEE Recommended Practice for Measurements and Computations of Radio Frequency Electromagnetic Fields With Respect to Human Exposure to Such Fields, 100 kHz-300 GHz (IEEE Std. C95-3-2002)*, 2002.

[10] IEC. *Determination of RF field strength and SAR in the vicinity of radiocommunication base stations for the purpose of evaluating human exposure (IEC-62232)*, 2011.

[11] S. Mann. *Assessing personal exposures to environmental radiofrequency electromagnetic fields*. Comptes rendus physique, 11:541–55, 2010.

[12] M. Röösli, P. Frei, J. Bolte, G. Neubauer, E. Cardis, M. Feychting, P. Gajsek, S. Heinrich, W. Joseph, S. Mann, L. Martens, E. Mohler, R. Parslow,

A. Poulsen, K. Radon, J. Schüz, G. Thuróczy, J. Viel, and M. Vrijheid. *Conduct of a personal radiofrequency electromagnetic field measurement study: proposed study protocol*. Environmental health, 9:23, 2010.

[13] M. Röösli, P. Frei, E. Mohler, C. Braun-Fahrländer, A. Bürgi, J. Fröhlich, G. Neubauer, G. Theis, and M. Egger. *Statistical analysis of personal radiofrequency electromagnetic field measurements with nondetects.* Bioelectromagnetics, 29(6):471–8, September 2008. doi:10.1002/bem.20417.

[14] IEC. *Human exposure to radio frequency fields from hand-held and body-mounted wireless communication devices - Human models, instrumentation, and procedures - Part 1: Procedure to determine the specific absorption rate (SAR) for hand-held devices used in close proximity to the ear (frequency range of 300 MHz to 3 GHz) (EN 62209-1:2006)*, 2006.

[15] IEC. *Human exposure to radio frequency fields from hand-held and body-mounted wireless communication devices - Human models, instrumentation, and procedures - Part 2: Procedure to determine the specific absorption rate (SAR) for wireless communication devices used in close proximity to the human body (frequency range of 30 MHz to 6 GHz) (EN 62209-2)*, 2010.

[16] A. Bamba, W. Joseph, J. B. Andersen, T. E, G. Vermeeren, D. Plets, J. O. Nielsen, and L. Martens. *Experimental Assessment of Specific Absorption Rate Using Room Electromagnetics*. IEEE Trans. Electromagn. Compat., Accepted, 2012.

[17] J. B. Andersen, J. O. Nielsen, G. F. Pedersen, G. Bauch, and M. Herdin. *Room Electromagnetics*. IEEE Antennas Propag. Mag., 49(2):27–33, April 2007.

[18] K. Kunz and R. Luebbers. *The finite difference time domain method for electromagnetics*. CRC Press, Boca Raton, FL, 1993.

[19] D. Davidson. *Computational Electromagnetics for RF and Microwave Engineering*. Cambridge University Press, 2005.

[20] S. Benkler, N. Chavannes, and K. N. *New powerful FDTD source based on huygens surface: Highly complex EM simulations performed on an ordinary PC*. In 31th Annual Meeting of the Bioelectromagnetics Society, Davos, Switzerland, Jun 1419, 2009, 2009.

[21] G. Gabriel. *Compilation of Dielectric Properties of Body Tissues at RF and Microwave Frequencies*. In Brooks Air Force Technical Report, AL/OE-TR-1996-0037, 1996.

[22] A. Christ, W. Kainz, E. G. Hahn, K. Honegger, M. Zefferer, E. Neufeld, W. Rascher, R. Janka, W. Bautz, J. Chen, B. Kiefer, P. Schmitt, H.-P. Hollenbach, J. Shen, M. Oberle, D. Szczerba, A. Kam, J. W. Guag, and N. Kuster. *The Virtual Family–development of surface-based anatomical models of two adults and two children for dosimetric simulations.* Physics in medicine and biology, 55(2):N23–38, January 2010. doi:10.1088/0031-9155/55/2/N01.

[23] T. Nagaoka, S. Watanabe, K. Sakurai, E. Kunieda, M. Taki, and Y. Yamanaka. *Development of realistic high-resolution whole-body voxel models of Japanese adult males and females of average hight and weight, and application of models to radio-frequency electromagnetic-field dosimetry*. Phys. Med. Biol., 49:1–15, 2004.

[24] A. Lee, W. Choi, M. Chung, H. Choi, and J. Choi. *Development of Korean male body model for computational dosimetry*. ETRI J, 28:107–10, 2006.

[25] C. Kim, S. Choi, J. Jeong, C. Lee, and M. Chung. *HDRK-man: a whole body voxel model based on high resolution color slice images of a Korean adult male cadaver*. Phys. Med. Biol., 53:4093–106, 2008.

[26] T. Wu. *Chinese Adult Anatomical Models and the Application in Evaluation of RF Exposures*. Phys Med Biol., 56:2075–89, 2011.

[27] P. Dimbylow. *The development of realistic voxel phantoms for electromagnetic field dosimetry*. pages 1–7, 1996.

[28] P. Dimbylow. *Development of the female voxel phantom, NAOMI, and its application to calculations of induced current densities and electric fields from applied low frequency magnetic and electric fields*. Phys Med Biol, 50(6):1047–70, 2005.

[29] I. Zubal, C. Harrell, E. Smith, Z. Rattner, G. Gindi, and B. Hoffer. *Computerized 3-dimensional segmented Human anatomy*. Phys. Med. Biol., 21:299–302, 1994.

[30] M. Ackerman. *Accessing the Visible Human Project*. Available from: http://www.nlm.nih.gov/research/visible/visible_human.html.

2

Averaging methods for local-averaged SAR

2.1 Introduction

Current exposure limits are based on thermal effects induced by the exposure to radio-frequency electromagnetic fields. To avoid local heating of the tissue, exposure guidelines define limits on the local-averaged SAR. To obtain the local-averaged SAR, the local SAR is averaged over a certain mass of the tissue (typically 1 g or 10 g). The obtained value not only depends on the averaging mass, but also on the shape of the averaging volume and the frequency. Obvioulsy, changing the shape of the averaging volume modifies the value of the local-averaged SAR. With increasing frequency, the absorption of electromagnetic energy in the lossy tissues such as the human body is pushed back towards the surface of the body due to the skin effect.

Studies on the averaging volume showed that an averaging volume containing 10 g of tissue better correlates with the induced temperature increase in the tissue than an averaging volume containing 1 g of tissue [1–3]. Razmadze et al. [1] also showed that the correlation improves when the averaging volume contains more air because averaging volumes becomes smoother at the surface when more air is allowed.

Standards for compliance testing of hand-held mobile communication devices [4, 5] describe various cubical averaging schemes to determine the local-averaged SAR. Stevens et al. [6] showed that the local-averaged SAR in 10 g in a homoge-

neous spherical phantom increases 20 % to 30 % when allowing air in the cubical averaging volume. McIntosh [2] showed that the spherical averaging scheme with a maximum allowed proportion of air of 20 % is equivalent to a cubical averaging scheme in terms of correlation with the temperature increase of the human tissues.

In Chapter 1, we shortly discussed the differences for local averaging of the SAR between the ICNIRP guidelines [7] and the IEEE recommendations [8]. One of the differences is that ICNIRP specifies a contiguous averaging scheme and IEEE defines a cube as averaging volume.

This chapter investigates the variation of the local averaged SAR with the applied averaging scheme. Three averaging schemes are compared and evaluated: a cubic, a contiguous and a spherical scheme. The averaging schemes are applied to three analytical functions defined by IEEE and IEC standards [5, 9] that represents the possible range of SAR distributions caused by hand-held devices and to two configurations consisting of a half wavelength dipole antenna in the proximity of a flat phantom and a spherical phantom. Each of the phantoms were filled with homogeneous tissue simulating liquid. These configurations with the phantoms are mostly encountered in measurement setups for compliance testing or as a validation or reference case. We evaluated the averaging schemes for four typical communication frequencies used in cellular communication systems and local area networks: 900 MHz (GSM 900 and LTE), 1800 MHz (GSM 1800), 2400 MHz (WiFi at 2 GHz), and 5800 MHz (WLAN in 5 GHz band).

2.2 Formulation of the problem and objectives of the study

Obviously, a cubic averaging scheme employs a cube or a deformed cube as averaging volume. Several disadvantages arise when applying a cubic averaging scheme, all of them resulting in an uncertainty on the calculated local-averaged SAR. The number of definitions of a cubic averaging scheme leads to just as manyA values of the local averaged SAR. Because a cubic volume is not symmetrical about a point, a rotation of the cube alters the value of the local averaged SAR. To find the peak local-averaged SAR value, a rotation of the cube about the normal to the surface of the phantom and through the point of maximum SAR value is necessary. In measurements as well as in simulations, the field - and likewise the SAR - are measured or calculated in a discrete set of points. After a rotation the cube will often not be aligned with the finite-difference time-domain (FDTD) or measurement grid resulting in a staircased approximation of the cube (see Figure 2.1a). Depending on the position of the cube and the density of the generated grid, the positioning of any surface slightly modifies (see Figure 2.1b). Consequently, the direction of the normal to the surface also varies and, thus also

the positioning of the cube (see Figure 2.1c).

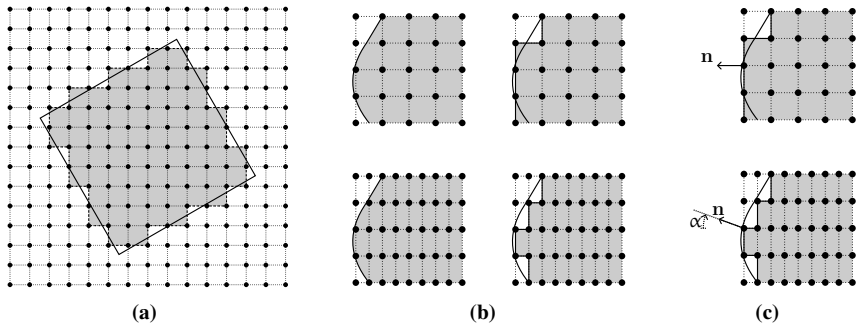

Figure 2.1: *Overview of the numerical disadvantages of the cubic averaging schemes (in 2D): (a) staircased cube when cube is not coincident with the grid, (b) surface variation due to a grid variation, and (c) variation of the normal to the surface due to a grid variation.*

Besides the variations of the local averaged SAR due to the discretization or numerical approach and the defined averaging algorithms, two other disadvantages have to be mentioned. The phantoms in which the measurements are made exist of two layers: the outer layer or the shell of the phantom and the tissue simulating liquid which fills the phantoms. The SAR distribution achieves its maximum SAR value at the interface between the phantom shell and the tissue simulating liquid in the proximity of the antenna. The reason for this is that the shell of the phantom is constructed with low permittivity dielectric material with low losses. Firstly, depending on the shape of the phantom, a merely cubic or spherical averaging volume will not always be completely enclosed by the phantom. In order to obtain the necessary volume of 1 g or 10 g mass, the averaging volume is enlarged and/or deformed (see Figure 2.3 and Figure 2.6). Secondly, in homogeneous tissue the SAR decreases with increasing distance from the point of peak SAR. None of the cubic averaging schemes will bring into account any physical property of the distribution of the SAR. Later, we will see that the volume of the spherical averaging scheme adapts partly to the distribution of the SAR in a homogeneous tissue and that the contiguous averaging scheme follows completely the distribution of the SAR in a homogeneous tissue. The better the averaging volume coincides with the SAR distribution, the higher the local-averaged SAR.

This chapter aims at evaluating the influence of the averaging schemes (i.e., shape of the volume) and averaging mass on the local averaged SAR for communication frequencies ranging from 900 MHz to 5.8 GHz. The research focussed on measurement setups consisting of a homogeneous tissue simulating liquid in a phantom, and radio-frequency sources positioned outside the phantom.

2.3 Averaging schemes

This section provides an overview of averaging schemes for local-averaged SAR defined in guidelines and standards. Several type of schemes exists: cubical (mostly defined by standardization bodies, such as IEC, CENELEC, and IEEE), contiguous or coherent schemes which follows the iso- or equi-SAR surfaces (found in ICNIRP guideline). We compared the existing averaging schemes with the proposed spherical averaging scheme.

2.3.1 The cubical averaging schemes

IEC [9] specifies four schemes for cubical averaging of the SAR: the method of three points, the method of the tangential face, the method of averaging and the extrude method of averaging. We investigated three of these methods. The method of three points was not selected as we strive for reducing computational complexity. We also considered the method for cubical averaging suggested by Stevens at al. [6], as they derived and evaluated a worst-case cubical averaging scheme for GSM frequencies at 900 MHz and 1800 MHz. Actually, we elaborated on this method but replaced the cube by a sphere to reduce computational complexity.

2.3.1.1 The method of the tangential face

Figure 2.2 illustrates the method of tangential face. The center of one face of the cube coincides with a point on the phantom surface. The face of the cube is oriented such that it lies tangential to the surface of the phantom in the center of the face of the cube. The cube is rotated about a vector normal to the phantom surface to obtain the peak local-averaged SAR. The surface of the cube that touches the phantom shell shall be made conformal to the phantom surface. The opposite face of the cube is then either extended or contracted to obtain a 1 g or 10 g averaging mass.

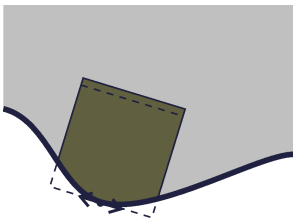

Figure 2.2: *The method of the tangential face of the cubic averaging schemes [9].*

2.3.1.2 The method of averaging

A second cubical averaging scheme is the method of averaging, which is defined as follows (see Figure 2.3): position one face of the cube tangential to the surface of the phantom. The point of contact is the center of the tangential face. Enlarge the cube until it contains the specified mass of the tissue. Now, shift and rotate the cube along the phantom surface until the maximum value of the local averaged SAR is achieved. Remark that for each position of the cube, the volume of the cube changes to keep the mass at its specified value.

In the case of the flat and the spherical phantom, the half-wavelength dipole antenna is positioned symmetrically with respect to the flat and the spherical phantom. Therefore, the center of the face tangential to the phantom surface coincides with the point of maximum SAR. Thus, the shift of the cube along the phantom surface is not necessary in these cases. Only a rotation of the averaging cube about the normal to the surface and through the point of maximum SAR is done to find the peak local-averaged SAR.

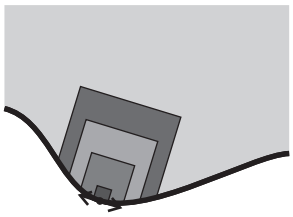

Figure 2.3: *The method of averaging of the cubic averaging schemes [9].*

2.3.1.3 The extrude method of averaging

In the extrude method of averaging, the cube conforms to the phantom surface as illustrated in Figure 2.4.

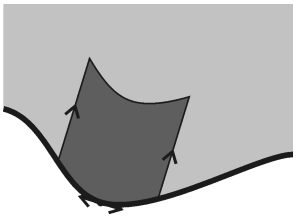

Figure 2.4: *The extrude method of averaging of the cubic averaging schemes [9].*

2.3.1.4 The modified method of averaging

The modified method of averaging, as suggested by Stevens [6], shifts the center of the cube along the axis normal to the phantom surface and through the point of peak SAR. Again, the cube is rotated to find the peak local-averaged SAR.

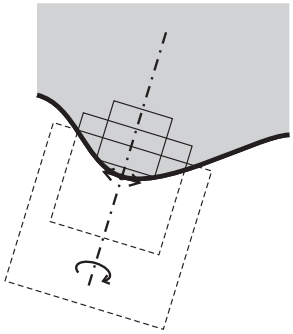

Figure 2.5: *The modified method of averaging as the cubic averaging scheme [6].*

2.3.2 The spherical averaging schemes

In general, finding the peak local-averaged SAR by means of cubic averaging implies several successive calculations of the local-averaged SAR because of the shifting and rotating of the averaging volume resulting in an increased processing time. To reduce the computational effort, a spherical averaging scheme is proposed: a sphere is centered at the shell-liquid interface where the peak SAR occurs. The length of the radius is changed until the part of the sphere inside the tissue liquid encloses the necessary mass of tissue liquid (see Figure 2.6). Using a spherical averaging scheme avoids the rotation of the averaging volume about the normal on the phantom surface that runs through the center of the sphere. Moreover, as opposed to cubical averaging, the spherical averaging follows partly the SAR distribution in homogeneous tissues.

Just as the modified method of cubic averaging, the center of the sphere can be shifted on a straight line normal to the phantom surface. Depending on the selected RF radiator, a maximum value for the local-averaged SAR is found for a certain position of the center of the sphere on the surface normal. Because we aim at a reduction of the complexity of the averaging scheme as well as a reduction of possible uncertainty in the averaged SAR value, the modified averaging methods were not considered.

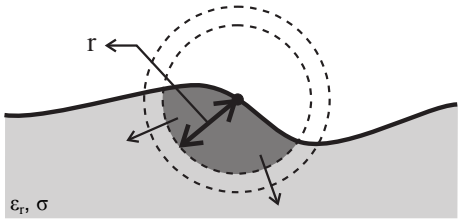

Figure 2.6: *The spherical averaging scheme.*

2.3.3 The contiguous averaging scheme

Neither the cubic averaging schemes nor the spherical averaging scheme will calculate the "absolute" peak local-averaged SAR. These averaging schemes select voxels according to the shape of the averaging volume. So, it is possible that a voxel inside the averaging volume has a lower SAR value than a voxel outside the averaging volume. The reason for this is that the surface bounding the averaging volume does not coincide with an iso-SAR surface. In the contiguous or coherent averaging scheme we ensure that the boundary surface of the coherent averaging volume does not cut through a surface of equal SAR values. In this way, the "absolute" peak local-averaged SAR is calculated. Figure 2.7a visualizes the contiguous averaging scheme and Figure 2.7 shows a spherical averaging volume cutting through the iso-SAR surfaces. Averaging schemes that cut through iso-SAR surfaces do not yield the "absolute" peak local-averaged SAR. The contiguous averaging scheme is the simplest averaging scheme to implement. Neither a rotation nor a shift of the averaging volume needs to be performed. At high frequencies, the SAR distribution is pushed back towards the surface of the phantom due to the smaller penetration depth of the fields. This means that at high frequencies the averaging volume spreads out near the phantom surface.

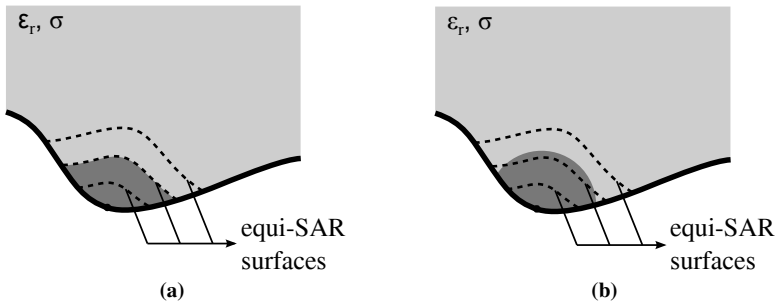

Figure 2.7: *(a) Adaptive averaging volume following equi-SAR surfaces and (b) spherical averaging volume cutting through equi-SAR surfaces.*

2.4 The configurations under study

Standards define three analytical functions (test functions f_1, f_2, and f_3) that represent the possible range of SAR distributions expected from handsets tested according to the procedures defined in the standards [5]. The largest gradient for SAR values in the averaging volume is obtained for test function f_3. The test functions are defined for the phantom surface at $z = 0$ and the half space tissue medium at $z > 0$:

$$f_1(x,y,z) = A\exp\left(-\frac{z}{2a}\right)\cos^2\left(\frac{\pi}{2}\frac{\sqrt{x'^2+y'^2}}{5a}\right) \tag{2.1}$$

$$f_2(x,y,z) = A\exp\left(-\frac{z}{a}\right)\frac{a^2}{a^2+x'^2}\left(3-\exp\left(-\frac{2z}{a}\right)\right)\cos^2\left(\frac{\pi}{2}\frac{y'^2}{3a}\right) \tag{2.2}$$

$$f_3(x,y,z) = A\frac{a^2}{\frac{a^2}{4}+x'^2+y'^2}\left(\exp\left(-\frac{2z}{a}\right)+\frac{a^2}{2(a+2z)^2}\right) \tag{2.3}$$

where $x' = x + d$ mm; $y' = y + d$ mm; d is an offset parameter; a = 20 mm; A = 1 W/kg.

First, we used the test functions to evaluate the three considered cubical averaging schemes, the spherical averaging scheme, and the contiguous averaging scheme. These test functions have an exponential decay with increasing distance z inside the liquid and a spherical or ellipsoidal distribution in planes parallel to the liquid surface $z > 0$. The test functions are originally developed for a flat phantom surface, but can be adapted to a smooth curved phantom surface according to [5].

From the evaluation of the cubical averaging schemes (method of the tangential face, extrude method of averaging, and method of averaging) only the scheme that yields the highest peak local-averaged SAR value is used for comparison with the spherical and contiguous averaging volume.

Next, we evaluated cubical, spherical and contigious averaging in a flat phantom and a spherical phantom irradiated by a dipole at 15 mm. The configurations are shown in Figure 2.8. Both setups are simulated using the commercial FDTD tool SEMCAD (SPEAG, Zurich, Switzerland). The total length of the dipole antennas equalled half a wavelength. The radius of the dipoles measured 1.8 mm and their gap was 1 mm. The simulations are performed for 900 MHz, 1800 MHz, 2400 MHz, and 5800 MHz. The shell of the flat and spherical phantom has a thickness of 2 mm and the dielectric properties of the shell satisfied: $\epsilon_r < 5$ and $\tan\delta < 0.05$. Remember that $\tan\delta = \frac{\sigma}{\omega\epsilon_0\epsilon_r}$. We have chosen a conductivity of 2.5 mS for the phantom shell. This value satisfies the above condition over the

frequency range of interest. The phantom was filled with tissue simulating liquid matching the dielectric properties of average muscle from the FCC dielectric database [10]. The distance from the feedpoint of the dipole antenna to the shell of the phantom was 15 mm in all the configurations.

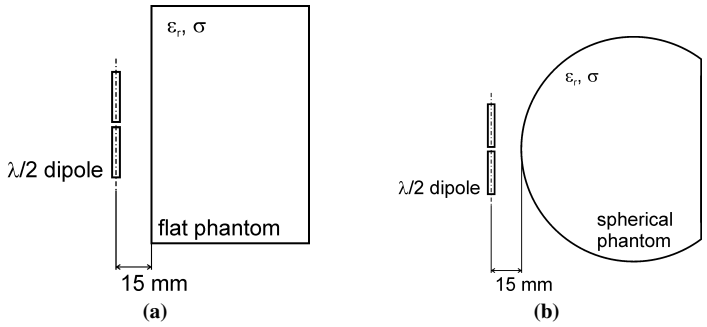

Figure 2.8: *The studied configurations: dipole next to (a) a flat phantom and (b) a spherical phantom.*

2.5 Results

Figure 2.9 and Figure 2.10 show the peak local-averaged SAR in 1 g and 10 g as a function of the averaging scheme (cubical, spherical and contiguous) for the three analytical test functions [5] in a flat and a curved phantom, respectively. The contiguous averaging scheme always returns the maximum value of the peak local-averaged SAR that occurs in the phantom (Figure 2.9). Spherical averaging gives a higher value for local-averaged SAR compared to cubical averaging. It is well known that in a homogenous tissue the highest SAR values occur at the surface of the phantom. The larger the number of averaging points close to the surface of the phantom, the higher the peak local-averaged SAR in 1 g or 10 g.

The three cubical averaging schemes are compared for the curved phantom in Figure 2.10. The averaging schemes are denoted by a letter. For the cubical averaging schemes this is: E for extrude method of averaging, T for method of tangential face, and A for the method of averaging. The spherical and contiguous schemes are denoted by S and C, respectively. The cubical averaging scheme A show a slightly higher peak local-averaged SAR in 1 g and 10 g because it takes into account more SAR values at the surface of the phantom.

We also observed that the steep gradient of test function f_3 results in a large variation between 1 g and 10 g averaged SAR, whereas the flat distribution of test function f_1 results in nearly equal values for local-averaged SAR in 1 g and 10 g. Thus, the 1 g averaging delivers higher values in case of steep SAR distributions, which will typically occur for RF sources radiating at higher frequencies.

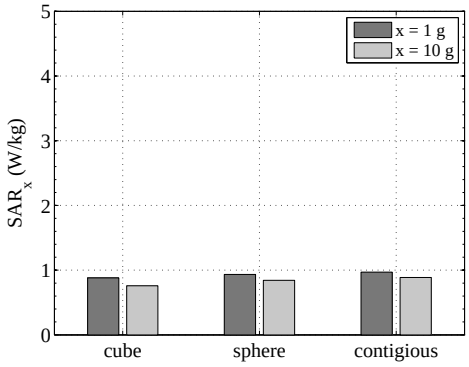

(a)

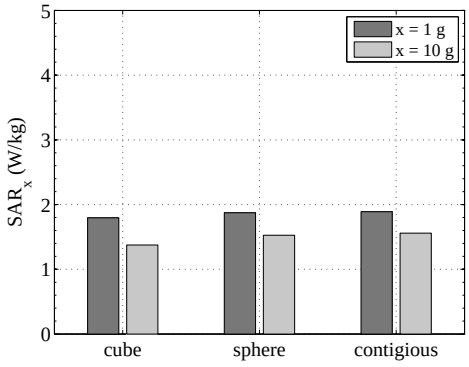

(b)

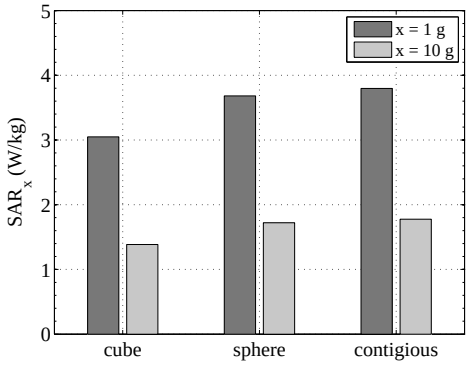

(c)

Figure 2.9: *The peak local-averaged SAR in 1 g and 10 g of tissue in a flat phantom for the test functions specified by IEEE: (a) test function 1, (b) test function 2, and (c) test function 3.*

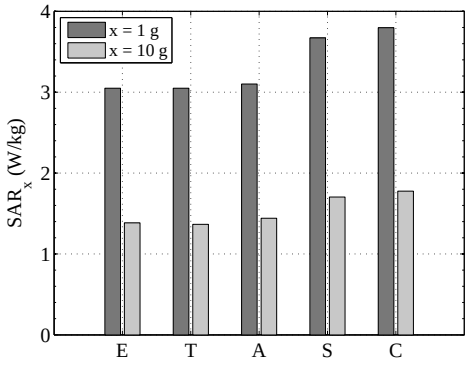

Figure 2.10: *The peak local-averaged SAR in 1 g and 10 g of tissue in a curved phantom for the test function 3 (specified by IEEE).*

Figure 2.11 shows the influence of the averaging schemes on the peak local-averaged SAR in 1 g and 10 g in a flat phantom and a sphere (with radius of 106.5 mm) irradiated by a half-wavelength dipole at 15 mm as a function of the frequency. We selected the method of averaging (A) for the cubical averaging scheme. In addition to the discussed averaging schemes, we also included the results of the averaging routine implemented in SEMCAD. SEMCAD calculated the peak local-averaged SAR according to IEEE Std. 1529 [11].

The local SAR in 1 g and 10 g reaches a maximum value as a function of the frequency. The peak local-averaged SAR in 1 g of tissue is higher than in 10 g of tissue. For a flat phantom the peak local-averaged SAR in 1 g and 10 g is obtained for 1800 MHz and 900 MHz, respectively, and for all averaging schemes. A different picture is viewed for the peak local-averaged SAR in 1 g when the dipole radiates next to the spherical phantom. The contiguous averaging volume reaches the highest value at 5.8 GHz and the spherical averaging shows a slightly smaller value at 5.8 GHz than at 2.4 GHz. The higher the frequency and the smaller the radiating device, the steeper the SAR distribution. So, the peak local-averaged SAR is lower for the largest averaging volume, i.e., the volume of 10 g of mass. Because the shape of the volume is determined by the averaging scheme, the peak local-averaged SAR varies with the selected scheme for averaging.

We distinguish two types of averaging schemes. First, there are the averaging schemes which specify a specific shape for the volume: cubic and spherical volume. Secondly, there is the averaging volume which adapts to the SAR distribution and, thus, the volume can take any shape. The contiguous averaging scheme renders the highest peak local-averaged SAR value. All other averaging schemes result in a lower local-averaged SAR value. The spherical averaging scheme calculates a higher local-averaged SAR than any cubic scheme when homogeneous

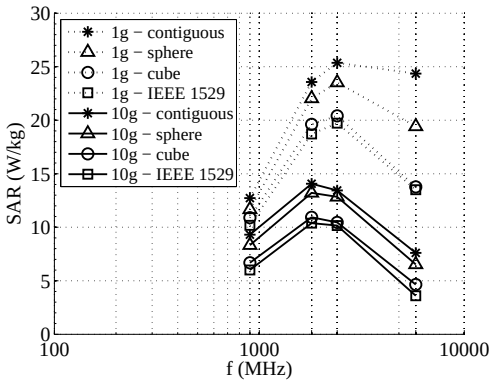

(a)

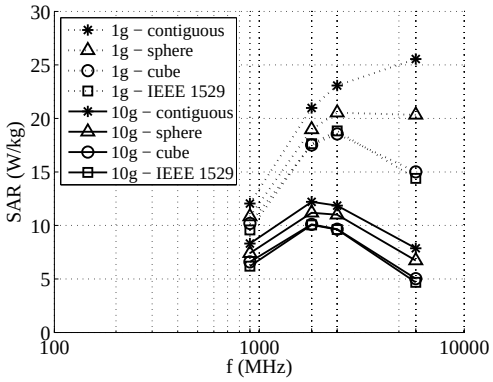

(b)

Figure 2.11: *Influence with frequency of averaging schemes on the local-averaged SAR in 1 g and in 10 g for a half-wavelength dipole at 15 mm of (a) a flat phantom and (b) a sphere. The input power is normalized to 1 W.*

tissues are considered. This is illustrated in Figure 2.12: the spherical averaging scheme takes into account more voxels at the phantom surface, and thus more voxels with a higher SAR value.

Spherical averaging best approximates the worst-case peak local-averaged SAR in 10 g obtained by the contiguous averaging of the considered averaging schemes. But, for an averaging volume of 1 g, spherical averaging underestimates worst-case local averaged SAR by up to 20 % at 5.8 GHz. Cubical averaging always underestimates the worst-case peak local-averaged SAR by up to 43 % for 1 g volume and up to 39 % for 10 g volume.

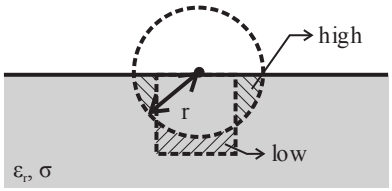

Figure 2.12: *Comparison of the spherical and cubic averaging scheme. (The source has been positioned outside the phantom.)*

2.6 Conclusions

Cubical averaging schemes are typically used in SAR assessment. The method of averaging shows a slightly higher local averaged SAR than the other cubical averaging schemes described in standardization.

Spherical averaging keeps the middle between cubic and contiguous averaging. On the one hand, spherical averaging reduces computational time because the positioning of the spherical volume is easy - no need to deform the volume to adapt it to the curved phantom surface, as it is the case for the cubic averaging - and no rotation of the volume to find the peak local-averaged SAR value. Furthermore, the spherical averaging has some knowledge of the distribution of the SAR in a homogeneous tissue as it takes into account more voxels at the surface of the phantom where the highest SAR value occurs. On the other hand, spherical averaging prevents the spreading of the averaging volume at high frequencies that is present for contiguous averaging.

The peak local-averaged SAR shows a maximum value as a function of frequency. The frequency of maximum local SAR depends on the size of the averaging volume, the applied averaging scheme, the shape of the body and the tissue properties.

References

[1] A. Razmadze, L. Shoshiashvili, D. Kakulia, R. Zaridze, G. Bit-Babik, and A. Faraone. *Influence of specific absorption rate averaging schemes on correlation between mass-averaged absorption rate and temperature rise*. Electromagnetics, 29:77–90, 2009.

[2] R. McIntosh and V. Anderson. *SAR versus VAR, and the Size and Shape that Provide the Most Appropriate RF Exposure Metric in the Range of 0.5-6 GHz*. Bioelectromagnetics, 32:312–21, 2011.

[3] A. Hirata and O. Fujiwara. *The correlation between mass-averaged SAR and temperature elevation in the human head model exposed to RF near-fields from 1 to 6 GHz*. Physics in Medicine and Biology, 54(23):7227–38, 2009.

[4] CENELEC. *European Standard EN50361: Product standard to demonstrate the compliance of mobile phones with the basic restrictions related to human exposure to electromagnetic fields (300 MHz - 3 GHz)*, 2001.

[5] IEEE. *IEEE recommended practice for determining the peak spatial-average specific absorption rate (SAR) in the human head from wireless communications devices: measurement techniques (Std. 1528)*, 2003.

[6] N. Stevens and L. Martens. *Comparison of averaging procedures for SAR distributions at 900 and 1800 MHz*. IEEE Transactions on Microwave Theory and Techniques, 48:2180–84, 2000.

[7] ICNIRP. *Guidelines for limiting exposure to time-varying electric, magnetic, and electromagnetic fields (up to 300 GHz)*. Health Physics, (November 1997), 1998.

[8] IEEE. *IEEE standard for safety levels with respect to human exposure to radio frequency electromagnetic fields, 3 kHz to 300 GHz (IEEE Std C95.1 (2005))*, 2006.

[9] IEC TC106/61/CDV. *Procedure to measure the Specific Absorption Rate (SAR) in the frequency range of 300 MHz to 3 GHz Part 1: hand-held mobile wireless communication devices*, 2004.

[10] FCC. *Body Tissue Dielectric Parameters*. Online. Available from: http://transition.fcc.gov/oet/rfsafety/dielectric.html.

[11] IEEE. *Recommended Practice for Determining the Peak Spatial-Average Specific Absorption Rate (SAR) Associated with the Use of Wireless Handsets - Computational Techniques (IEEE Std. 1529)*.

3

Evaluation of a walkie-talkie in free space

3.1 Introduction

The vast amount of studies on dosimetry deals with the exposure due to mobile devices and base station antennas for cellular communication systems. Walkie-talkies are used as an alternative for cellular phones for short-range communication. The advantages of walkie-talkies are the ease-of-use (push-to-talk), the cheap price, and the free-of-charge connection fee and the improved voice quality by the use of frequency modulation (FM). Family Radio Service (FRS) is used in the United States, whereas Personal Mobile Radio at 446 MHz (PMR 446) is authorized in Europe for license-free short-range voice communication [1–4]. FRS uses fourteen channels within the frequency bands 462.5625 - 462.7125 MHz and 467.5625 - 462.7125 MHz. PMR 446 specifies eight channels within the frequency range 446.0 - 446.1 MHz. Each channel has a bandwidth of 25 kHz for FRS and 12.5 kHz for PMR 446, respectively. The maximum allowed Effective Radiated Power (ERP) is 500 mW for both systems. Frequency modulation (FM) has been adopted as the modulation scheme.

The relative low frequency, the effective radiated power of 500 mW, the use of walkie-talkies by children, and the limited number of exposure studies for walkie-talkies attracted our attention to these devices.

The objective of this study is to develop and evaluate an accurate helical monopole antenna model of a walkie-talkie for compliance assessment with ICNIRP [5] and

FCC guidelines [6]. The model is obtained by reverse engineering and is validated by reflection, near-field, and far-field measurements. The use of helical monopole antennas as a model for portable hand-held devices have been mainly discussed for mobile-phone technologies [7, 8] operating in frequency bands around 900 MHz and 1800 MHz. In this study, a helical monopole antenna model of a walkie-talkie operating at 446 MHz is designed to study the electromagnetic fields induced in the human head by walkie-talkies. A model is preferred above a real walkie-talkie device for mainly two reasons. Firstly, the antenna characteristics, e.g., the reflection at the input terminals, of a model can be measured accurately. Secondly, the input power is easily adjustable as one can feed using a signal generator contrary to a real device. The model also allows to study the influence of dimensions and material parameters on the antenna characteristics and the absorption.

3.2 Free-space evaluation of a generic walkie-talkie model

We developed a model of a walkie-talkie by reverse engineering of a commercially available PMR 446 radio. We selected randomly a device from the supermarket. The selected walkie-talkie was the COBRA MT500 from Motorola. The device is shown in Figure 3.1.

Figure 3.1: *The COBRA MT500 from Motorola, a commercial PMR 446 radio.*

We dismantled the COBRA MT500 and developed the walkie-talkie model based on the physical dimensions of the antenna structure (including the coating around the antenna) and the Printed Circuit Board (PCB). A picture of the antenna model with and without coating around the antenna is shown in Figure 3.2. The model consists of a helical antenna mounted on a rectangular ground plane. The terminals of the source connect the helical antenna and the ground plane of the model. In order to limit the complexity of the model, the PCB of the walkie-talkie was replaced by a PEC ground plane and the case was removed. The helical antenna fits in a dielectric cover. This cover around the helical antenna influences the

antenna characteristics of the model. The dielectric properties of the coating were unknown and we derived the properties by tuning the simulated antenna characteristics and near-field distributions to the measured results.

(a) (b)

Figure 3.2: *The model of a walkie-talkie (viewed from the back): (a) the PEC model and (b) the model with the helical antenna in a coating.*

Figure 3.3 shows the dimensions of derived model of a walkie-talkie at 446 MHz and the coordinate system used in this study. The dimensions and dielectric parameters of the model are listed in Table 3.1. These values can be modified to the specific dimensions of different types of walkie-talkies. The helical antenna fits in a dielectric cover with a relative permittivity (ϵ_r) of 3.9 and a conductivity (σ) of 12 mS/m.

The measurement model and the coaxial feeding line have an asymmetric structure. Consequently, the input current at the terminals of the measurement model is unbalanced. In order to realize a balanced feed current at the terminals of the measurement model, the measurement model is fed through a bazooka or a sleeve balun [9]. The operating frequency of the bazooka balun is 446 MHz. (The bazooka balun is not shown in Figure 3.2).

3.2.1 Methodology

To evaluate the model of Section 3.2, measurements and simulations have been performed. For the simulations, SEMCAD-X (SPEAG, Zurich, Switzerland), a commercially available 3D electromagnetic solver based on FDTD method, is employed to investigate numerically the input impedance, the near fields, the efficiency, and the gain of the model. The measurements of the reflection and the input impedance have been performed in an anechoic room using a vector network analyzer (VNA) (type HP8710). The far-field characteristics in terms of Total Radiated Power (TRP) and the Effective Radiated Power (ERP) were mea-

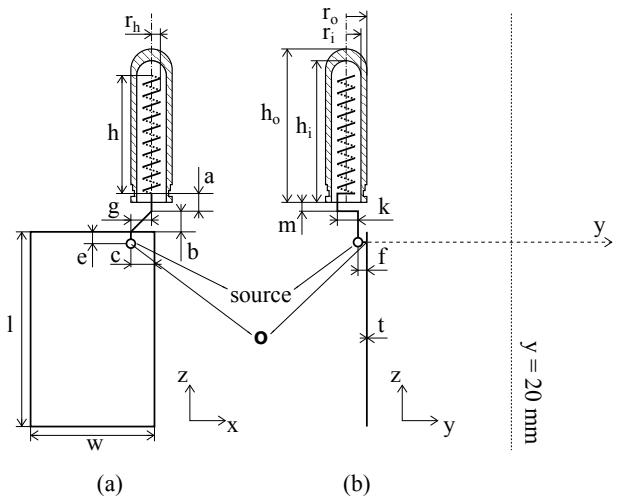

Figure 3.3: *The model of a walkie-talkie in (a) xz-plane and (b) yz-plane. The measurement line (y-axis) and plane (y = 20 mm) for the near fields are also shown.*

Helical antenna		**Ground plane**	
a	4.2 mm	l	80 mm
b	9.8 mm	w	45 mm
c	10 mm	t	0.5 mm
e	5 mm	**Antenna housing**	
f	2 mm	r_i	3.5 mm
g	8.54 mm	r_o	7 mm
h	42 mm	ϵ_r	4
k	7.2 mm	σ	12 mS/m
n_{turns}	21	h_i	51 mm
r_h	2.4 mm	h_o	53 mm
r_w	0.5 mm	m	1 mm

Table 3.1: *Dimensions of the model of a walkie-talkie.*

sured at the SP Technical Research Institute of Sweden. The TRP measurements were performed in a reverberation chamber according to TCO'01 Certification of Mobile Phones. The measurement uncertainty is 1 dB. The ERP measurement is performed in an anechoical room according to the ETSI standard EN 300 296-2:2001-03 [3]. The measurement uncertainty is 3.3 dB, which is within the uncertainty boundary of 6 dB specified by the ETSI standard. This large uncertainty is due to the simplifications built into the measurement methodology to reduce time and cost of the tests. For the walkie-talkies the ERP was only measured in 8 different directions in the azimuth plane resulting in an uncertainty of 3.3 dB. The near

fields were measured in an indoor environment using a robot and DASY3 measurement system with the following probes: E-field probe ER3DV6 and H-field probe H3DV6 (SPEAG, Zurich, Switzerland). Reflections of the environment and the robot arm are minimized by placing absorbers. To compare the simulations with the measurements, the bazooka balun has to be de-embedded in order to get the scattering parameters at the terminals of the measurement model. If we assume that the coaxial line with bazooka balun behaves as an ideal transmission line, the reflection coefficient at the terminals $S_{11,\mathrm{terminals}}$ of the measurement model can be calculated using:

$$S_{11,\mathrm{terminals,meas}} = S_{11,\mathrm{meas}} \exp\left(\mathrm{i}2\beta d\right) \tag{3.1}$$

with d the distance from the measurement port to the terminals of the model, β the phase constant of the line and $S_{11,\mathrm{meas}}$ the reflection with respect to 50 Ω reference impedance measured with the VNA. The length d measured 24.5 mm.

3.2.2 Reflection coefficient

The Smith chart of the simulated and measured reflection coefficient $S_{11,\mathrm{terminals}}$ and the return loss $|S_{11,\mathrm{terminals}}|$ in dB of the model with respect to 50 Ω are shown in Figure 3.4. The triangle denotes a frequency of 446 MHz. A very good agreement is observed between simulations and measurements. The resonance frequency f_{res} calculated by the FDTD tool is 436.5 MHz and deviates only 0.3 % of the measured value fres, i.e. 435.2 MHz. The simulated input impedance at resonance $Z_{\mathrm{in,res}}$ equals 20.8 Ω, the measured input impedance equals 24.5 Ω. At the operating frequency of 446 MHz, the input impedance, at the terminals of the model, Zin is 28.6 + i30.4 Ω and 23.0 + i23.6 Ω for the measurement and FDTD simulation, respectively.

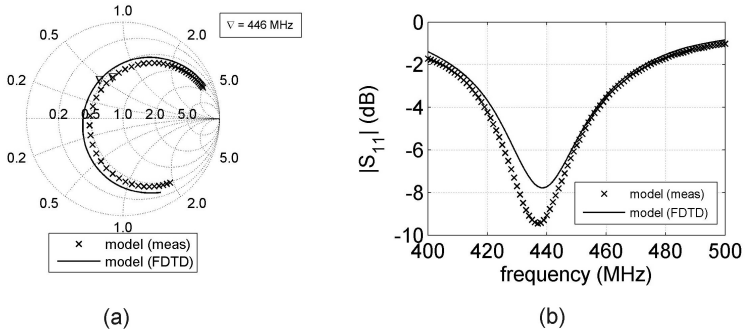

Figure 3.4: *The (a) Smith chart and (b) return loss of the model (▽ denotes the value at a frequency of 446 MHz).*

3.2.3 Influence of the coating around the helical antenna

We already mentioned that the dielectric parameters of the antenna coating were derived by tuning these parameters until the simuations agree with the measurements in term of resonance frequency. We obatined a relative permittivity of 3.9 and a conductivity of 12 mS/m. Figure 3.5 illustrates the influence of the coating by comparing the return loss of the walkie-talkie model with and without coating. The dielectric parameters of the coating shift the resonance frequency from 500 MHz to 435 MHz. The return loss reduces to -9.5 dB when the helical antenna is covered by the coating. This is partly due to the ohmic losses of the coating which improves the matching.

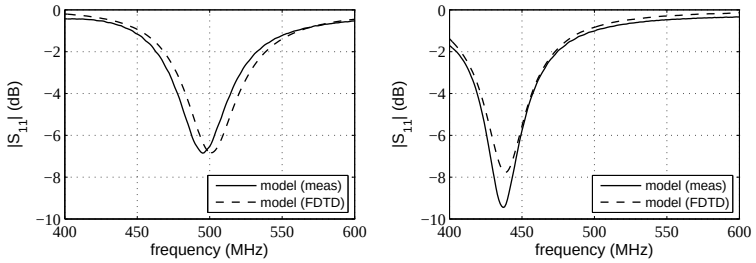

Figure 3.5: *The return loss of the walkie-talkie model (a) without coating and (b) with coating.*

3.2.4 Radiation efficiency

The radiation efficiency (η) of an antenna is defined as the ratio of the radiated power ($\mathrm{P_{rad}}$) and the input antenna power ($\mathrm{P_{in}}$), or $\eta = \mathrm{P_{rad}}/\mathrm{P_{in}}$ [9]. The radiation efficiency is calculated using FDTD simulations. We obtain for the model with coating an efficiency of 53 % at 446 MHz. This low efficiency is due to the reflection at the input terminals of the helical antenna and the ohmic losses in the housing around the helical antenna introduced by the conductivity (σ) of 12 mS/m.

3.2.5 Gain and effective radiated power

The far-field behavior of the model of the walkie-talkie has been investigated numerically in terms of the gain (G). Using FDTD a gain of 1.07 for the simulation model is obtained. This value is lower than the gain of a dipole antenna ($\mathrm{G_d}$), mainly due to the losses in the dielectric cover around the helical antenna of the model. The effective radiated power (ERP) can be calculated as follows [9]:

$$ERP = \frac{G}{G_{\mathrm{d}}} P_{\mathrm{in}} \tag{3.2}$$

In accordance with the PMR 446 system and the FRS system, the maximum allowed ERP of 500 mW is reached if the input power of the helical antenna (or output power of the generator) is as high as 1042 mW. This input power is used to determine the compliance of the model with safety guidelines [5, 6] in the next chapter.

The effective radiated power was also measured for the walkie-talkie model with coating. For an input power of 10 mW, the measured maximum ERP was 4.9 mW (the measurement uncertainty was 3.3 dB). This agreed very well with the simulated ERP of 4.8 mW (the relative error was 2 %).

3.2.6 The electromagnetic near fields

The near fields of the model have been simulated and measured in an arbitrarily selected y-plane at 20 mm from the model (y = 20 mm) according to the setup shown in Figure 3.3. The ERP is set to 500 mW. Figure 3.6 shows the simulated ((a) and (b)) and measured ((c) and (d)) RMS electric $\mathrm{E_{rms}}$ ((a) and (c)) and RMS magnetic $\mathrm{H_{rms}}$ ((b) and (d)) near fields of the model at y = 20 mm. One observes that the distribution of the electric and magnetic field as well as the absolute field values of the simulations agree very well with the measurements. The dots in Figure 3.6 show the position of the maximum field values. The position of the maximum RMS E-field and H-field is situated near the helical antenna and the terminals of the model, respectively. In the plane y = 20 mm, the simulated $\mathrm{E_{rms,max}}$ (Figure 3.6a) equals 762 V/m in the point (x = 10 mm, z = 55 mm) and deviates only 1.6 % from the measured value, i.e., $\mathrm{E_{rms,max}}$ of 750 V/m in the point (x = 5 mm, z = 50 mm). In the same plane y = 20 mm, the simulated $\mathrm{H_{rms,max}}$ is 1080 mA/m in (x = 5 mm, z = 15 mm) and deviates 7.7 % from the measured $\mathrm{H_{rms,max}}$ of 1003 mA/m in (x = 5 mm, z = 15 mm). Figure 3.7 shows the electric and magnetic field along the y-line which runs through the point of maximum electric and magnetic field (see the dots in Figure 3.6) in the plane y = 20 mm. The maximum relative deviation on the electric and magnetic field along this line is only 6.5 % and 12.7 %, respectively.

3.3 Free-space evaluation of four walkie-talkies available on the market

Besides the COBRA MT500, three other PMR 446 radios were acquired. In this section, the radiation characteristics of all the walkie-talkies and the near-field

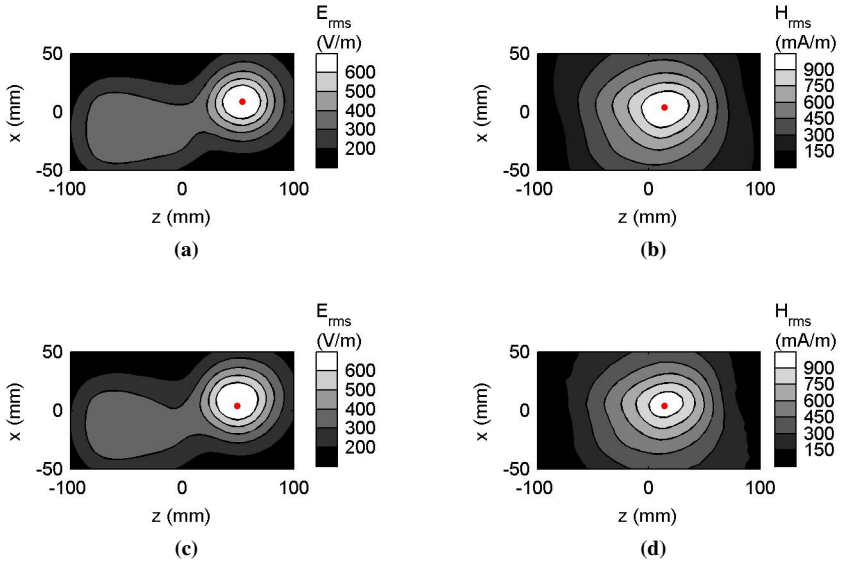

Figure 3.6: *The ((a) and (b)) simulated and ((c) and (d)) measured electromagnetic near fields at y = 20 mm of the model.*

behavior of the COBRA MT500 are investigated. Table 3.2 lists the details of the four real walkie-talkies.

Walkie-talkie (Manufacturer)
COBRA MT500 (Motorola)
TwinTalker 3300 (Topcom)
TwinTalker 1300 (Topcom)
Alecto FR-20 (Alecto)

Table 3.2: *Four commercially available walkie-talkies.*

3.3.1 Radiation characteristics

The radiation characteristics of the real devices were measured by SP Technical Research Institute of Sweden (Borås, Sweden). The total radiated power (TRP) of the real devices can be used to obtain realistic estimates of the absorption in realistic head models. Table 3.3 lists TRP, maximum ERP, and the averaged ERP. The maximum effective radiated power varies from 16.4 dBm to 20.2 dBm. This is about 11.5 to 3.6 times below the specification of the allowed ERP for PMR 446 radios.

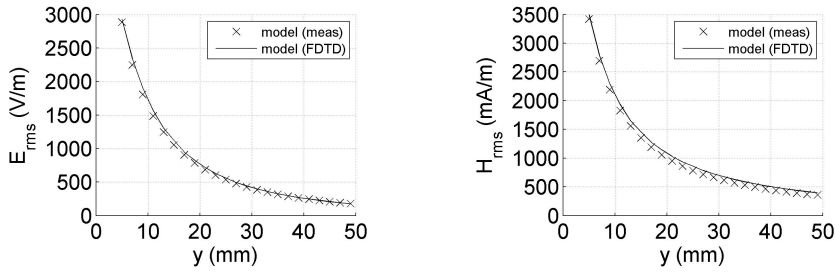

Figure 3.7: *The RMS (a) electric and (b) magnetic near field of the model along a line and through the point where the field reaches its maximum value in the plane y = 20 mm.*

Walkie-talkie (Manufacturer)	TRP (dBm)	Max. ERP (dBm)	Avg. ERP (dBm)
COBRA MT500 (Motorola)	20.2	21.4	20.7
TwinTalker 3300 (Topcom)	17.7	19.0	18.3
TwinTalker 1300 (Topcom)	17.1	18.4	18.0
Alecto FR-20 (Alecto)	16.4	17.1	16.7

The measurement uncertainty on TRP and ERP is 3.3 dB.

Table 3.3: *Total Radiated Power and Effective Radiated Power of four commercial walkie-talkies.*

3.3.2 The electromagnetic near fields

The near fields of COBRA MT500 are measured and compared to the model of the walkie-talkie (which has dimensions based on the dimensions of the COBRA MT500). We have positioned the walkie-talkie in the same way as the model (see Figure 3.3) such that the feed point coincided with the origin of the coordinate system. We normalized the fields to the maximum field value in the plane y = 20 mm, because we were not able to determine the input power for the real walkie-talkie. Figure 3.8 shows the normalized electric and magnetic field in a plane for the real walkie-talkie (only measurements). The measured field distributions of the real walkie-talkie agree very well with the simulated (see Figure 3.6a and Figure 3.6b) and the measured (see Figure 3.6c and Figure 3.6d) near field distributions of the model. Finally, the normalized fields along a line (through the point of maximum field value in the plane y = 20 mm) for the measured real walkie-talkie together with the simulated and measured ones for the model are shown in Figure 3.9. Again, a very good agreement is observed between measurements for the real walkie-talkie, and the simulations and measurements for the model. Compared to the real walkie-talkie, the maximum relative error for the measured and simulated model on the normalized electric field is only 1.2 % and 5.2 %, respectively.

For the normalized magnetic near field, the maximum relative error for the measured and simulated model is 5.2 % and 5.5 %, respectively. These low deviations show that the model behaves electromagnetically like a real walkie-talkie and can be used for analysis of the interaction with the human body.

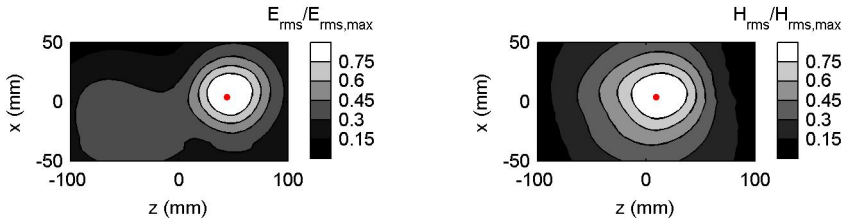

Figure 3.8: *The normalized RMS (a) electric and (b) magnetic near field at y = 20 mm of a real walkie-talkie.*

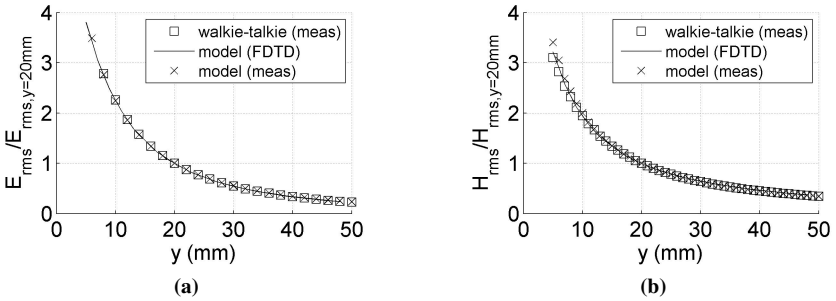

Figure 3.9: *The normalized RMS (a) electric and (b) magnetic near field along a y-line through the point where the field reaches its maximum value in the plane y = 20 mm for the real walkie-talkie and the model.*

3.4 Conclusions

An accurate model for a walkie-talkie has been developed and very good agreement has been reported from simulations and measurements in terms of reflection and transmission characteristics. The near fields of the model have been validated with the measured near fields of a real walkie-talkie. A relative error of less than 5.5 % has been observed on the near electric and magnetic field indicating that the walkie-talkie model behaves electromagnetically as a real walkie-talkie. Therefore the model can be used to determine the electromagnetic interaction with the hu-

man body and to test the compliance with safety limits. The total radiated power and the effective radiated power were measured. The measured effective radiated power is about 3.6 to 11.5 times lower than the allowed effective radiated power for PMR 446 radios. These powers of the real PMR 446 radios will be used to estimate the realistic local absorption in a realistic human head model.

References

[1] ERC (European Radio communications Committee). *ERC decision of 23 November 1998 on the harmonised frequency band to be designated for PMR 446*, 1998.

[2] ETSI. *ETSI European Standard, Electromagnetic compatibility and Radio spectrum Matters (ERM); Land Mobile Service; Radio equipment using integral antennas intended primarily for analogue speech; Part 1: Technical characteristics and methods of measurement, ETSI EN 300 296-1*, 2001.

[3] ETSI. *ETSI European Standard, Electromagnetic compatibility and Radio Spectrum Matters (ERM); Land Mobile Service; Radio equipment using integral antennas intended primarily for analogue speech; Part 2: Harmonized EN covering essential requirements under article 3.2 of the R&TTE Directive, ETSI EN 300 296-2*, 2001.

[4] Federal Communications Commission (FCC). *Family Radio Service (FRS)*. Available from: http://www.fcc.gov/encyclopedia/family-radio-service-frs.

[5] ICNIRP. *Guidelines for limiting exposure to time-varying electric, magnetic, and electromagnetic fields*. Health Phys., 74:494–522, 1998.

[6] Federal Communications Commission (FCC). *Evaluating compliance with FCC guidelines for human exposure to radiofrequency electromagnetic fields*. Technical Report Tech. Rep. Supplement C to bulletin 65, Federal Communications Commission (FCC), Washington DC 20554, USA, June 2001.

[7] G. Lazzi and O. Gandhi. *On Modeling and Personal Dosimetry of Cellular Telephone Helical Antennas with the FDTD Code*. IEEE Transactions on Antennas and Propagation, 46:525–30, 1998.

[8] S. Koulouridis and K. S. Nikita. *Study of the Coupling Between Human Head and Cellular Phone Helical Antennas*. IEEE Transactions on Electromagnetic Compatibility, 46:62–70, 2004.

[9] C. A. Balanis. *Antenna Theory, Analysis and Design*. Harper and Row, 1982.

4

SAR assessment of a PMR446 radio

4.1 Introduction

The vast amount of studies on dosimetry deals with the exposure due to mobile devices and base station antennas for cellular communication systems. However, the mobile phone is not the only device operated in the proximity of the human head. With the case study of the walkie talkie, we draw the attention to a device that gained interest as an alternative for cellular phones for short-range communications. Walkie talkies or two-way radios operate close to the human head as is the case for mobile phones. The typical operating positions of a walkie talkie are in front of the face whereas a mobile phone is typical operated next to the ear. When operating a walkie talkie, the antenna of a walkie talkie could be just in front of the eye. ICNIRP restricts the local mass-averaged specific absorption rate in 10 g (applicable in Europe) based on cataract in the eye of a rabbit. As opposed to mobile phones, no or little attention is payed to walkie-talkies in dosimetry, although compliance tests also apply to these devices.

In recent years, walkie-talkies are more frequently encoutered as a short-range communication device. Adults give a walkie talkie to their children when they go to play outside their house. Parking lot attendants employ a walkie-talkie to direct the traffic inside a parking lot to help drivers to find a free parking spot. As mentioned in Chapter 3, the advantages of walkie talkies are their ease-of-use (push-to-talk), their cheap price, and their free-of-charge communication.

In Europe, a walkie talkie operates according to the Private Mobile Radio at

446 MHz (PMR 446) standard. Whereas Family Radio Service (FRS) is authorized in the United States. The relative low frequency, the effective radiated power of 500 mW, the use of walkie talkies by children, the position in front of the face, and the limited number of exposure studies for walkie talkies attracted our attention to these devices.

In this chapter we investigate the specific absorption rate (SAR) in the human head induced by the electromagnetic fields irradiated by a walkie talkie. First, the walkie-talkie model developed in Section 3 is validated for dosimetric assessment. Secondly, reference points and lines are defined on the walkie-talkie as well on the human head. These lines assist in positioning the walkie talkie next to the head. Next, the SAR induced by a walkie talkie is evaluated in homogeneous head phantoms and in realistic human body models. Finally, the local and whole-body SAR is assessed in realistic human body models and the influence of the ageing on the local-averaged specific absorption rate in child head phantoms is evaluated.

4.2 Assessment of SAR induced by walkie-talkies in the flat phantom

This section describes the investigation of the expiremental and numerical assessment of the SAR induced in the oval flat phantom by a model of a walkie-talkie and real walkie-talkie devices. The oval flat phantom setup is used for compliance testing of hand-held and body-worn devices operated near the human body at locations other than the ear [1]. The peak local-averaged SAR will be discussed and compared with SAR limits according to international standards [2] and [3].

4.2.1 Walkie-talkie model and real devices

Two models and four walkie-talkie devices are placed at a distance d below an oval flat phantom as shown in Figure 4.16. In Chapter 3, we designed and validated a model of a walkie-talkie. This model consists of a helical antenna mounted on a ground plane representing the PCB of a real walkie-talkie. The helical antenna is enclosed by a dielectric housing with a relative permittivity, ϵ_r, of 4 and a conductivity, σ, of 7 mS/m. The dimensions of the walkie-talkie are listed in Table 3.1. The measurement model of the walkie-talkie is fed through a bazooka balun. The bazooka balun imposes a balanced antenna input current at the terminals of the walkie-talkie model.

We did not take into account the hand of the user. The IEC standard 62209-2 [1] for compliance testing does not specify a hand position because dosimetric studies [4–7] suggest that, excluding the hand in modelling constitutes a conservative case scenario for SAR in the head.

4.2.2 The measurement setup and procedure

The measurement setup consists of a robot (Staubli Type Rx90B L), a DASY4 measurement system (SPEAG, Zurich, Switzerland), a power meter (Agilent E4419B, power sensors: 8482H), a directional coupler (HP775D Dual Directional Coupler 450-940 MC), an RF termination (Meca 480-1), a generator (HP8647A), a network analyzer (HP8753E), and the flat phantom (SPEAG ELI4) filled with head simulating liquid (HSL450). The DASY4 measurement system consists of data aquisition electronics (DAE3 from SPEAG) and a dosimetric probe (ET3DV6 from SPEAG). Figure 4.1 shows the setup for performing the dosimetric measurements. The dosimetric system (probe and data acquisition electronics) is attached to a robot. The robot and the data aqcuistion electronics are connected to a server and managed through the graphical user interface of a laptop or desktop computer. The walkie-talkies or the walkie-talkie models are placed at short distance of the oval flat phantom. The oval flat phantom is filled with head simulating liquid (HSL450 from SPEAG) as suggested by IEC62209 [8]. The dielectric properties of the liquid at 450 MHz are σ = 0.87 S/m and ϵ_{r} = 43.5. In case of the walkie-talkie model, the model is connected to an RF generator. The input power of the antennas is measured by a power meter via a directional coupler.

The worst-case uncertainty of the DASY4 measurement system is mentioned in the manual [9] provided with the system. The combined standard uncertainty on the local-averaged SAR in 1 g and 10 g equals $\pm$10.9 % and $\pm$10.7 %, respectively; the expanded standard uncertainty on the local-averaged SAR in 1 g and 10 g equals $\pm$21.9 % and $\pm$21.4 %, respectively. This worst-case uncertainty budget for DASY4 was assessed according to IEEE 1528 [10]. For specic tests and congurations, the uncertainty can be considerable smaller [9].

A System Performance Check (SPC) was carried out according to IEC62209 [8] to check for possible short-time drifts and to determine possible uncertainties of the measurement system. We placed a standard dipole antenna at 450 MHz (D450V3, SPEAG, Zurich, Switzerland) below the oval flat phantom and compared the local SAR values obtained from the SPC with the reference SAR values [11]. The main causes of uncertainty are the positioning of the dipole and the deviation of the liquid parameters from the specified parameters due to evaporation of the liquid. According to IEC62209 [8], the acceptable tolerance must be determined for each system check and shall be within $\pm$ 10 % of the previously recorded system check target values. We assumed that these target values equal the reference SAR values at 450 MHZ found in IEC62209. The SPC showed that relative error from the reference value is within the acceptable tolerance of $\pm$ 10 %, except from the $SAR_{10\mathrm{g}}$ which slightly exceeded the acceptable tolerance by 3 %.

The peak local-averaged SAR ($SAR_{1\mathrm{g}}$ and $SAR_{10\mathrm{g}}$) generated by the devices and the models were measured using a DASY 4 measurement system from SPEAG (Zurich, Switzerland). The measurements were performed in the reseach labs of

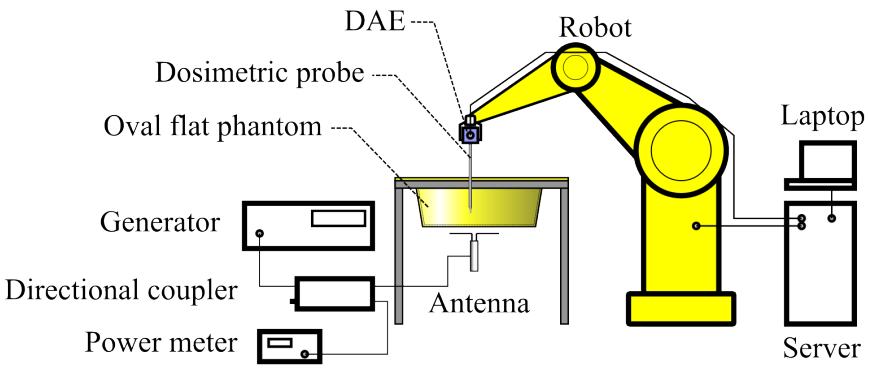

Figure 4.1: *A drawing of the setup for dosimetric measurements.*

IT'IS in Zurich, Switzerland. The devices and models have been placed below the oval flat phantom (ELI4 from SPEAG) at several distances from the liquid: touch, 15 mm, 20 mm, 30 mm and 50 mm.

The commercially available walkie-talkies were placed below the flat phantom with their push-to-talk button fixed during the measurement in order to transmit continuously. Before every measurement new batteries were placed in the walkie-talkies so that the walkie-talkies transmitted at maximum power. A walkie-talkie uses half-duplex communication resulting in a varying duty cycle from 0 % to 100 %. A continuously transmitting device has a duty-cycle of 100 %. A worst-case duty cycle of 100 % is selected for compliance testing.

Besides the four commercially available walkie-talkies, we also assessed the peak local-averaged SAR in 1 g and 10 g for two hand-made walkie-talkie models: the first walkie-talkie model, designated as M1, is a simple PEC model consisting of a PEC ground plane and a helical antenna rod. The other walkie-talkie model M2 included the coating around the helical antenna. The measured peak SAR values are compared with the simulations.

4.2.3 Measurement procedure

The procedure to measure the peak local-averaged SAR consisted of the following consecutive steps:

a) Power Reference Measurement in a single point

b) Delay of 180 sec

c) Area scan

d) Zoom scan

e) Power Drift Measurement in the same point as a)

The delay of 180 sec was selected to reduce the influence of the drift on the measurements. One device showed an initial drift after it was operated. Afterwards, the drift was reduced and the power of the device remained nearly constant during the SAR measurement.

The peak local-averaged SAR was determined from the volume scan and estimated from the area scan using the method of Kanda et al. [12].

4.2.4 The numerical method

We used the finite-difference time-domain (FDTD) technique available in the 3D full-wave electromagnetic software package SEMCAD-X (SPEAG, Zurich, Switzerland) for performing the numerical assessment in the oval flat phantom and in the child head phantoms. In FDTD calculations the simulation domain is finite and boundary conditions are used to mimic freespace. We applied uni-axial perfectly matched layers (UPML) at the boundaries. The number of layers are automatically set by the FDTD solver to obtain a selected efficiency of 99.9 %. The padding (minimum distance between absorbing boundaries (UPML) and the bounding box around the combination of walkie-talkie and human head model or flat phantom was a quarter of a wavelength. The grid step for the helical antenna equalled 0.5 mm, and the grid step in the flat phantom and the child head phantoms was maximum was maximum 2 mm except from the back of the child heads were the grid step was increased to 2.5 mm. Based on these settings we estimated the uncertainty on the peak local-averaged SAR from the study of Bakker et al [13, 14]. The expanded uncertainty U (k = 2) on $SAR_{10\mathrm{g}}$ in the flat phantom filled with tissue-simulating liquid equalled 11.9 % (there is no uncertainty on the dielectric properties of tissue-simulating liquid because the values are specified in standards). In the heterogeneous human head model the uncertainty increases to 23.4 % due to the uncertainty of the assessment of the dielectric properties of the human body tissues. The dielectric properties of the of the human body tissues are taken from the Gabriel database [15–17] and mapped to the corresponding tissues of the heterogeneous head model.

4.2.5 SAR assessment of the real walkie-takies

Figure 4.2 shows the peak local-averaged SAR in 1 g and 10 g estimated from the area scan [12] — The area scan estimates quickly (as compared to the volume scan) the peak local-averaged SAR from an area scan and the known transmit frequency — , whereas Figure 4.3 shows the $SAR_{1\mathrm{g}}$ and $SAR_{10\mathrm{g}}$ determined from the volume scan. The presented values are for a duty-cycle of 100 % (when

continuous talking during at least 6 minutes). The "Alecto" was not measured at a distance of 15 mm between the device and the liquid inside the flat phantom. Every measurement started with inserting new batteries into the device except from the "Alecto" for which we did not change the batteries for the measurements at 20 mm, 30 mm and 50 mm. Except from the touch position, the "Cobra MT500" shows a higher SAR in 1 g and 10 g than the walkie-talkies from Topcom and Alecto. The highest values of the $SAR_{1\mathrm{g}}$ and $SAR_{10\mathrm{g}}$ occured when the walkie-talkie touched the flat phantom: $SAR_{1\mathrm{g}}$ = 0.52 W/kg (Alecto) and $SAR_{10\mathrm{g}}$ = 0.35 W/kg (Alecto) on basis of the volume scan. These values for the touch position comply with the SAR-limits for 1 g (i.e., 1.6 W/kg) and 10 g (i.e., 2 W/kg), respectively, even for a worst-case duty-cycle of 100 %.

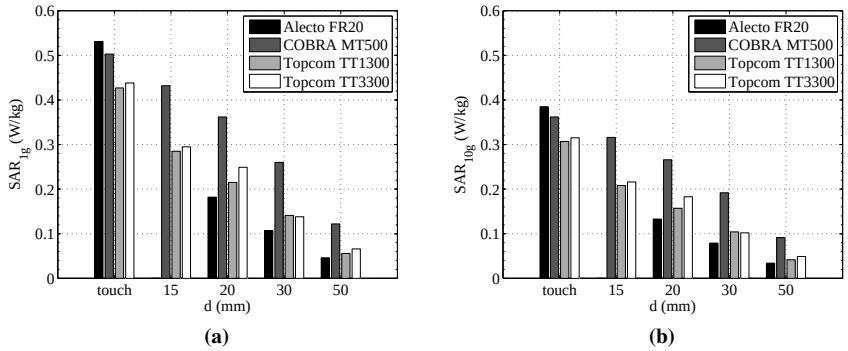

Figure 4.2: *The peak local-averaged SAR in 1 g and 10 g estimated from the area scan in four walkie-talkie devices (duty cycle is 100 %).*

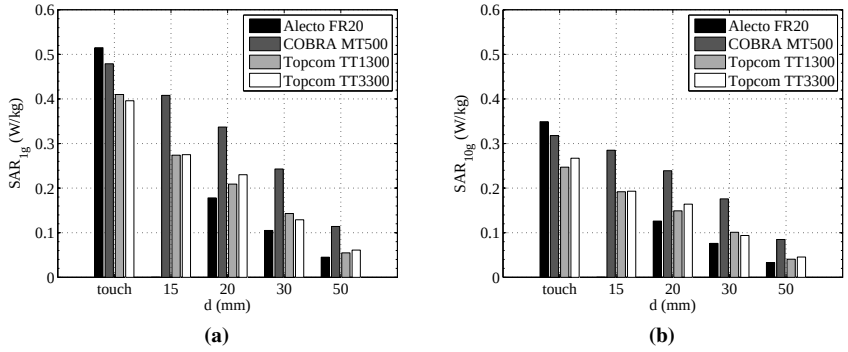

Figure 4.3: *The peak local SAR in 1 g and 10 g determined from the volume scan in four walkie-talkie devices (duty cycle is 100 %).*

Figure 4.4 shows the drift of the power measured in a user-defined reference point inside the flat phantom. The power drift is measured from the electric field value in the selected reference point once before and once after the actual SAR measurement. This measurement gives us an idea about the stability of the transmitted power of the walkie-talkies. The reference point was located near the surface of the flat phantom where the walkie-talkies were positioned. The power drift varies between -0.3 dB and -1.4 dB. The largest drift was observed in the Topcom T3300 followed by the COBRA MT500. On average, the power drift of the Alecto and Topcom TT1300 were comparable. The power drift does not only depend on the walkie-talkie device, but also on the quality of the batteries.

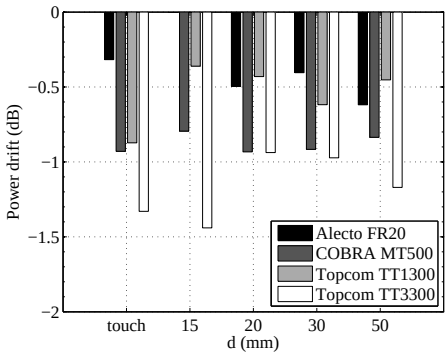

Figure 4.4: *Power drift of the commercially available walkie-talkies with distance between the device and the liquid inside the flat phatom.*

4.2.5.1 SAR assessment of the walkie-takie models

The input power of the walkie-talkie models has been set to 10 dBm during the measurement taking into account the reflection losses. Figure 4.5 shows the measured and the simulated peak local-averaged SAR over 1 g and 10 g estimated from the area scan [12]. The maximum relative deviation on the peak local-averaged SAR in 10 g equals 16 % for the PEC model M1 at a distance of 20 mm. Figure 4.6 shows the peak local-averaged SAR determined from the volume scan. As could be expected these measurements agreed better with the simulations. The largest absolute relative deviation is 11 % on $SAR_{1\mathrm{g}}$ for PEC model M2 at a distance of 30 mm. So, a good agreement (relative error within $\pm$ 10 %) is observed between the measurements of the local-averaged SAR based on the volume scan and the simulations. In what follows, we will only consider the results from the volume scans.

For a separation up to 15 mm, both walkie-talkie models resulted in similar peak local-averaged SAR values. For larger distances, the PEC model induced a

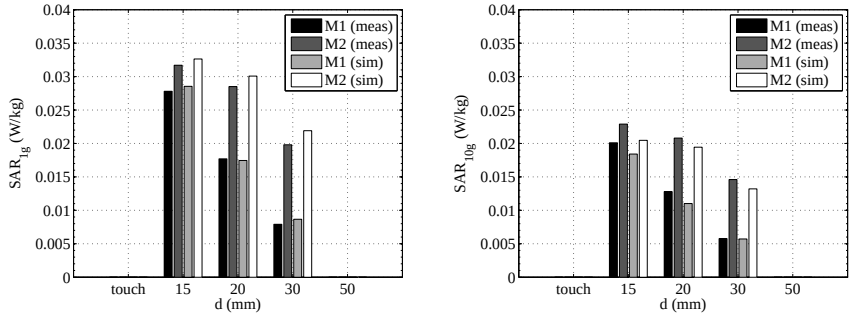

Figure 4.5: *The peak local-averaged SAR in (a) 1 g and (b) 10 g estimated from the area scan for a PEC model (M1) and model with coating around the helical antenna (M2) for an input power of 10 dBm.*

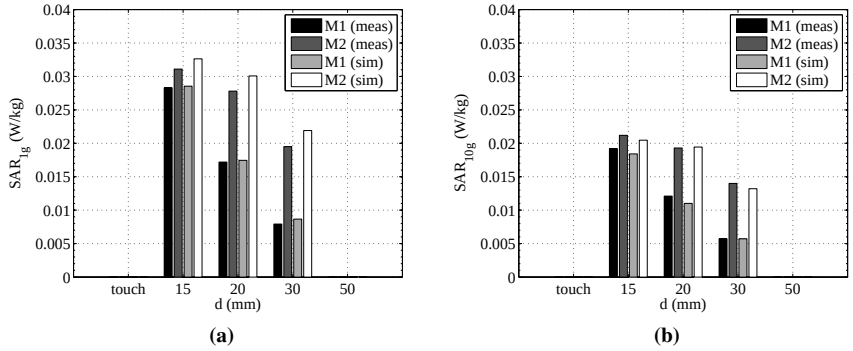

Figure 4.6: *The peak local-averaged SAR in (a) 1 g and (b) 10 g estimated from the volume scan for a PEC model and model with coating around the helical antenna .*

SAR value that was about half the value obtained by the model with the coating. The difference between the two models was the coating. Thus, the shape and the dielectric properties of the coating caused the difference. The relative permittivity shifts the resonance frequency towards the PMR 446 communication band (see Section 3.2.3). We also observed that the coating provides some kind of matching between the antenna and the flat phantom in terms of absorption.

We validated the use of the PEC model (M1) and the model with coating (M2) as a substitute for real devices by comparing the local SAR values of the real devices with the ones of the model for the same ERP of the real devices and for the same magnetic near field. In Section 3.3.1 we discussed the ERP values of

the four walkie-talkie devices. We observed that the ERP of the considered devices was at least 3.6 times smaller than the maximum allowed ERP for PMR 446 radios. We rescaled the ERP of the model with coating to the values listed in Table 3.3. The antenna input power that was needed to reach the ERP of the walkie-talkies is applied during the dosimetric measurement. Figure 4.7 shows the $SAR_{1\mathrm{g}}$ and $SAR_{10\mathrm{g}}$ of the walkie-talkie model with coating (M2). We observed that the walkie-talkie model overestimates the peak local-averaged SAR of the real devices. Rescaling the input power based on the ERP (a far-field characteristic) is inadequate for the assessment of the SAR in human tissue despite the use of the helical antenna with coating from the COBRA MT500. The maximum absolute deviation on $SAR_{1\mathrm{g}}$ and $SAR_{10\mathrm{g}}$ between the model and the device was 4.5 dB and 3.4 dB, respectively. The deviation originates from uncertainties on the ERP and SAR measurements, the simplifications of the model with respect to the real device and from differences in the coupling when the device or model operates at close distance to the phantom. The deviation for the other models was maximum 4.5 dB (Topcom tt3300) and 3.4 dB (Topcom tt3300) for $SAR_{1\mathrm{g}}$ and $SAR_{10\mathrm{g}}$, respectively. For further analysis of the absorption by walkie-talkies in head phantoms based on a rescaling of the ERP, we will take into account a correction factor of 3 dB.

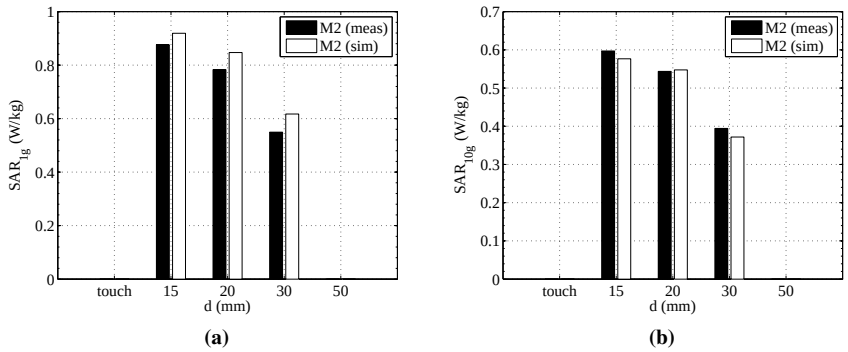

Figure 4.7: *The peak local-averaged SAR in (a) 1 g and (b) 10 g estimated from the volume scan for the PEC model with coating around the helical antenna for the same ERP as the COBRA MT500 (100 % duty cycle).*

A better quantity for validating the walkie-talkie model as a substitute for the real device for assessing the peak local-averaged SAR is the magnetic near field. Kuster et al showed that the SAR is mainly proportional to the incident magnetic near field [18]. We rescaled the maximum of the magnetic field in a plane at a distance of 20 mm of the ground plane of the walkie-talkie model to the maximum value of the magnetic field in the same plane above the real device. The maximum

deviation on the peak local-averaged SAR is less than 1 dB. The magnetic near field is a better quantity than the far-field parameter ERP for estimating the peak local-averaged SAR of a real device.

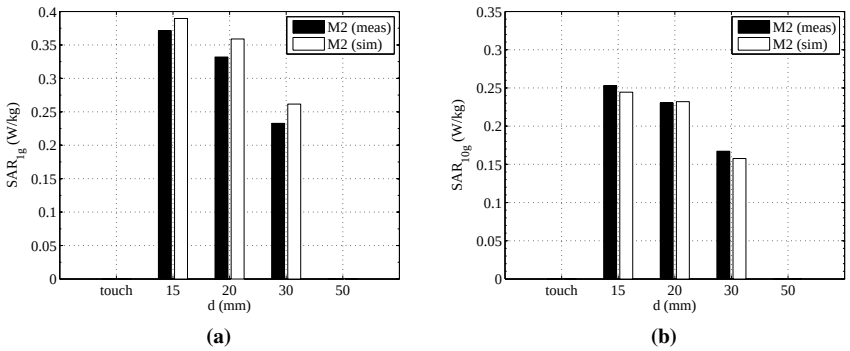

Figure 4.8: *The peak local-averaged SAR in (a) 1 g and (b) 10 g estimated from the volume scan for the PEC model with coating around the helical antenna for the same magnetic field at 20 mm above the ground plane as the COBRA MT500 (100 % duty cycle).*

Finally, we estimated the worst-case peak local-averaged SAR for the walkie-talkie devices. We determined the peak local-averaged SAR in 1 g and 10 g for an input power that gives an ERP of 500 mW in free space (we assumed a duty-cycle of 100 % for worst-case evaluation) for the walkie-talkie model with coating and taking into account a correction factor of 2. Figure 4.9 shows that the walkie-talkie model is not compliant to the FCC limit of 1.6 mW/kg in a cube of 1 g at 15 mm. The worst-case peak local-averaged SAR in 1 g of tissue exceeded the FCC limit by up to 0.3 dB (based on the simulated value). If we compared the peak local-averaged SAR in 10 g of tissue with the ICNIRP basic restriction of 2 W/kg, then we observed that the walkie-talkies are compliant.

4.3 Definition of walkie-talkie positions in front of the head

The assessment of the absorption in human tissue induced by communication devices operating in the proximity of the human body starts with defining test positions of the communication device next to the human body. Test positions leading to worst-case absorption of the electromagnetic energy is of interest in compliance testing. But, in exposure assessment also typical positions of the device not inducing worst-case absorption are also of interest. In this section, we defined four test positions for when a walkie-talkie is operated next to the human head. The defined

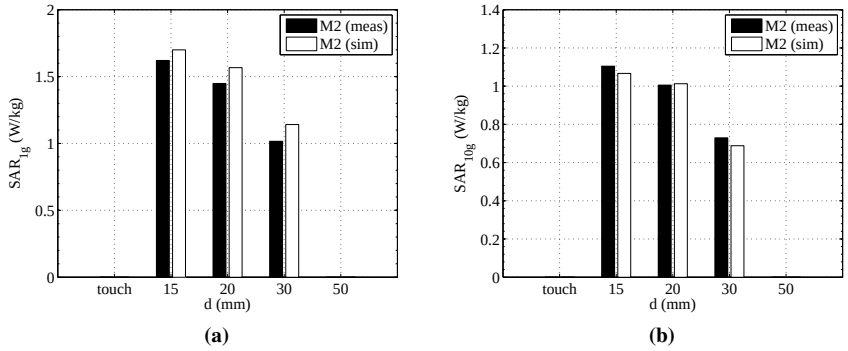

Figure 4.9: *Worst-case assessment of the peak local-averaged SAR in (a) 1 g and (b) 10 g induced by the PEC model with coating for ERP = 500 mW (100 % duty cycle).*

test positions covered both worst-case and typical positions of a walkie-talkie next to the head.

4.3.1 Defining reference points, reference axes and reference planes

The positioning of a portable, wearable or hand-held device in the proximity of a phantom is done by means of predefined reference-points, reference-axes and reference-planes on the mobile terminal equipment (MTE) and the phantom. In the case of a walkie-talkie operating near the head, the following points, lines and planes of reference can be defined:

- walkie-talkie
  - VCL: Vertical Center Line
  - HCL: Horizontal Center Line
  - SCL: Sagittal Center Line
  - A: Audible Point (center of the microphone)
- head-phantom
  - M: Mouth Point
  - RCM: Right Corner of Mouth Point
  - LCM: Left Corner of Mouth Point
  - Rα-HP: Right Alpha Half Plane
  - Lα-HP: Left Alpha Half Plane

- Rβ-HP: Right Beta Half Plane
- Lβ-HP: Left Beta Half Plane
- SP: Sagittal Plane

Figure 4.10 shows the reference lines and point defined for a generic walkie-talkie. A walkie-talkie consist typically of a case that encloses the circuitry and houses the batteries, and a protruding antenna on top of the case. We defined three perpendicular lines on the walkie-talkie: the vertical center line (VCL), the horizontal center line (HCL), and the sagittal center line (SCL). All three lines intersect at the audible point of the device (A). The sagittal center line runs from the front of the walkie-talkie to the back of the device.

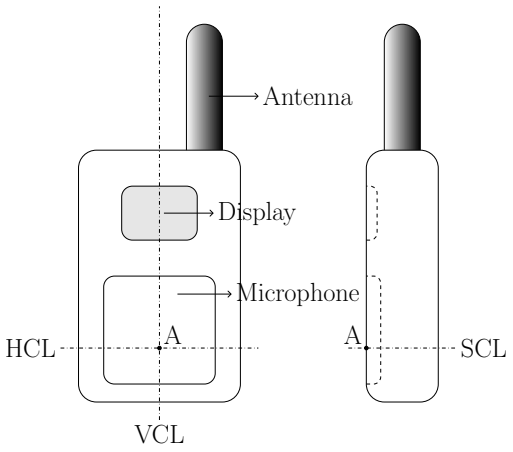

Figure 4.10: *Reference points and reference lines of a generic walkie-talkie.*

Currently, one reference plane for the SAM-head has been defined in the CENELEC standard EN50361 [2] to place a mobile phone close to the head. To position a walkie-talkie, two pairs of half planes (HP) are defined in addition to CENELEC EN50361. Each pair of half planes consists of one half plane at the right side of the head and one half plane at the left side of the head. A frequently encountered position of the walkie-talkie is obtained by lying the VCL of the walkie-talkie in an α-plane so that it touches the cheek of the user. Of special interest is the assessment of the SAR in the eye. This leads to the definition of a second pair of half planes (Rβ-half plane and Lβ-half plane) along which the walkie-talkie is positioned and places the radiating part of the walkie-talkie closer to the eye. To obtain an α-half plane, we rotate the sagittal plane about an angle of +/-70 deg as indicated in Figure 4.11. The origin of the rotation axis (horizontal axis through M-point from front to back) lies in the M-point. To obtain a β-half plane we rotate

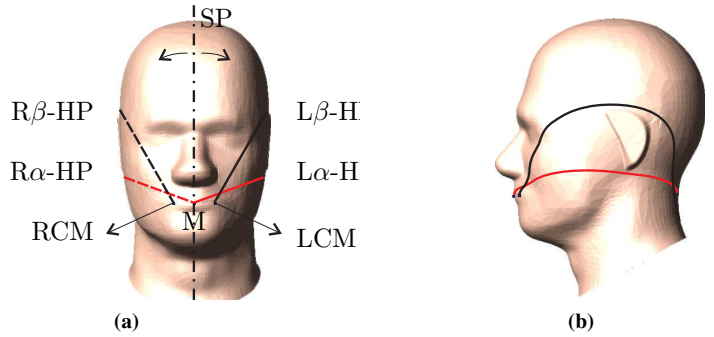

Figure 4.11: *Reference points and reference lines of the Specific Anthropomorphic Mannequin (SAM) head phantom.*

the sagittal plane about an angle of +/-30 deg and shift the sagittal plane horizontally until it passes through the RCM point or the LCM point. (See Figure 4.11.) The values of the angles for the half planes are based on the positioning against the Specific Anthropomorphic Mannequin (SAM) head phantom, which is used for compliance testing of mobile phones next to the ear.

4.3.2 Typical positions of a PMR446 radio

In the following four examples, a consumer walkie-talkie – also called PMR 446 radio – is positioned in front of the SAM head. The sagittal plane and the half planes, α-HP and β-HP, support the placement of the walkie-talkie in the proximity of the SAM head. Positions 3 and 4 turn into a worst-case position by rolling the walkie-talkie over the shell of the SAM-phantom until the antenna touches the shell of the SAM phantom. As explained in Section 4.2.1, the hand of the user is not taken into account because dosimetric studies suggest that excluding the hand yields a conservative peak local-averaged SAR value in the head [4–7].

4.3.2.1 Vertical position in front of the face (Position 1)

The first position is the vertical position in front of the face. Position 1 is shown in Figure 4.12 and is defined as follows:

1. Place the walkie-talkie vertically in front of the face of the SAM head. The VCL of the walkie-talkie lies in the SP of the SAM head and the SCL of the walkie-talkie runs through the M of the SAM phantom.

2. Shift the walkie-talkie towards the SAM phantom until the case of the walkie-talkie touches the nose of the SAM head.

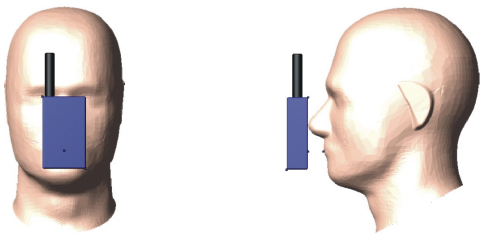

Figure 4.12: *Position 1: Vertical position in front of the face.*

4.3.2.2 Backward tilted position in front of the face (Position 2)

The second position (Position 2) is the position where the walkie-talkie is kept vertically against the nose and the bottom of the device is tilted towards the mouth of the head model. Position 2 is shown in Figure 4.13:

1. Ditto as in Position 1.
2. Rotate the walkie-talkie backward (upper part of the walkie-talkie away from the head) about an angle of 20 deg in the SP of the SAM head. The point A of the walkie-talkie serves as the origin of the rotation axis HCL.
3. Shift the walkie-talkie horizontally in the direction of the SAM phantom until the case of the walkie-talkie touches the nose of the SAM head.

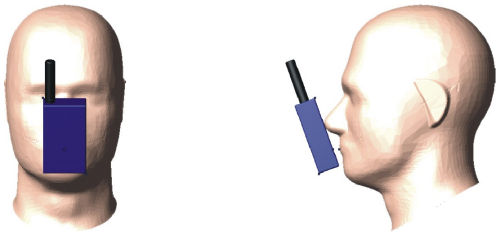

Figure 4.13: *Position 2: Backward-tilted position in front of the face.*

4.3.2.3 Cheek position (Position 3)

The third position (Position 3) is the position where the walkie-talkie is hold against the cheeck of the head model. A worst-case position happens when the

antenna is pushed against the cheeck. The walkie-talkie can be positioned in front of the right side or the left side of the face. In general, both positions will yield different peak local-averaged SAR values because walkie-talkies are typically not symmetric. Position 3 in front of the left side of the face is shown in Figure 4.14:

1. Ditto as in Position 1.
2. Ditto as in Position 1.
3. Rotate the walkie-talkie around the SCL until the VCL of the walkie-talkie lays parallel to a α-half plane of the SAM head.
4. Position the walkie-talkie until the distance between the shell of the SAM head and the VCL is minimized. This is done by a sequence of rotations (around HCL in the α-HP and around VCL) and shifts towards the head phantom (translation vector lying in the α-half plane).
5. **Worst-case step**: roll the walkie-talkie along the cheek until any point of the external antenna touches the shell of the SAM-head.

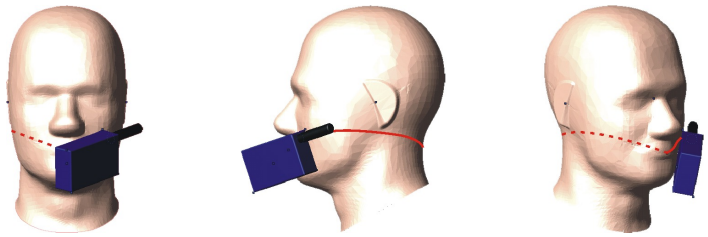

Figure 4.14: *Position 3: Cheek position at the left side of the face.*

4.3.2.4 Eye position (Position 4)

The last position (Position 4) is the position where the antenna of the walkie-talkie is in front of the eye. A worst-case position occurs when the antenna is pushed against the cheeck. Again, the walkie-talkie can be positioned in front of the right side or the left side of the face. In general, both positions will yield different peak local-averaged SAR values because walkie-talkies are typically not symmetric. Position 4 in front of the left side of the face is shown in Figure 4.15 and defined as follows:

1. Ditto as in Position 1.
2. Ditto as in Position 1.

3. Rotate the walkie-talkie around the SCL until the VCL of the walkie-talkie lies in a β-half plane of the SAM head.

4. Shift the walkie-talkie horizontally along HCL until the audible A of the device is aligned with the RCM or LCM of the head phantom.

5. Position the walkie-talkie until the distance between the shell of the SAM head and the VCL is minimized. This is done by a sequence of rotations (around HCL in the β-HP and around VCL) and shifts towards the head phantom (translation vector lying in the β-half plane).

6. **Worst-case step** Roll the walkie-talkie along the cheek until any point of the external antenna touches the shell of the SAM-head.

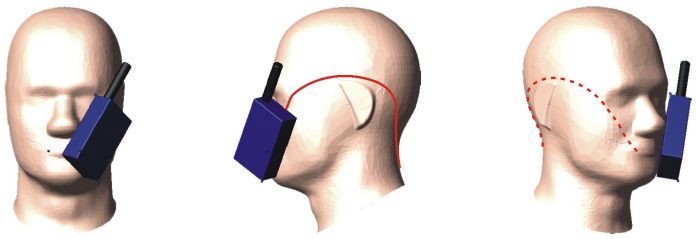

Figure 4.15: *Position 4: Eye position at the left side of the face.*

4.4 Evaluation of the oval flat phantom and the SAM head for compliance testing of walkie-talkies

The Specific Anthropomorphic Mannequin (SAM) is designed for compliance testing of mobile phones. The mobile phone, transmitting at maximum power, is positioned next to the ear of the SAM phantom which is filled with a homogeneous tissue simulating liquid. This setup is designed as to provide a worst-case absorption measure. For body-worn devices, the oval flat phantom is designed for compliance testing [8]. In this section, we will evaluate the oval flat phantom and the SAM phantom for compliance testing of walkie-talkie devices. The absorption results obtained in the standardized phantoms are compared to the absorption in a planar infinite medium and a realistic adult and a child head model. We selected the Visible Human (VH) and the 3-year-old child [19] as the adult and child head model, respectively.

We selected the PEC model of the walkie-talkie because it allows the numerical evaluation of the absorption in an half-infinite medium. A half infinite medium can only be approximated in an FDTD solver due to the finite simulation domain.

Therefore, we used the Method-of-Moments (MoM) method implemented in the 3D electromagnetic solver FEKO (EMSS, South-Africa) for solving this configuration. In FEKO special Green's functions are used to model a multi-layered substrate. The use of the Green's functions does not allow us to include the dielectric coating around the helical antenna (only perfectly conducting structures are allowed). Therefore, we selected the PEC model of the walkie-talkie for this investigation.

In a SAR assessment, the SAR values are normalized to constant power or constant input current. These two normalizations originate from the two types of RF sources used in mobile communication devices, i.e. sources that generate a constant power and sources that keep the current constant. The constant input power is set to 500 mW because the ERP for PMR 446 equals 500 mW and the model does not introduce losses and the gain of the antenna is 1. The constant input current has been determined as the input current which is necessary to generate an input antenna power of 500 mW in free space. With an input impedance of $14.6 - i0.7$, see Section 3.2, the input rms-current is $|I_{rms}|$ = 184.8 mA.

4.4.1 Results for the flat-phantom setup

The flat-phantom setup is drawn in Figure 4.16. The oval flat phantom is used in measurements as a model for a half-infinite medium. The oval flat phantom has been modelled in SEMCAD as well as in FEKO and is filled with head simulating liquid. The dielectric properties of the liquid equalled the properties of head tissue as suggested by IEC62209 [8]. The dielectric properties for an operating frequency of 450 MHz are: ϵ_r = 43.5 and σ = 0.87 S/m. The ground plane of the walkie-talkie model is placed at a distance d below the liquid-shell interface of the phantom. We considered a minimum distance d of 15 mm between the ground plane of a PMR446 radio and the phantom when the (case of the) PMR446 radio touches the phantom. The input power is 500 mW.

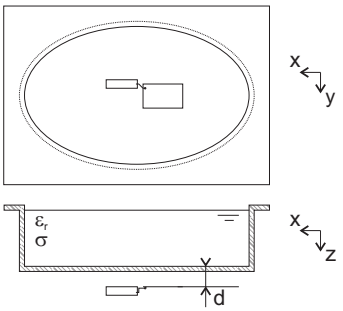

Figure 4.16: *Configuration: the model of a walkie-talkie placed at a distance* d *below the oval flat phantom.*

The measured local-averaged SAR in 1 g and 10 g of the liquid with varying distance d is shown in Figure 4.17. Regarding the maximum allowed ERP of 500 mW as specified by the standard for PMR446 radio, one observes that for our model the limits are exceeded for an averaging volume over 1 g and 10 g of head tissue. The basic restrictions on $SAR_{1\mathrm{g}}$ (FCC) and $SAR_{10\mathrm{g}}$ (ICNIRP) are 1.6 W/kg and 2 W/kg, respectively. Due to the smaller averaging volume, the peak local-averaged SAR in 1 g is always higher than in 10 g. The local-averaged SAR complies with limits for a distance of 50 mm and 30 mm for the averaging volume of 1 g and 10 g, respectively. Figure 4.17 also shows the figures for a semi-infinite layered flat phantom. For a distance d up to 20 mm, the $SAR_{1\mathrm{g}}$ and $SAR_{10\mathrm{g}}$ in the semi-infinite layered phantom set an upper limit for the values obtained with the oval flat phantom. Or in other words, the semi-infinite layered phantom yields conservative values for the local-averaged SAR in a flat phantom for these short distances.

4.4.2 Results for the head phantoms

A typical position of a walkie-talkie during operation is the vertical position in front of the face as depicted in Figure 4.18. The distance d is now defined as the horizontal distance between the walkie-talkie model and the tip of the nose. The audible (A) of the walkie-talkie (see Section 4.3.2) has been vertically aligned with the center of the mouth of the head phantom (M).

Figure 4.19 shows the mass-averaged SAR for the SAM head, Visible Human head and the head of a 3-year-old child. Three simple compositions of the head tissue are investigated: head-air-skin (has), head-air (ha), and head (h). These simple tissue compositions are applied to a head phantom where possible and are selected to investigate the influence of the skin and the lumina (e.g., nasal cavity) on the peak local-averaged SAR. Furthermore, the SAR has also been evaluated in the heterogeneous Visible Human head (het). The mass-averaged SAR has been normalized to a constant antenna input power of 500 mW and a constant antenna input rms-current of 184.8 mA.

Concerning the compliance of the model to the current safety limits, the results of the numerical study (see Figure 4.19) learn that a walkie-talkie is able to exceed the limits for the local-averaged SAR in 1 g of tissue for distances up to 50 mm (for C3Y (ha) and constant input power) and in 10 g of tissue for distances up to 20 mm. Moreover, the considered vertical position of the walkie-talkie can not be assumed to be the worst-case position. So, one can expect even higher mass-averaged SAR values. To lower the absorbed electromagnetic power in the head it will be necessary to decrease the antenna input power or input current.

Comparing the plots in Figure 4.19, a different picture of the mass-averaged SAR is viewed for a constant input power and a constant input current. It is ob-

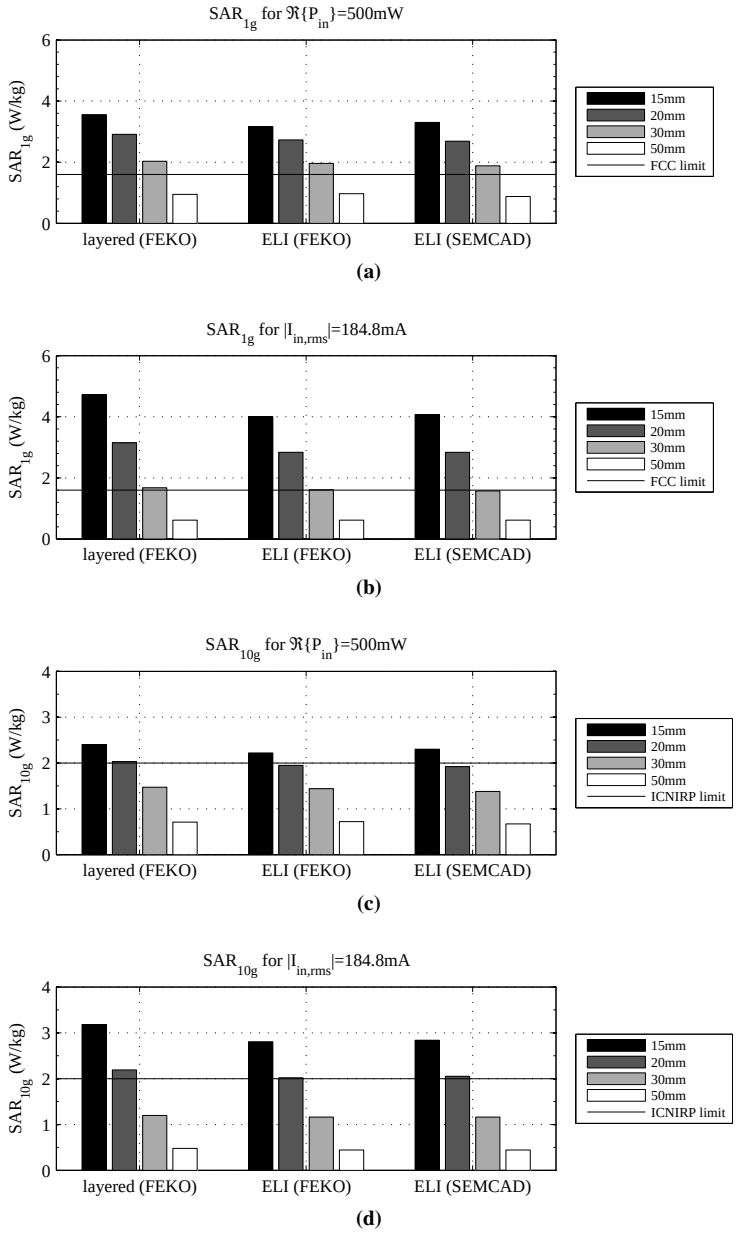

Figure 4.17: *Simulations of the local-averaged SAR of the walkie-talkie model for the flat phantom models: half space ("layered") and the oval flat phantom ("ELI").*

vious that increasing the distance d lowers the mass-averaged SAR. Figure 4.20

Figure 4.18: *The vertical position of the walkie-talkie in front of the face of the Visible Human Head.*

shows the input impedance $\mathrm{Z_{in}}$ for the considered setups. We observed that the mass-averaged SAR for constant input current only exceeds the mass-averaged SAR for constant input power if the real part of the input impedance $\Re\{\mathrm{Z_{in}}\}$ is larger than the real part of the input impedance in free space $\Re\{\mathrm{Z_{in,fs}}\}$. Consequently, the antenna input power $\mathrm{P_{in}}$ will be larger than 500 mW for a constant $|\mathrm{I_{rms}}|$ of 184.8 mA. Thus, resulting in a higher mass-averaged SAR. The real part of the input impedance of the walkie-talkie $\Re\{\mathrm{Z_{in}}\}$ at a distance of 15 mm and 20 mm from the flat phantom and 15 mm from the heterogeneous Visible Human head takes a larger value than $\Re\{\mathrm{Z_{in,fs}}\}$ (the real part of the free space input impedance of the walkie-talkie).

Consider only the homogeneous phantoms: flat, SAM, Visible Human (VH (h)) and 3-year-old child (C3Y (h)). For a constant input power of 500 mW, the flat phantom setup is not conservative in comparison with the homogeneous head phantoms. Moreover, for a constant input current of 184.8 mA, the mass-averaged SAR over 1 g takes a larger value in the homogeneous Visible Human Head and the 3-year-old child head ('VH (h)' and 'C3Y (h)' in Figure 4.19) than in the flat phantom for distances larger than 20 mm.

The mass-averaged SAR for the heterogeneous Visible Human head (VH(het)) is also found in Figure 4.19. Although the mass-averaged SAR exceeds the limit in 1 g of tissue, the values are significantly lower compared with the cases where a simple tissue configuration has been adopted. The homogeneous Visible Human head phantom has been assigned the IEC62209 recommended values for the dieletric properties.

Including all the air cavities in the homogeneous head phantoms alters the mass-averaged SAR significantly. The assessed mass-averaged SAR in the 3 year old child head increases, whereas the mass-averaged SAR decreases for the Visible Human head.

Taking into account the skin of the head does not alter the mass-averaged SAR significantly, because the dielectric properties of the skin are almost equal to those

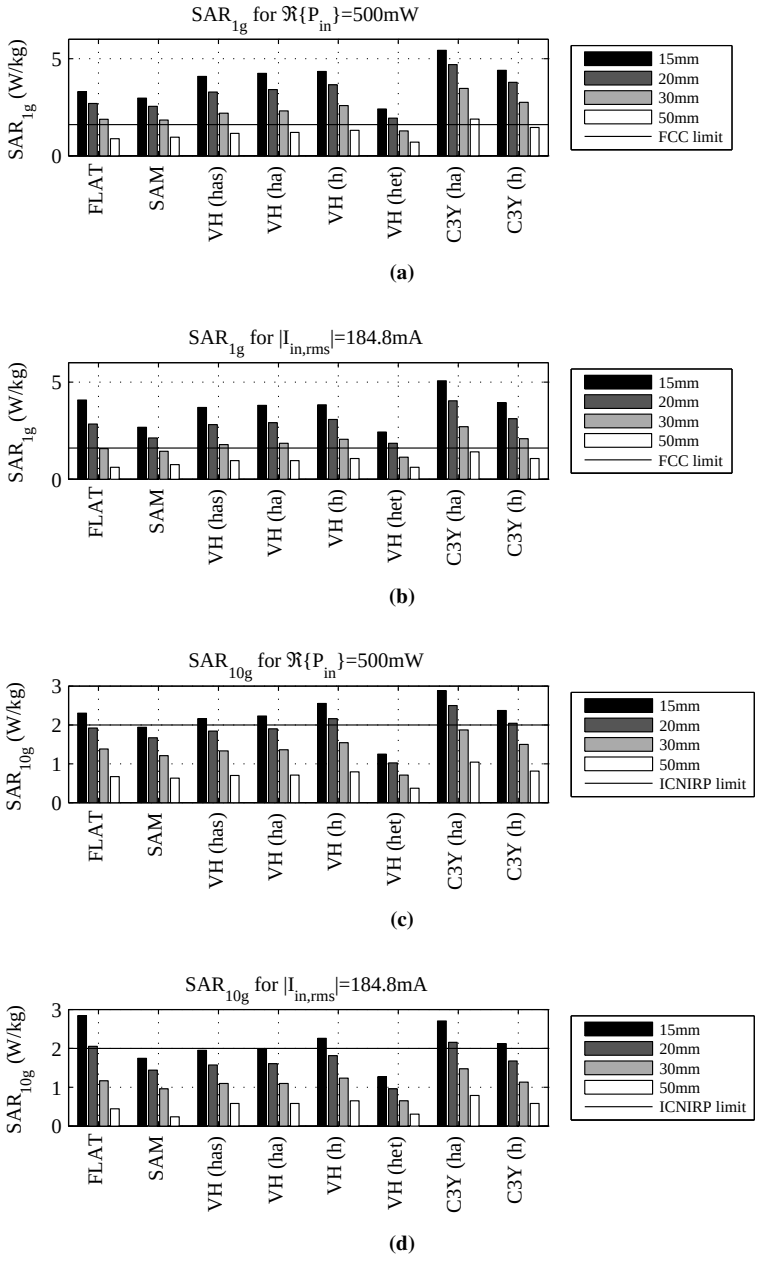

Figure 4.19: *The local-averaged SAR of the walkie-talkie model for the flat and the homogeneous and heterogeneous head models: homogeneous oval flat phantom (FLAT); homogeneous Specific Anthropomorphic Mannequin (SAM); Visible Human (VH) and the three-year-old child with homogeneous (h) and heterogeneous tissues (ha = head-air, has = head-air-skin).*

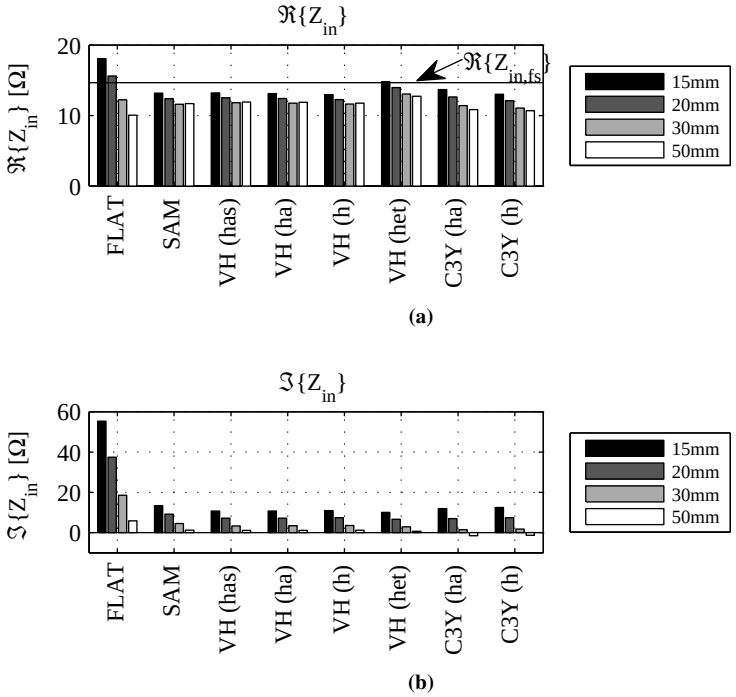

Figure 4.20: *The real (a) and imaginary (b) part of the antenna input impedance* $\mathrm{Z_{in}}$ *in the proximity of the oval flat phantom and the homogeneous and heterogeneous head phantoms: homogeneous oval flat phantom (FLAT); homogeneous Specific Anthropomorphic Mannequin (SAM); Visible Human (VH) and the three-year-old child with homogeneous (h) and heterogeneous tissues (ha = head-air, has = head-air-skin).* $\mathrm{Z_{in,fs}}$ *is the free-space impedance.*

of the average head tissue.

4.5 Effect of the ageing on the SAR values in children when exposed to walkie-talkie equipment

We have investigated the influence of the ageing of the human head to emissions from walkie-talkie devices. The metric used for the assessment is the peak local-averaged SAR in 10 g in two child head models.

4.5.1 Materials and methods

The walkie-talkie operates at a frequency of 446 MHz with a time-averaged effective radiated power (ERP) of 500 mW (assuming a duty-cycle of 100), further

details can be found in Section 3 and [20]. Two child head models and two typical positions of a walkie-talkie relative to the head have been investigated with respect to electromagnetic exposure. The head models correspond to 3-year (C3Y) and 7-year (C7Y) old child heads (Figure 6). The walkie-talkie is held in a vertical position in front of the face (Position 1, see Figure 4.12) and the eye position (Position 4, see Figure 4.15).

(a) **(b)**

Figure 4.21: *The two child head models: (a) the 3-year-old child and (b) the 7-year-old child.*

The dielectric properties of the tissues of the child head phantoms have been assigned the values of the tissues determined by Peyman et al. [21] whereby the 1-4 year-old were assigned the 10 kg pig data, the 11-13 year-old the 50 kg pig data and adults the 250 kg data. The numerical assessment of the exposure was carried out using the 3D electromagnetic solver SEMCAD-X (SPEAG, Zurich, Switzerland), which is a commercial finite-difference time-domain tool. The grid step in the head phantoms did not exceed 2.5 mm in all the three dimensions. The SAR calculations for each head in both positions were carried out using the 3 sets of dielectric properties.

The peak local-averaged SAR in 10 g is determined according to [22] as implemented in SEMCAD-X for maximum constant input power as well as for maximum constant input current, corresponding to the two types of sources that can be used in real walkie-talkies. The maximum input power $\mathrm{P_{in}}$ is calculated from the maximum effective radiated power (ERP) of 500 mW in free space. The maximum RMS input current equals the value of the input current necessary to achieve an ERP of 500 mW for the walkie-talkie in free-space and is 217 mA. In order to estimate the peak local-averaged SAR for a real walkie-talkie from the above results, the ERP of several commercially available walkie-talkies have been measured.

4.5.2 Results

The results of the assessment of the peak local-averaged SAR in 10 g are shown in Figure 4.22. For all the investigated cases, the local-averaged SAR in 10 g exceeds the 2 W/kg limit except from the eye position for the 3-year-old child and constant input power, and the influence of the ageing of the tissues on the $SAR_{10\mathrm{g}}$ in the child head phantoms is limited, i.e. deviations on $SAR_{10\mathrm{g}}$ are less than 10 % for the investigated configurations. The deviation on $SAR_{10\mathrm{g}}$ varies with the position of the peak local-averaged SAR in 10 g, whether constant input power or constant input current is considered, and with the human head model.

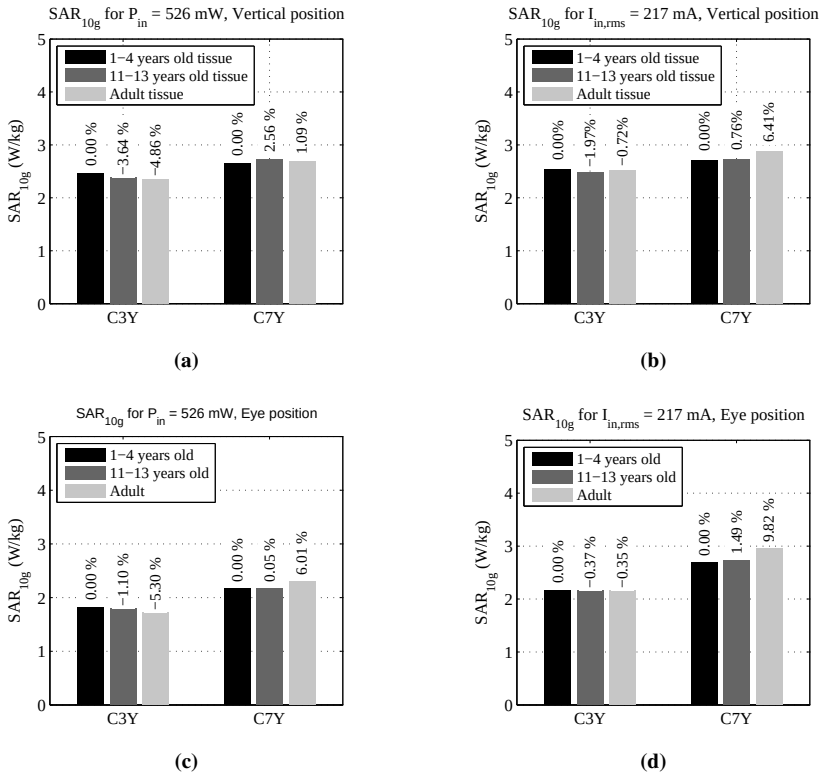

Figure 4.22: *Influence of the ageing on the 10 g peak local-averaged SAR in a 3-year-old (C3Y) and a 7-year-old child (C7Y) head phantom for the walkie-talkie model in (a)-(b) the vertical position and (c)-(d) the eye position, and for (a)-(c) the constant input power* $\mathrm{P_{in}}$ *and (b)-(d) the constant RMS input current* $\mathrm{I_{in,rms}}$.

The peak local-averaged SAR in 10 g is located at the left side of the nose for the eye position of the walkie-talkie and just above the nose and between the eyes for the vertical position of the walkie-talkie. As an example Figure 4.23 shows

SAR_{10g} in the C3Y for the two investigated walkie-talkie positions (vertical and eye position). The location of the peak SAR_{10g} is designated by a square. At the location at the side of the nose, the tissue within the averaging volume mainly consists of skin, connective tissue and the nasal cavity. At the position between the eyes, the tissues from the outside to the inside of the head are skin, connective tissue, nasal cavity and frontal sinus. Table 4.1 lists a mapping between these tissues where their dielectric properties have been obtained experimentally and those tissues in the head phantoms. Using this mapping, Figure 4.24 shows the variation of the dielectric properties with age of these tissues. The variation of the tissue properties are not really reflected in a variation of the SAR_{10g} as shown in Figure 4.22. Several arguments explain this observation. First, the averaging of the SAR dilutes the effect of the change in the SAR_{10g} as observed by De Salles et al. [23]. Secondly, head tissues do not contribute equally in the averaging volume. Thirdly, not all the tissues in the averaging volume have the same variation of the dielectric properties with age, in this case, only skin contributed to the variation of the dielectric properties within the 10 g cube. The marginal effect of the variation of dielectric properties on the 10 g local-averaged SAR has also been observed by Christ et al. [19]. They used C3Y and C7Y head models with the same dielectric data [21] as in this study and modeled the exposure of the children heads to 900 and 1800 MHz from generic wireless phones held to the ear. They observed up to 30 % variation in 10 g average SAR due to age dependent tissue properties. However, the variation was neither clearly systematic nor sufficiently large to establish variation in the dielectric properties as an important factor in the assessment of the exposure of children to wireless devices.

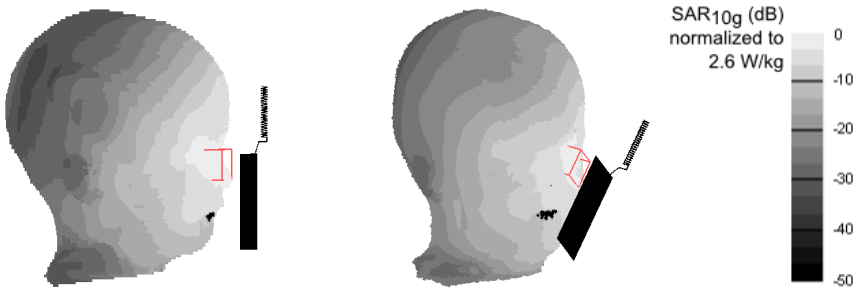

Figure 4.23: *The SAR_{10g} on the surface of the face for C3Y with the walkie-talkie in (a) vertical position and (b) eye position. The tissues were assigned the dielectric properties for the age of 1–4 years. The square designates the position of the peak SAR_{10g}.*

In Section 3.3.1 we reported the ERP of several commercially available walkie-talkies measured according to the ETSI standards. The ERP ranged from 50 mW

Tissue in child head models	Tissue measured experimentally
Connective tissue	Cartilage[a]
Nasal cavity (air and mucosa)	Air
Skin	Skin

[a]Only measured for 50 kg pigs.

Table 4.1: *Relation between dielectric data obtained experimentally and the tissues in the 10 g volume of maximum peak SAR_{10g}.*

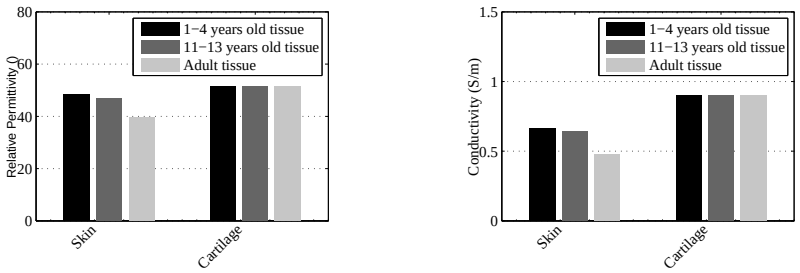

(a) **(b)**

Figure 4.24: *The dielectric properties as a function of age of the tissues in the 10 g volume where the peak SAR_{10g} occurs: (a) permittivity and (b) conductivity.*

to 140 mW, which is more than 70 % lower than the maximum allowed ERP of 500 mW. The results in Figure 4.22 are therefore likely to be over-estimates of the exposure of children from real walkie-talkie devices.

4.6 Conclusions

We investigated the compliance to the SAR safety limits of a walkie-talkie. An effective radiated power as specified by the PMR446 radio standard can cause a local-averaged SAR which exceeds the limits. But, based on the effective radiated power of four real walkie talkies, we showed that the peak local-averaged SAR values are unlikely to exceed the current SAR limits.

We also observed that the oval flat phantom yields a conservative SAR value for realistic head models, but not for homogeneous head models. The homogeneous Visible Human head and the oval flat phantom significantly overestimate the peak local-averaged SAR obtained in the heterogeneous Visible Human head. Air cavities in the head, such as the mouth and the nose cavity, significantly alter the peak local-averaged SAR in the frontal face.

The extent to which the dielectric properties could affect dosimetric results was

investigated numerically for child head exposure to emissions from walkie-talkies. The effect on 10 g local-averaged SAR was marginal. Finally, the peak 10 g local-averaged SAR in the child head phantoms caused by a walkie-talkie might exceed the limits when radiating at the maximum allowed ERP of 500 mW.

Acknowledgment

I would like to thank IT'IS for using their laboratory and DASY4 system for performing the dosimetric measurements of the walkie-talkies below the flat phantom.

References

[1] IEC. *Human exposure to radio frequency fields from hand-held and body-mounted wireless communication devices - Human models, instrumentation, and procedures – Part 2: Procedure to determine the Specific Absorption Rate (SAR) in the head and body for 30 MHz to 6 GHz Handheld and Body-Mounted Devices used in close proximity to the Body (TC/SC 106/90/NP)*, 2005.

[2] CENELEC. *European Standard EN50361: Product standard to demonstrate the compliance of mobile phones with the basic restrictions related to human exposure to electromagnetic fields (300 MHz - 3 GHz)*, 2001.

[3] FCC. *Evaluating Compliance with FCC Guidelines for Human Exposure to Radiofrequency Electromagnetic Fields (FCC OET Bulletin 65 - Supplement C)*. Technical report, 2001.

[4] N. Kuster, Q. Balzano, and J. Lin. *Mobile Communications Safety*. Chapman & Hall, 1997.

[5] Q. Balzano, O. Garay, and T. Manning. *Electromagnetic energy exposure of the users of portable cellular telephones*. IEEETrans.Vehic. Technol., 44(3):390–403, Aug 1995.

[6] N. Kuster, R. Kastle, and T. Schmid. *Dosimetric evaluation of hand- heldmobile communications equipment with known precision*. IEICE Trans. Commun., pages 645–52, 1997.

[7] F. Meyer, K. Palmer, and U. Jakobus. *Investigation into the accuracy, efficiency and applicability of the method of moments as numerical dosimetry tool for the head and hand of a mobile phone user*. Appl. Comput. Electromagn. Soc. J., 16:114–25, 2001.

[8] International Electrotechnical Commission (IEC). *Procedure to measure the Specific Absorption Rate (SAR) for hand-held mobile wireless devices in the frequency range of 300 MHz to 3 GHz (IEC62209)*, 2001.

[9] SPEAG, Zurich, Switzerland. *DASY4 System Handbook*, April 2008.

[10] IEEE Std. 1528-2003. *IEEE Recommended Practice for Determining the Spatial-Peak Specific Absorption Rate (SAR) in the Human Body from Wireless Communications Devices: Experimental Techniques*, December 2003.

[11] Institute of Electrical and Electronics Engineers (IEEE). *IEEE recommended practice for determining the peak spatial-average Specific Absorption Rate*

(SAR) in the human head from wireless communication devices: Measurement techniques (IEEE Std. 1528), 2003.

[12] M. Y. Kanda, M. D. Douglas, E. D. Mendivil, M. Ballen, A. V. Gessner, and C. K. Chou. *Faster Determination of Mass-Averaged SAR From 2-D Area Scans*. IEEE Transactions on Microwave Theory and Techniques, 52:2013–20, 2004.

[13] J. Bakker, M. Paulides, A. Christ, N. Kuster, and G. van Rhoon. *Assessment of induced SAR in children exposed to electromagnetic plane waves between 10 MHz and 5.6 GHz*. Phys. Med. Biol., 55:3115–30, 2010.

[14] J. Bakker, M. Paulides, A. Christ, N. Kuster, and G. van Rhoon. *Corrigendum for assessment of induced SAR in children exposed to electromagnetic plane waves between 10 MHz and 5.6 GHz*. Physics in Medicine and Biology, 56:2883, 2011.

[15] C. Gabriel, S. Gabriel, and E. Corthout. *The dielectric properties of biological tissues: I. Literature survey*. Physics in Medicine and Biology, 41:2231–49, 1996. doi:10.1088/0031-9155/41/11/001.

[16] S. Gabriel, R. W. Lau, and C. Gabriel. *The dielectric properties of biological tissues: III. Parametric models for the dielectric spectrum of tissues*. Physics in Medicine and Biology, 41:2271–93, 1996. doi:10.1088/0031-9155/41/11/003.

[17] S. Gabriel, R. W. Lau, and C. Gabriel. *The dielectric properties of biological tissues: II. Measurements in the frequency range 10 Hz to 20 GHz*. Phys Med Biol, 41:2251–69, 1996. doi:10.1088/0031-9155/41/11/002.

[18] N. Kuster and Q. Balzano. *Energy Absorption Mechanism by Biological Bodies in the Near Field of Dipole Antennas above 300 MHz*. IEEE Transactions on Vehicular Technology, 41(1):17–23, January 1992.

[19] A. Christ, M. C. Gosselin, M. Murbach, S. Ryf, M. Christopoulou, E. Neufeld, C. Gabriel, A. Peyman, and N. p. . Kuster. *Age dependent changes in SAR and temperature distribution induced in the users head by cellular phones*. In BEMS Annual Meeting San Diego Abstract Book, 2008.

[20] L. Martens and G. Vermeeren. *Dosimetric Evaluation for Walkie-Talkies used by Children*. In Abstract book of FGF-Workshop: Do children represent an especially sensitive group of EMF exposed people?, volume 27-29 November 2006, Stuttgart, Germany, page 30, Stuttgart, Germany, November 2006.

[21] a. Peyman, C. Gabriel, E. H. Grant, G. Vermeeren, and L. Martens. *Variation of the dielectric properties of tissues with age: the effect on the values of SAR in children when exposed to walkie-talkie devices.* Physics in medicine and biology, 54(2):227–41, January 2009. doi:10.1088/0031-9155/54/2/004.

[22] IEEE. *Recommended Practice for Determining the Peak Spatial-Average Specific Absorption Rate (SAR) Associated with the Use of Wireless Handsets - Computational Techniques (IEEE Std. 1529).*

[23] A. A. De Salles, G. Bulla, and C. E. Fernandez Rodriguez. *Electromagnetic absorption in the head of adults and children due to mobile phone operation close to the head.* Electromagnetic Biology and Medicine, 25:349–60, 2006.

5

Influence of a highly reflective environment on the absorption from occupational exposure of base station antennas

5.1 Introduction

The Specific Absorption Rate (SAR) induced in the human body exposed to radio frequency electromagnetic fields not only depends on the anatomy [1, 2] and the posture of the human [1, 3–7], but also on the environment. In wireless communication the environment is part of the propagation channel. Dynamics of the environnment influence the propagation channel resulting in a varying exposure to the electromagnetic fields emmitted for communication. Most of the exposure studies investigating the influence of the environment were performed in the far-field of base station antennas [6, 8–11]. Compared to single-incident plane waves, an increase of the whole-body SAR up to 5 dB were reported in realistic environments at the GSM downlink frequency of 950 MHz [12] (see also Chapter 6). A limited number of studies exist on the influence of the environment near base station antennas located on the roof of buildings [13, 14]. All these studies aimed at assessing the exposure for the general public and only for a limited frequency range up to 2100 MHz. The influence of the environment on the exposure of a worker approaching the antenna of a base station has not been studied yet.

The present study aims at assessing the whole-body and peak local absorption in 10 g of tissue in an adult male in the near field of a base station antenna in three reflective environments. Several base station antennas (BSA) were modelled covering the frequency range from 300 MHz to 5 GHz. This study focusses on occupational exposure as the human body model was placed at distances up to 10 m from the outdoor base station antennas. From the literature review it is clear that worst-case exposure scenarios can be expected in an environment consisting of perfectly conducting walls and ground, because such boundaries are reflecting all the power back into the domain. Considering realistic walls and grounds decreases the variation on the calculated SAR values. Hence, only highly reflecting environments are considered in this study. In contrast to the previous studies, the present study investigates the influence of reflective environments in a large number of configurations, i.e. 72.

Section 5.2 gives an overview of the considered base station antennas, the selected human body model and the environments. Also, the positioning of the human body model with respect to base station antenna and the environment is discussed. Section 5.3 deals with the methodology of the absorption calculation. Different numerical techniques are used: FDTD, MoM technique and the generalized Huygens' box (GHB) method [15] which combines both techniques. Section 5.4 discusses the validation of the generalized Huygens'box method and the uncertainty of the simulations. The discussion of the obtained results is the subject of Section 5.5. Whole-body and peak local-averaged SAR values in the Duke, a 34-year-old male from the Virtual Family [16] are compared for the various configurations and with the results in the free-space case. The location of the peak local-averaged SAR in the trunk and limbs are shown. Furthermore, the conservativeness of ICNIRP reference levels with respect to the basic restrictions is evaluated, and the ratio of the peak local-averaged SAR and whole-body SAR is investigated. Section 5.6 compares the presented results with earlier findings. Finally, conclusions are drawn in Section 5.7.

5.2 Configurations

We investigated numerically the influence of a reflecting environment near base station antennas on the induced SAR in a human body. The human body model was placed at four distances in front of six base station antennas in three reflective environments. The operating frequencies of the base station antennas range from 300 MHz to 3 GHz. A total of 72 configurations (3 environments, 4 separations and 6 frequencies) are investigated.

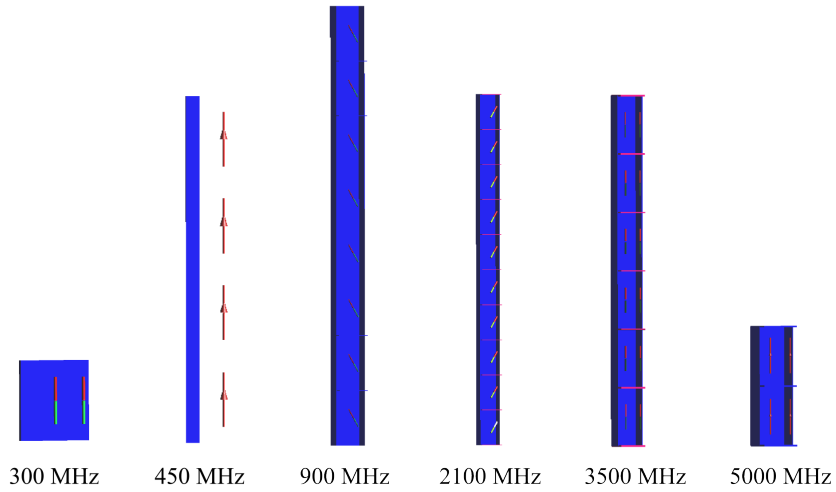

Figure 5.1: *The generic base station antennes at 300 MHz, 450 MHz, 900 MHz, 2100 MHz, 3500 MHz, and 5000 MHz. (Remark that the base station antennas are rescaled for improving visibility.)*

5.2.1 Exposure environments

Three reflecting scenarios are considered: perfectly conducting ground (denoted as *Ground*), perfectly conducting wall (denoted as *Wall*), and the combination of perfectly conducting ground and wall (denoted as *Ground + Wall*). All the environments are infinite in extent and perfectly conducting and, thus, reflect all the incident power density back into the simulation domain. If the environment is not perfectly conducting, only a fraction of the incident power density is reflected at the boundary. Hence, a perfectly conducting boundary can be expected to be a worst-case boundary in SAR assessment.

5.2.2 Generic base station antennas

The generic base station antenna models are designed in the frequency range of 300 MHz to 5 GHz (see Figure 5.1). Commercial single-frequency base station antennas served as model for these generic antennas. Table 5.1 lists dimensions, operating frequency and radiation properties of the generic base station antennas. All antennas are from the reflector type and the radiating elements are dipoles. The base station antennas are vertically positioned without mechanical tilt. The antennas of the base station antennas are fed in phase and have equal amplitude except from the base station antennas at 900 MHz, and 2100 MHz.

Operating Frequency (MHz)	3 dB Beamwidth (deg)		Polarization	Gain (dBi)	Number of dipoles	Height (mm)	Width (mm)
	Horiz.	Vert.					
300	65	64	Vertical	9.0	2	1000	750
450	180	19	Vertical	10.5	4	1960	140
900	65	7	Cross	17.5	8	2562	300
2100	65	7	Cross	18.0	10	1302	130
3500	65	9	Vertical	17.3	6	482	60
5000	65	35	Vertical	11.8	2	81	40

Table 5.1: *The selected base station antennas and their radiation parameters.*

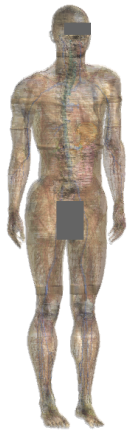

Figure 5.2: *Duke, a 34-year-old male human body model selected from the Virtual Family.*

5.2.3 Anatomical human body model

We investigated the specific absorption rate in Duke, a 34-year-old male human body model selected from the Virtual Family [16] and depicted in Figure 5.2, as the study aims at the occupational exposure of mast workers. The Virtual Family models are based on magnetic resonance images (MRI) of healthy volunteers. Duke is 1.80 m tall, weigths 72.2 kg and consists of 81 different tissues. The dielectric properties of the body tissues are taken from the Gabriel database [17–19]. The dielectric properties of intestine and stomach lumen depend on what we eat. These lumina are assigned the properties of muscle tissue to avoid reflections due to air enclosures.

Duke is placed in front of the base station antenna with a separation of 0.3 m, 1 m, 3 m and 10 m. The separation is defined as the horizontal distance between the bounding box of the body model and the bounding box of the base station antenna

(see Figure 5.3). The vertical center of Duke is aligned with the vertical center of the base station antenna if the height of the antenna was smaller than the length of Duke. The feet of Duke is aligned with the bottom of the base station antenna if the height of the antenna was larger than the length of Duke. The perfectly conducting ground is placed at a distance of 5 cm below the feet of the human body model to isolate the body from the ground. The horizontal centers of the base station antenna and Duke are aligned together; the wall is placed at a distance of 10 cm from the widest of the two. The position of the body model with respect to the antenna and the wall and ground are depicted in Figure 5.3.

5.3 Methodology

We selected the finite-difference time-domain (FDTD) method to compute the specific absorption rate in Duke. The FDTD technique discretizes the simulation domain in a rectilinear cartesian grid. The maximum grid step ($\Delta_{\max}$) decreases with frequency to obtain accurate SAR distributions in the body: $\Delta_{\max}$ equals 2 mm up to 2100 MHz and 1 mm at 3500 MHz and 5000 MHz. The FDTD technique is known as a very efficient method for complex material distributions, such as large heterogeneous human body models: the computational effort scales linearly with the number of unknowns and the number of cells [20, 21]. In FDTD calculations the simulation domain is finite and boundary conditions are used to mimic free space. We applied uni-axial perfectly matched layers (UPML) at the boundaries that did not represent a ground or wall to avoid reflections back into the simulation domain. The number of layers s automatically set by the FDTD solver to obtain a selected efficiency of $\geq 99.9\,\%$. The padding (minimum distance between absorbing boundaries (UPML) and the bounding box around human body model and the antenna) was chosen half a wavelength. However, the FDTD algorithm discretizes the whole simulation domain resulting in large simulations for large separations between human body model and the antenna. Running such a simulation is an excessive task due to the limitations of the computer hardware in terms of memory requirements. A hybrid technique called the generalized Huygens' box method (GHB) [15] is used to reduce the memory requirements and to speed up these large simulations.

The GHB is a two-step method: in a first simulation, the incident fields are computed on a closed box (Huygens' surface) surrounding the human body model (see Figure 5.3), in a second simulation, the complex incident fields on the bounding box around the human body model are used as excitation to compute the SAR distribution inside the human body model. The GHB method assumes no coupling between the human body, on the one hand, and the reflective environment and the base station antenna, on the other hand.

The configurations for which the GHB have been applied are listed in Ta-

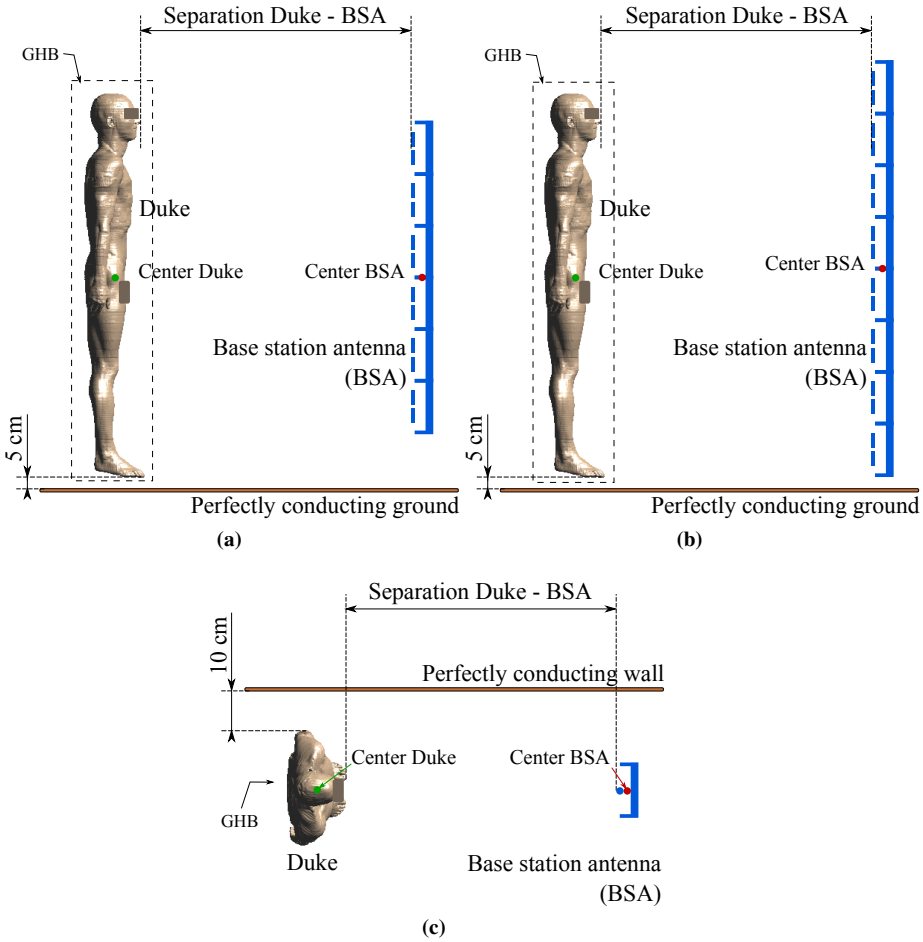

Figure 5.3: *The positioning of Duke with respect to the generalized Huygens' box (GHB), the base station antenna and the reflective environment: (a) perfectly conducting ground with antenna aligned with the center of Duke, (b) perfectly conducting ground with the antenna aligned with the feet of Duke and (c) perfectly conducting wall.*

ble 5.2. The base station antennas are denoted by their frequency, horizontal (H) and vertical (V) beamwidth in degrees, and their polarization (VPol and XPol for vertical and cross polarization, respectively) in Table 5.2. We used the FDTD technique for the calculation of the incident field as well as the absorption. Only at 5 GHz and for separations larger than 1 m, we computed the incident fields using the Method of Moments (MoM). The MoM is best suited for computing fields at large distances from scatterers and sources [22]. The method of moments does not discretize the whole simulation domain, only the surfaces of the antennas are

meshed. The GHB method has been validated thoroughly using full-wave FDTD and full-wave MoM/FEM (only for homogeneous phantoms) simulations.

Base Station Antenna	Separation distance
900MHz_H65V7_XPol	≥ 1 m
2100MHz_H65V7_XPol	≥ 3 m
3500MHz_H65V9_VPol	≥ 1 m
5000MHz_H65V35_VPol	≥ 0.3 m

Table 5.2: *The configurations for which the generalized huygens' box method has been used.*

The reflective environments are modelled by applying symmetry in the MoM computations and perfectly conducting boundary conditions in the FDTD computations.

The position of the GHB source with respect to Duke is shown in Figure 5.3. The minimum distance between the Huygens' box and Duke is 1.5 cm, divided into 6 grid steps.

We selected the commercially available tools SEMCAD (SPEAG, Switzerland) and Feko (EMSS, South-Africa) for the FDTD and the MoM/FEM calculations, respectively. The FDTD calculations were accelerated using GPU based computing provided by SPEAG. For the MoM simulations a dual core 64-bit machine with 16 GB of RAM was employed.

5.4 Validation and uncertainty analysis

The uncertainty of the simulations depends on the parameters of the numerical technique and the properties of the tissues. For the FDTD technique, discretization (of the models), padding (distance between boundaries and the modelled objects), and time duration influence uncertainty. For the properties of the tissues, the uncertainty is caused by the mass density, the age dependency of the dielectric properties [23], and the measurement uncertainty of the dielectric properties [17–19].

We estimated the uncertainty of the FDTD technique and of the tissue properties based on earlier findings [6, 7, 24]. Because our simulation settings are similar and for some parameters even better, we estimate that the uncertainty of the FDTD is not larger than the uncertainty in [7]. Bakker at al. [7] estimated an expanded uncertainty (k=2) on whole-body SAR and peak local-averaged SAR in 10 g of 21.2 % and 23.4 %, respectively, caused by mass density and the dielectric properties of the tissues (due to age-dependency, dielectric measurement uncertainty, 4-Cole-Cole model, and post-mortal changes of the tissues).

The generalized Huygens' box method reduces the computational time for the configurations at higher frequencies and larger separations as listed in Table 5.2.

The uncertainty on SAR_{wb} and $SAR_{10\mathrm{g}}$ introduced by the use of the GHB method is estimated by a validation of the method proposed here. A Huygens' box source, replacing the base station antenna and the perfectly conducting environment, is used in the FDTD solver and validated with simulations including all objects [15]. We selected the smallest human body model of the Virtual Family, i.e., Thelonious, a 6-year-old boy from the Virtual Family [16], to limit the computational time of the validation simulations. We assigned the dielectric properties of equivalent head [25] to the tissues of Thelonious resulting in a homogeneous human body model. Three base station antennas operating at 300 MHz, 900 MHz, and 2100 MHz exposed Thelonious to electromagnetic fields in free space and three reflecting environments: ground plane, wall at the left side of Thelonious, and wall at the back of the base station antenna. The ground plane was separated by 5 cm from the combination of Thelonious and the base station antenna, the walls were placed at 10 cm from the combination of Thelonious and the base station antenna. The separation between the bounding box of Thelonious and the base station antenna was 30 cm, 1 m, and 3 m. Due to limitations in memory of the simulation hardware the uncertainty could not be estimated for frequencies above 2100 MHz.

Figure 5.4 and Figure 5.5 show the results of the validation for whole-body and peak local-averaged SAR, respectivily. The Huygens' box only encloses the human body and neglects the coupling between the human body and the base station antenna, and between the human body and the conducting environment. Coupling decreases with increasing distance between the human body and the combination of the environment and the base station antenna. This decrease with distance depends on the frequency: the lower the frequency, the larger the coupling. At 300 MHz coupling can not be neglected. Comparing the uncertainty for the considered environments, we observe that the wall at the left side of the human body has the largest impact on the uncertainty indicating a larger coupling.

Based on the validation of the Huygens' box method we did not apply this method for frequencies below 900 MHz. For the configurations of Table 5.2, we estimate the uncertainty on the Huygens' box method to be less than 3 % for the whole-body SAR and less than 7 % for the peak local-averaged SAR. Overall, the estimated expanded uncertainty (k=2) with 95 % confidence interval equals 22.0 % and 27.3 % for SAR_{wb} and $SAR_{10\mathrm{g}}$, respectively.

5.5 Results

5.5.1 Comparison with the free-space results

To evaluate the variation on the whole-body and peak local-averaged SAR in the considered reflective environments with respect to free space, the following ratio

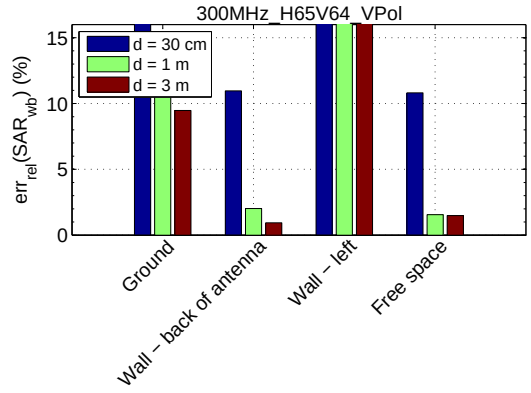

(a)

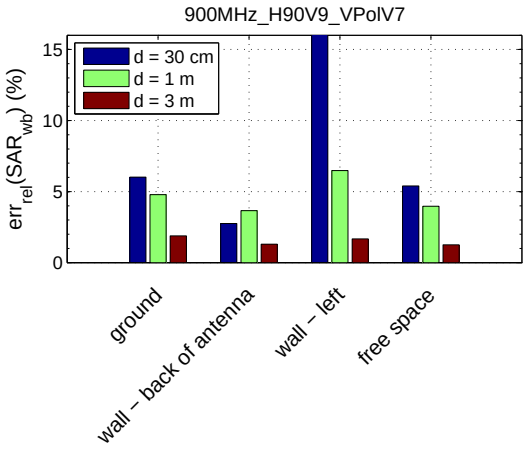

(b)

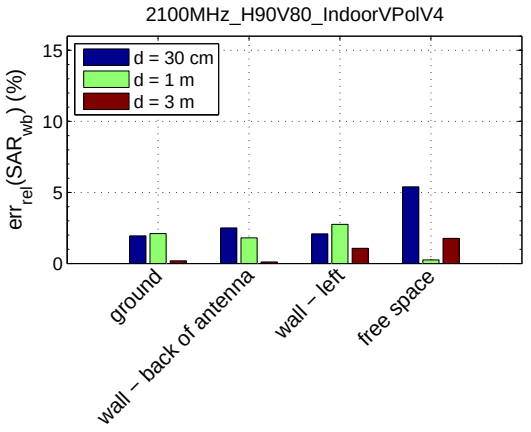

Figure 5.4: *The uncertainty of the generalized Huygens' box on SAR_{wb} in the homogeneous Thelonious exposed to base station antennas operating at (a) 300 MHz, (b) 900 MHz, and (c) 2100 MHz.*

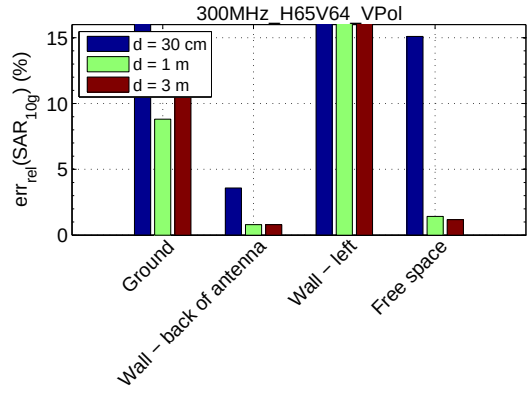

(a)

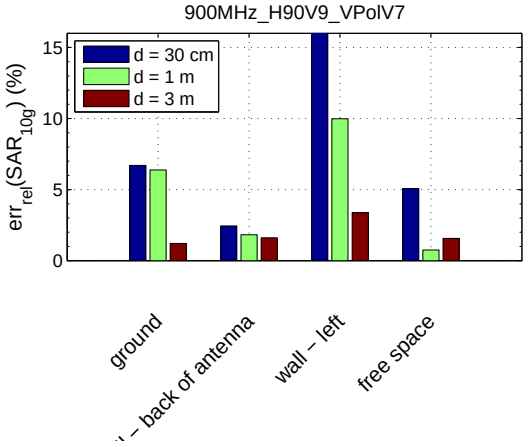

(b)

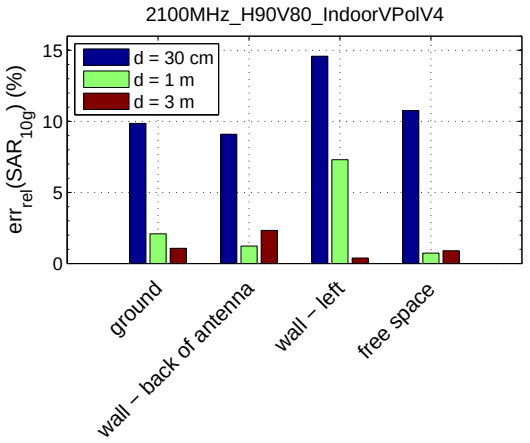

Figure 5.5: *The uncertainty of the generalized Huygens' box on peak SAR_{10g} in the homogeneous Thelonious exposed to base station antennas operating at (a) 300 MHz, (b) 900 MHz, and (c) 2100 MHz.*

is defined and investigated:

$$R_x = \frac{SAR_{x,\text{reflect.env.}}}{SAR_{x,\text{freespace}}} \qquad \text{with } x = 10\,\text{g or wb} \tag{5.1}$$

with 10 g and wb indicating the peak local-averaged SAR in 10 g and whole-body averaged SAR, respectively.

R_{x} is the ratio of the SAR (wb or peak 10 g averaged) in a reflective environment and the SAR (wb or peak 10 g averaged) in free space. The free-space SAR values are obtained from the study of Gosselin et al. [26]. Figure 5.6 shows the ratio R_x for the investigated reflective environments. The largest deviations occur at low frequencies: -8.7 dB for SAR_{wb} at 300 MHz and 8.0 dB for $SAR_{10\text{g}}$ at 450 MHz. The highest SAR values (for both whole-body SAR and peak local averaged SAR in 10 g) with respect to the free-space environment are found for the reflective environments with a wall. But, for the 300 MHz and 450 MHz base station antenna and a separation of 10 m, the ratio R_x is the highest for the ground environment. Remark also that a reflective environment yields a smaller SAR value than the SAR in the free space for the investigated configurations due to destructive interference between incident and reflected field. A worst-case (reflective) environment could not be determined.

5.5.2 Correlation between incident fields and absorption

In on-site exposure assessment, the incident electric field is typically assessed. Therefore, we also investigated to what extend a variation of the incident electric field is reflected in a variation of the whole-body and local absorption.

The specific absorption rate varies quadratically with the induced RMS electric field strength in the human body:

$$SAR = \frac{\sigma E^2_{\text{induced,rms}}}{\rho} \tag{5.2}$$

with σ the conductivity (S/m) and ρ the mass density (kg/m^3) of the tissue. Due to the linearity of Maxwell equations, we know that the induced field varies linearly with the incident field that causes the induced field. Hence, the specific absorption rate varies quadratically with the incident field or linear with the incident power density:

$$SAR \sim E^2_{\text{inc,rms}} \sim S_{\text{inc}} \tag{5.3}$$

with S_{inc} the incident power density.

Bernardi et al. [13] and Kühn et al. [6] reported that the whole-body SAR correlates well with the RMS incident electric field averaged over the bounding box of the human body and the peak local-averaged SAR correlates with the peak of

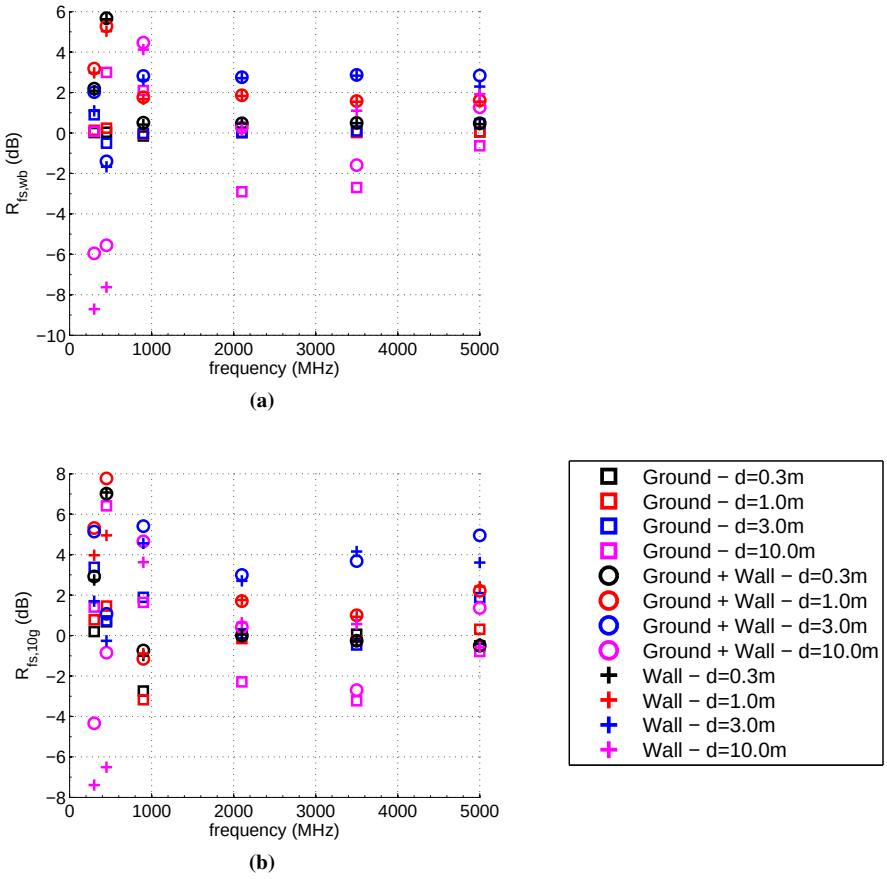

Figure 5.6: *The ratio R for (a) whole-body SAR and (b) peak local-averaged SAR in 10 g as a function of frequency.*

the RMS incident electric field over the bounding box of the human body. In this section, we verified this correlation in the investigated highly reflective environments.

We determined the spatially-averaged squared RMS incident electric field ($E^2_{\mathrm{inc,rms,avg}}$) and the peak squared RMS incident electric field ($E^2_{\mathrm{inc,rms,peak}}$) over the bounding box enclosing the human body model when the human body is not present. We observed that high squared field values over the bounding box of the human body result in high values for the absorption indicating a correlation between the induced SAR and the squared incident field levels. To further investigate this, the correlation coefficient (r) is calculated between, on the one hand, the whole-body and peak local-averaged SAR and, on the other hand, the peak spatial and averaged squared RMS incident field over the bounding box of Duke. Pearson's correlation coefficient is defined as follows:

$$r(x,y) = \frac{\sum_{i=1}^{N}(x_i-\bar{x})(y_i-\bar{y})}{\sqrt{\sum_{i=1}^{N}(x_i-\bar{x})^2\sum_{i=1}^{N}(y_i-\bar{y})^2}} \tag{5.4}$$

with N the total number of observations, x_i and y_i the i-th observation of x and y, and $\bar{x}$ and $\bar{y}$ the mean values of x and y. Figure 5.7 shows the correlations. The whole-body SAR as well as the local SAR correlate strongly with the peak and the averaged squared RMS incident electric field strengths: Pearson's correlation coefficient is larger than 84.8 %. The correlation between the whole-body SAR and peak or spatial-averaged squared RMS incident field varies from 91.3 % to 99.8 %. The correlation between the peak local-averaged SAR in 10 g of tissue and peak-spatial or spatial-averaged squared RMS incident field ranges from 84.8 % and 99.0 %. Our results do not allow to propose which of the incident field quantities, peak or averaged, best correlates with the whole-body and local-averaged SAR.

5.5.3 Location of the peak local-averaged SAR

The location of peak $SAR_{10\mathrm{g}}$ in the limbs and the trunk + head is shown in Figure 5.8. A distinction is made between the trunk + head and the limbs corresponding to the difference in basic restrictions for trunk + head and limbs as specified by ICNIRP. For the base station antennas with lower operating frequencies, i.e., up to 900 MHz, the locations of peak $SAR_{10g,\mathrm{trunk}}$ are spread over the trunk and head. Up to 450 MHz peak $SAR_{10\mathrm{g}}$ in the limbs is mainly located in the legs (ankles). For the base station antennas operating at 900 MHz and above, the peak $SAR_{10g,\mathrm{limbs}}$ is mainly observed in the fingers of the left arm. The peak $SAR_{10g,\mathrm{trunk}}$ is mainly located in the penis (considered as a part of the trunk + head) for the antennas with operating frequencies above 900 MHz.

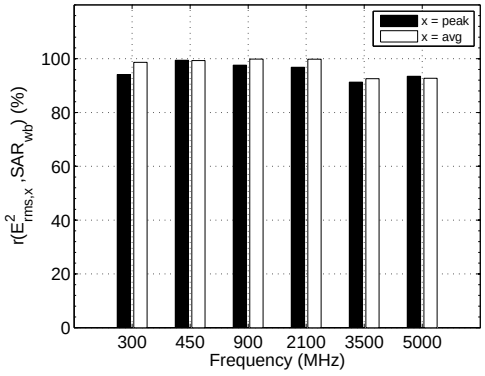

(a)

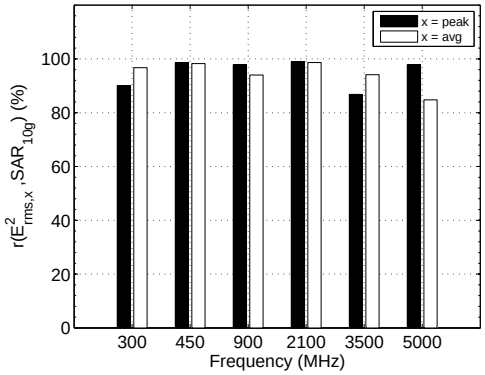

(b)

Figure 5.7: *The correlation coefficient between (a) whole-body SAR and (b) the peak local-averaged SAR in 10 g and the spatial-averaged and peak-spatial RMS incident electric field over the bounding box around Duke.*

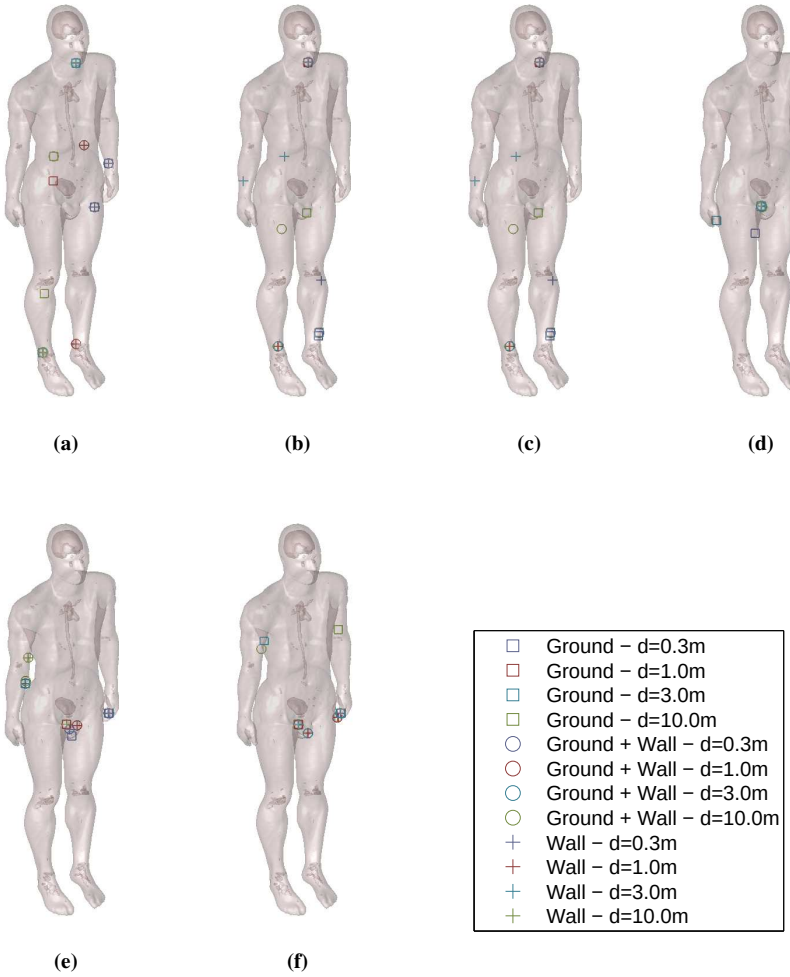

Figure 5.8: *The location of peak SAR_{10g} in 'trunk + head' and 'limbs' of Duke exposed to BSA operating at (a) 300 MHz, (b) 450 MHz, (c) 900 MHz, (d) 2100 MHz, (e) 3500 MHz, and (f) 5000 MHz.*

5.5.4 Evaluation of the ICNIRP reference levels against the basic restrictions

In this section we calculated whether the ICNIRP reference levels are conservative for heterogeneous human body models exposed to radio-frequency electromagnetic fields radiated by a base station antenna in reflective environments. The ICNIRP reference levels are derived from the basic restrictions for a horizontally single plane wave incident on homogeneous human body models. To evaluate the ICNIRP reference levels against the basic restrictions (see Table 5.3), we defined the following ratios:

$$A_{\mathrm{BR},x} = \frac{SAR_x}{BR_x} \qquad \text{with } x \text{ = 10 g in limbs, 10 g in trunk or wb} \quad (5.5)$$

$$A_{\mathrm{RL}} = \frac{P_{\mathrm{D,Duke}}}{RL} \quad (5.6)$$

$$A_x = \frac{A_{\mathrm{BR},x}}{A_{\mathrm{RL}}} \qquad \text{with } x \text{ = 10 g in limbs, 10 g in trunk or wb} \quad (5.7)$$

with BR_x the corresponding basic restriction (in W/kg) and RL the reference level for the incident power density (in W/m^2). $P_{\mathrm{D,Duke}}$ is the average incident power density through a plane with the same height and width as Duke. This plane is placed at the same distance from the base station antenna as Duke. The antenna-body distances assessed in this study are typically encountered by workers. The ICNIRP basic restrictions and reference levels for occupational exposure are listed in Table 5.3. $A_{\mathrm{BR},x}$ is the ratio of the SAR_{wb} or peak $SAR_{10\mathrm{g}}$ to the basic restriction for a specific antenna input power, e.g. 1 W. Likewise, A_{RL} is the ratio of the averaged incident power density through the plane to the reference level for the same antenna input power. Eq. (5.7) is the ratio of $A_{\mathrm{BR},x}$ and A_{RL}. So, if A_x exceeds 1 (or 0 dB), then the reference level is not compliant with the basic restriction.

	Basic restrictions			Reference levels
Frequency	SAR_{wb}	$SAR_{10\mathrm{g}}$ (W/kg)		P_{D}
(MHz)	(W/kg)	Head + trunk	Limbs	(W/m^2)
300	0.4	10	20	10
450	0.4	10	20	11.25
900	0.4	10	20	22.5
2100	0.4	10	20	50
3500	0.4	10	20	50
5000	0.4	10	20	50

Table 5.3: *The ICNIRP basic restrictions and reference levels for occupational exposure.*

Figure 5.9 shows the ratio for the whole-body averaged SAR (A_{wb}), the peak

local-averaged SAR in 10 g in the trunk ($A_{10g,\mathrm{trunk}}$) and the limbs ($A_{10g,\mathrm{limbs}}$). We observe that the basic restriction on the whole-body averaged SAR complies with the reference levels for the investigated configurations. But, for the peak local-averaged SAR in the trunk and the limbs (Figure 5.9), the basic restrictions are exceeded when the average incident power density equals the reference level in several configurations. In the trunk, the basic restrictions are exceeded up to a maximum of 3.8 dB for small separations of 30 cm and 1 m, for the BSA with operating frequencies of 2100 MHz, 3000 MHz, and 5000 MHz, and in all the considered environments. The peak local-averaged SAR in the limbs exceeds the basic restriction at a separation of 3 m for the base station antenna operating at 3500 MHz, and in all the environments. The maximum observed ratio is 2.0 dB and occurs for the wall environment. For a separation of 10 m between BSA and Duke, the peak local-averaged SAR stays more than 5 dB below the basic restrictions.

5.5.5 Ratio of peak local-averaged SAR and whole-body averaged SAR

In this section we investigate which of both whole-body SAR or peak spatial SAR first reaches the basic restrictions when the incident power increases. Therefore, we define the following ratio:

$$B_x = \frac{A_{\mathrm{BR},x}}{A_{\mathrm{BR},wb}} \qquad \text{with } x \text{ = 10 g in trunk or 10 g in limbs} \tag{5.8}$$

Figure 5.10 shows the ratio $B_{10g,\mathrm{trunk}}$ and $B_{10g,\mathrm{limbs}}$. For the ratio expressed in dB, a positive value indicates that peak local-averaged $SAR_{10\mathrm{g}}$ first exceeds the basic restriction, whereas a negative value means that SAR_{wb} is the restrictive quantity.

In the trunk, $B_{10g,\mathrm{trunk}}$ exhibits a trend to increase with operating frequency for $f \geq 900$ MHz because the absorption will be more localized near the surface of the body with increasing frequency. Likewise, short distances tend to result in an increased $B_{10g,\mathrm{trunk}}$, especially at higher frequencies of 2100 MHz and above. At 2100 MHz $B_{10g,\mathrm{trunk}}$ becomes positive for separation distances of 1 m and below. This means that peak SAR_{10g} reaches its basic restriction before SAR_{wb}. The maximum $B_{10g,\mathrm{trunk}}$ equals 6.7 dB for the 5000 MHz base station antenna, the ground environment and a separation of 30 cm. The minimum ratio of -7.4 dB occurs for the 300 MHz base station antenna, the ground environment and a separation of 10 m. A clear trend with changing environment could not be observed.

In the limbs, $B_{10g,\mathrm{limbs}}$ exhibits a less explicit trend with operating frequency. On average, $B_{10g,\mathrm{limbs}}$ increases above 900 MHz. $B_{10g,\mathrm{limbs}}$ becomes positive at 3500 MHz for seperation distances for 3 m and below except for a separation of 30 cm and the ground plane. At 5000 MHz $B_{10g,\mathrm{limbs}}$ is positive for distances ≤ 3 m. The maximum ratio in the limbs of 3.8 dB is observed for the Duke standing

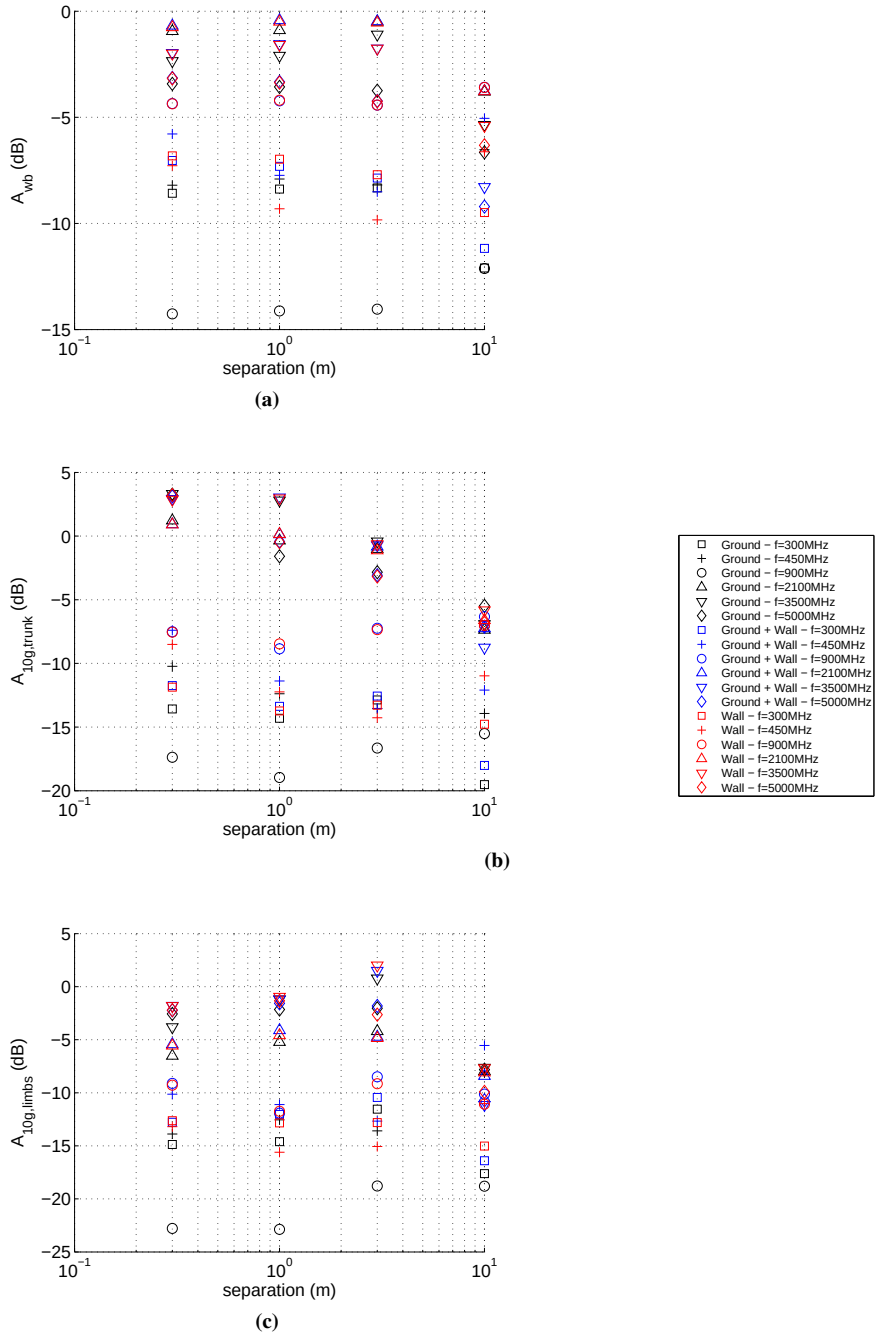

Figure 5.9: *The ratio (a) A_{wb}, (b) $A_{10g,\mathrm{trunk}}$, and (c) $A_{10g,\mathrm{limbs}}$ for occupational exposure.*

next to the wall at a distance of 3 m from the 3500 MHz base station antenna. The minimum ratio is -8.8 dB for Duke in the ground environment at 1 m from the 900 MHz base station antenna.

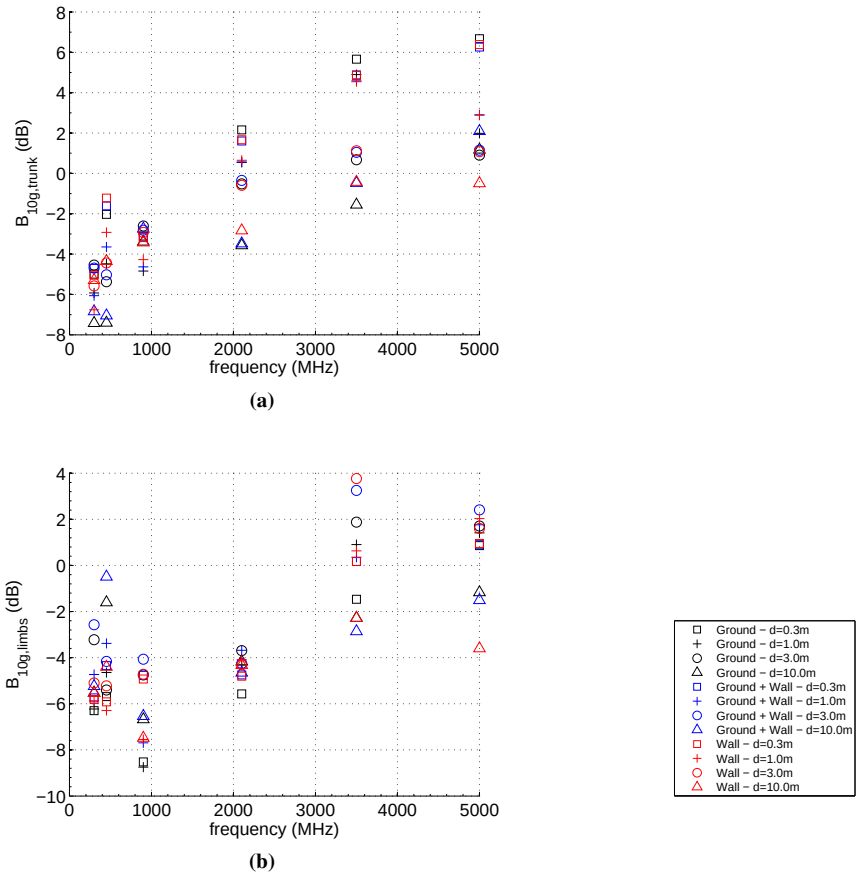

Figure 5.10: *The ratio of peak local-averaged SAR in trunk and limbs to the whole-body averaged SAR.*

5.6 Discussion

The presented research aims at assessing the influence of the reflective environment on the absorption in the human body of workers. In order to keep the investigation within the time frame of the project, the number of simulated configurations was limited: a single human body model was selected, i.e., Duke, the adult male of the Virtual Family, and three different reflective environments were considered.

We mainly aimed at investigating the influence of the environment on the absorption in the human body and not the compliance with current safety limits. Hence, only a single human body phantom is selected. An adult human body model is selected because the focus is on the exposure of workers. Besides the influence of the environment on the absorption, the compliance to the ICNIRP reference levels is also discussed for the considered configurations. In order to assess better the compliance to safety limits, other human body models and postures should be considered.

With respect to the environment the influence of a ground (which could represent the roof of a building on which a BSA is placed) and a wall was of main interest. The placement of the wall was at the side of the human body and the antenna. The minimum distance between the wall, and the combination of the human body and the antenna was limited to 10 cm in order to keep the simulation domain small especially for the configurations where the generalized Huygens' box method could not be used. The wall is not placed behind the antenna because the base station antennas were all of the reflector type. The wall is not placed behind the human body model either because due to the shadowing of the human body, it was not possible to use the generalized Huygens' box method. In this case the environments are all perfectly conducting. Hence, all power was reflected back into the simulation domain. Moreover, using only perfectly conducting grounds and walls one expects to show larger variations in absorption than when the environments are not totally reflective.

The considered frequency range was selected to encompass the carrier frequencies of current and future RF communication technologies.

The considered exposure conditions mainly apply for workers. Nevertheless, occasionally these exposures could also occur for the general public, e.g., people can have access to roof decks and, thus, be able to approach a base station antenna. For the considered frequency range from 300 MHz to 5 GHz, the ICNIRP basic restrictions and reference levels in terms of incident power density for general public exposure are 5 times lower than those for occupational exposure. Thus, the ratios A shown in Figure 5.9 also apply to general public exposure.

The ratio of SAR_{wb} and peak $SAR_{10\mathrm{g}}$ in a perfectly reflecting environment and free space depends on the frequency (see Figure 5.9) and varies between -4 dB and 6 dB from 300 MHz to 5 GHz in our investigation. Variations reported in earlier studies are all within this range. Bernardi et al. [13] reported an increase of 3 dB in whole-body absorption for reflecting walls with a reflection coefficient of 0.7 %. Vermeeren et al. [12] examined the influence of realistic environments on the whole-body absorption in homogeneous spheroid human body models at 950 MHz. They reported an increase of 1.3 dB for SAR_{wb} in the spheroid average man in a multipath environment compared to the worst-case single incident plane wave. Kühn et al. [6] investigated influence of worst-case scattered fields on peak

local-averaged SAR at 2140 MHz. They reported an increase of about 3 dB for SAR_{10g}. We remark that the configurations were not completely identical to the ones we have investigated. The environments in these studies except from Kühn et al. [6] could not be considered as perfectly conducting.

5.7 Conclusions

We investigated the whole-body SAR and peak local-averaged SAR induced in Duke standing in a perfectly conducting environment and exposed to the radio-frequency electromagnetic fields radiated by base station antennas operating in the frequency range 300 MHz to 5000 MHz. The perfectly conducting environment consisted of an infinite ground and / or an infinite vertical wall. The wall was placed at the left side of the human body model. A total of 72 simulations are executed.

From this study, we concluded that the whole-body and local absorption in a reflective environment vary a lot with respect to the absorption in free space. The ratio of the whole-body and peak local-averaged SAR in Duke in a reflective environment to those in the free-space environment ranged from -8.7 dB up to 8.0 dB. The whole-body SAR and peak local-averaged SAR in 10 g correlated strongly with the peak and averaged RMS incident fields over the bounding box around the body. Thus, worst-case exposure can be determined from an investigation of the RMS incident field in a certain environment. The location where the RMS field achieves the highest value coincides with the location where the highest absorption can be expected. A worst-case reflective environment could not be determined.

In a reflective environment, the ICNIRP reference levels are not always conservative with respect to the basic restrictions, especially for separation distances of up to 1 m between base station antennas and Duke. From 2100 MHz and distances up to 3 m, the peak local-averaged SAR is the most restrictive quantity. For frequencies below 2100 MHz the whole-body SAR is the most restrictive quantity.

References

[1] T. Uusitupa, I. Laakso, S. Ilvonen, and K. Nikoskinen. *SAR variation study from 300 to 5000 MHz for 15 voxel models including different postures*. Phys. Med. Biol., 55:1157–76, 2010.

[2] L. Sandrini, A. Vaccari, C. Malacarne, L. Cristoforetti, and R. Pontalti. *RF dosimetry: a comparison between power absorption of female and male numerical models from 0.1 to 4 GHz.* Phys Med Biol, 49:5185–201, 2004.

[3] P. Dimbylow. *Fine resolution calculations of SAR in the human body for frequencies up to 3 GHz.* Phys. Med. Biol., 47:2835–46, 2002.

[4] P. Dimbylow and W. Bolch. *Whole-body-averaged SAR from 50 MHz to 4 GHz in the University of Florida child voxel phantoms*. Phys. Med. Biol., 52:6639–49, 2007.

[5] E. Conil, A. Hadjem, F. Lacroux, M. Wong, and J. Wiart. *Variability analysis of SAR from 20 MHz to 2.4 GHz for different adult and child models using finite-difference time-domain*. Phys. Med. Biol., 53:1511–25, 2008.

[6] S. Kühn, W. Jennings, A. Christ, and N. Kuster. *Assessment of induced radio-frequency electromagnetic fields in various anatomical human body models*. Phys. Med. Biol., 54:875–90, 2009.

[7] J. Bakker, M. Paulides, A. Christ, N. Kuster, and G. van Rhoon. *Assessment of induced SAR in children exposed to electromagnetic plane waves between 10 MHz and 5.6 GHz.* Bioelectromagnetics, 55:3115–30, May 2010. doi:10.1088/0031-9155/55/11/009.

[8] M. J. Hagmann and O. P. Gandhi. *Numerical calculation of electromagnetic energy deposition in models of man with grounding and reflector effects*. Radio Science, 14(6S):23–29, November - December 1979.

[9] C. Durney, H. Massoudi, and M. Iskander. *Radiofrequency Radiation Dosimetry Handbook.* Number no. Rep. USAFSAM-TR-85-73. USAF School of Aerospace Medicine, Brooks Air Force Base, TX, 1986.

[10] G. Vermeeren, W. Joseph, L. Martens, P. Preiner, S. Cecil, N. Mitrevski, G. Neubauer, S. Kuehn, and N. Kuster. *Influence of a perfectly conducting ground on the whole-body SAR*. In Book of Abstracts of the 8th International Congress of the European BioElectromagnetics Association (EBEA 2007), Bordeaux, France, 2007.

[11] R. Findlay and P. Dimbylow. *Calculated SAR distributions in a human voxel phantom due to the reflection of electromagnetic fields from a ground plane between 65 MHz and 2 GHz*. Phys. Med. Biol., 53:2277–89, 2008.

[12] G. Vermeeren, W. Joseph, and L. Martens. *Whole-body SAR in spheroidal adult and child phantoms in realistic exposure environment*. Electron. Lett., 44:790–1, 2008.

[13] P. Bernardi, M. Cavagnaro, S. Pisa, and E. Piuzzi. *Human exposure to radio base-station antennas in urban environment*. IEEE Trans. Microwave Theory Tech., 48:1996–2002, 2000.

[14] P. Bernardi, M. Cavagnaro, R. Cicchetti, S. Pisa, E. Piuzzi, and O. Testa. *A UTD/FDTD investigation on procedures to assess the compliance of cellular base-station antennas with human-exposure limits in a realistic human urban environment*. IEEE Trans. Microwave Theory Tech., 51:2409–17, 2003.

[15] S. Benkler, N. Chavannes, and N. Kuster. *New powerful FDTD source based on huygens surface: Highly complex EM simulations performed on an ordinary PC*. In 31th Annual Meeting of the Bioelectromagnetics Society, Davos, Switzerland, June 14-19, 2009, June 2009.

[16] A. Christ, W. Kainz, E. Hahn, K. Honegger, M. Zefferer, E. Neufeld, W. Rascher, R. Janka, W. Bautz, J. Chen, B. Kiefer, P. Schmitt, H. Hollenbach, J. Shen, M. Oberle, D. Szczerba, A. Kam, J. Guag, and N. Kuster. *The Virtual Family – development of surface-based anatomical models of two adults and two children for dosimetric simulations*. Phys. Med. Biol., 48:N23–N28, 2010.

[17] C. Gabriel, S. Gabriel, and E. Corthout. *The dielectric properties of biological tissues: I. Literature survey*. Physics in Medicine and Biology, 41:2231–49, 1996. doi:10.1088/0031-9155/41/11/001.

[18] S. Gabriel, R. W. Lau, and C. Gabriel. *The dielectric properties of biological tissues: II. Measurements in the frequency range 10 Hz to 20 GHz*. Phys Med Biol, 41:2251–69, 1996. doi:10.1088/0031-9155/41/11/002.

[19] S. Gabriel, R. W. Lau, and C. Gabriel. *The dielectric properties of biological tissues: III. Parametric models for the dielectric spectrum of tissues*. Physics in Medicine and Biology, 41:2271–93, 1996. doi:10.1088/0031-9155/41/11/003.

[20] N. Kuster, Q. Balzano, and J. Lin. *Mobile Communications Safety*. Chapman & Hall, 1997.

[21] D. Davidson. *Computational electromagnetics for RF and microwave engineering*. Camebridge University Press, 2005.

[22] J. Hand. *Modelling the interaction of electromagnetic fields (10 MHz - 0 GHz) with the human body: methods and applications*. Phys. Med. Biol., 53:243–286, 2008.

[23] A. Peyman, C. Gabriel, E. Grant, G. Vermeeren, and L. Martens. *Variation of the dielectric properties of tissues with age: the effectect on the values of SAR in children when exposed to walkie-talkie devices*. Phys Med Biol, 54:227–41, 2009.

[24] R. Findlay and P. Dimbylow. *Variations in calculated SAR with distance to the perfectly matched layer boundary for a human voxel model*. Phys Med Biol, 51:N411–5, 2006.

[25] IEC. *Human exposure to radio frequency fields from hand-held and body-mounted wireless communication devices - Human models, instrumentation, and procedures - Part 1: Procedure to determine the specific absorption rate (SAR) for hand-held devices used in close proximity to the ear (frequency range of 300 MHz to 3 GHz) (EN 62209-1:2006)*, 2006.

[26] M. Gosselin, G. Vermeeren, S. Kühn, V. Kellerman, S. Benkler, T. Uusitupa, W. Joseph, A. Gati, J. Wiart, F. Meyer, L. Martens, T. Nojima, T. Hikage, Q. Balzano, A. Christ, and N. Kuster. *Estimation Formulas for the Specific Absorption Rate in Humans Exposed to Base-Station Antennas*. IEEE Transactions on Electromagnetic Compatibility, 53:909–22, 2011.

6

Numerical method to assess the absorption in a human body model for a realistic exposure

6.1 Introduction

The advent of broadcasting and wireless communication systems caused a large growth of the exposure of people to radio-frequency (RF) electromagnetic fields (EMF). To protect people against adverse health effects of EMF exposure, international guidelines [1, 2] are issued and adopted by standardization bodies, such as CENELEC [3]. The basic quantities for the limits of RF EMF defined in these guidelines are the whole-body (wb) and local absorption of electromagnetic energy in the body of the humans in terms of Specific Absorption Rate (SAR). Unfortunately, it is not possible to measure the absorption in a living person. In contrast to SAR, the levels of the incident field that causes the absorption are easy to measure. Therefore, reference levels (RL) for the incident electromagnetic fields have been derived from the basic restrictions (BR) on the absorption. The reference levels have been set in such a way that if the incident electromagnetic fields comply with the reference levels, then the basic restriction for the whole-body averaged SAR (SAR_{wb}) should not be exceeded. The reference levels have been derived from the basic restrictions based on measurements and numerical computations using a spheroidal homogeneous phantom exposed to a horizontally polarized incident plane wave [1].

The assessment of the absorption in a real environment based on the measured field levels is a very difficult and complex task. On the one hand, the RF absorption in a human body depends on the external and internal morphology [4–8] and the posture of the human body [9–11]. On the other hand, the exposure in a real environment is heterogeneous due to reflections, refractions, and attenuations of the propagating waves in the environment [12].

In the early days of dosimetry, back in the late 70's, absorption of electromagnetic energy in the human body under far-field conditions, was studied using simple canonical models of man such as a prolate spheroids, cilinders, and ellipsoids [13]. These simple human body models were exposed to single incident plane waves. In [14] an empirical formula for SAR_{wb} in a spheroid human body model exposed to a single incident plane wave was derived. This formula was based on calculations and empirical results and allowed a fast estimation of the SAR_{wb} over a broad frequency range. The disadvantage of this approach is that a single plane-wave exposure situation will never occur in a realistic environment.

In the years after, advances in computer hardware and software enabled the development of numerical tools such as the finite-difference time-domain method (FDTD) and the finite elements method (FEM) to solve complex electromagnetic field situations. Besides improvements in computer hardware and software, improvements in magnetic resonance imaging enabled the development of realistic human body models. Finally, the advent of GPU computing in recent years allows researchers to investigate the electromagnetic fields in complex environments and heterogeneous human body models in a reasonable time. In the meanwhile, Gabriel et al developped a database with the dielectric properties of tissues based on studies with pigs [15].

The aim of this chapter is the numerical assessment of the whole-body averaged SAR in a real environment for simple homogeneous and realistic heterogeneous human body models exposed to electromagnetic fields irradiated by base station antennas. Several approaches exist to estimate the whole-body averaged SAR whether or not in a real environment. These approaches can be classified in two categories, i.e., deterministic or statistical. Examples of deterministic approaches are the worst-case assessment as in [8, 16] and the exposure assessment in a particular area or location [17]. In the latter the surrounding area of the measurement location is taken into account by modeling the environment for the numerical computations [18, 19] or by measuring the incident fields in the environment [20].

In a deterministic approach, the value obtained for the SAR_{wb} by one of these methods is meaningless if we want to quantify the exposure in an environment with statistically varying electromagnetic fields. Electromagnetic waves interact with the environment through which they propagate. Shadowing, large-scale, and small-scale fading results in a spatial- and time-varying electromagnetic field distribution. Thus, the exposure of a person who moves around in a realistic environ-

ment is constantly changing. Therefore, a statistical investigation of the electromagnetic absorption in a human body in a realistic environment is required.

In the statistical approach the incident fields or exposure in an environment are described by an appropriate statistical model. Within the statistical approach, different methods can be distinguished to assess the absorption. In (Olivier 2007) the whole-body averaged SAR is determined analytically for the canonical human body model of a spheroid. Despite the fact that calculating SAR_{wb} is analytically very fast, it can not be used for realistic human body models. Other methods encountered in literature are surrogate modelling as in [21] and Monte-Carlo analysis [22, 23]. The surrogate model presented in [21] is based on only five simulations with single incident plave-wave exposure. Although, the surrogate model predicts very well the statistics of SAR_{wb} in a real exposure environment, the relationship between the incident fields and the absorption is lost.

This chapter presents a new numerical method for the assessment of the SAR_{wb} in a realistic environment. The presented method rapidly calculates the SAR_{wb} from the incident electric and magnetic fields. The method has to be fast because the spatial- and time-varying nature of the incident electromagnetic fields demands a statistical investigation which requires a lot of exposure situations or cases to be quickly calculated. The presented method estimates very fast the SAR_{wb} in a particular environment. This will be of interest not only for epidemiological studies but also to detect worst-case situations in a complex environment during compliance testing. The presented method also allows one to ascertain whether the ICNIRP reference levels comply with the basic restrictions for a realistic electromagnetic exposure.

6.2 Fast method to assess the absorption in a human body model in a realistic environment

A new and fast method is presented to determine the whole-body averaged SAR in a human body based on statistical data of electromagnetic fields in different realistic environments. The method to calculate quickly the whole-body absorption in a human body for heterogeneous or multipath plane-wave exposure is based on the linearity of Maxwell's equations, on the knowledge of the total fields on a closed surface around the human body for a limited set of single-incident plane waves, and on an appropriate choice of interpolation schemes.

A flow-chart of the method is drawn in Figure 6.1. First, the human body phantom is selected (Step A). For the selected human body phantom a minimum set of basic incident plane waves ($\widetilde{\mathbf{E}}_{\mathrm{inc,TE}}$ and $\widetilde{\mathbf{E}}_{\mathrm{inc,TM}}$) are determined (Step B). The basic fields are indicated with a tilde ($\sim$) above the field vector. The set of basic total fields ($\widetilde{\mathbf{E}}_{\mathrm{tot,TE}}$, $\widetilde{\mathbf{E}}_{\mathrm{tot,TM}}$, $\widetilde{\mathbf{H}}_{\mathrm{tot,TE}}$ and $\widetilde{\mathbf{H}}_{\mathrm{tot,TM}}$) for the set of basic incident

plane waves are simulated with a 3D EM-solver (Step C). Hereinafter, we denote these basic total field distributions (in short, basic field distributions) as BFDs. The numerical calculation of the basic total field distributions (Steps A, B, and C of the flow-chart) have to be performed only once for a particular human body model and frequency. Based on this set of basic total field distributions, the whole-body averaged SAR can be calculated fast for any environment (Steps 1, 2, 3, and 4 of the flow-chart). N_s exposure cases ($E_{\mathrm{inc},n}$, $\alpha_{\mathrm{inc},n}$, $\phi_{\mathrm{inc},n}$, $\theta_{\mathrm{inc},n}$, $\psi_{\mathrm{inc},n}$) are generated based on the statistical distributions that characterize the exposure in realistic multipath environments (Step 2). For every exposure case the total electric and magnetic fields are determined on the surface surrounding the human body phantom (Step 3). Finally, from these total electric and magnetic field distributions, the SAR_wb is calculated (Step 4). We will now discuss the different steps of Figure 6.1 in more detail.

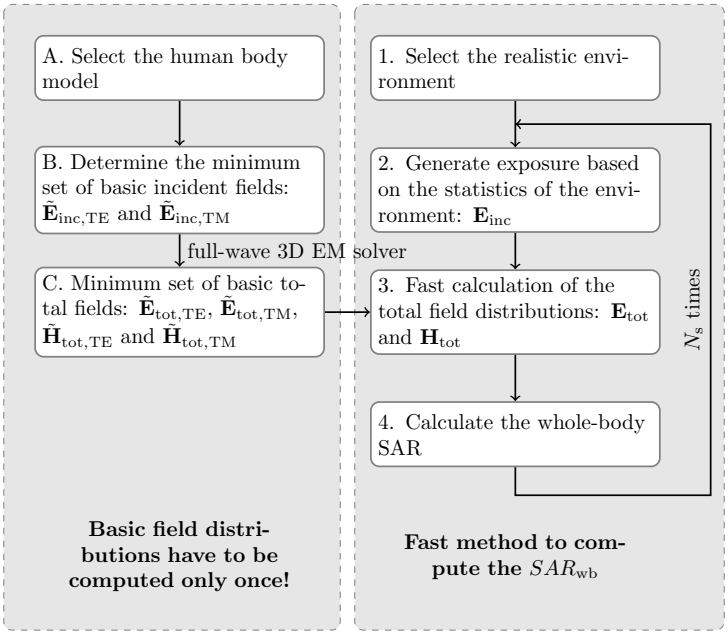

Figure 6.1: *The flow chart of the statistical multipath exposure (SME) method.*

6.2.1 Selection of the human body model (Step A)

In dosimetry, different human body models have been used to investigate numerically the whole-body and local absorption. In the early days of dosimetry homogeneous, canonical shaped human body models were used, such as prolate spheroids,

cilinders, and ellipsoids. In [13] dimensions of prolate spheroids with age are listed. Later, a block model of man was developped to investigate the whole-body and local absorption in a human body under near-field conditions. In recent years, a large number of MRI based models of a human body have been developped, such as the Virtual Family [24], Virtual Classroom [24], etc. At the moment, a total of more than 20 human body models are available to the scientific community, amongst others: the Visible Human [25], the UK model [26], the Korean models [27, 28], the Japanese models [29], and the European models [24]. There are models of children and adults, of obese people, of pregnant woman, etc. In what follows we will discuss the fast method for the homogeneous prolate spheroid with height a and half width b [13] and the realistic human body model Thelonious, the 6-year-old Virtual Family boy [24]. Both models are shown in Figure 6.2. The selection of the human body model is important as it influences partly the methodology of the presented fast calculation method.

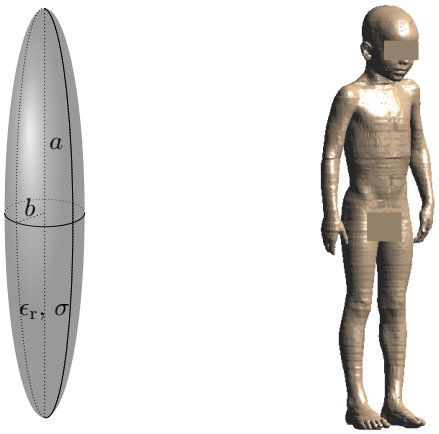

(a) **(b)**

Figure 6.2: *(a) A prolate spheroid human body model and (b) Thelonious, the realistic 6-year-old Virtual Family Boy.*

6.2.2 Numerical determination of the basic electromagnetic field distributions (Step B and C)

The whole-body SAR can be calculated from the total electric and magnetic field distribution on a closed surface around the human body (see later in Section 6.2.5).

The statistical model of (Vermeeren and Olivier 2007), and (Olivier 2007) describes the spatial electromagnetic field distribution as a finite sum of incident

plane waves. When a person is present in this realistic electromagnetic environment, the incident electromagnetic fields are perturbed. Scattering and penetration of the incident fields occur on the body of the person. Due to the linearity of the Maxwell's equations, the total field in a location $\mathbf{r}$, $\mathbf{E}_{\mathrm{tot}}(\mathbf{r})$, can be written as:

$$\mathbf{E}_{\mathrm{tot}}(\mathbf{r}) = \mathbf{E}_{\mathrm{inc}}(\mathbf{r}) + \mathbf{E}_{\mathrm{pert}}(\mathbf{r}) \tag{6.1}$$

with $\mathbf{E}_{\mathrm{inc}}(\mathbf{r})$ the incident field and $\mathbf{E}_{\mathrm{pert}}(\mathbf{r})$ the perturbation of the incident field. Later, in Eq. (6.13) of Section 6.2.3, we will see that the incident field in a realistic multipath environment in the far field of the antenna can be modeled as a finite sum of incident plane waves. Every single plane wave in $\mathbf{E}_{\mathrm{inc}}$ will have its corresponding perturbation in $\mathbf{E}_{\mathrm{pert}}$. The components n ($n = 1, \ldots, N$) of the perturbation of the incident field $\mathbf{E}_{\mathrm{pert},n}$ are independent from each other. Thanks to the linearity of the Maxwell's equations, we obtain:

$$\begin{aligned}
\mathbf{E}_{\mathrm{tot}}(\mathbf{r}) &= \sum_{n=1}^{N_{\mathrm{inc}}} \mathbf{E}_{\mathrm{inc},n}(\mathbf{r}) + \sum_{n=1}^{N_{\mathrm{inc}}} \mathbf{E}_{\mathrm{pert},n}(\mathbf{r}) \\
&= \sum_{n=1}^{N_{\mathrm{inc}}} \left[\mathbf{E}_{\mathrm{inc},n}(\mathbf{r}) + \mathbf{E}_{\mathrm{pert},n}(\mathbf{r})\right] \\
&= \sum_{n=1}^{N_{\mathrm{inc}}} \mathbf{E}_{\mathrm{tot},n}
\end{aligned} \tag{6.2}$$

Eq. (6.2) shows that the total field can be determined by the superposition of the total fields of all the incident plane waves present in $\mathbf{E}_{\mathrm{inc}}(\mathbf{r})$. A single incident plane wave can be decomposed in two components: a transverse electric (TE) and a transverse magnetic (TM) plane wave as illustrated in Figure 6.3. We designate a plane wave as TE-polarized when the incident electric field vector is transverse to the z- or polar-axis of the phantom. TM-polarization occurs when the plane wave has the magnetic field transverse to the z- or polar-axis of the phantom. Thus, an incident plane wave can be written as:

$$\mathbf{E}_{\mathrm{inc},n}(\mathbf{r}) = \mathbf{E}_{\mathrm{inc,TE},n}(\mathbf{r}) + \mathbf{E}_{\mathrm{inc,TM},n}(\mathbf{r}) \tag{6.3}$$

and the total field as:

$$\mathbf{E}_{\mathrm{tot},n}(\mathbf{r}) = \mathbf{E}_{\mathrm{tot,TE},n}(\mathbf{r}) + \mathbf{E}_{\mathrm{tot,TM},n}(\mathbf{r}) \tag{6.4}$$

The total field for a TE-polarized plane wave is then given by:

$$\begin{aligned}
\mathbf{E}_{\mathrm{tot,TE},n}(\mathbf{r}) &= \mathbf{E}_{\mathrm{inc,TE},n}(\mathbf{r}) + \mathbf{E}_{\mathrm{pert,TE},n}(\mathbf{r}) \\
&= E_{\mathrm{inc,TE},n}\exp\left(i\alpha_{\mathrm{inc,TE},n} - i\mathbf{k}_{\mathrm{inc},n}\cdot\mathbf{r}\right)\mathbf{u}_{\mathrm{inc,TE},n} \\
&\quad + \mathbf{E}_{\mathrm{pert,TE},n}(\mathbf{r}) \\
&= E_{\mathrm{inc,TE},n}\exp\left(i\alpha_{\mathrm{inc,TE},n}\right) \\
&\quad \left[\exp\left(-i\mathbf{k}_{\mathrm{inc},n}\cdot\mathbf{r}\right)\mathbf{u}_{\mathrm{inc,TE},n} + \frac{\mathbf{E}_{\mathrm{pert,TE},n}(\mathbf{r})}{E_{\mathrm{inc,TE},n}\exp\left(i\alpha_{\mathrm{inc,TE},n}\right)}\right] \\
&= E_{\mathrm{inc,TE},n}\exp\left(i\alpha_{\mathrm{inc,TE},n}\right)\left[\widetilde{\mathbf{E}}_{\mathrm{inc,TE},n} + \widetilde{\mathbf{E}}_{\mathrm{pert,TE},n}\right] \\
&= E_{\mathrm{inc,TE},n}\exp\left(i\alpha_{\mathrm{inc,TE},n}\right)\widetilde{\mathbf{E}}_{\mathrm{tot,TE},n} \qquad (6.5)
\end{aligned}$$

with $E_{\mathrm{inc,TE},n}$ the TE-polarized electric field strength, $\alpha_{\mathrm{inc,TE},n}$ the phase of the TE-polarized electric field, $\mathbf{k}_{\mathrm{inc,TE},n}$ the wave vector of the n-th incident TE-polarized plane wave, and $\mathbf{u}_{\mathrm{inc,TE},n}$ designates the direction of the TE-polarized electric-field vector of the n-th plane wave (see also Section 6.2.3).

Likewise, the total field for a TM-polarized plane wave is given by:

$$\begin{aligned}
\mathbf{E}_{\mathrm{tot,TM},n}(\mathbf{r}) &= E_{\mathrm{inc,TM},n}\exp\left(i\alpha_{\mathrm{inc,TM},n}\right) \\
&\quad \left[\exp\left(-i\mathbf{k}_{\mathrm{inc},n}\cdot\mathbf{r}\right)\mathbf{u}_{\mathrm{inc,TM},n} + \frac{\mathbf{E}_{\mathrm{pert,TM},n}(\mathbf{r})}{E_{\mathrm{inc,TM},n}\exp\left(i\alpha_{\mathrm{inc,TM},n}\right)}\right] \\
&= E_{\mathrm{inc,TM},n}\exp\left(i\alpha_{\mathrm{inc,TM},n}\right)\left[\widetilde{\mathbf{E}}_{\mathrm{inc,TM},n} + \widetilde{\mathbf{E}}_{\mathrm{pert,TM},n}\right] \\
&= E_{\mathrm{inc,TM},n}\exp\left(i\alpha_{\mathrm{inc,TM},n}\right)\widetilde{\mathbf{E}}_{\mathrm{tot,TM},n} \qquad (6.6)
\end{aligned}$$

The vector between brackets in Eq. (6.5) and Eq. (6.6) represents the basic total field distributions for a TE-polarized ($\widetilde{\mathbf{E}}_{\mathrm{inc,TE},n}$) and TM-polarized ($\widetilde{\mathbf{E}}_{\mathrm{inc,TM},n}$) incident plane wave. The basic total field distribution equals the vector sum of the basic incident field $\widetilde{\mathbf{E}}_{\mathrm{inc},n}$ and the basic perturbed field $\widetilde{\mathbf{E}}_{\mathrm{pert},n}$. As is clear from Eq. (6.5) and Eq. (6.6) the incident field of the basic field distributions has been assigned an electric field strength of 1 V/m.

The basic TE-polarized and TM-polarized field distributions are a function of the angles of incidence ($\phi_{\mathrm{inc},n}$,$\theta_{\mathrm{inc},n}$) and the frequency (f) of the plane wave. If we determine these basic field distributions for every azimuth angle $\phi_{\mathrm{inc},n} = 0\ldots2\pi$ and every elevation angle $\theta_{\mathrm{inc},n} = 0\ldots\pi$ for a particular human body phantom, then we can determine very fast the total field distribution $\mathbf{E}_{\mathrm{tot}}$ for any incident field distribution or exposure of a human body of Eq. (6.13) by using Eq. (6.6), Eq. (6.5), Eq. (6.4) and Eq. (6.2). The basic total field distributions have to be determined by numerical means. Commercially available numerical tools are used, such as the hybrid MoM/FEM and FDTD tool.

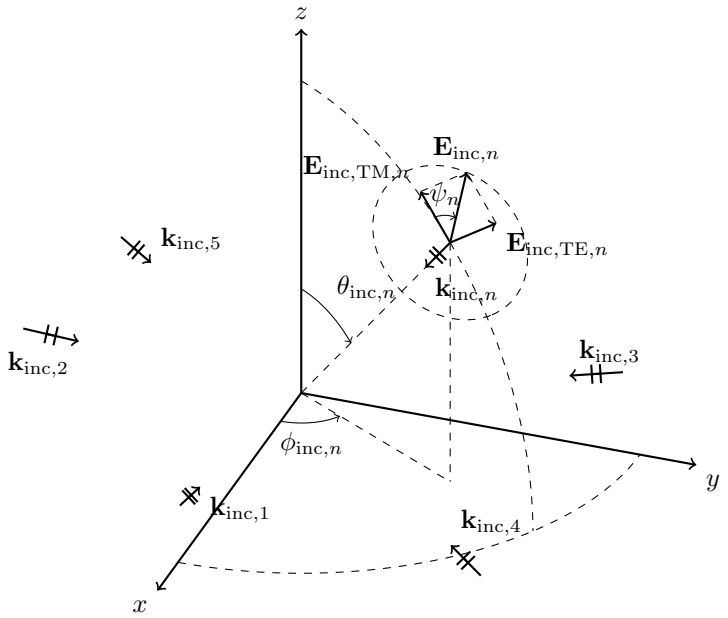

Figure 6.3: *Decompostion of the incident field.*

Practically, it is impossible to determine the basic total field distributions for every azimuth and elevation angle as an infinite number of 3D numerical simulations would be required. Fortunately, the basic total field distributions are smooth functions of the azimuth angle and the elevation angle, so that we can use a proper interpolation scheme to reduce the set of basic total field distributions to be calculated. The basic total field distributions are calculated for a uniformly distributed set of angles of incidence:

$$\phi_{\mathrm{inc},l} = l\Delta\phi_{\mathrm{inc}} \qquad \text{for } l = 0, \ldots, L-1 \tag{6.7}$$

$$\theta_{\mathrm{inc},k} = k\Delta\theta_{\mathrm{inc}} \qquad \text{for } k = 0, \ldots, K-1 \tag{6.8}$$

$\Delta\phi_{\mathrm{inc}}$ and $\Delta\theta_{\mathrm{inc}}$ denote the stepsize along azimuth and elevation, respectively. K and L are the number of elevation angles and the number of azimuth angles, respectively. For intermediate angles of incidence, an appropriate interpolation routine is used to determine the remaining BFDs. Using an interpolation scheme reduces largely the number of computed BFDs and, thus, the total simulation time. The price we pay is an additional interpolation error. But, we limit this error to maximum $1\,\%$ by an appropriate choice of the number of computed BFDs and interpolation scheme.

Picking angles of incidence that are uniformly distributed around a sphere (spatial domain) is a better choice in terms of minimizing the number of BFDs. Nevertheless, we computed the BFDs for a uniformly set of angles of incidence in the angular domain (ϕ,θ) because it allows more simple interpolation routines (e.g., a 2D-interpolation in the angular domain will be obtained by two 1D-interpolations.)

A 2D interpolation is performed in the (ϕ_{inc},θ_{inc})-plane. The interpolation for the total electric field is visualized in Figure 6.4. For clarity, the subscripts inc and tot are omitted in Figure 6.4 for angles of incidence and total fields, respectivily. The total electric field $\mathbf{E}$ for the arbitrary angles of incidence (ϕ_i,θ_j) is obtained by performing, first, a 1D interpolation along the elevation or θ-direction resulting in $\mathbf{E}(\phi_k, \theta_j)$ and $\mathbf{E}(\phi_{k+1}, \theta_j)$. Next, a 1D interpolation along the azimuth or ϕ-direction results in $\mathbf{E}(\phi_i, \theta_j)$. — We used two 1D interpolation schemes to perform the 2D interpolation because in this way we could best optimize the matlab code in terms of speed. — Three interpolation schemes have been compared: nearest, linear and cubic-spline interpolation.

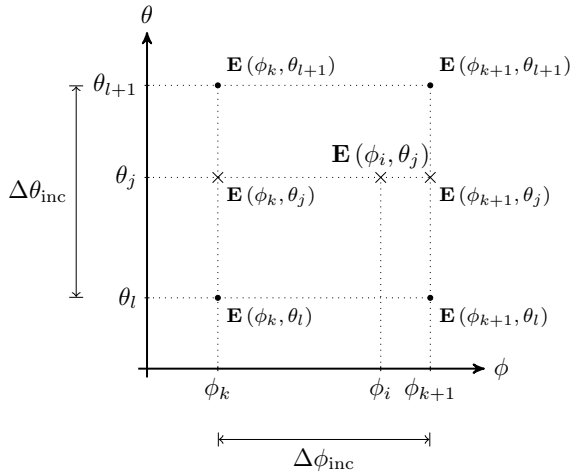

Figure 6.4: *The 2D interpolation to obtain the fields for any angle of incidence (ϕ_i,θ_j) from the basic field distributions.*

The maximum of the azimuth angle $\phi_{\mathrm{inc},L-1}$ and the elevation angle $\theta_{\mathrm{inc},K-1}$ is given by:

$$\phi_{\mathrm{inc},L-1} = \phi_{\mathrm{inc,max}} - \Delta\phi_{\mathrm{inc}} \tag{6.9}$$

$$\theta_{\mathrm{inc},K-1} = \theta_{\mathrm{inc,max}} \tag{6.10}$$

with $\phi_{\mathrm{inc,max}}$ and $\theta_{\mathrm{inc,max}}$ the maximum angle over which the human body model

has no symmetry along the azimuth and the elevation direction, respectively.

From Eq. (6.7), Eq. (6.8), Eq. (6.9) and Eq. (6.10) it follows that the uniform step along azimuth and elevation equals:

$$\Delta\phi_{\mathrm{inc}} = \frac{\phi_{\mathrm{inc,max}}}{L} \tag{6.11}$$

$$\Delta\theta_{\mathrm{inc}} = \frac{\theta_{\mathrm{inc,max}}}{K-1} \tag{6.12}$$

K and L depend on the frequency because the $\Delta\phi_{\mathrm{inc}}$ and $\Delta\theta_{\mathrm{inc}}$ decrease with increasing frequency. The values of K and L will be determined in Section 6.3.3 for a spheroid and realistic human body model. $\phi_{\mathrm{inc,max}}$ and $\theta_{inc,max}$ for different types of human body models are listed in Table 6.1. The total number of BFDs to be computed equals $2KL$. The factor 2 comes from the two polarizations (TE and TM) for every angle of incidence.

Human body model	$\phi_{\mathrm{inc,max}}$	$\theta_{\mathrm{inc,max}}$
Realistic	π	2π
Sphere	0 ($K=1$)	0 ($L=1$)
Spheroid	$\pi/2$	0 ($L=1$)
Ellipsoid	$\pi/2$	$\pi/2$

Table 6.1: *$\phi_{\mathrm{inc,max}}$ and $\phi_{\mathrm{inc,max}}$ for different types of human body models*

If the human body phantom has symmetry about an axis (rotation symmetry) and/or about a plane (reflection symmetry), then the number of basic total field distributions can be reduced significantly by using this symmetry if the observation surface has the same symmetry as the human body model (see also Section 6.2.5). This is the case for a prolate spheroid human body model. Because a homogeneous spheroid model has rotation symmetry around the major axis and reflection symmetry across the plane defined by the minor axes, the field distribution of any incident plane wave can be determined from the field distributions of the TE and TM polarized incident plane waves for an elevation angle θ_{inc} between 0 and π/2, and a single azimuth angle ϕ_{inc} as listed in Table 6.1 and shown in Figure 6.5. The BFDs for other azimuth angles are obtained by rotation of the fields from a single azimuth angle. Thus, the number of azimuth angles L equals 1. Because $\theta_{\mathrm{inc},K-1} = \pi/2$, the number of calculated basic field distributions will only depend on $\Delta\theta_{\mathrm{inc}}$ according to Eq. (6.8).

Using the interpolation and the symmetry only a minimum set of the basic fields $\widetilde{\mathbf{E}}_{\mathrm{inc,TE}}$, $\widetilde{\mathbf{E}}_{\mathrm{inc,TM}}$, $\widetilde{\mathbf{H}}_{\mathrm{inc,TE}}$, and $\widetilde{\mathbf{H}}_{\mathrm{inc,TM}}$ have to be calculated by numerical means. Remark that the observation surface must have the same symmetry of the human body phantom. The fields of these incident TE- and TM-polarized plane waves form a minimum and complete set of basic field distributions and have

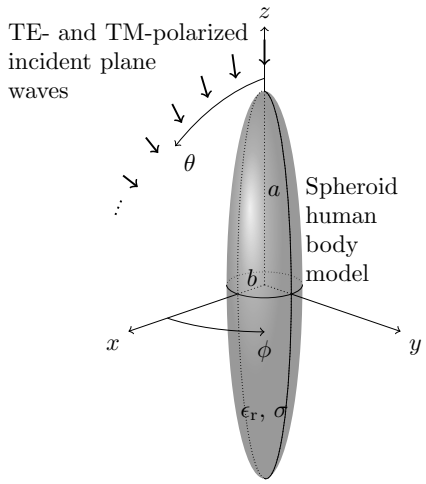

Figure 6.5: *The exposure of a spheroid in a complex environment.*

to be calculated with an FDTD or Method of Moments/Finite Elements Method (MoM/FEM) tool.

The choice of the shape of the closed surface depends on the presence of symmetry in the human body model. Thus, for a spheroid human body model, the fields are determined on a closed spheriod surface around the human body model as shown in Figure 6.6a. On the other hand, a realistic human body model has no symmetry at all. In order not to extend the overall simulation domain and, thus, the simulation time, a rectangular box around the body model is chosen for the closed observation surface (see Figure 6.6b). The total electric and magnetic field is determined in a discrete set of points on the closed observation surface. The distance between two points on the closed surface is not larger than $\lambda/10$ to obtain accurate results.

The BFDs are calculated numerically by a hybrid MoM/FEM method or an FDTD method. The MoM/FEM has only been applied for homogeneous spheroid human body models in the frequency range of 100 MHz to 950 MHz. The FDTD technique has been used for both the homogeneous and the realistic human body models for frequencies above 400 MHz, because for heterogeneous realistic human body models the FDTD technique is known as an efficient numerical technique.

If the MoM/FEM is used, the fields are immediately determined in the points of the closed surface. This is not the case when the FDTD technique is used because the FDTD technique calculates the fields on a rectangular (non-uniform) grid. Thus, in order to determine the fields in the points on the observation surface, an interpolation has to be performed from the rectangular FDTD grid to the points

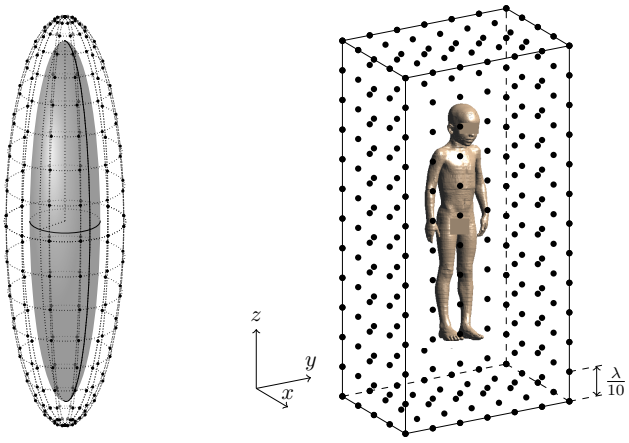

(a) **(b)**

Figure 6.6: *The closed observation surface around (a) a prolate spheroid human body model and (b) the realistic Virtual Family boy.*

of the closed surface. For a spheroid observation surface a 3D interpolation is needed, while for the rectangular box observation surface a 2D interpolation is sufficient if the observation surfaces of the box coincides with the FDTD grid.

Figure 6.7a shows the 3D interpolation for the spheroid human body model. The field in a point on the closed observation surface (indicated by the indices m, n, and p) are interpolated from the points of the FDTD grid (indicated by the indices $i(+1)$, $j(+1)$, and $k(+1)$). A linear interpolation scheme is applied and gives sufficient accuracy because the grid step in the FDTD scheme is typically $\leq \lambda/10$. The arrows in the figure show the order in which the tri-linear interpolation is performed: first interpolation along the x-axis, then along the y-axis, and finally along the z-axis. Because of the rectangular box around the realistic human body model, only a 2D interpolation is performed if the rectangular box coincides with the FDTD grid. Figure 6.7b shows the interpolation in an xz-plane. Again, the arrows indicate the order in which the interpolation is carried out. In Figure 6.7b first along the x-axis, then along the z-axis.

6.2.3 The spatial electromagnetic field distribution in a realistic environment (Step 1 and 2)

An electromagnetic wave interacts with the environment through which it propagates. Before an electromagnetic wave arrives at the receiving antenna, it has been transmitted through the air and may have experienced reflections from the ground

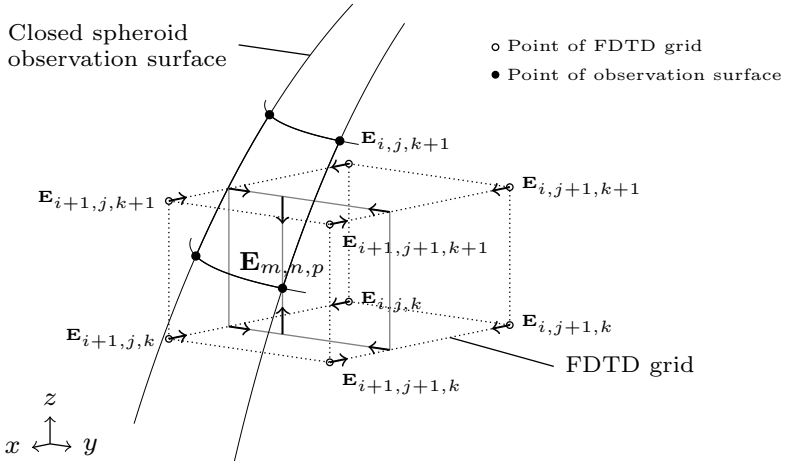

(a)

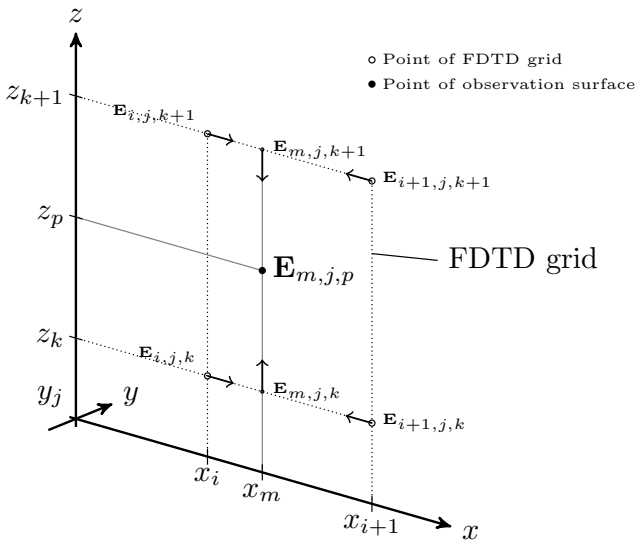

(b)

Figure 6.7: *The (a) 3D-interpolation for the spheroid observation surface and (b) 2D-interpolation for the rectangular box observation surface.*

or objects, or refractions through, and diffractions by objects, and has been attenuated due to losses. Due to the presence of the environment, the electromagnetic waves travel along multiple paths from sender to receiver. Suppose that the location, where we want to determine the electromagnetic field, is in the far field of all the transmitting antennas, then the effects (reflections, refractions, diffractions, and attenuations) of the environment can be modeled as combinations of simple mechanisms operating on plane waves [12]. Therefore, in a realistic environment, the electromagnetic field ($\mathbf{E}_{\mathrm{inc}}(\mathbf{r})$, $\mathbf{H}_{\mathrm{inc}}(\mathbf{r})$) in a location $\mathbf{r}$ sufficiently far from the sources can be decomposed in a vector sum of incident plane waves, i.e. its angular spectrum of incident plane waves:

$$\mathbf{E}_{\mathrm{inc}}(\mathbf{r}) = \sum_{n=1}^{N_{\mathrm{inc}}} E_{\mathrm{inc},n} \exp\left(i\alpha_{\mathrm{inc},n} - i\mathbf{k}_{\mathrm{inc},n} \cdot \mathbf{r}\right) \mathbf{u}_{\mathrm{Einc},n} \tag{6.13}$$

$$\mathbf{H}_{\mathrm{inc}}(\mathbf{r}) = \sum_{n=1}^{N_{\mathrm{inc}}} \frac{E_{\mathrm{inc},n}}{Z_0} \exp\left(i\alpha_{\mathrm{inc},n} - i\mathbf{k}_{\mathrm{inc},n} \cdot \mathbf{r}\right) \mathbf{u}_{\mathrm{Einc},n} \tag{6.14}$$

with N_{inc} the total number of incident plane waves, $E_{\mathrm{inc},n}$ the electric field strength, $\alpha_{\mathrm{inc},n}$ the phase of the electric field, $\mathbf{k}_{\mathrm{inc},n}$ the wave vector of the n-th incident plane wave and Z_0 the free-space wave impedance. The wave vector $\mathbf{k}_{\mathrm{inc},n}$ relates to the angles of incidence ($\phi_{\mathrm{inc},n}$, $\theta_{\mathrm{inc},n}$) as illustrated in Figure 6.8. $\mathbf{u}_{\mathrm{Einc},n}$ designates the direction of the electric-field vector of the n-th plane wave, whereas $\mathbf{u}_{\mathrm{kinc},n}$ represents the direction of the wave vector of the n-th incident plane wave. The polarization angle $\psi_{\mathrm{inc},n}$ is zero when the electric field vector $\mathbf{E}_{\mathrm{inc},n}$ has the same direction as the unit vector for zero-polarization $\mathbf{u}_{\psi,0}$. The unit vector $\mathbf{u}_{\psi,0}$ is perpendicular to the wave vector $\mathbf{k}_{\mathrm{inc},n}$ and lies in the plane defined by the z-axis and the wave vector $\mathbf{k}_{\mathrm{inc},n}$. This far-field model of the incident electromagnetic fields in a location $\mathbf{r}$ is valid at far-field distances (distance $> 2D^2/\lambda$, with D the largest dimension of the antenna and λ the wavelength in free-space [30]) from all the transmitting antennas in the environment.

In a realistic environment, the number of incident plane waves N_{inc}, the electric field strength $E_{\mathrm{inc},n}$, the phase $\alpha_{\mathrm{inc},n}$, the polarization angle $\psi_{\mathrm{inc},n}$, the azimuth angle $\phi_{\mathrm{inc},n}$ and the elevation angle $\theta_{\mathrm{inc},n}$ of the incident plane wave n behave as statistical variables. In the literature, several papers have been published which describe the propagation channel for wireless communications in several realistic environments [31–41]. Based on the results of these measurement campaigns, a probability distribution function (pdf) for each of these field parameters has been proposed in [42, 43]. A Gao distribution has been selected for the number of incident plane waves N_{inc} [38]. N_{T} is the maximum number of incident plane waves and η is parameter related to the average of the number of incident plane waves. The electric field strength $E_{\mathrm{inc},n}$ has a log-normal distribution with

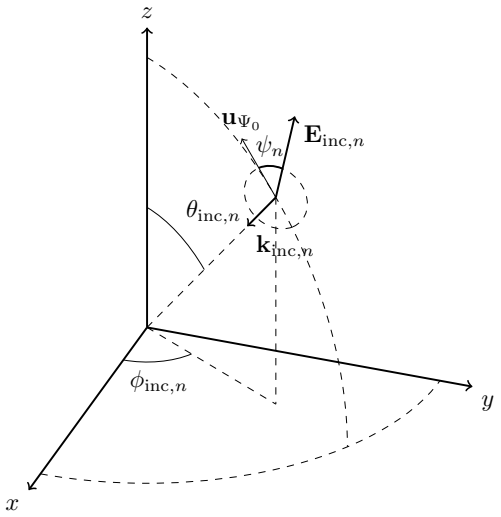

Figure 6.8: *The angles of incidence $\phi_{\mathrm{inc},n}$, $\theta_{\mathrm{inc},n}$ and the polarization angle $\psi_{\mathrm{inc},n}$.*

shadowing σ_{E}. Small-scale fading is implicetely taken into account by considering multiple incident plane waves. In addition, for higher frequencies the body of the human becomes much larger than the scale for multi-path fading and, hence, it does not need to be taken into account. The phase $\alpha_{\mathrm{inc},n}$ and the azimuth angle $\phi_{\mathrm{inc},n}$ have a uniform distribution between 0 and 2π. The elevation angle $\theta_{\mathrm{inc},n}$ has a double-exponential distribution [36]. θ_0 represents the peak elevation angle. The spreading of the double exponential function below and above θ_0 is given by $\sigma-$ and $\sigma+$, respectively. The polarization angle $\psi_{\mathrm{inc},n}$ has a normal distribution around the mean of the polarization angle, Ψ_{T}, at the transmitting antenna [36]. The environments listed in Table 6.2 assume vertical polarized base station antennas (Ψ_{T} = 0 deg). The variance of the distribution for the polarization $\sigma^2_{\Psi n}$ is related with the cross polarization ratio XPR as $XPR = \coth\left(\sigma^2_{\Psi n}\right)$. The parameters of these distributions depend on the type of the environment: urban, outdoor, indoor, etc. The parameters for four typical environments are listed in Table 6.2.

6.2.4 Determination of the electric and magnetic field for an arbitrary exposure sample (Step 3)

The generation of an exposure case results in assigning values to the plane wave parameters depending on their statistical distribution: the electric field strength $E_{\mathrm{inc},n}$, the phase $\alpha_{\mathrm{inc},n}$, the angles of incidence $\phi_{\mathrm{inc},n}$ and $\theta_{\mathrm{inc},n}$, and the polarization angle $\psi_{\mathrm{inc},n}$ of the n-th incident plane wave. The basic field distributions

Environment	Urban-macro cell	Urban-micro cell	Indoor-pico cell	Outdoor-Indoor
Elevation [36]				
θ_0	87.8	88.0	88.0	90.2
$\sigma-$	3.9	4.3	6.9	5.4
$\sigma+$	17.8	8.2	9.4	5.5
Polarization [36]				
XPR (dB)	7.3	11.1	7.0	10.7
Number of paths [38]				
η	2.7	3.5	4.7	4.5
N_{T}	22	14	16	21
Shadowing				
σ_{E} (dB)	6	9	6	12

Table 6.2: *Statistical parameters of the incident fields in four different realistic enviroments. [42]*

for any angle of incidence are determined from the smaller set of calculated basic field distributions of Section 6.2.2 using the symmetry of the phantom, if available, and a linear interpolation scheme. This delivers us the expression between brackets in equation Eq. (6.5) and Eq. (6.6) taking into account the polarization angle $\psi_{\mathrm{inc},n}$. Multiplication of these expressions with the complex amplitude of the TE- and TM-polarized electric field component n results in the total electric field component n. The summation of Eq. (6.2) delivers the total electric field. Similarly, the total magnetic field is determined. The linearity of the Maxwell equations together with a set of basic fields distributions and the linear interpolation scheme allow us to evaluate the total field on the observation surface for any combination of incident plane waves. The SAR_{wb} is easily calculated from this total electromagnetic field.

6.2.5 Calculation of the SAR (Step 4)

The SAR is the rate at which electromagnetic energy is absorbed in a human body. The SAR is proportional to the square of the RMS electric field inside the body. In case of the whole-body SAR, it is not necessary to determine the electric fields inside the entire body. To investigate the SAR_{wb} in a body, it is sufficient to determine the Poynting vector from the total electric and the total magnetic field distribution on a closed surface around the body, as illustrated for the spheroid human body model in Figure 6.9.

In accordance to the standard IEEE C95.3-2002 [44], the whole-body SAR is

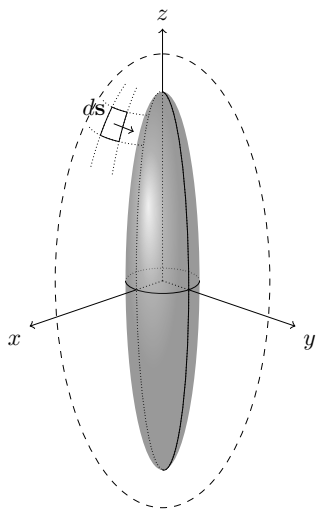

Figure 6.9: *Poynting vector in a point on the closed obervation surface.*

averaged over the mass of the human body model and is defined as:

$$SAR_{\mathrm{wb}} = \frac{1}{M}\int_R SAR(\mathbf{r})dm \tag{6.15}$$

with R the region over which the SAR is averaged over the mass M of the human body. The mass-averaged whole-body SAR is equal to the ratio of the absorbed power in the body (P_{abs}) and M:

$$SAR_{\mathrm{wb}} = \frac{P_{\mathrm{abs}}}{M} \tag{6.16}$$

The absorbed power can be determined from the net power flux through a closed surface (S) around the body by integrating the Poynting vector ($\wp$) over the closed surface and taking the real part of it:

$$P_{abs} = \Re\left\{\oint_S \wp \cdot d\mathbf{s}\right\} \tag{6.17}$$

The Poynting vector in every point of the closed surface is determined from the total electric ($\mathbf{E}_{\mathrm{tot}}$) and the total magnetic field vector ($\mathbf{H}_{\mathrm{tot}}$). The total fields are the superposition of the incident fields ($\mathbf{E}_{\mathrm{inc}}$, $\mathbf{H}_{\mathrm{inc}}$) and the fields scattered ($\mathbf{E}_{\mathrm{scat}}$, $\mathbf{H}_{\mathrm{scat}}$) at the surface of the body.

6.3 Validation of the method

The presented fast method to determine SAR_{wb} in a human body aims to be used as a substitute for a full-wave numerical tool in a statistical study of the SAR_{wb}. A statistical analysis requires thousands of simulations to obtain statistically relevant results. Obviously, full-wave calculations with an FDTD or MoM/FEM numerical tool are not suitable for a statistical investigation due to the time-consuming nature of these tools.

The fast method is validated in terms of the SAR_{wb} (or P_{abs}) and the total electric and magnetic field on the closed observation surface around the human body model. Because our method is presented as a fast alternative for full-wave numerical calculations, it is only validated with the results obtained by a full-wave numerical tool. For 100 exposure cases, the absorption and the total fields on the observation surface are determined by both a full-wave tool and the fast method. The relative error on the SAR_{wb} between our fast method ($SAR_{\mathrm{wb,fast}}$) and the full-wave method ($SAR_{\mathrm{wb,fw}}$) is defined as follows:

$$err_{\mathrm{rel,SAR_{wb}}}\ (\%) = 100 \times \frac{SAR_{\mathrm{wb,fast}} - SAR_{\mathrm{wb,fw}}}{SAR_{\mathrm{wb,fw}}} \tag{6.18}$$

Because the whole-body SAR is averaged over the mass of the body according to IEEE C95.3-2002 [44], the relative error on SAR_{wb} equals the relative error on P_{abs}, or:

$$err_{\mathrm{rel,SAR_{wb}}} = err_{\mathrm{rel,P_{abs}}}\ (\%) = 100 \times \frac{P_{\mathrm{abs,fast}} - P_{\mathrm{abs,fw}}}{P_{\mathrm{abs,fw}}} \tag{6.19}$$

In what follows, the relative error on SAR_{wb} and P_{abs} is designated in short as err.

Strictly speaking, only the validation of SAR_{wb} (or P_{abs}) is sufficient. However, the fundamental quantities are the electric and magnetic fields on the observation surface surrounding the human body model (see Figure 6.6). Hence, we have also validated the total electric and magnetic fields on the observation surface. The latter gives a better insight in possible causes of inaccuracies of the method. The error on the RMS total electric field ($E_{\mathrm{tot,rms}}$) and magnetic field ($H_{\mathrm{tot,rms}}$) is defined as follows:

$$err_{\mathrm{rel,E_{tot,rms}}}\ (\mathbf{r})\ (\%) = 100 \times \frac{E_{\mathrm{tot,rms,fast}} - E_{\mathrm{tot,rms,fw}}}{E_{\mathrm{tot,rms,fw}}} \tag{6.20}$$

$$err_{\mathrm{rel,H_{tot,rms}}}\ (\mathbf{r})\ (\%) = 100 \times \frac{H_{\mathrm{tot,rms,fast}} - H_{\mathrm{tot,rms,fw}}}{H_{\mathrm{tot,rms,fw}}} \tag{6.21}$$

with indices fast = our method, and fw = full wave.

Because we only want one error figure on the total electric and magentic field for every exposure sample, we take the mean and standard deviation of the relative error on the RMS electric and RMS magnetic field over all the points on the observation planes (op):

$$\text{mean}\left(err_{\text{rel,E}_{\text{tot,rms}}}(\mathbf{r})\right), \mathbf{r} \in op \tag{6.22}$$

$$\text{std}\left(err_{\text{rel,E}_{\text{tot,rms}}}(\mathbf{r})\right), \mathbf{r} \in op \tag{6.23}$$

$$\text{mean}\left(err_{\text{rel,H}_{\text{tot,rms}}}(\mathbf{r})\right), \mathbf{r} \in op \tag{6.24}$$

$$\text{std}\left(err_{\text{rel,H}_{\text{tot,rms}}}(\mathbf{r})\right), \mathbf{r} \in op \tag{6.25}$$

$$\tag{6.26}$$

Validating the method does not only give us an idea about the uncertainty, but will also give us an idea about the number of basic field distributions which need to be computed using a full-wave numerical tool. Or, in other words, the validation will also determine the optimum settings for the spacing between the angles of incidence ($\Delta\phi_{\text{inc}}$,$\Delta\theta_{\text{inc}}$) for which the BFDs are computed. Furthermore, we will also look how the interpolation scheme, nearest, linear or cubic spline influences the uncertainty and the spacing ($\Delta\phi_{\text{inc}}$,$\Delta\theta_{\text{inc}}$) when determining the fields for an arbitrary angle of incidence.

6.3.1 Configuration

The presented fast method is validated for a homogeneous spheroid and a heterogeneous realistic human body model exposed to EMF exposure of the GSM downlink at 950 MHz in an urban macro-cell environment. The dimensions of the spheroid equalled those of the average man as specified in [13], i.e., a height ($2a$) of 1.75 m and a half width (b) of 0.138 m. The dielectric properties of the spheroid have been assigned the dielectric properties of head tissue simulating liquid suggested by IEC 62209 [45] for compliance testing: $\epsilon_{\text{r}} = 41.4$ and $\sigma = 0.99$ S/m. For the heterogeneous human body model, Thelonious, the 6-year-old Virtual Family boy [24] shown in Figure 6.2b is selected. The Virtual Family human body models are based on magnetic resonance images (MRI) of healthy volunteers. Thelonious is 6 years old, is 1.17 m tall and has a weight of 19.5 kg. This model consists of 81 different tissues. The dielectric properties of the body tissues have been taken from the Gabriel database [15]. Intestine and stomach lumen was substituted by muscle tissue.

The incident electric field strength averaged over the entire body of the phantom ($\langle E_{\text{inc,rms}} \rangle_{\text{phantom}}$) is set equal to the ICNIRP-limit for the reference level, i.e., 42.38 V/m at 950 MHz.

6.3.2 Nearest, linear and cubic-spline interpolation

As mentioned in Section 6.2.2, it is impossible to simulate the BFDs for all angles of incidence. Hence, the BFDs are only simulated for a limited set of angles of incidence. The BFDs for intermediate angles of incidence are determined by interpolation because the total fields around the human body are smooth. The 2D-interpolation in $(\phi_{\mathrm{inc}}, \theta_{\mathrm{inc}})$-plane is achieved by performing two 1D-interpolations as explained in Section 6.2.2. This section discusses the uncertainty for three well-known interpolation schemes: nearest, linear and cubic spline. In the nearest interpolation scheme, the total fields of a single incident plane wave equal the BFDs computed for the nearest angle of incidence. Linear and cubic-spline schemes interpolate between BFDs. The spacing between the angles of incidence are fixed to 10° for azimuth angles ($\Delta\phi_{inc} = 10^\circ$) and 5° for elevation angles ($\Delta\theta_{inc} = 5^\circ$). Later, in Section 6.3.3 this choice for the stepsize of the angles of incidence is justified.

6.3.2.1 Spheroid human body model

For a spheroid human body model the 2D-interpolation is reduced to a 1D-interpolation along the elevation as explained in Section 6.2.2. Figure 6.10, Figure 6.11, and Figure 6.12 show the relative error on SAR_{wb} (or P_{abs}) and on the electromagnetic fields on closed spheroid surface surrounding the spheroid model for nearest, linear and cubic-spline interpolation of the BFDs, respectively. The corresponding mean and standard deviation of these errors on the SAR_{wb} are listed in Table 6.3.

Interpolation scheme	$\mu\,(err)$ (%)	$\sigma\,(err)$ (%)
Nearest	-0.48	2.74
Linear	-10.42	3.26
Cubic spline	-0.76	0.34

Table 6.3: *The mean (μ) and standard deviation (σ) on the relative errors of the absorption in the spheriod average man.*

It is observed that the fast method underestimates the whole-body absorption irrespective of the applied interpolation scheme. For the cubic-spline scheme an excellent agreement between the fast method and the full-wave FDTD method simulations with SEMCAD-X (SPEAG, Zurich, Switzerland) is obtained as the mean (μ) and the standard deviation (σ) on the relative error is very small, i.e., -0.76 % and 0.34 %, respectively. In contrast, the nearest and linear interpolation scheme show an increase in σ up to 2.74 % and 3.26 %, respectively. With a mean relative error of only -0.48 %, the nearest interpolation scheme outperforms the linear scheme ($\mu = -10.42\%$). The large underestimation for the linear scheme is due to the underestimation of the field levels on the closed spheroid observation

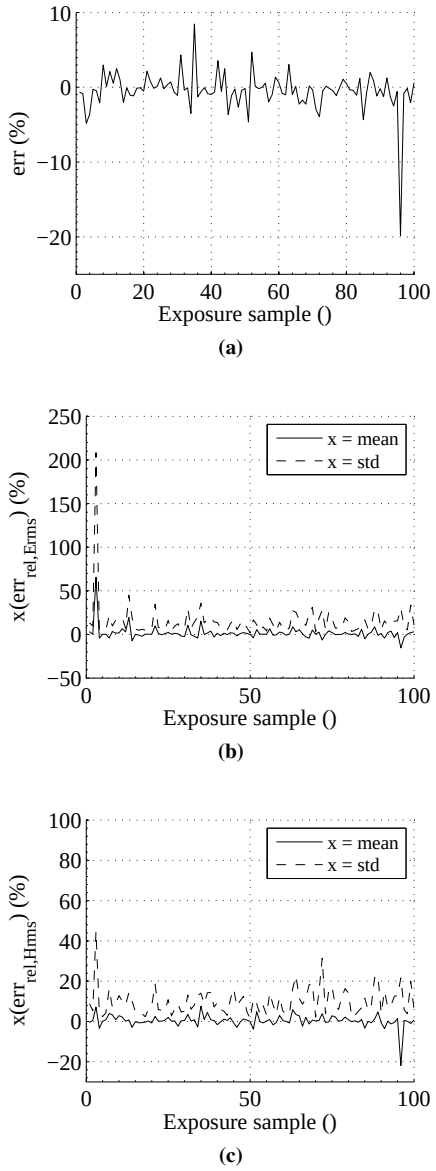

Figure 6.10: *The (a) relative error on SAR_{wb}, (b) relative error on the RMS electric field and (c) relative error on the RMS magnetic field on the closed observation surface using the* ***nearest interpolation scheme*** *for* ***spheroid average man*** *exposed to EMF from GSM downlink at 950 MHz in an urban-macrocell environment.*

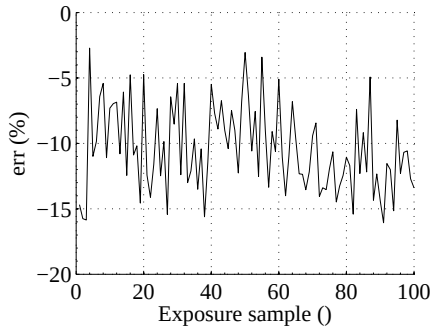

(a)

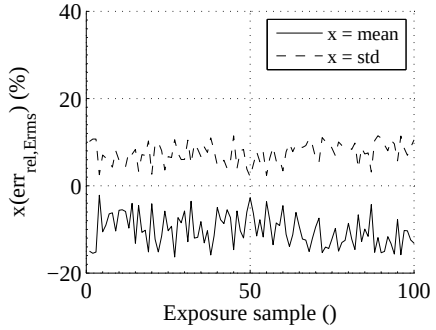

(b)

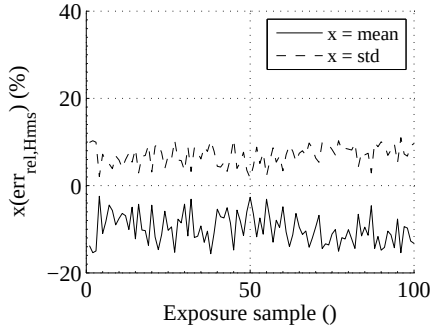

(c)

Figure 6.11: *The (a) relative error on SAR_{wb}, (b) relative error on the RMS electric field and (c) relative error on the RMS magnetic field on the closed observation surface using the **linear interpolation scheme** for **spheroid average man** exposed to EMF from GSM downlink at 950 MHz in an urban-macrocell environment.*

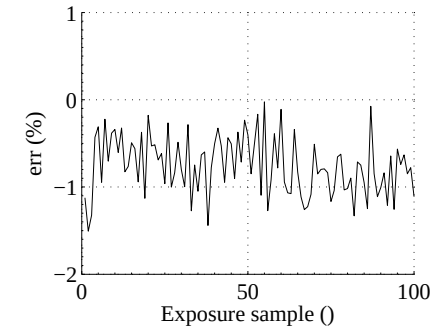

(a)

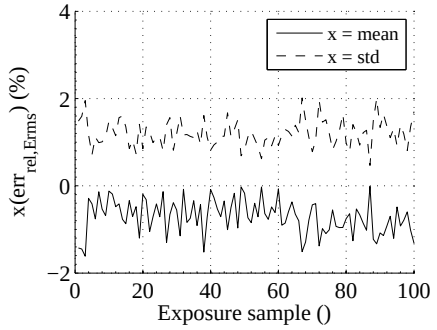

(b)

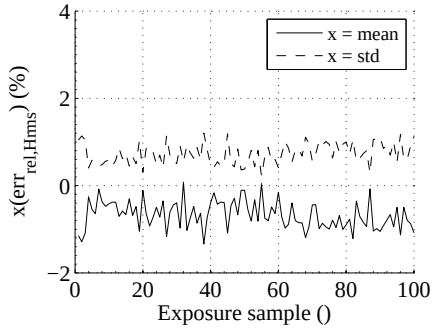

(c)

Figure 6.12: *The (a) relative error on SAR_{wb}, (b) relative error on the RMS electric field and (c) relative error on the RMS magnetic field on the closed observation surface using the* ***cubic-spline interpolation scheme*** *for* ***spheroid average man*** *exposed to EMF from GSM downlink at 950 MHz in an urban-macrocell environment.*

surface as shown in Figure 6.11. As opposed to the linear scheme, the nearest scheme does not, on average, reduce the field levels nor the absorption in the human body (Figure 6.10). The cubic-spline scheme is the most accurate scheme as all observed errors are within 2 % (Figure 6.12).

6.3.2.2 Realistic human body model

Figure 6.13, Figure 6.14 and Figure 6.15 show the relative error on SAR_{wb} (or P_{abs}) and on the electromagnetic fields on the rectangular box surrounding the phantom for nearest, linear and cubic-spline interpolation of the BFDs, respectively. The corresponding mean and standard deviation of these errors are listed in Table 6.4.

Interpolation scheme	$\mu\,(err)$ (%)	$\sigma\,(err)$ (%)
Nearest	-0.11	2.67
Linear	-7.52	2.16
Cubic spline	-0.30	0.39

Table 6.4: *The mean (μ) and standard deviation (σ) on the relative errors of the absorption in Thelonious.*

The observations for the realistic human body model are in line with those for the spheroid human body model. An excellent agreement has been observed between the fast method and the Semcad-X calculations for the cubic-spline interpolation as μ and σ of the relative error on the absorption in the human body is -0.30 % and 0.39 %, respectively (see Figure 6.15a). For a linear interpolation scheme a large underestimation for the absorption is observed as $\mu\,(err)$ equals -7.52 % with $\sigma\,(err)$ of 2.16 %. Moreover, in Figure 6.14a large over- and underestimation are observed of 7.42 % and 15.66 %, respectively. In contrast with the linear scheme, the nearest scheme shows a good mean value of the error (-0.11 %). However, large deviations are possible as the standard deviation is 2.67 %.

The differences in the relative error on the absorption is also reflected by the mean and the standard deviation of the errors on the fields around the human body model as shown in Figure 6.13, Figure 6.14, and Figure 6.15. Again it is observed that cubic-spline interpolation is more accurate than nearest and linear interpolation. First, the mean of the relative error on the rms fields varies from -1.21 % to 0.93 %, from -11.34 % to -1.89 %, and from -15.66 % to 7.42 % for cubic-spline, linear and nearest interpolation, respectivily. The cubic-spline interpolation also shows to have a smaller standard variation of the error on the rms fields, i.e., between -0.31 % and 0.05 %. Furthermore, it is also observed that the error plots for the electric field and the magnetic field are similar.

A cubic-spline scheme estimates better the total fields around the human body than the nearest and linear scheme. The cost of a cubic-spline interpolation is

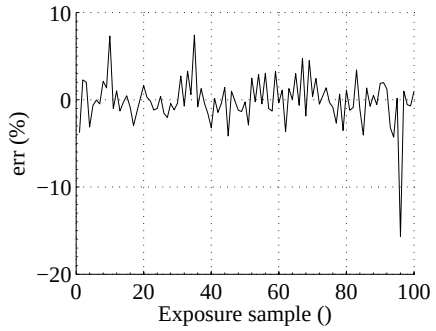

(a)

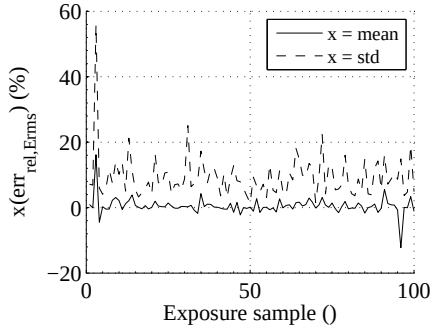

(b)

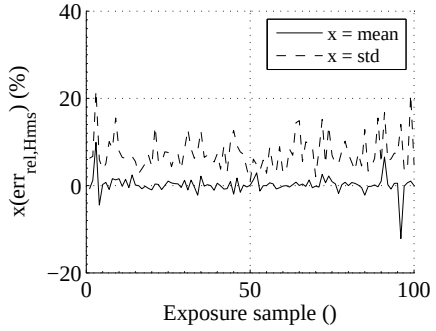

(c)

Figure 6.13: *The (a) relative error on SAR_{wb}, (b) relative error on the RMS electric field and (c) relative error on the RMS magnetic field on the closed observation surface using the **nearest interpolation scheme** for **Thelonious** exposed to EMF from GSM downlink at 950 MHz in an urban-macrocell environment.*

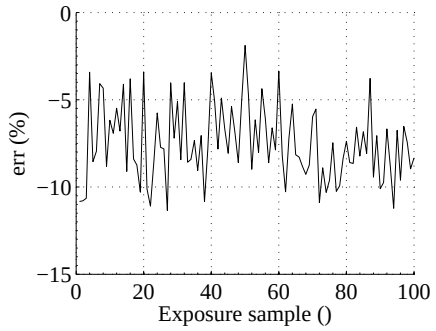

(a)

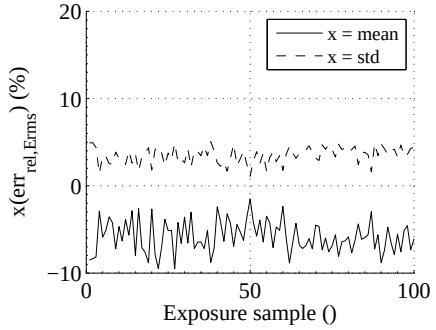

(b)

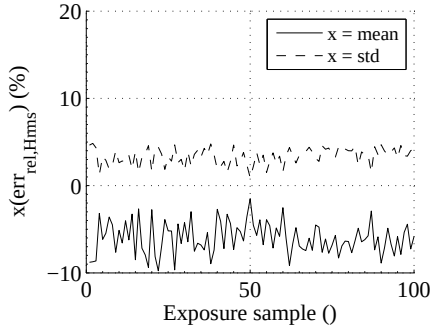

(c)

Figure 6.14: *The (a) relative error on SAR_{wb}, (b) relative error on the RMS electric field and (c) relative error on the RMS magnetic field on the closed observation surface using the **linear interpolation scheme** for **Thelonious** exposed to EMF from GSM downlink at 950 MHz in an urban-macrocell environment.*

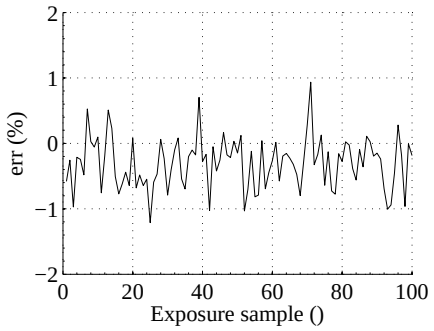

(a)

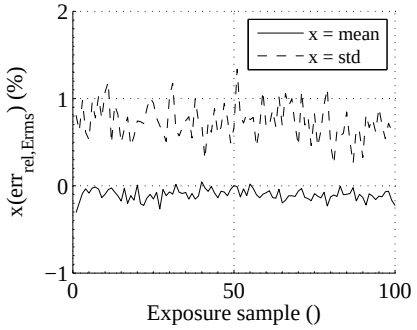

(b)

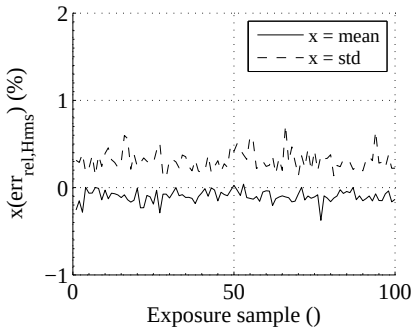

(c)

Figure 6.15: *The (a) relative error on SAR_{wb}, (b) relative error on the RMS electric field and (c) relative error on the RMS magnetic field on the closed observation surface using the* ***cubic-spline interpolation scheme*** *for* ***Thelonious*** *exposed to EMF from GSM downlink at 950 MHz in an urban-macrocell environment.*

an increase of the average computing time per exposure sample to approximately 6 seconds on a 64 bit computer with a quad core CPU at 3 GHz and 4 GB of RAM. This is approximately a doubling of the computing time of the nearest and linear interpolation scheme which have equal computing times. Nevertheless, the cubic-spline interpolation is preferred because it reduces significantly the number of computed BFDs which have to be determined by a full-wave 3D EM solver. Therefore, the cubic-spline interpolation scheme has been selected and is used from this point on unless otherwise stated.

6.3.3 Optimal spacing for $\Delta\phi_{inc}$ and $\Delta\theta_{inc}$

An important step in the validation process is the determination of the number of basic field distributions which have to be calculated by a full-wave numerical tool. The number of BFDs which have to be calculated by 3D numerical means is mainly determined by the performance of the interpolation scheme for the angles of incidence $(\phi_{inc}, \theta_{inc})$. The better the interpolation scheme, the larger the spacing between the angles of incidence, and the less BFDs to calculate. In the previous section it is observed that the cubic-spline interpolation is preferable over a nearest and linear interpolation scheme.

6.3.3.1 Spheroid human body model

Figure 6.16 shows the absolute value (because the mean value is negative for all considered cases) of the mean μ and the standard deviation σ of the relative error on SAR_{wb} averaged over 100 exposure cases for varying $\Delta\theta_{\mathrm{inc}}$. A cubic-spline interpolation scheme has been selected (Section 6.2.2). An excellent agreement is observed between the full-wave simulations and the presented fast method for separations of 5 deg and less. At 950 MHz, the absolute value of the mean of the relative error equals 0.76 % with a standard deviation of 0.34 % for $\Delta\theta_{\mathrm{inc}} = 5$ deg. For this $\Delta\theta_{\mathrm{inc}}$ and $\theta_{\mathrm{inc},K-1} = \pi/2$ (because of reflection symmetry of the spheroid human body model), it follows from Eq. (6.12) that $K = 19$.

The deviation of the results of the fast method from the ones of the full-wave method has several causes. Firstly, the basic field distributions have only been calculated for a single azimuth angle $\phi_{\mathrm{inc},l}$ and a discrete set of elevation angles $\theta_{\mathrm{inc},k}$. For intermediate angles of incidence, a cubic-spline interpolation scheme has been used to calculate the basic field distributions for these angles and causes an uncertainty. Further, the numerical integration of the surface integral of equation Eq. (6.17) to determine the absorbed power within a closed surface is also a cause of uncertainty.

For a frequency of 950 MHz, the basic fields for the TE- and TM-polarized incident plane waves have been numerically determined for $\theta_{\mathrm{inc},k}$ ranging from 0 to $\pi/2$ in steps of $\pi/36$ ($\Delta\theta_{\mathrm{inc}} = 5$ deg). In total, $2KL$ or 38 simulations of basic

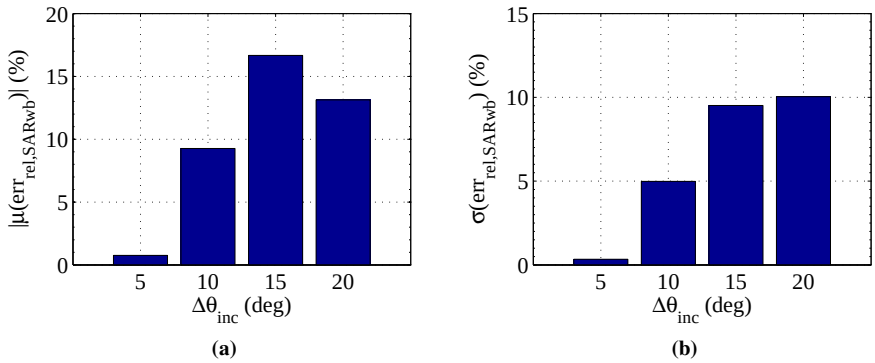

Figure 6.16: *The absolute value of (a) the mean and (b) the standard deviation of the relative error on SAR_{wb} as a function of the step in elevation angle $\Delta\theta_{\mathrm{inc}}$ between two consecutive basic field distributions.*

field distributions have to be performed. The numerical calculations have been performed with a commercially available FDTD-tool on a 64 bit machine with a 3.4 GHz dual-core processor and 4 GByte of RAM. A hardware accelerator has been used to speed up the simulations.

6.3.3.2 Realistic human body model

The influence of the spacing $\Delta\phi_{\mathrm{inc}}$ and $\Delta\theta_{\mathrm{inc}}$ on $\mathrm{err}_{\mathrm{rel,SAR_{wb}}}$ is also investigated for realistic human body models. Due to the abscence of rotation symmetry for these models, a step along the azimuth is defined, i.e., $\Delta\phi_{\mathrm{inc}}$, in addition to $\Delta\theta_{\mathrm{inc}}$. The spacing along azimuth is varied between 10° and 40° in steps of 10°. The spacing along elevation is varied between 5° and 20° in steps of 5°. The mean and standard deviation of $\mathrm{err}_{\mathrm{rel,SAR_{wb}}}$ are shown in Figure 6.17. As expected, the smallest error is found for the smallest spacing, i.e., $\Delta\phi_{\mathrm{inc}} = 10°$ and $\Delta\theta_{\mathrm{inc}} = 5°$. The mean of $\mathrm{err}_{\mathrm{rel,SAR_{wb}}}$ varies between 0.3 % ($\Delta\phi_{\mathrm{inc}} = 10°$, $\Delta\theta_{\mathrm{inc}} = 5°$) and 23 % for ($\Delta\phi_{\mathrm{inc}} = 40°$, $\Delta\theta_{\mathrm{inc}} = 20°$). Also the standard variation increases with increasing spacing between the azimuth and elevation angles. Furthermore, it is also observed that the variation of $\mathrm{err}_{\mathrm{rel}}$ along the elevation angle is larger than along the azimuth angle.

6.3.4 Overall uncertainty assessment

The previous section validated the statistical multipath exposure (SME) calculations with respect to full-wave numerical computations. The error can be less than 1 % depending on the number of available BFDs and the interpolation routines. To

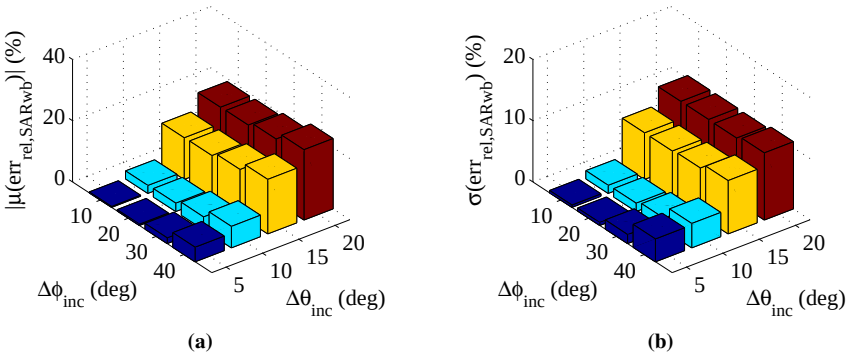

Figure 6.17: *The (a) mean and (b) standard deviation of the relative error on the absorption in the Virtual Family boy exposed to electromagnetic fields from GSM downlink at 950 MHz in an urban-macrocell environment for varying number of BFDs.*

assess the overall uncertainty [46] we also have to take into account the uncertainties introduced by the computations of the BFDs. In this study the FDTD method available in SEMCAD-X (Speag, Switzerland) is applied to compute the BFDs. A comprehensive uncertainty analysis of the FDTD calculations is outside the scope of the present study. Hence, we assessed the uncertainty for the BFD calculations based on previous studies [8, 47, 48]. The expanded uncertainty U ($k = 2$) on SAR_{wb} in a heterogeneous human body model exposed to a single-incident plane wave equals 21.2 % using the FDTD method according to [48]. Assuming that the error of the SME method with respect to the full-wave FDTD calculations is not correlated with the FDTD uncertainties and taking into account an additional error of 1 % for the SME calculations, the expanded uncertainty U ($k = 2$) becomes 21.3 %. The error of the SME calculations is almost negligible with respect to the uncertainty of 21.2 % for the FDTD computations.

6.3.5 Computational time

The SMEtool is designed to reduce the duration of the calculations in a statistical analysis of the specific absorption rate.

The FDTD computations were done on a 2.2 GHz dual-core workstation (Precision 690, Dell, Round Rock, Texas, USA) with Graphics Processing Unit (GPU) computing (NVIDIA Quadro Plex 2200 Model D2, NVIDIA, Santa Clara, California, USA) and 32 GB of RAM. The calculations for the SME method were performed on a 3 GHz quad-core PC with 4 GB of RAM (Optiplex 760, Dell, Round Rock, Texas, USA). Computing the BFDs took 9.3 days. Once the BFDs are available, assessing SAR_{wb} in a single environment and a sample size of 5000 expo-

Method	time for sample size of 5000
FDTD	17.4 days
SMEtool spline	9.3 days + 1.4 days
SMEtool linear	9.3 days + 1.4 days
SMEtool nearest	9.3 days + 25.8 min

Table 6.5: *Comparison of the computing time of the SMEtool with FDTD calculations for realistic human body models.*

sures took only 25.8 min for nearest interpolation, whereas assessing SAR_{wb} with only full-wave computations would take 17.4 days. So, using the SME method is up to 45 % faster than using solely full-wave calculations (based on an exposure sample size of 5000). Moreover, the gain in time increases when more environments are considered as the BFDs have to be calculated only once! The SME tool is faster for rotation symmetric human body models (such as the spheroid) than for realistic human body models because for the former the fields only need to be interpolated along the elevation direction.

6.3.6 The number of exposure cases for statistical relevance

Before we start our analysis, it is necessary to know how many exposure cases are required to obtain statistically relevant results. Therefore, the mean μ and the standard deviation σ of the SAR_{wb} have been determined as a function of the number of exposure cases N_{s}. Figure 6.18 shows the results for the configuration of Section 6.3.1 and the urban macro-cell environment. A good estimate for μ of the SAR_{wb} is already obtained with 100 exposure cases as the relative error on the mean is below 1 % (Figure 6.18a). However, the standard deviation σ of the SAR_{wb} shows a large variation below 4000 exposure cases. When the number of exposure cases exceeds 4000, then the relative error on the standard deviation falls below 2 % (Figure 6.18b). For this case, statistical relevance is obtained after approximately 4000 exposure cases. Thus, a large number of exposure cases is needed to determine worst-case exposure situations in realistic environments, which are in the right tail of the probability distribution of the whole-body SAR.

6.3.7 Coupling of the human body with the environment

The SME method assumes that the human is in the far field of all (base station) antennas and that there is no coupling between the human and the environment. The far-field assumption is almost always fulfilled in case of general public exposure because the general public is not allowed to approach closely a base station antenna. In the SME method, we isolate the human from any object in the environment; no ground nor walls are modelled by the SME method. But, in real

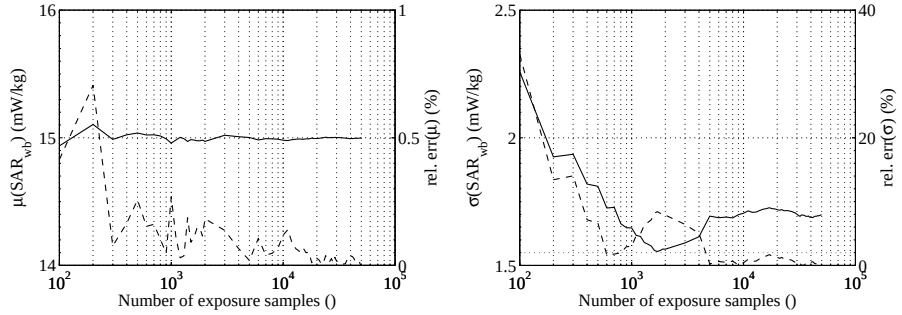

Figure 6.18: *The influence of the number of exposure cases on (a) the mean (–) and (b) the standard deviation (–) together with their corresponding absolute relative errors (- -) for an urban macro-cell environment.*

life, there's always a ground beneath our feet or people can lean against or walk along a wall. In this section, we validate the isolated condition and estimate the uncertainty on the absorption when coupling with the environment occurs.

We distinguish three different mechanisms through which the environment influences the absorption in the human body: (1) the environment obstructs travelling electromagnetic waves resulting in multi-path propagation caused by attenuation and reflections, diffractions and refractions at boundaries; (2) conducting effects may occur when the human touches the ground or objects; (3) capacitive coupling occurs at short distances between the body and the environment. The statistical exposure model that is implemented in the SME method accounts for the multi-path propagation, but the conducting and capacitive effects are not taken into account as the human body is isolated from the environment.

We also investigate shadowing due to the body. In practise, stochastical models for the incident electric fields or incident power density are based on free-space measurements and do not take into account the human body. But, a human body close to a wall shadows the incident fields from reflecting at the wall. Thus, the human body is mainly exposed by the incident fields and not the reflected fields at the wall. This shadowing of the body is not taken into account when deriving the stochastical models for the incident fields and introduces uncertainty on the whole-body SAR assessed in isolated conditions.

6.3.7.1 Configurations

We investigated the coupling between the body and the environment for a spheriod human body model standing on a perfectly conducting (PEC) ground as depicted

in Figure 6.19a. We selected a perfectly conducting ground to obtain a worst-case estimate for the coupling. Capacitive coupling is considered for a separation of 10 mm, which represents the spacer of the sole of a shoe. When the body touches the ground (separation equals zero) also conducting effects are considered.

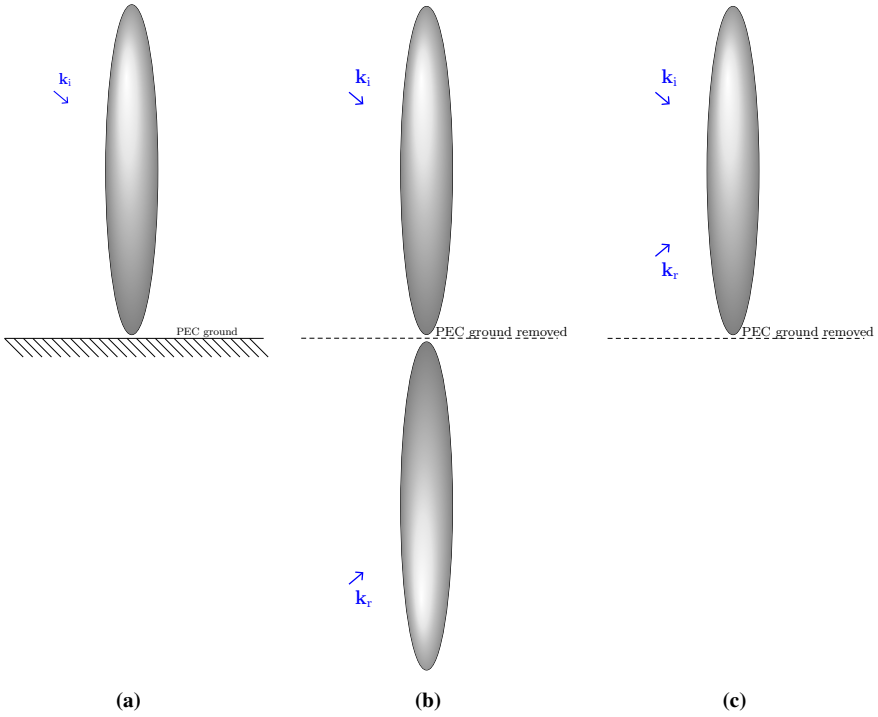

Figure 6.19: *A spheroid human body model standing on a perfectly conducting (PEC) ground and exposed to a single incident plane wave: (a) real configuration, (b) modelled by mirror symmetry, and (c) modelled as an isolated human body model exposed to an incident and reflected plane wave.*

The spheroid human body model has the size of an average man as specified by Durney et al. [13] (half width and half height equals 13.8 cm and 87.5 cm, respectively). The homogeneous prolate spheroid has been assigned the dielectric properties of head tissue simulating liquid suggested by IEC 62209 [45] for compliance testing.

The spheroid human body model is exposed to a single incident plane wave ($\mathbf{k}_i$). We consider two perpendicular polarizations of the incident plane wave: transverse-electric (TE) and transverse-magnetic (TM). The incident plane wave is reflected ($\mathbf{k}_i$) at the PEC ground. Figure 6.20 shows the incident and reflected plane wave on a PEC ground for TE and TM polarization. In case of TE polar-

ization, the electric field vector lies in a plane parallel to the PEC ground plane, whereas for TM polarization, the H vector is parallel to the PEC ground plane. We only considered angles of incidence along the direction of elevation because the spheroid human body model is rotation symmetric about its long axis.

The capacitive coupling and conducting effects are investigated as a function of frequency from 100 MHz (FM) to 900 MHz (GSM) and for two elevation angles, i.e., elevation of 80 deg and 85 deg (most incident plane waves in the far field of base station antennas have a nearly horizontal angle of incidence). The shadowing effect is shown for a frequency of 950 MHz and for elevation angles ranging from 0 deg to 85 deg.

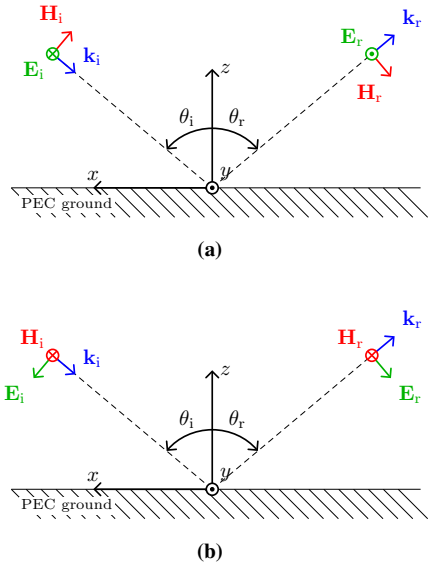

Figure 6.20: *A (a) TE and (b) TM-polarized incident plane wave reflected at a perfectly conducting infinite ground.*

6.3.7.2 Modelling the reflective ground plane

We investigate the capacitive coupling, conducting effects and shadowing of the body between the human body and the environment using the FDTD technique as implemented in the software suite SEMCAD-X (SPEAG, Zurich, Switzerland). In FDTD, the "total-field scattered-field" is used for the excitation of the plane wave [49]. The incident plane wave propagates in the part of the calculation domain that is delimited by the rectangular boundary of the plane wave source. This is denoted as the total-field region. Outside the boundaries of the plane wave-source (or the total-field region) only the scattered field propagates towards

the (absorbing) boundaries of the calculation domain. When using the total-field scattered-field method, all scatterers must be inside the total-field region.

The PEC ground plane is infinite in extent (see Figure 6.19) and cannot be enclosed by the total-field scattered-field plane-wave source. Truncating the infinite ground plane introduces boundary effects where the PEC ground is truncated. Therefore, we modelled the PEC ground by mirroring the human body model and including the reflected plane wave by an additional plane-wave source (see Figure 6.19b). The plane of mirror symmetry is the plane of the ground plane. By using mirror symmetry, we removed the infinite ground plane at the cost of doubling the calculation domain. In the SME method, no coupling is modelled and the environment – here represented by a PEC ground – is neglected at the cost of an increased uncertainty (see Figure 6.19c).

6.3.7.3 Capacitive coupling and conducting effects

Figure 6.21 shows the relative error (in %) on the whole-body SAR in a spheroid average man when coupling between the body and the environment is neglected (see Figure 6.19c). We did not observe capacitive coupling for a TE-polarized incident plane wave: the maximum absolute value for the relative error equalled 2.3 %. Coupling occurs for TM-polarized incident plane waves when the electric field vector has a component perpendicular to the ground and the bottom of the body. Coupling is more pronounced at frequencies below 550 MHz with relative errors ranging from 7 % up to 36 % for a highly reflecting ground (see Figure 6.21). The relative error on the whole-body absorption decreases with frequency. At 550 MHz and above the relative error on the whole-body SAR decreases below 5 % for a separation of 10 mm.

If we take a zero separation between the human body and the PEC ground, then conducting effects appear in addition to the capacitive coupling. Figure 6.21a indicates a slight increase in relative error when the body touches the ground with respect to a separation of 10 mm as shown in Figure 6.21b. Only at a frequency of 100 MHz, the relative error increases by more than 5 %, namely 8 % and 5 % for an elevation angle of 80 deg and 85 deg, respectively. In general, capacitive coupling dominates conducting effects because the human body only touches the ground in a single point for a spheroid human body model and the conductivity of the human body is small (e.g., 0.97 S/m at 900 MHz).

6.3.7.4 Shadowing due to the human body

Figure 6.22 shows the relative error on the whole-body SAR as a function of elevation angle when the PEC ground is modelled by a reflected incident plane wave (for a separation of 0 mm between the human body and the ground). The relative error on SAR_{wb} increases for decreasing elevation angle and is maximum when

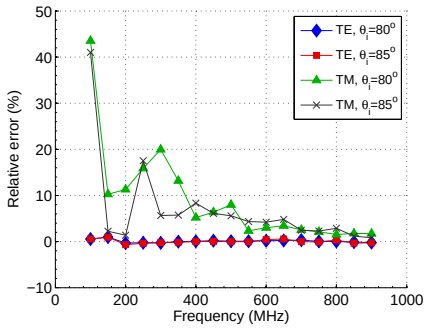

(a)

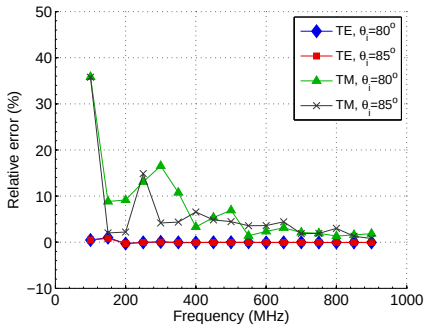

(b)

Figure 6.21: *Relative error on the whole-body SAR in the spheroid average man standing on a perfectly conducting ground when coupling is not taken into account for a separation of (a) 0 mm and (b) 10 mm.*

the incident plane wave is coming from the top ($\theta_i = 0$ deg). This behavior is caused by the shadowing of the spheroid human body model. The body attenuates the incident plane wave before it reflects at the PEC ground. This attenation is not taken into account when the PEC ground is replaced by a reflected plane wave. Or, the PEC ground can be substituted by an additional plane-wave source that represents the reflections from the ground plane for angles of incidence larger than 30 deg. For these elevation angles, the relative error is less than 4 %.

6.3.7.5 Discussion

We investigated capacitive coupling and conducting effects for a spheroid human body standing on a perfectly conducting ground for communication frequencies ranging from 100 MHz up to 900 MHz. Capacitive coupling and conducting effects occur when the electric-field vector is perpendicular to the ground and the

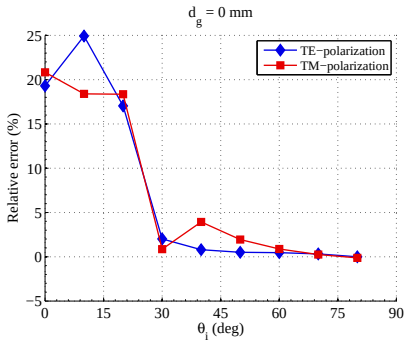

Figure 6.22: *Relative error on the whole-body SAR due to shadowing for a separation of 0 mm.*

body (thus, mainly for a vertical polarized electric field). Assessing the whole-body SAR in isolated conditions neglects capacitive coupling and conducting effects. This is fine for frequencies above 550 MHz, but below 550 MHz an additional uncertainty has to be taken into account. This uncertainty increases for decreasing frequencies and ranges from 8 % (at 500 MHz) to 44 % (at 100 MHz). Capacitive coupling dominates conducting effects as the uncertainty due to conducting effects is less than a fifth of the uncertainty due to capacitive coupling.

The shadowing of the human body is also not taken into account in isolated configurations. The presence of the human body attenuates the incident field resulting in less power to be reflected by the ground. Exposure models are typically determined without the presence of the body and, thus, the reflected power does not include the attenuation of the body. In the case of human body standing on a ground plane, the overestimation occurs for waves coming from above up to an elevation angle of 30 deg. In realistic exposure situations in the far-field of an antenna, shadowing has a minor effect because at least 99.3 % of the incident plane waves have an elevation angle larger than 30 deg (from the vertical axis or z-axis) for the environments of Table 6.2.

Finally, we remark that a perfectly conducting ground is a worst-case environment reflecting all the power impinged on the boundary. In most situations, the environment does not consist of perfectly conducting objects resulting in a partly scattered and transmitted incident power density. The uncertainties determined in this section can, thus, be considered as worst-case values.

6.4 Applications

The presented SME method enables a statistical analysis of induced SAR_{wb} in a human body in a realistic environment. A sample size of less than 100 exposures

is sufficient to obtain the average whole-body SAR, but assessing the complete distribution of SAR_{wb} values requires a sample size of up to 4000 exposures (see Section 6.3.6). We used the SME method to investigate the distribution of the induced whole-body SAR in different human body models for different environments and for commmunication frequencies up to 2.45 GHz. Topics of interest were amongst others: influence of the size of the human, the environment, operating frequency, the averaging of the incident fields on the whole-body SAR, and checking compliance of the whole-body SAR with safety guidelines for prolate spheroid and realistic human body models.

6.4.1 The whole-body SAR in a spheroid human male exposed in a realistic environment

We assessed the whole-body SAR in homogeneous spheroid human body models for 50000 exposures in four realistic environments: urban-macro cell, urban-micro cell, outdoor-indoor, and indoor-pico cell. Table 6.2 lists the parameters describing the exposure in these environments. The homogeneous spheroid has a height of 1.75 m and a half-width of 13.8 cm and represents an average male according to Durney et al. [13] (See also Section 6.3.1). The dielectric properties of the spheriod equals the values used for head simulating tissue as suggested in IEC 62209 [45].

Figure 6.23 shows the cumulative distribution function of the induced SAR_{wb} for the different environments for an RMS incident (i.e., in abscence of the human body) electric field averaged over the volume of the body equal to the ICNIRP reference level at 950 MHz (ICNIRP 1998), i.e., 42.38 V/m. We annotated Figure 6.23 with the summary statistics of the induced whole-body SAR in terms of the 50^{th} (p_{50} or median), 90^{th} (p_{90}), 95^{th} (p_{95}) and 99^{th} (p_{99}) percentiles. One can observe that the summary statistics are almost equal in the different environments: the median or the 50^{th} percentile of the SAR_{wb} is about 0.015 W/kg and 99 % of the exposure situations have an SAR_{wb} below 0.023 W/kg.

All the exposures of the investigated environments resulted in an SAR_{wb} lower than the basic restriction of 0.08 W/kg for general public (ICNIRP 1998). This shows that at 950 MHz, for a spheroid human body model representing an average man, the ICNIRP basic restrictions are satisfied when the field in a realistic complex environment averaged over the human body is equal to the ICNIRP reference level.

The markers on the cdf indicate the location of whole-body SAR for single incident plane-wave exposure in the distribution for multi-path exposure. Three polarizations for single incident plane wave are shown with, respectively, the wave vector (K-pol), the electric field (E-pol) and the magnetic field (H-pol) parallel to the z-axis. The worst-case single incident plane wave exposure at 950 MHz is obtained for H-pol with SAR_{wb} equal to 0.017 W/kg. This maximum value of

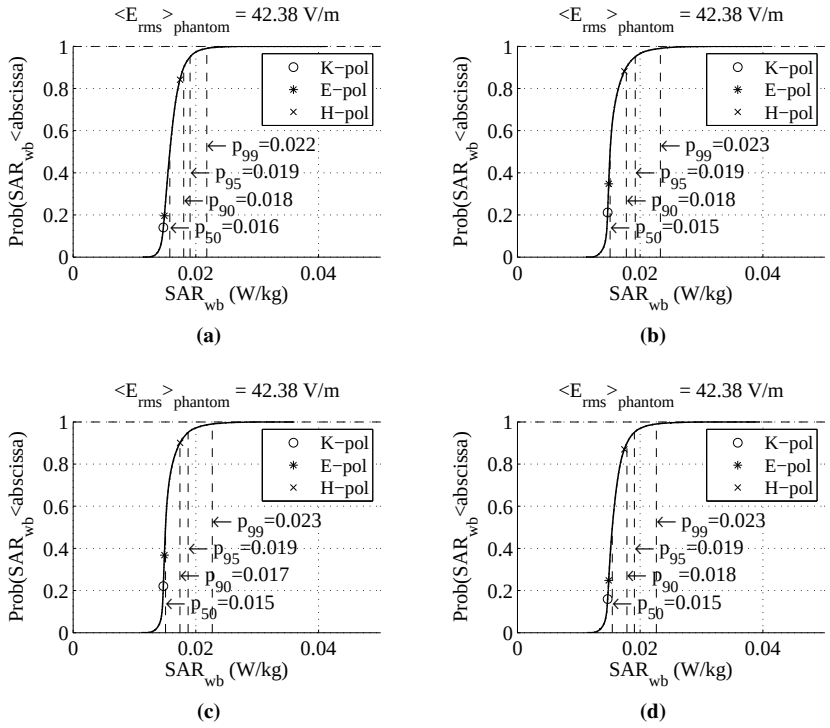

Figure 6.23: *The cumulative distribution function (cdf) of the whole-body SAR in a spheroid human body model in (a) an urban macro-cell, (b) an urban micro-cell, (c) an indoor pico-cell, and (d) an outdoor-indoor environment at 950 MHz.*

SAR_{wb} for single plane-wave exposure approximates the 90^{th} percentile (p_{90}) of SAR_{wb} in a complex environment (heterogeneous exposure). Thus, the whole-body averaged SAR in a homogeneous spheroid human body phantom in a complex environment exceeds in more than 10 % of the cases the SAR_{wb} for worst-case single incident plane wave exposure. This shows that SAR_{wb} for worst-case single incident plane wave exposure (used for the ICNIRP guidelines) can thus be exceeded by heterogeneous exposure.

6.4.2 Influence of size and frequency on the whole-body SAR in homogeneous spheroid human body models

ICNIRP's reference levels [1] are derived from the basic restrictions using the worst-case single incident plane wave exposure of a prolate spheroid human body model placed in free space or isolated conditions. The homogeneous exposure of a single incident plane wave never occurs in reality; a person experiences an expo-

sure varying in time and space because travelling electromagnetic waves interact with the environment (reflections, refractions and diffractions occur at grounds, walls and (moving) objects).

In this section, we investigated the whole-body averaged SAR in homogeneous prolate spheroid human body models for realistic exposure and for communication frequencies ranging from 100 MHz to 2.45 GHz. This frequency range covers broadcasting systems, cellular systems, and indoor systems. We selected five spheroids of different size representing three childs of age 1, 5 and 10 year and an adult female and adult male. For frequencies up to 950 MHz all models were used, but for frequencies above 950 MHz only the spheroid for average male and 1-year-old child were selected.

6.4.2.1 Materials and methods

The influence of the phantom size on SAR_{wb} is investigated using a homogeneous spheroid human body phantom as defined in [13]. The sizes of the spheroid for an average man, an average woman, a 10-year-old child, a 5-year-old child and a 1-year-old child are taken from [13]. The homogeneous tissue of the spheroid human body models is assigned the dielectric properties (permittivity ϵ_{r} and conductivity σ (S/m)) of average head tissue suggested by IEC 62209 [45] for compliance testing.

We selected the urban-macro cell environment for frequencies of 950 MHz and above because we observed in Section 6.4.1 that SAR_{wb} becomes independent of the environment for frequencies at 950 MHz. We assume the same behavior for frequencies above 950 MHz because the wavelength decreases with frequency and remains much smaller than the size of the human body models. For frequencies below 950 MHz the induced SAR_{wb} is determined for the four environments listed in Table 6.2.

We generated 5000 realistic exposures to obtain statistically relevant results for every frequency and every size of the human body model in the four environments listed in Table 6.2. In addition, the SAR_{wb} has been numerically assessed for single incident plane wave exposure with E-polarization, H-polarization and k-polarization as defined by [13]. For every exposure, the RMS value of the incident electric field was averaged over the volume of the human body ($\langle E_{\mathrm{rms}} \rangle_{\mathrm{phantom}}$) as specified by ICNIRP [1]. The whole-body SAR is determined for $\langle E_{\mathrm{rms}} \rangle_{\mathrm{phantom}}$ equal to the ICNIRP reference level allowing to determine if compliance to the reference levels ensures compliance to the basic restriction for a heterogeneous exposure in the investigated human body phantoms.

6.4.2.2 Results

The cumulative distribution function (cdf) of the SAR_{wb} for realistic exposure and SAR_{wb} for a k-, E-, and H-polarized incident plane wave (indicated by $\square$, $\triangle$, and $\circ$, respectively) at 950 MHz are shown in Figure 6.24. It is clearly observed that the single incident plane waves are not the worst-case exposure and that decreasing the phantom size shifts the cdf to higher SAR_{wb}-values. Table 6.6 shows the results for the worst-case single incident plane wave exposure. The polarization of the worst-case single plane wave (wcpw) as well as the corresponding whole-body SAR (denoted as SAR_{wbwcpw}) are listed. One observes that the worst-case single plane wave is E-polarized at 150 MHz, 300 MHz, and 450 MHz for all the considered phantoms. At 950 MHz (GSM downlink), the worst-case single plane wave is H-polarized for average man, average woman, and 10-year-old child (larger phantoms), and is E-polarized for the 5-year-old child, and 1-year-old child (smaller phantoms). The polarization of the worst-case incident plane wave depends on the size of the phantom compared to the wavelength: if the phantom becomes sufficiently small compared to the wavelength, the worst-case polarization will change from E-polarization to H-polarization. One also observes from Table 6.6 that the whole-body SAR for worst-case single plane wave exposure increases with decreasing phantom size for the investigated frequencies. The highest SAR_{wb}-values are obtained for the 1-year-old child ranging from 0.055 W/kg (at 150 MHz) to 0.0321 W/kg (at 950 MHz). However, the absorbed power (P_{abs}) increases with increasing phantom size above resonance of the phantoms (the resonance frequency for the 1-year old child is 174 MHz). Thus, the SAR_{wb} will largely depend on the mass of the phantom above resonance [13]. SAR_{wb} in a homogeneous spheroid human body model does not exceed the basic restriction for general public (0.08 W/kg) in case of worst-case single plane wave exposure for the investigated frequencies and phantom sizes.

Table 6.7 summarizes the results for a realistic exposure. This table lists the 99^{th} percentile of SAR_{wb} (p_{99}), the percentage of realistic exposures for which SAR_{wb} is larger than the worst-case single plane wave ($n_{\mathrm{s>pw}}$) listed in Table 6.6, and the percentage of realistic exposures for which SAR_{wb} is larger than the ICNIRP basic restriction for general public exposure, i.e. 0.08 W/kg ($n_{\mathrm{s>BR}}$). Again, it is observed that the smaller the size of the phantom, the higher the p_{99} (SAR_{wb}). The highest value for p_{99} (SAR_{wb}) occurs for the 1-year old child phantom at 150 MHz, i.e., 0.094 W/kg and exceeds the ICNIRP basic restriction for general public. Moreover, Table 6.7 indicates that SAR_{wb} is not compliant to the basic restriction inside all the considered phantoms at 150 MHz for some exposure cases: for the 1-year old child 1.59 % of the examined exposure sample resulted in an SAR_{wb} exceeding the basic restriction. Also at 300 MHz, 450 MHz, and 950 MHz exposures are observed for which the compliance to the reference level does not ensure the compliance to the basic restriction for phantoms with a size

	150 MHz		300 MHz		450 MHz		950 MHz	
	Polarization	SAR_{wb} (W/kg)	Polarization	SAR_{wb} (W/kg)	Polarization	SAR_{wb} (W/kg)	Polarization	SAR_{wb} (W/kg)
Man	E	0.0123	E	0.0088	E	0.0084	H	0.0167
Woman	E	0.0138	E	0.0097	E	0.0091	H	0.0172
Child 10-y	E	0.0258	E	0.0164	E	0.0129	H	0.0218
Child 5-y	E	0.0491	E	0.0180	E	0.0169	E	0.0256
Child 1-y	E	0.0550	E	0.0258	E	0.0205	E	0.0321

Table 6.6: *Worst-case single plane wave exposure for $\langle E_{\mathrm{rms}} \rangle_{\mathrm{phantom}}$ equal to the ICNIRP reference level.*

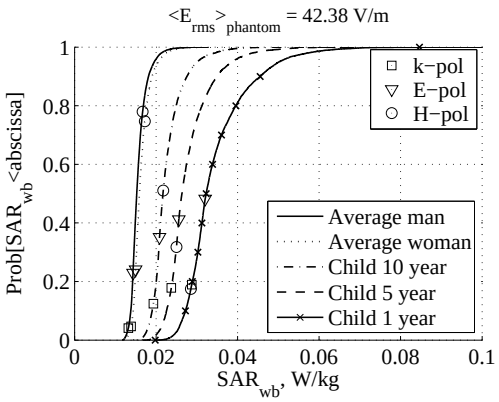

Figure 6.24: *The cumulative distribution function of SAR_{wb} in spheroidal human body phantoms for a realistic exposure, and SAR_{wb} for the single plane wave exposures at 950 MHz.*

smaller than a 10-year-old child, 5-year-old child, and 1-year-old child, respectively. Table 6.7 also shows that $n_{\mathrm{s>pw}}$ ranges from 13.1 % (1-year old child and 150 MHz) to 58.8 % (5-year old child at 950 MHz). The ratio of $p_{99}\left(SAR_{\mathrm{wb}}\right)$ to $SAR_{\mathrm{wb,wcpw}}$ is shown in Figure 6.25 for frequencies up to 950 MHz for all spheroid human body models and up to 2.45 GHz for the average man and the 1-year-old child. It is observed that the worst-case single plane wave exposure is always exceeded by the $p_{99}\left(SAR_{\mathrm{wb}}\right)$ for multipath exposure by 1.32 dB (average man at 950 MHz) to 4.97 dB (5-year old child at 300 MHz). The presented results indicate that the ICNIRP reference levels (determined for worst-case single plane wave exposure) should be reviewed for realistic exposure scenarios.

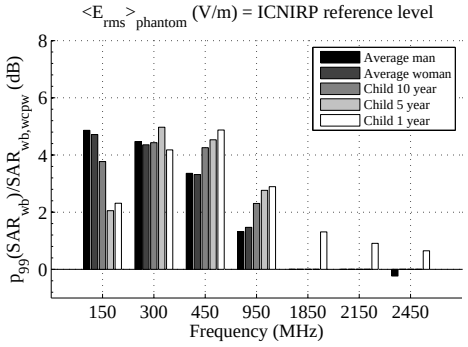

Figure 6.25: *The ratio of the 99^{th} percentile of SAR_{wb} in spheroid human body models in an urban macrocell environment and SAR_{wb} for the single plane wave exposures.*

Finally, we also evaluated the 99^{th} percentile of SAR_{wb} against the ICNIRP

	150 MHz			300 MHz			450 MHz			950 MHz		
	p_{99} (W/kg)	$n_{s>pw}$ (%)	$n_{s>BR}$ (%)	p_{99} (W/kg)	$n_{s>pw}$ (%)	$n_{s>BR}$ (%)	p_{99} (W/kg)	$n_{s>pw}$ (%)	$n_{s>BR}$ (%)	p_{99} (W/kg)	$n_{s>pw}$ (%)	$n_{s>BR}$ (%)
Man	0.038	34.0	**0.04**	0.025	43.5	0	0.018	49.4	0	0.023	22.1	0
Woman	0.041	30.0	**0.06**	0.027	38.6	0	0.020	45.9	0	0.024	25.3	0
Child 10-y	0.061	21.1	**0.51**	0.046	31.0	**0.02**	0.034	44.6	0	0.037	49.0	0
Child 5-y	0.079	13.7	**0.96**	0.057	35.6	**0.25**	0.048	40.8	**0.01**	0.048	58.8	0
Child 1-y	0.094	13.1	**1.59**	0.067	30.5	**0.56**	0.063	39.7	**0.26**	0.062	51.8	**0.07**

Table 6.7: *Realistic exposure for $\langle E_{\mathrm{rms}} \rangle_{\mathrm{phantom}}$ equal to the ICNIRP reference level.*

basic restriction for the RMS electric field averaged over the volume of the body scaled to the ICNIRP reference level [1]. Figure 6.26 shows that for the 1-year-old child the 99^{th} percentile exceeds the ICNIRP basic restriction at 150 MHz and at 1850 MHz and 2150 MHz. The high absorption at 150 MHz in the 1-year-old child is due to the resonance of the body. Around 2 GHz the high absorption is due to the relaxation of the ICNIRP reference levels at these frequencies. These results confirms the findings of Uusitupa et al. [11] and Kühn et al. [8].

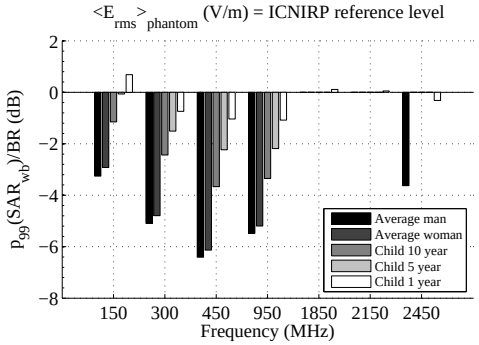

Figure 6.26: *The ratio of the 99^{th} percentile of SAR_{wb} in spheroid human body models in an urban macrocell environment and the ICNIRP basic restriction for whole-body SAR.*

6.4.2.3 Conclusions

The whole-body averaged SAR has been investigated in homogeneous prolate spheroid human body models at different frequencies for a realistic exposure scenario using our statistical multipath exposure tool. The smaller the size of the human body phantom relative to the wavelength, the higher the whole-body SAR. The worst-case whole-body SAR in a realistic exposure environment exceeds the whole-body SAR for worst-case single plane wave in 13.2 % to 58.8 % of the realistic exposure situations. Moreover, it has been shown that the ICNIRP reference levels not always ensure the compliance to the basic restrictions (1.6 % of the exposures for a 1-year-old child exposed at a frequency of 150 MHz exceed them) if a realistic exposure is considered, and therefore the ICNIRP reference levels should be reviewed for realistic exposure scenarios.

6.4.3 The whole-body averaged SAR in the Virtual Family Boy in a realistic environment for the GSM downlink frequency

In the previous sections Section 6.4.1 and Section 6.4.2, we discussed the whole-body SAR induced in spheroid humna body models in a realistic environment characterized by multi-path exposure. Spheroid human body models are a rough

approximation of a human disregarding the tissue distribution and the irregular shape of the body. The influence of the size of a humna on the absorption is clearly indicated by the spheroids, but the influence of the heteroneous tissues and the shape of the human (with respect to simple homogeneous spheroid models) remains unanswered for realistic exposure.

Exposure assessment distinguishes two aims: testing the compliance of worst-case exposure situations and assessing the exposure under realistic or typical conditions. With respect to compiance testing we will refer to the ICNIRP guidelines. Many international and national authoroties built their regulations on these guidelines. However, deviations exist. Our aim is to check if the reference levels stipulated by ICNIRP are compliant with the corresponding basic restrictions

6.4.3.1 Compliance of the ICNIRP reference levels with the basic restrictions for heteregeneous exposure

Figure 6.27a shows the cumulative distribution function (cdf) of the whole-body averaged SAR in Thelonious, the 6-year-old boy of the Virtual Family, for four realistic exposure environments, i.e., urban-macrocell, urban-microcell, outdoor-indoor, and indoor-picocell for the GSM downlink frequency of 950 MHz. The incident power density (S_{in}) for all the exposures equaled the ICNIRP reference level (RL). For general public exposure, RL is 4.75 W/m^2 at 950 MHz. In order to verify easily the compliance of SAR_{wb} with basic restrictions, the following ratio is defined:

$$R_{\mathrm{wb}} = \frac{SAR_{\mathrm{wb}}|_{S_{\mathrm{in}}=RL}}{BR_{\mathrm{wb}}} \tag{6.27}$$

with BR_{wb} the basic restriction for the whole-body SAR and for the corresponding reference level. Figure 6.27b shows the cdf for R_{wb} for the investigated configurations. In every environment the whole-body SAR is calculated for 5000 multi-path exposures in order to obtain the statistics in every environment. The 50$^{\mathrm{th}}$ (p_{50}), 90$^{\mathrm{th}}$ (p_{90}), 95$^{\mathrm{th}}$ (p_{95}), and 99$^{\mathrm{th}}$ (p_{99}) percentile of SAR_{wb} and R_{wb} in Thelonious in the different environments are shown in Figure 6.28. It is observed that the reference level is not always compliant with the whole-body basic restriction (see Figure 6.27), but it is unlikely that the basic restriction will be exceeded for an incident power density equal to the reference level as SAR_{wb} exceeds BR_{wb} in only 0.26 % of the exposures (averaged over the different investigated environments). All percentiles (up to p_{99}) in Figure 6.27 satisfy the ICNIRP basic restrictions. The median of R_{wb} or $p_{50}(SAR_{\mathrm{wb}})$ is about 2.5 dB lower than the BR_{wb}.

The whole-body SAR for single plane-wave exposure is also shown in Figure 6.27 and is indicated by markers. Only frontal incidence in a horizontal plane is considered as this yields the worst-case single plane-wave exposure in heterogeneous human body models according to [8]. Two different polarizations are

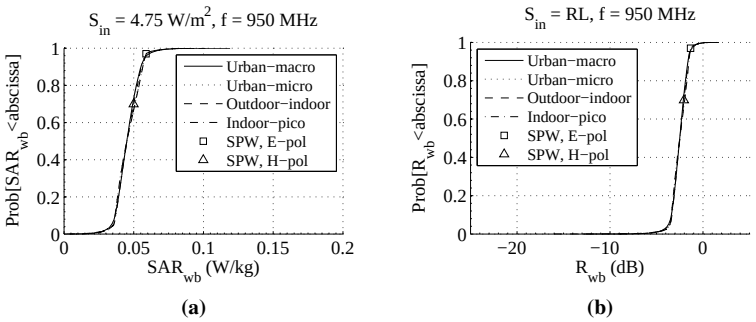

Figure 6.27: *The cumulative distribution function of (a) SAR_{wb} and (b) R_{wb} in Thelonious in four realistic environments exposed to electromagnetic fields from GSM downlink at 950 MHz. The incident power density equalled the ICNIRP reference level for general public exposure, i.e. 4.75 W/m^2 at 950 MHz. The results for an* **E***- and* **H***-polarized frontal incident plane wave is indicated by markers.*

considered, i.e., vertical or **E**-polarization, and horizontal or **H**-polarization. The worst-case single incident plane wave for Thelonious is **E**-polarized and induces a SAR_{wb} value which is 1.3 dB below the basic restriction. Averaged over the four considered environments, 3.6 % of the multi-path exposures (or, heterogeneous exposure) have a higher SAR_{wb} than for worst-case single incident plane-wave exposure (or, homogeneous exposure).

The cdf of SAR_{wb} does not differ significantly between the considered environments for a constant incident power density as shown in Figure 6.27 and Figure 6.28. The maximum of p_{50}, p_{90}, p_{95}, and p_{99} of the whole-body SAR is 0.5 %, 2.4 %, 1.2 %, and 2.2 % larger than the minimum percentiles of the whole-body SAR, respectively.

6.4.4 Comparison of the results of the heterogeneous and the speroid human body model

Section 6.4.2 (see also [5]) investigated the whole-body SAR in spheroid human body models in realistic exposure environments for frequencies ranging from 150 MHz to 950 MHz. In this section, we compared the whole-body SAR in the realistic human body model Thelonious to the whole-body SAR obtained in spheroid models. Because the statistics of SAR_{wb} do not show a signicant difference between different environments at 950 MHz (see Section 6.4.1), in what follows only the urban-macro cell environment is considered. Figure 6.29a shows the cdf of the whole-body SAR for Thelonious and the spheroid human body models in an urban-macro cell environment for the GSM downlink frequency of 950 MHz. It is clearly observed that the spheroid homogeneous human body models underesti-

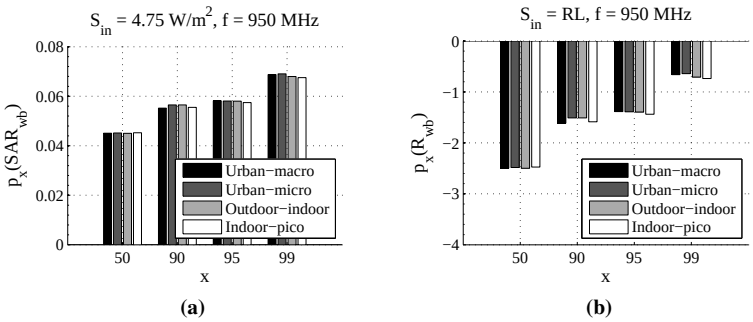

Figure 6.28: *The 50$^{\text{th}}$-, 90$^{\text{th}}$-, 95$^{\text{th}}$-, and 99$^{\text{th}}$-percentile of (a) the whole-body SAR and (b) R_{wb} in Thelonious exposed to electromagnetic fields from GSM downlink at 950 MHz in different environments. The incident power density equalled the ICNIRP reference level for general public exposure, i.e. 4.75 W/m^2 at 950 MHz.*

mate the whole-body SAR in the realistic heterogeneous model Thelonious. The median or p_{50} of SAR_{wb} for the 5-year-old spheriod model is 2.5 dB lower than for the 6-year-old Thelonious (see Figure 6.29b). Because the exposure for the various models is identical, the difference in SAR_{wb} is caused by differences in morphology of the human body models. The increase in SAR_{wb} in Thelonious cannot be completely attributed to the difference in weight and size of the models because SAR_{wb} in Thelonious is larger than for all the spheroid human body models. Hence, the tissue properties as well as the shape of the model play an important role in the difference of SAR_{wb}. To investigate the influence of the tissue properties and the shape of the models, the whole-body SAR for single incident plane-wave exposure is determined in the heterogeneous and homogeneous Thelonious, and the homogeneous 1-year-old spheroid child. For the homogeneous Thelonious, the dielectric properties of all the tissues and air cavities are assigned the same value as for the spheroid models. Figure 6.30 shows SAR_{wb} for different elevation angles of the incident plane wave. Vertical ($\mathbf{E}$) and horizontal polarization ($\mathbf{H}$) are considered. Assigning a homogeneous tissue to Thelonious reduces the whole-body absorption. The difference between the homogeneous Thelonious and the homogeneous 1-year-old spheroid child is due to the difference in mass and shape of the body models. So, the heterogeneous tissues and the irregular shape of realistic human body models increases the whole-body averaged SAR compared to homogeneous canonical human body models, such as spheroids.

Figure 6.29 also shows that the variability of the SAR_{wb} around the mean is the largest in the realistic human body model Thelonious. Table 6.8 lists the standard deviation (σ) of SAR_{wb} in the different human body models for an urban-macro cell environment. For the spheroid human body models, σ increases with

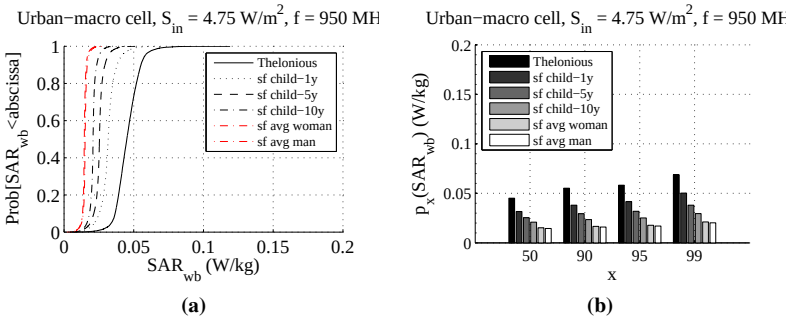

Figure 6.29: *(a) The cumulative distribution function of SAR_{wb} and (b) the 50$^{\mathrm{th}}$-, 90$^{\mathrm{th}}$-, 95$^{\mathrm{th}}$-, and 99$^{\mathrm{th}}$-percentile of SAR_{wb} in Thelonious and SF human body models in an urban-macro cell environment exposed to electromagnetic fields from GSM downlink at 950 MHz. The incident power density equalled the ICNIRP reference level for general public exposure, i.e. 4.75 W/m^2 at 950 MHz.*

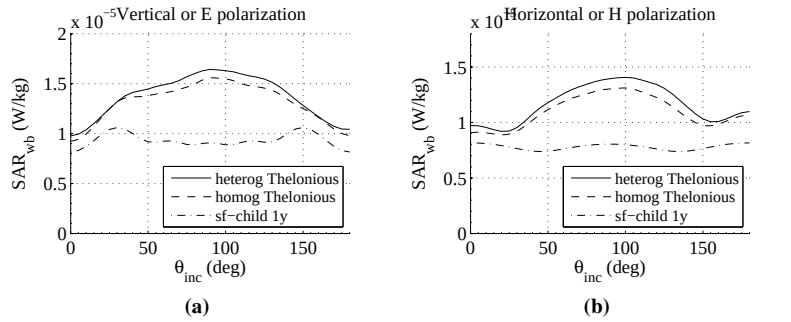

Figure 6.30: *The whole-body SAR in the heterogeneous and homogeneous Thelonious, and the 1-year old spheroid human body model for (a) vertical and (b) horizontal polarized single incident plane-wave exposure at 950 MHz with varying elevation angle.*

Human body model	σ (mW/kg)
Spheroid 1-year old	1.6
Spheroid 5-year old	1.8
Spheroid 10-year old	2.7
Spheroid average woman	4.0
Spheroid average man	5.9
Thelonious	8.2

Table 6.8: *The standard deviation of SAR_{wb} in Thelonious and spheroid human body models in an urban-macro cell environment exposed to electromagnetic fields from GSM downlink at 950 MHz. The incident power density equalled the ICNIRP reference level for general public exposure, i.e. 4.75 W/m^2 at 950 MHz.*

age. The highest σ is observed for the realistic model Thelonious. The larger variability of SAR_{wb} is caused by the irregular shape of Thelonious. This can be partly explained from Figure 6.30. Figure 6.30 shows the variation of SAR_{wb} along the elevation direction (E- and H-polarization) for single incident plane wave exposure. The variation of SAR_{wb} is larger for the irregular-shaped, realistic human body model of Thelonious. The heterogenity of the tissues has a minor effect on the variation of SAR_{wb}. Moreover, the spheroid human body models do not show a variation of SAR_{wb} along the azimuth direction because of the rotation symmetry. Due to the abscence of rotation symmetry in the Thelonious, SAR_{wb} in the Thelonious varies also along the azimuth direction.

6.4.5 Whole-body absorption in Thelonious model in indoor environments

Vermeeren et al. [50] measured the exposure in four indoor microenvironments in Greece and Belgium for different sources that produce a far-field exposure. In this section, we applied the statistical SME method to quantify the absorption in these four indoor environments. The results of the exposure measurements in Belgium are shown in Figure 6.31. The measured electric field levels were below the ICNIRP limits. The maximum measured electric field strength and the maximum mean electric field strength were measured for the GSM downlink signal at 950 MHz in schools and offices, respectively.

The aim of this section is to apply the SME tool to evaluate the whole-body SAR, in terms of the mean and 95th-percentile, in a model of a child when exposed to the incident field levels measured in the indoor environments and to verify if the basic restrictions are fulfilled.

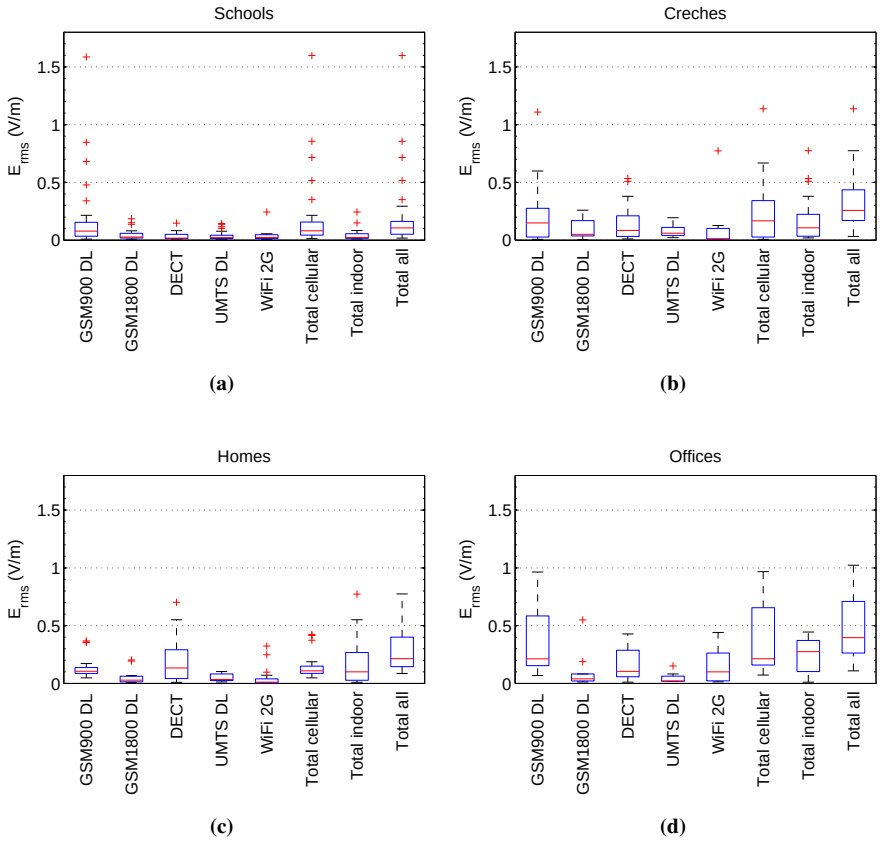

Figure 6.31: *The box plot of the measured incident electric field in four Belgian environments: (a) schools, (b) creches, (c) homes, and (d) offices. [50]*

6.4.5.1 Methodology

We applied the statistical multipath exposure (SME) method to quantify the induced whole-body SAR in the body of a child in these four indoor environments. Although the SME method reduces the computational time by at least 45 % (see Section 6.3.5), investigating the whole-body SAR for different operating frequencies requires a huge amount of basic field distributions (BFDS) because the BFDs have to be computed at every frequency. In order to reduce the number of computed BFDs, we limited the angles of incidence for which the BFDs are computed with a 3D full-wave electromagnetic solver and mapped every incident plane wave of an exposure case to the nearest pre-computed plane wave. The pre-computed fields were calculated in elevation at every 5 deg from 10 deg below to 10 deg above the horizontal plane and in azimuth at every 30 deg. By mapping each incident plane wave of an exposure case to the nearest pre-computed incident-plane wave ("nearest" interpolation scheme, see Section 6.3.2), the error on the whole-body SAR for a single exposure can increased by more than 10 %. But, the error on the statistics of the sample (4000 exposure cases) remains small: the deviation on the 95^{th} percentile of the whole-body SAR in Thelonious is less than 5 % at 950 MHz.

We determined the whole-body absorption induced by cellular communication systems and indoor wireless radio-frequency (RF) sources by using the SME method. The broadcasting systems are excluded because part of these systems operate at frequencies below 450 MHz for which the SME tool is not valid because of the electromagnetic coupling between the human body and the environment [16]. The cellular communication systems are GSM 900, GSM 1800, and DECT. The indoor signals are DECT (digital cordless phones and baby phones) and Wi-Fi.

Thelonious, shown in Figure 6.2b, consists of 81 different tissues. The tissues of the model are mapped to the tissues available in the Gabriel database for which the dielectric properties have been determined based on a literature survey and measurements [51–53].

For every measured incident field value (see Figure 6.31) the SME method calculated the range of whole-body averaged SAR values that can be induced by this electric field level. We used the outdoor-indoor environment (see Section 6.2.3) for indoor exposure to the electromagnetic fields (EMF) of wireless cellular networks, the indoor picocell environment (see Section 6.2.3) is used for indoor exposure to electromagnetic fields of indoor transmitters such as DECT base stations and Wi-Fi routers. The sample size equalled 4000 exposure cases or observations. From this range of SAR_{wb}-values we selected the 95^{th} percentile to obtain a single SAR_{wb}-value for each measured field level. The estimated SAR_{wb}-values presented in the results section show the mean and the 95^{th} percentile of the distribution of the 95^{th} percentile values of the whole-body averaged SAR for the different RF signals in the considered indoor microenvironments.

6.4.5.2 Results

Figure 6.32 and Figure 6.33 present the computed whole-body averaged SAR (SAR_{wb}) induced in Thelonious by wireless cellular communication systems and indoor radio-frequent sources in Belgian and Greek indoor microenvironments. The vertical axis shows the mean or the 95^{th} percentile of the whole-body SAR for each signal as well as for the total of cellular, indoor, and all signals.

In general, the values for the whole-body absorption reflect the results of the exposure or the incident electric field measurements, shown in Figure 6.31. For frequencies above resonance (70 MHz – 150 MHz), the whole-body absorption depends mainly on the incident power density or the incident field strength. The mean values of the whole-body absorption induced by the total signals are comparable in Belgium and Greece, but the 95^{th} percentiles were larger in Greece. In Belgium, the whole-body absorption induced by the the total signal ranged from 3 μW/kg to 7 μW/kg for the mean and from 15 μW/kg to 33 μW/kg for the 95^{th} percentile. The whole-body SAR induced by the total signal was the highest in Belgian offices. In Greece, the whole-body SAR induced by the total signal varied from 5 μW/kg to 11 μW/kg for the mean and from 6 μW/kg to 92 μW/kg for the 95^{th} percentile. We excluded the electric field value measured at a distance of 0.5 m from a DECT base station antenna in a Greek home because the SME method is not valid at this short distance to the antenna. The mean whole-body SAR induced by the total signal was the lowest in homes and the highest in offices. All calculated whole-body SAR values were below the basic restriction of 0.08 W/kg for general public specified by the International Commission on Non-Ionizing Radiation Protection [1]. In Belgium, GSM 900 contributes the most to the absorption induced by cellular communication systems. GSM 900 induced the highest absorption in offices (offices were mainly located in urban areas) and the lowest in homes (most of the homes were located in rural environment). In Greece, the highest whole-body SAR induced by the total signal of cellular systems was observed in schools and offices. Cellular systems induced the lowest absorption in homes. From the indoor signals, DECT signals contributed the most to the whole-body SAR induced by the indoor sources in Belgian houses. In Belgian schools, DECT and Wi-Fi induced the lowest absorption indicating that this technology was less used in schools. Absorption due to Wi-Fi was mainly encountered in Belgian offices and Greek homes.

6.4.5.3 Discussion

The results of the whole-body SAR are higher than the results reported by Joseph et al. [54]. They reported a whole-body SAR induced by the total signal of 11 μW/kg based on personal electric field measurements with an exposimeter while Vermeeren et al. [50] used a tri-axial probe with spectrum analyzer and a broadband

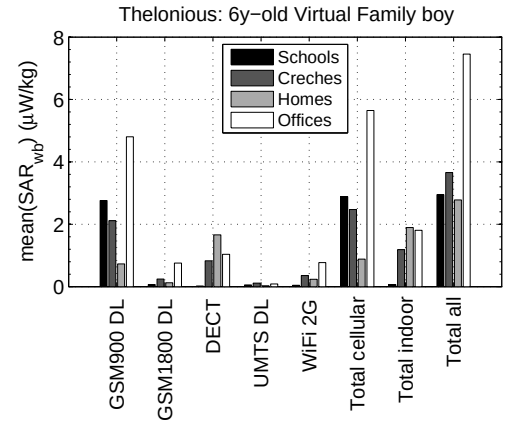

(a)

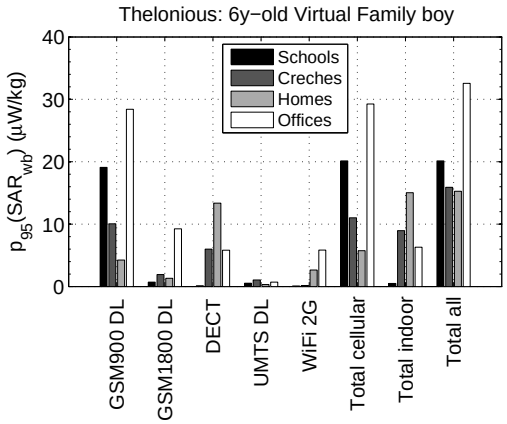

(b)

Figure 6.32: *The (a) mean and (b) 95^{th} percentile of the estimated whole-body averaged SAR induced in Thelonious by the exposure from cellular communication networks and indoor RF sources for the investigated indoor microenvironments in Belgium.*

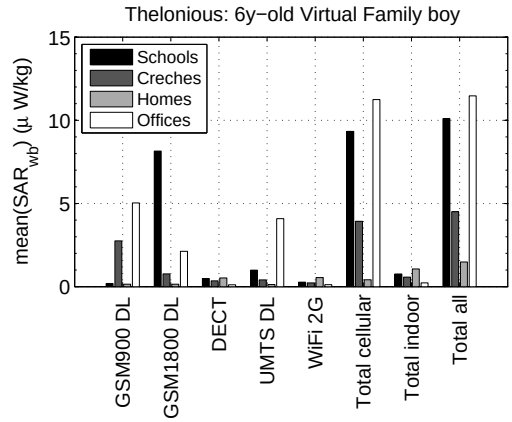

(a)

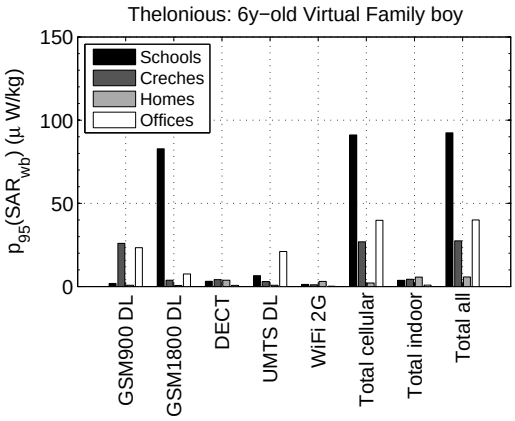

(b)

Figure 6.33: *The (a) mean and (b) 95^{th} percentile of the estimated whole-body averaged SAR induced in Thelonious by the exposure from cellular communication networks and indoor RF sources for the investigated indoor microenvironments in Greece.*

probe. Another difference in methodology is that they applied the SME tool for spheroid homogeneous human body models for estimating the whole-body SAR in the human body. In Section 6.4.4 we observed that the spheroid human body models underestimate the whole-body SAR in realistic human body models.

The uncertainties of the SME method are due to the full-wave computations for the pre-computed fields, the large uncertainty on the tissue properties (dielectric properties as well as the mass density of human body tissues), and the algorithms of the SME method to speed up the calculation of SAR_{wb} for multi-path exposure. The pre-computed fields are computed using the finite-difference time-domain (FDTD) method as implemented in the software tool SEMCAD-X (SPEAG, Zurich, Switzerland). Bakker et al. [48, 55] studied thoroughly the uncertainty in FDTD computations. The SME algorithms introduce an additional uncertainty of 5 %. The errors of the SME algorithms increased to 5 % compared with the errors obtained in [56] because we based our computations on a reduced set of pre-computed fields and a nearest interpolation scheme. The expanded uncertainty on the whole-body SAR of the applied method equalled 23.4 %.

The values of the whole-body SAR presented in Figure 6.32 and Figure 6.33 are only valid for the standing 6y-old Virtual Family boy. The whole-body SAR not only depends on the exposure but also on the human: changing the posture (sitting, standing with arms up, etc.) changes the whole-body absorption [11], and every human has a different morphology, which also influences the whole-body absorption [8, 11, 57].

Vermeeren et al. [50] measured the exposure in indoor microenvironment using spectrum analyzer and triaxial probe in Belgium, and the broadband SRM probe (Narda safety test solutions) in Greece. Every measurement comes with uncertainties and these are reflected in the calculation of the whole-body averaged SAR. The measured uncertainty is ± 3 dB for the setup with spectrum analyser and triaxial probe [58, 59] and +3.2 / -5.3 dB for the SRM setup (SRM-3000 technical specifications).

Another limitation of the study of Vermeeren et al. [50] is the small sample size of exposures obtained in the measurement campaign. Of course, this is reflected in the SAR assessment. The trends observed in the whole-body SAR are indicative and can be due to a particular choice of the measurement location: the high values for DECT in Greek homes are due to the high electric fields measured close (at 50 cm) to the DECT base station at one location.

A final limitation is the exclusion of broadcasting antennas for radio and TV because part of these antennas operates at frequencies below 450 MHz where the SME method is not applied. The power emitted by base station antennas of wireless cellular networks (outdoor sources) is much higher than the power emitted by indoor sources as DECT and Wi-Fi. Still, exposure due to indoor sources can exceed exposure of outdoor sources because they can be easily approached.

6.4.5.4 Conclusion

We discussed the whole-averaged SAR in the 6-year-old Virtual Family boy (Thelonious) if he would be exposed to the incident field values measured in Belgian and Greek indoor environments. The 95th percentile of the whole-body SAR ranged from 15 μW/kg to 33 μW/kg in Belgium, and from 6 μW/kg to 92 μW/kg in Greece and were below the ICNIRP basic restricions of 0.08 W/kg for general public. The whole-body absorption induced by indoor sources can become larger than the values induced by outdoor sources if the indoor wireless sources are approached.

6.5 Discussion

In this study, a fast numerical method is presented for the assessment of the whole-body averaged SAR induced in heterogeneous human body models in a multi-path environment. Assessing the whole-body SAR in a real environment requires a statistical analysis [57] (see Section 6.3.6). Different approaches exist. In specific cases, deterministic methods using, e.g., 3D ray-tracing tools are applied [19]. For more generic environments such as urban and indoor-outdoor environments, surrogate modelling, monte-carlo analysis, and the proposed SME method can be applied. With respect to the surrogate modelling and the Monte-Carlo method, the SME method keeps the relation between the incident fields and the induced whole-body SAR. The price for this relationship is a larger set of 3D numerical computations. Keeping the relationship between the incident fields and the induced SAR allows us to investigate in the future which exposures cause high induced SAR.

Despite the increased number of full-wave computations with respect to surrogate modelling and Monte-Carlo simulations, still a huge reduction in simulation time is obtained with the presented approach with respect to an analysis performed by solely full-wave computations. The SME method is at least 45 % faster than using solely full-wave calculations (based on a sample of 5000 exposures). Moreover, the gain in time increases when more environments are considered as the BFDs have to be calculated only once!

The uncertainties of the SME method are due to the applied full-wave numerical technique (FDTD, MoM/FEM) for calculating the BFDs and the algorithms used to assess SAR_{wb} for multi-path exposure (referred to as SME calculations). As discussed in the validation, errors of less than 1 % can be obtained with respect to the full-wave computations. Thus, the uncertainty is mainly determined by the uncertainty of the brute-force tool. Uncertainty of FDTD computations is studied thoroughly in [48]. The overall uncertainty is here estimated to be equal to 21.2 % [48].

The fast SME method is applied to Thelonious in four realistic environments

for the GSM downlink frequency at 950 MHz. This study confirms the findings of [5, 8, 21] that multiple plane-wave exposure can induce a higher whole-body SAR than the worst-case single incident plane-wave exposure. The influence of the morphology was also investigated. We showed that internal and external morphology largely influence the whole-body SAR. Our findings agree with those from [4, 6]. The increase in whole-body SAR in heterogeneous tissue distribution with respect to a homogeneous tissue distribution can be attributed to the difference in tissue properties and standing wave effects in tissues with low water content [60]. The influence of posture on SAR_{wb} was not investigated, but based on [11] it is expected that the variation of SAR_{wb} will increase when taking into account different postures of the human body model. We also showed that at higher frequencies the influence of the environment on the statistics of the whole-body SAR is negligible.

The current SME method only applies for assessing the whole-body SAR because the absorption is determined from the electromagnetic fields on a closed surface around the body. To calculate the organ-specific and local-averaged SAR the fields inside the human body are required.

6.6 Conclusion

We developed a fast method for the statistical evaluation of the whole-body SAR in spheroid and realistic a human body models in a realistic exposure environment. The method uses a set of basic electromagnetic field distributions obtained by a 3D electromagnetic solver. For 5000 exposures a 45 % gain in time is observed for realistic human body models. For spheroid human body models, a single multi-path exposure is calculated within one second. The SME method has been validated with full-wave FDTD simulations and a good agreement has been obtained. The whole-body SAR in a spheroid human body phantom in four different environments is examined using this fast method. We observed that the whole-body SAR in a complex environment complies with the ICNIRP basic restriction when the averaged field over the human body is equal to the ICNIRP reference level. It is also shown that the H-polarized single incident plane wave is not a worst-case exposure situation as assumed in the past. The numerical method is also applied to investigate thoroughly the whole-body SAR in the 6-year-old boy of the Virtual Family [24] exposed to the GSM downlink frequency of 950 MHz for several realistic environments. The exposure can not only be generated by statistical methods such as those from Olivier et al. [42], but can also be exported from a 3D ray tracing tool. It is shown that the whole-body SAR exceeds the basic restrictions for an incident power density equal to the ICNIRP reference level for 0.26 % of the exposures at the GSM downlink frequency of 950 MHz. The whole-body SAR for realistic exposure also exceeds for 3.6 % of the exposure cases the whole-body

SAR for worst-case single plane wave exposure. Furthermore, it is also shown that the whole-body SAR in homogeneous spheroid human body models and for realistic multi-path exposure underestimates the whole-body SAR in heterogeneous realistic human body models.

References

[1] ICNIRP. *Guidelines for limiting exposure to time-varying electric, magnetic, and electromagnetic fields*. Health Phys., 74:494–522, 1998.

[2] I. SCC39. *IEEE Standard for Safety Levels with Respect to Human Exposure to Radio-Frequency Electromagnetic Fields, 3 kHz to 300 GHz*, 2006.

[3] CENELEC. *EN50360: Basic standard for the measurement of specific absorption rate related to human exposure to electromagnetic fields (300 MHz - 3 GHz)*, 2001.

[4] A. Habachi, E. Conil, A. Hadjem, E. Vazquez, M. Wong, A. Gati, G. Fleury, and J. Wiart. *Statistical analysis of whole-body absorption depending on anatomical human characteristics at a frequency of 2.1 GHz*. Phys. Med. Biol., 55:1875–87, 2010.

[5] G. Vermeeren, W. Joseph, and L. Martens. *Whole-body SAR in spheroidal adult and child phantoms in realistic exposure environment*. Electron. Lett., 44:790–91, 2008.

[6] E. Conil, A. Hadjem, F. Lacroux, M. Wong, and J. Wiart. *Variability analysis of SAR from 20 MHz to 2.4 GHz for different adult and child models using finite-difference time-domain.* Phys. Med. Biol., 53:1511–25, 2008.

[7] P. Dimbylow, A. Hirata, and T. Nagaoka. *Intercomparison of whole-body averaged SAR in European and Japanese voxel phantoms*. Phys. Med. Biol., 53:5883–97, 2008.

[8] S. Kühn, W. Jennings, A. Christ, and N. Kuster. *Assessment of induced radio-frequency electromagnetic fields in various anatomical human body models*. Phys. Med. Biol., 54:875–90, 2009.

[9] R. Findlay and P. Dimbylow. *Effects of posture on FDTD calculations of specific absorption rate in a voxel model of the human body*. Phys. Med. Biol., 50:3825–35, 2005.

[10] R. Findlay, A. Lee, and P. Dimbylow. *FDTD calculations of SAR for child voxel models in different postures between 10 MHz and 3 GHz*. Radiat. Prot. Dosim., 135:226–31, 2009.

[11] T. Uusitupa, I. Laakso, S. Ilvonen, and K. Nikoskinen. *SAR variation study from 300 to 5000 MHz for 15 voxel models including different postures*. Phys. Med. Biol., 55:1157–76, 2010.

[12] S. Saunders and A. Aragon-Zavala. *Antennas and Propagation for Wireless Communication Systems (2nd ed.)*. John Wiley & Sons, 2007.

[13] C. H. Durney, H. Massoudi, and M. F. Iskander. *Radiofrequency Radiation Dosimetry Handbook*. 4th ed. Texas, USA: USAF School of Aerospace Medicine, Brooks Air Force Base, 1986.

[14] C. H. Durney, M. F. Iskander, H. Massoudi, and C. C. Johnson. *An empirical formula for the broad-band sar calculations of prolate spheroidal models of humans and animals*. IEEE Trans. Microw. Theory Tech., 27:758–763, 1979.

[15] S. Gabriel, R. Lau, and C. Gabriel. *The dielectric properties of biological tissues: Iii. parametric models for the dielectric spectrum of tissues*. Phys. Med. Biol., 41:2271–93, 1996.

[16] G. Vermeeren, M. Gosselin, S. Kühn, V. Kellerman, A. Hadjem, A. Gati, W. Joseph, j. Wiart, F. Meyer, N. Kuster, and L. Martens. *The influence of the reflective environment on the absorption of a human male exposed to representative base station antennas from 300 MHz to 5 GHz*. Phys. Med. Biol., 55:5541–55, 2010.

[17] W. Joseph, L. Verloock, and L. Martens. *Reconstruction of the polarization ellipse of the EM field of telecommunication and broadcast antennas by a fast and low-cost measurement method*. IEEE Trans. Electromagn. Compat., 48:385–96, 2006.

[18] G. Lazzi and O. Gandhi. *A Mixed FDTD-Integral Equation Approach for On-Site Safety Assessment in Complex*. IEEE Trans. Antennas Propag., 48:1830–6, 2000.

[19] G. Neubauer, S. Cecil, P. Preiner, N. Mitrevski, G. Vermeeren, W. Joseph, L. Martens, S. Kühn, and N. Kuster. *The relation between SAR and the electromagnetic field distribution for heterogeneous exposure conditions*. In First European Conference on Antennas and Propagation 2006, volume electronic version, 2006.

[20] O. P. Ghandi and M. S. Lam. *An on-site dosimetry system for safety assessment of wireless base stations using spatial harmonic components*. IEEE Trans. Antennas Propag, 51:840–47, 2003.

[21] T. Kientega, E. Conil, A. Hadjem, E. Richalot, A. Gati, M. Wong, O. Picon, and J. Wiart. *A surrogate model to assess the whole body SAR induced by multiple plane waves at 2.4 GHz*. Annals of Telecommunications, 66:419–28, 2011.

[22] O. Jawad, D. Lautru, S. Roy, J. Dricot, F. Horlin, and P. Doncker. *Statistical Study of SAR in Clustered Wireless Channels*. In Proceedings of the 5th European Conference on Antennas and Propagation (EUCAP), pages 2727–31, 2011.

[23] S. Iskra, R. McKenzie, and I. Cosic. *Monte Carlo simulations of the electric field close to the body in realistic environments for application in personal radiofrequency dosimetry*. Radiat. Prot. Dosim., 147(4):517–27, 2011.

[24] A. Christ, W. Kainz, E. G. Hahn, K. Honegger, M. Zefferer, E. Neufeld, W. Rascher, R. Janka, W. Bautz, J. Chen, B. Kiefer, P. Schmitt, H.-P. Hollenbach, J. Shen, M. Oberle, D. Szczerba, A. Kam, J. W. . Guag, and N. Kuster. *The Virtual Family – development of surface-based anatomical models of two adults and two children for dosimetric simulations*. Phys. Med. Biol., 48:N23–38, 2010.

[25] M. Ackerman. *The Visible Human Project*. Proc. IEEE, 86:504–11, 1998.

[26] P. Dimbylow. *FDTD calculations of the whole-body averaged SAR in an anatomically realistic voxel model of the human body from 1 MHz to 1 GHz*. Phys. Med. Biol., 42:479–90, 1997.

[27] C. Kim, S. Choi, J. Jeong, C. Lee, and M. Chung. *HDRK-man: a whole body voxel model based on high resolution color slice images of a Korean adult male cadaver*. Phys. Med. Biol., 53:4093–106, 2008.

[28] A. Lee, W. Choi, M. Chung, H. Choi, and J. Choi. *Development of Korean male body model for computational dosimetry*. ETRI J., 28:107–10, 2006.

[29] T. Nagaoka, S. Watanabe, K. Sakurai, E. Kunieda, M. Taki, and Y. Yamanaka. *Development of realistic high-resolution whole-body voxel models of Japanese adult males and females of average height and weight, and application of models to radio-frequency electromagnetic-field dosimetry*. Phys. Med. Biol., 49:1–15, 2004.

[30] C. A. Balanis. *Antenna Theory Analysis and Design*. 2005.

[31] R. B. Ertel, P. Cardieri, K. W. Sowerby, T. S. Rappaport, and J. H. Reed. *Overview of spatial channel models for antenna array communication systems*. IEEE Personal Commun. Mag., 5:10–22, 1998.

[32] C. Olivier and L. Martens. *Measurements of Exposure to Electromagnetic Radiation around GSM Base Stations in Belgium*. In 23rd Annual Meeting of the Bioelectromagnetics Soc. St-Paul, Minnesota, USA, pages 102–4, 2001.

[33] C. Olivier and L. Martens. *A Practical Method for Compliance Testing of Base Stations for Mobile Communications with Exposure Limits*. In Proc. IEEE Int. AP-S Symp. Boston, USA, pages 64–7, 2001.

[34] C. Olivier, W. Joseph, and L. Martens. *Preliminary electromagnetic measurements of the exposure around a UMTS base station*. In 5th International Congress of the European Bioelectromagnetics Association, Helsinki, Finland, pages 120–1, 2001.

[35] J. B. Andersen. *Statistical distributions in mobile communications using multiple scattering*. In The Journal of The Institute of Telecommunications Professionals, 2002. paper 565.

[36] K. Kalliola, K. Sulonen, H. Laitinen, O. Kiveks, J. Krogerus, and P. Vainikainen. *Angular power distribution and mean effective gain of mobile antenna in different propagation environments*. IEEE Trans. Veh. Technol., 51:823–38, 2002.

[37] H. Lehmann, P. Fritschi, and B. Eicher. *Indoor Measurements of the Electrical Field close to Mobile Phone Base Stations*. In Proceedings of XXVIIth General Assembly of URSI, Maastricht, The Netherlands, page paper 2112, 2002.

[38] X. Zhao, J. Kivinen, P. Vainikainen, and K. Skog. *Propagation characteristics for wideband outdoor mobile communications at 5.3 GHz*. IEEE J. Sel. Areas Commun, 20:507–14, 2002.

[39] G. Neubauer, W. Giczi, and G. Schmid. *An Optimized Method to determine exposure due to GSM Base stations applied in the city of Salzburg*. In 24th Annual Meeting of the Bioelectromagnetics Soc. Quebec, Canada, pages 46–7, 2002.

[40] G. Neubauer, H. Haider, M. Riederer, and R. Coray. *Measurement methods and legal requirements for exposure assessment next to GSM base stations*. In EMC Zurich symposium, Zurich, Switzerland, pages 143–48, 2003.

[41] C. Olivier and L. Martens. *Electromagnetic Field Measurements in Multi-Path Exposure Conditions*. In International NIR workshop & Symposium, Seville, Spain, 2004. Session 4.

[42] C. Olivier. *Characterisation of the electromagnetic radiation close to broadcast and wireless communications antennas*. PhD thesis, Ghent University, Ghent, Belgium, 2007.

[43] G. Vermeeren, C. Olivier, W. Joseph, and L. Martens. *Statistical model of the electromagnetic fields in a realistic environment*. In 29th Annual Meeting of the Bioelectromagnetics Society, Kanazawa, Japan, 2007. P-24.

[44] IEEE. *IEEE recommended practice for measurements and computations of radio frequency electromagnetic fields with respect to human exposure to such fields,100 kHz-300 GHz, Annex E*, 2002.

[45] IEC. *Human Exposure To Radio Frequency Fields From Hand-held And Body-mounted Wireless Communication Devices Human Models, Instrumentation, And procedures To Determine The Specific Absorption Rate (SAR) For Hand-held Devices Used In The Close Proximity To The Ear (Frequency Range Of 300 MHz To 3 GHz)*, 2005.

[46] B. Taylor and C. Kuyatt. *Guidelines for Evaluating and Expressing the Uncertainty of NIST Measurement Results*. Nist technical note 1297, NIST, 1994.

[47] R. Findlay and P. Dimbylow. *Variations in calculated SAR with distance to the perfectly matched layer boundary for a human voxel model*. Phys. Med. Biol., 51:N411–5, 2006.

[48] J. Bakker, M. Paulides, A. Christ, N. Kuster, and G. van Rhoon. *Assessment of induced SAR in children exposed to electromagnetic plane waves between 10 MHz and 5.6 GHz*. Phys. Med. Biol., 55:3115–30, 2010.

[49] SPEAG. *SEMCAD-X Reference guide*. Zurich, Switzerland.

[50] G. Vermeeren, I. Markakis, F. Goeminne, T. Samaras, L. Martens, and W. Joseph. *Spatial and Temporal RF Electromagnetic Field Exposure of Children and Adults in Indoor Micro Environments in Belgium and Greece*. Progress in Biophysics and Molecular Biology, 2013.

[51] C. Gabriel, S. Gabriel, and E. Corthout. *The dielectric properties of biological tissues: I. Literature survey*. Physics in Medicine and Biology, 41:2231–49, 1996. doi:10.1088/0031-9155/41/11/001.

[52] S. Gabriel, R. W. Lau, and C. Gabriel. *The dielectric properties of biological tissues: III. Parametric models for the dielectric spectrum of tissues*. Physics in Medicine and Biology, 41:2271–93, 1996. doi:10.1088/0031-9155/41/11/003.

[53] S. Gabriel, R. W. Lau, and C. Gabriel. *The dielectric properties of biological tissues: II. Measurements in the frequency range 10 Hz to 20 GHz*. Phys Med Biol, 41:2251–69, 1996. doi:10.1088/0031-9155/41/11/002.

[54] W. Joseph, L. Vermeeren, G.and Verloock, and L. Martens. *Estimation of Whole-Body SAR From Electromagnetic Fields Using Personal Exposure Meters*. Bioelectromagnetics, 31:286–95, 2010.

[55] J. Bakker, M. Paulides, A. Christ, N. Kuster, and G. van Rhoon. *Corrigendum for assessment of induced SAR in children exposed to electromagnetic plane waves between 10 MHz and 5.6 GHz*. Physics in Medicine and Biology, 56:2883, 2011.

[56] G. Vermeeren, W. Joseph, and L. Martens. *Statistical multi-path exposure method for assessing the whole-body sar in a heterogeneous human body model in a realistic environment*. Bioelectromagnetics, 34(3):240–51, April 2013.

[57] G. Vermeeren, W. Joseph, C. Olivier, and L. Martens. *Statistical multi-path exposure of a human in a realistic electromagnetic environment*. Health Phys., 94:345–54, 2008.

[58] CENELEC. *European Committee for Electrotechnical Standardisation TC 106x WG1 (EN 50492) in situ. Basic standard for the in-situ measurement of electromagnetic field strength related to human exposure in the vicinity of base stations*, 2008.

[59] W. Joseph, L. Verloock, F. Goeminne, G. Vermeeren, and L. Martens. *Assessment of RF exposures from emerging wireless communication technologies in different environments.* Health physics, 102(2):161–72, February 2012. doi:10.1097/HP.0b013e31822f8e39.

[60] A. Christ, A. Klingenböck, T. Samaras, C. Goiceanu, and N. Kuster. *The dependence of electromagnetic far-field absorption on body tissue composition in the frequency range from 300 MHz to 6 GHz.* IEEE Trans Microw Theory Tech, 54:2188–95, 2006.

7

Influence of the body on the dosimeter reading

7.1 Introduction

Nowadays, personal exposure meters, also called exposimeters or dosimeters, are extensively used in epidemiological studies to assess the daily exposure of a human to the electromagnetic fields used for radio-frequency communication [1, 2]. Exposimeters are typically worn on the body: belt, back, chest, etc. But, when worn on the body, it measures the total fields (incident + scattered) instead of the incident fields, which are generally referred to as the exposure.

This study investigated numerically the difference in exposimeter reading when worn on the body (measuring total fields) and placed off the body (measuring incident fields).

7.2 Methodology

This study investigated numerically the variation of the field levels between on-body and off-body exposimeter positions under identical exposure conditions. We assumed an ideal exposimeter characterized by an isotropic radiation pattern, perfect linearity, infinite dynamic range, and no coupling with the human body. Such an exposimeter would measure the electric field vector exactly in a point without disturbing the field. The ideal exposimeter is modelled as a point sensor in the

numerical computations.

In Chapter 6, we discussed the SME method for the assessment of the whole-body absorption in terms of specific absorption rate for rotationally symmetric and realistic human body models [3, 4]. For the evaluation of the body influence on the exposimeter reading, it is sufficient to determine the total electric fields in the exposimeter positions (points) around the human body. In the SME method for the absorption, we needed to determine the total electric and magnetic field on a closed surface around the isolated human body from which the whole-body absorption is assessed. Figure 7.1 depicts the flowchart to quickly assess the total electric field in exposimeter points on a human body. The SME method calculates very fast the fields in any exposimeter position around the human body for any (multipath) exposures. This tool is based on the knowledge of the total electromagnetic fields around the human body for a limited set of single incident plane waves and on the linearity of Maxwells equations. The total fields are precomputed by a 3D full-wave electromagnetic solver based on the FDTD or the MoM/FEM technique.

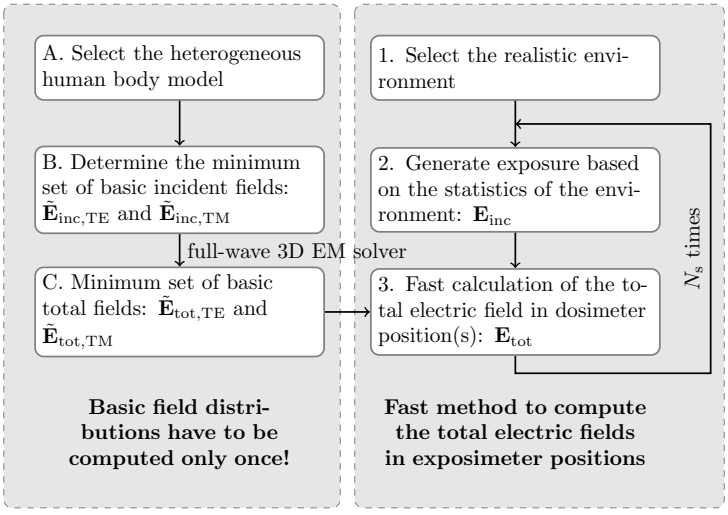

Figure 7.1: *Flowchart of the SME method for exposimeters positioned on the human body.*

The uncertainty of the SME method when calculating the whole-body SAR depends on the number of angles of incidence for which the Basic Field Distributions (BFDs) are determined and can be less than 1 %. We estimate that the uncertainty of the SME method for exposimeters is within the uncertainty obtained for the SME method for the absorption (see Section 6.3.4), because the whole-body SAR is determined from the electromagnetic fields outside the human body. The SME method for exposimeters calculates the total electric fields near the human body.

The SME method for absorption computes the absorption from the total fields on a closed surface near the human body. Hence, we estimate that the uncertainty of the SME method for exposimeters not larger than the one for the SME method for absorption.

7.3 Configurations

We examined the influence of the body on the exposimeter reading in a total of 416 locations around the human body. The locations are subdived in four sets: a single point in front of the body, waist (16 positions), chest-to-ankle (304), and torso (95). Figure 7.2 shows the exposimeter positions around the human body which are considered in this study. The exposimeter points are at 5 cm from the body. This is a typical separation for the center of the antenna(s) of current commercially available exposimeters.

The human body is exposed to single incident plane-wave exposure as well as multipath exposure in an urban-macro cell environment [5] at the GSM downlink frequency of 950 MHz. We selected the same heterogeneous human body model as for the study of the absorption, i.e., the 6-year-old virtual family boy (VFB) [6]. The tissues have been assigned the dielectric properties as available in the Gabriel database [7–9].

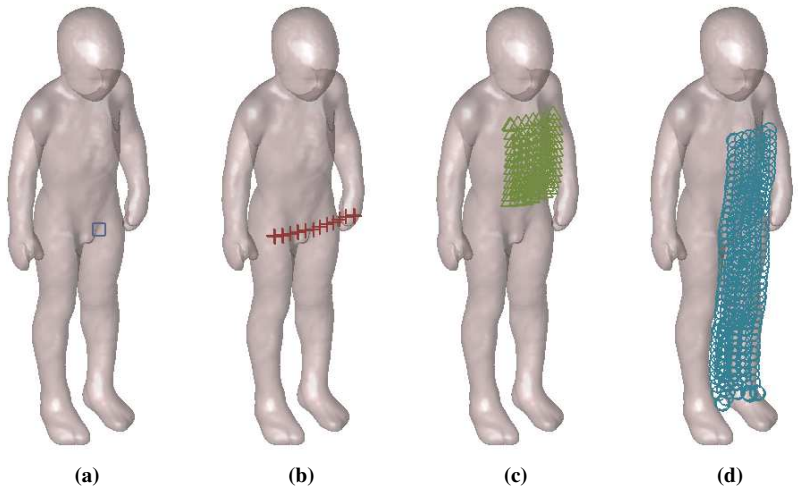

Figure 7.2: *Dosimeter locations at the body of Thelonious: (a) point, (b) waist, (c) torso, and (d) chest-to-ankle.*

7.4 Results

7.4.1 Single plane-wave exposure

Figure 7.3a shows the fields in the exposimeter position "point" for a horizontal incident plane wave ($\theta_{\rm inc}$ = 90 deg) and varying azimuth angle of the incident plane wave (plane waves incident from any side of the body). Two polarizations are considered: TE and TM. The free-space RMS electric field (without the presence of the body) of a single incident plane wave is independent of the angle of incidence and the polarization, so only one line is shown in Figure 7.3a. Frontal incidence (on the human body) occurs for $\phi_{\rm inc} = 0\,$deg and dorsal incidence occurs for $\phi_{\rm inc} = 180\,$deg.

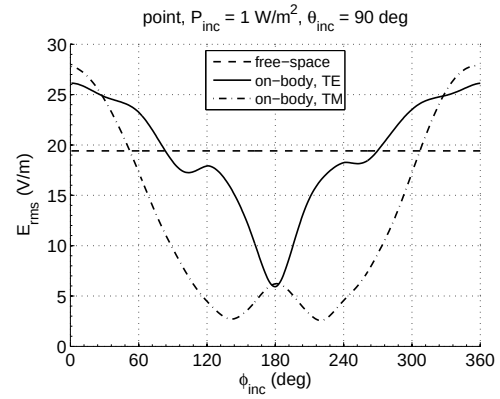

(a)

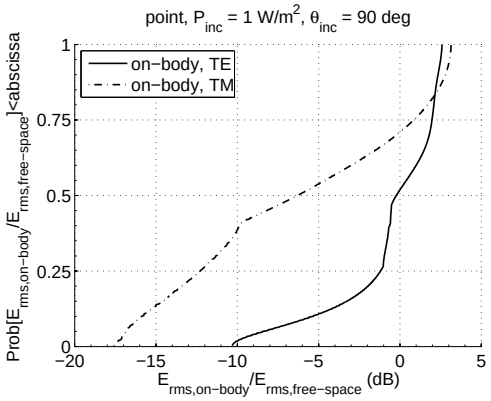

(b)

Figure 7.3: *"Exposimeter" reading for a horizontal incident plane wave in free space and in a point on the body of Thelonious: (a) as a function of the azimuth angles, (b)* cdf *of the ratio of the RMS total electric field to the RMS incident electric field.*

We observed that the total electric field (measured by the simulated exposimeter) underestimates the incident field values for azimuth angles from 84 deg to 269 deg and 53 deg to 307 deg for TE and TM polarization, respectively. For TE polarized incident plane waves, underestimation agrees very well with plane waves incident from the back or NLOS exposure conditions (for $\phi_{\mathrm{inc}} = 90$ deg to 270 deg). For TM polarization (E-field vertically polarized), underestimation also occurs for plane waves incident from the front of the body (the exposimeter and the incident plane wave in LOS). Thus, the underestimation can not be attributed to the screening of the body, but is due to destructive interference of the incident and scattered fields at the position of the exposimeter.

Figure 7.3b shows cdf of the ratio (R_{E}) of the RMS electric field measured with the exposimeter on-body and in free space, i.e., with the exposimeter at the same position but without the body. When the body is present, the exposimeter records the (RMS) total electric field, which is a superposition of the incident and the scattered fields. Without the body, the exposimeter only measures the (RMS) incident fields. The ratio R_{E} on a decibel scale is defined as follows:

$$R_{\mathrm{E}} = 20 \log \left(\frac{E_{\mathrm{rms,on-body,point}}}{E_{\mathrm{rms,free-space,point}}} \right) \tag{7.1}$$

The ratios vary from -10.3 dB ($\phi_{\mathrm{inc}} = 180$ deg) to 2.6 dB ($\phi_{\mathrm{inc}} = 1$ deg) and from -17.6 dB ($\phi_{\mathrm{inc}} = 220$ deg) to 3.1 dB ($\phi_{\mathrm{inc}} = 357$ deg) for TE-polarized and TM-polarized incident plane wave, respectively. An exposimeter placed on the body overestimates up to 3 dB the incident field for TE and TM polarization at the GSM downlink frequency. Overestimation happens when the exposimeter is in LOS with the incident plane wave: the scattered fields on the body increases the total field strength with respect to the incident field strength due to constructive interference.

The exposimeter underestimates the RMS incident field strength by up to -17.6 dB in NLOS conditions. The amount of underestimation exceeds the amount of overestimation by more than 14 dB. This is mainly due to the presence of the body. When a plane wave propagates through the body, it attenuates due to the lossy nature of the human tissues. The underestimation is about 8 dB larger for TE-polarization. This is due to the larger absorption of the electromagnetic energy in the body in case of TE-polarization (see also Section 6.4.3).

A similar analysis is performed for the elevation angles for frontal incidence. Figure 7.4 shows the fields in the frontal exposimeter position "point" for a frontal incident plane wave ($\phi_{\mathrm{inc}} = 0$ deg) and varying elevation angle of the incident plane wave. Again, two polarizations are considered: TE and TM. In this case, the exposimeter and the incident plane wave are in LOS for the majority of the elevation angles. The total field overestimated the incident field of a TM-polarized incident plane wave for almost all elevation angles suggesting that there is almost

no destructive interference between incident field and scattered field. For a TE polarized incident plane wave, the total field overestimates the incident electric field for a smaller range of elevation angles (for $\theta_{\mathrm{inc}} = 50\,\mathrm{deg}$ to $142\,\mathrm{deg}$). In this case, overestimation and underestimation are mainly caused by (destructive and constructive) interference as mainly LOS conditions are fulfilled between exposimeter and incident plane wave.

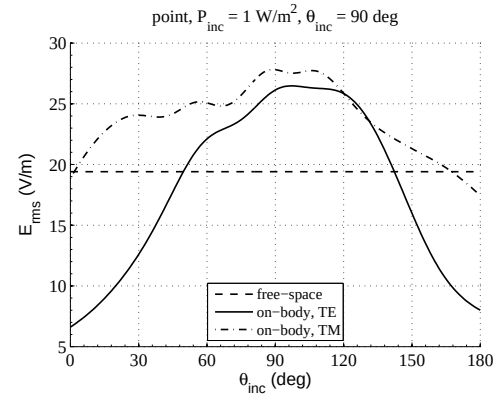

(a)

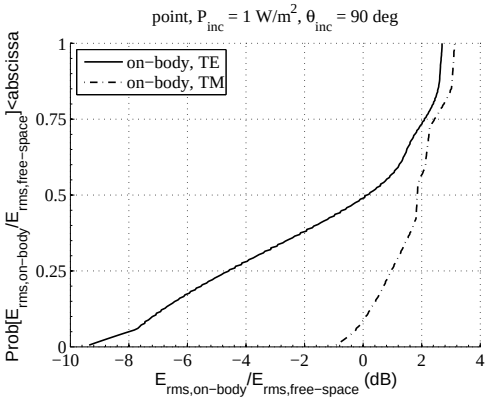

(b)

Figure 7.4: *exposimeter reading for an incident plane wave in free space and in a point on the body of Thelonious: (a) as a function of the elevation angles, (b)* cdf *of the ratio of the RMS total electric field to the RMS incident electric field.*

Figure 7.4b shows the cdf of the ratio R_{E} of the total (exposimeter worn on the body) and incident (exposimeter without the body) RMS electric field at the position of the exposimeter. For TE polarization, an equal proportion of elevation angles underestimated and overestimated the incident field strength ($p_{50} = 0\,\mathrm{dB}$).

The mean of R_{E} (-1.3 dB) takes a negative value indicating that the exposimeter on the body on average underestimates the incident field because the amount of underestimation (maximum 9.6 dB) is larger than the amount of overestimation (maximum 2.7 dB).

The exposimeter overestimates TM-polarized incident fields for almost all the elevation angles ($\theta_{\mathrm{inc}} = 2$ deg to 167 deg) resulting in a positive mean for the ratio R_{E} of 1.7 dB. These results indicate that for TM polarization constructive interference at the position of the exposimeter dominates.

In realistic exposure conditions the angles of incidence have a uniform distribution in the azimuth direction and a double exponential distribution in the elevation direction [5]. The elevation angles are concentrated around an angle of 90 deg (horizontal incidence). Hence, we expect that the exposimeter on average will underestimate the incident fields, mainly because the underestimation occurs for a wider range of azimuth angles and to a larger extend than overestimation.

7.4.2 Multipath exposure

Figure 7.5 shows the cdf of the RMS electric field ($\mathbf{E}_{\mathrm{rms}}$) in a single exposimeter position at 5 cm in front of Thelonious (at belt height) and at the same location but without Thelonious for 5000 exposure cases in an urban-macro cell environment at the GSM downlink frequency of 950 MHz. We observed that the field measured on the body underestimates the field measured in free space by 2.2 dB on average. As explained in Section 7.4.1 shadowing (attenuation) of the body causes this underestimation when the exposimeter is worn on the body and the incident plane wave is not in LOS with the exposimeter.

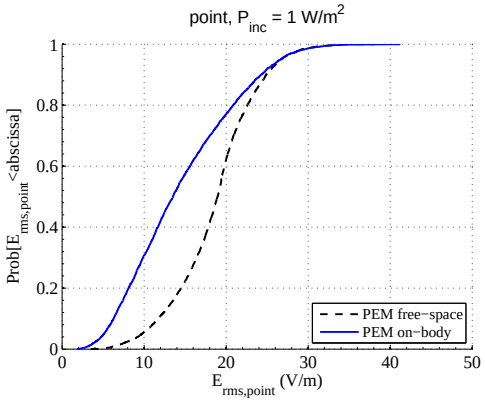

Figure 7.5: cdf *of* $\mathbf{E}_{\mathrm{rms}}$ *in a point at 5 cm in front of the VFB (belt height) and in the same point without VFB for 5000 exposure cases in an urban-macro cell environment for the GSM downlink frequency of 950 MHz.*

We also analysed the ratio R_{E} for three sets of exposimeter positions at different body parts: waist, torso, and chest-to-ankle region. For every exposimeter position in the three sets, we determined the mean and the standard deviation of R_{E} for 5000 exposure cases, denoted as $\mu\,(R_{\mathrm{E}})$. The total incident power (P_{inc}) for every exposure was 1 W/m^2. The minimum and maximum ratio R_{E} over all exposure case was -21 dB (underestimation) and 11 dB (overestimation), respectivily. The results are shown in Figure 7.6. Table 7.1 lists the ranges of $\mu\,(R_{\mathrm{E}})$ for each set of positions. The mean values of R_{E} are all below 0 dB, indicating an underestimation. The mean of R_{E} does not differ significantly for different parts of the body. We found the largest variation of $\mu\,(R_{\mathrm{E}})$ for the chest-to-ankle region (i.e, from -3.4 dB to -0.9 dB). The chest-to-ankle region is also the widest region of the three. The waist and torso regions are both located at the abdomen and, hence, show almost equal ranges for the mean of R_{E}: $\mu\,(R_{\mathrm{E}})$ ranged from -2.4 dB to -1.3 dB and from -2.1 dB to -1.2 dB for waist and torso, respectively.

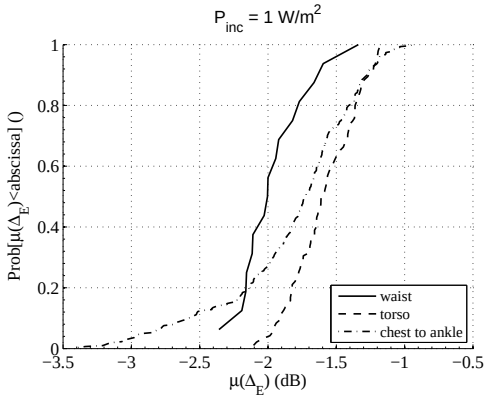

Figure 7.6: cdf *of* $\mu\,(R_{\mathrm{E}})$ *for three sets of exposimeter positions at 5 cm from the body of Thelonious exposed to GSM downlink at 950 MHz in an urban-macro cell environment.*

Area	Δ_μ (dB)
Waist (16 positions)	-2.4 to -1.3
Torso (95 positions)	-2.1 to -1.2
Chest-to-ankle (304 positions)	-3.4 to -0.9

Table 7.1: *Maximum and minimum deviation between* μ *and* σ *in a point with body and without body for three different areas of the body.*

7.5 Discussion

This study showed that an exposimeter worn on the body of a human body underestimates the exposure (incident fields). The underestimation ranged from by -3.4 dB to -0.9 dB for Thelonious exposed to the electromagnetic fields of GSM downlink at 950 MHz in an urban-macro cell environment. The underestimation depends on the location of the exposimeter on the body.

Our results are in line with results found in literature. Iskra et al. [10] investigated the influence of the body on dosimeter reading for eight different environments. They found an underestimation of 2.6 dB to 5.7 dB for frequencies ranging from 450 MHz to 2.1 GHz and for an exposimeter-body separation ranging from 1 cm to 5 cm. Iskra et al. [10] used the NORMAN human body models [11]. Comparing our results with the results of Iskra we can conclude that the influence of the body on the exposimeter reading is similar for different human body models. Bolte et al. [12] derived a correction factor of 1.1 to 1.6 for the electric field and suggested a protocol for wearing an exposimeter during a measurement campaign in order to be able to compare and combine measurements performed by different persons.

The present study assumed ideal exposimeters. As mentioned before, an ideal exposimeter measures the exact electric field vector in a point without disturbing the field. In reality, ideal exposimeters do not exist and measurement uncertainties have to be taken into account.

For the generation of the exposure samples by the statistical model, we have selected a uniform distribution for the azimuth angle of incidence. This suggests that plane waves arrive from all directions. If there would be a dominant direction of arrival (or non-uniform distribution), the on-body field would overestimate the incident field for frontal exposure and underestimate it for back exposure. On the other hand when a person is moving around in an environment (e.g., turning), a uniform distribution is the best choice even for environments with a dominant (LOS) path. When there is NLOS, reflections arrive from all directions and also here a uniform distribution is the best choice.

7.6 Conclusions

Exposimeters worn on the body underestimate the incident field due to the proximity of the body. We observed very large differences between the incident field and the field measured by an exposimeter in a single position on the body: -17.6 dB to 3.1 dB for single plane wave and -21 dB to 11 dB for multipath exposure. The mean of the ratio of the incident field and the field measured with the exposimeter (on the body) varied from -3.4 dB to -0.9 dB suggesting an average underestimation of the incident field when the exposimeter is worn on-body.

The SME tool can assist in the calibration of exposimeters to correct for the underestimation as well as in the design of future dosimeters to take better into account the influence of the body on the dosimeter reading.

References

[1] W. Joseph, P. Frei, M. Röösli, G. Thuroczy, P. Gajsek, T. Trcek, J. Bolte, G. Vermeeren, E. Mohler, P. Juhasz, V. Finta, and L. Martens. *Comparison of personal radio frequency electromagnetic field exposure in different urban areas across Europe.* Environmental Research, 110(7):658–63, 2010.

[2] P. Juhasz, J. Bakos, N. Nagy, G. Janossy, V. Finta, and G. Thuroczy. *RF personal exposimetry on employees of elementary schools, kindergartens and day nurseries as a proxy for child exposures*. Progress in Biophysics and Molecular Biology, 107:449–55, 2011.

[3] G. Vermeeren, W. Joseph, C. Olivier, and L. Martens. *Statistical multi-path exposure of a human in a realistic electromagnetic environment*. Health Phys., 94:345–54, 2008.

[4] G. Vermeeren, W. Joseph, and L. Martens. *Statistical multi-path exposure method for assessing the whole-body sar in a heterogeneous human body model in a realistic environment*. Bioelectromagnetics, 34(3):240–51, April 2013.

[5] C. Olivier. *Characterisation of the electromagnetic radiation close to broadcast and wireless communications antennas*. PhD thesis, Ghent University, Ghent, Belgium, 2007.

[6] A. Christ, W. Kainz, E. G. Hahn, K. Honegger, M. Zefferer, E. Neufeld, W. Rascher, R. Janka, W. Bautz, J. Chen, B. Kiefer, P. Schmitt, H.-P. Hollenbach, J. Shen, M. Oberle, D. Szczerba, A. Kam, J. W. . Guag, and N. Kuster. *The Virtual Family – development of surface-based anatomical models of two adults and two children for dosimetric simulations*. Phys. Med. Biol., 48:N23–38, 2010.

[7] C. Gabriel, S. Gabriel, and E. Corthout. *The dielectric properties of biological tissues: I. Literature survey*. Physics in Medicine and Biology, 41:2231–49, 1996. doi:10.1088/0031-9155/41/11/001.

[8] S. Gabriel, R. W. Lau, and C. Gabriel. *The dielectric properties of biological tissues: III. Parametric models for the dielectric spectrum of tissues*. Physics in Medicine and Biology, 41:2271–93, 1996. doi:10.1088/0031-9155/41/11/003.

[9] S. Gabriel, R. W. Lau, and C. Gabriel. *The dielectric properties of biological tissues: II. Measurements in the frequency range 10 Hz to 20 GHz*. Phys Med Biol, 41:2251–69, 1996. doi:10.1088/0031-9155/41/11/002.

[10] S. Iskra, R. McKenzie, and I. Cosic. *Monte Carlo simulations of the electric field close to the body in realistic environments for application in personal radiofrequency dosimetry.* Radiation protection dosimetry, 147(4):517–27, January 2011. doi:10.1093/rpd/ncq580.

[11] P. Dimbylow. *FDTD calculations of the whole-body averaged SAR in an anatomically realistic voxel model of the human body from 1 MHz to 1 GHz.* Phys. Med. Biol., 42:479–90, 1997.

[12] J. F. B. Bolte, G. van der Zande, and J. Kamer. *Calibration and uncertainties in personal exposure measurements of radiofrequency electromagnetic fields.* Bioelectromagnetics, 32(8):652–63, December 2011. doi:10.1002/bem.20677.

8 Conclusion

8.1 Conclusions

This dissertation covers aspects on local as well whole-body exposure to radio-frequency electromagnetic fields from wireles communication devices. The first part of the dissertation deals with the local averaging schemes applied in compliance testing and evaluates the peak local-averaged SAR induced by walkie-talkies or two-way radios.

Chapter 2 evaluates the use of a spherical volume for local averaging of the SAR in 1 g or 10 g of tissue against cubical averaging, which is typically used in SAR assessment, and contiguous averaging, which yields worst-case averaged SAR values. Spherical averaging keeps the middle between cubic and adaptive averaging. On the one hand, spherical averaging reduces the computational processing time because the positioning of the spherical volume is easy — no need to deform the volume to adapt it to the curved phantom surface, as it is the case for the cubic averaging — and no rotation of the volume to find the maximum local-average SAR value. Furthermore, the spherical averaging better approximates the distribution of the SAR in a homogeneous tissue as it takes into account more voxels at the surface of the phantom where the highest SAR values occur. Consequently, spherical averaging underestimates the contiguous averaging as defined by ICNIRP, but to a lesser extend than than the cubical schemes that are defined in the measurement standards.

In the past, dosimetry mainly focussed on the mobile phone next to the ear.

With the advent of wireless data networks, also laptops and RFID devices were considered. But, laptops and RFID devices communicate over short ranges in the order of tens of meters and duty cycles for WLAN are typically below 11 %. A device which has not been considered is the walkie-talkie. However, walkie-talkie provide short-range communication over hundreds of meters and are allowed to transmit an effective radiated power of 500 mW. Taking into account that these devices are operated in front of the face, we assessed the local-averaged SAR induced in the head by these devices. An accurate model for a walkie-talkie was developed in Chapter 3 and very good agreement was reported from simulations and measurements in terms of reflection and transmission characteristics. We verified that the model behaves electromagnetically as a real walkie-talkie by validating the near fields of the model with the measured near fields of a real walkie-talkie. The total radiated power and the effective radiated power of the model and four commercially available walkie-talkies were measured. The measured effective radiated power of real walkie-talkies is about 3.6 to 11 times lower than the allowed effective radiated power for PMR 446 radios.

In Chapter 4, the walkie-talkie model, developed in Chapter 3, is used to investigate the electromagnetic interaction with the human body and to verify the compliance with safety limits. In compliance testing a duty cycle of 100 % is taken into account. We showed that walkie-talkies comply with ICNIRP basic restrictions on the local-averaged SAR. But, based on the walkie-talkie models, the ICNIRP basic restrictions are exceeded in the unlikely event that a users continuously speaks during more than six minutes and the effective radiated power of the device equals the maximum allowed value of 500 mW. The SAR assessment of real devices showed that the peak local-averaged SAR in 10 g values are more than 5 times lower than the ICNIRP basic restriction (for a duty cycle of 100 %). We also investigated numerically the extent to which the ageing and morphology of the human head could affect dosimetry for child head exposure to emissions from walkietalkies. The effect on 10 g averaged SAR was marginal.

Besides local exposure issues, we also characterized the influence of the environment on the local and whole-body averaged absorption in the human body. Chapter 5 investigates the influence of highly reflective environments (ground and wall) on the exposure at short distances ($<$ 10 m) of base station antennas in the frequency range of 300 MHz and 5 GHz. These exposure situations can be encountered by workers (occupational exposure) on roof tops. We showed that the ratio of the whole-body and peak local-averaged SAR in Duke (34-year-old male of the Virtual Family human body models) in a reflective environment to those in the free-space environment ranged from -8.7 dB up to 8.0 dB. The ICNIRP reference levels are not always conservative with respect to the basic restrictions in a highly reflective environment, especially for separation distances of up to 1 m between base station antenna and Duke. From 2100 MHz and distances up to 3 m,

the peak local-averaged SAR is the most restrictive quantity. For frequencies below 2100 MHz the whole-body SAR is the most restrictive quantity. A worst-case reflective environment could not be determined.

In Chapter 6 we turn to general public exposure with the development of a fast method for the statistical evaluation of the whole-body SAR in spheroid and realistic human body models exposed to RF EMF in a realistic environment. In a real environment, the exposure is modeled as multiple propagating plane waves. The statistical multipath exposure (SME) method uses a set of basic electromagnetic field distributions obtained by a 3D electromagnetic solver. For 5000 exposure cases a 45 % gain in computing time is observed for realistic human body models while the relative error introduced by the numerical method can be as low as 1 % as compared to full-wave computations. For spheroid human body models, a single multi-path exposure case is calculated within one second. The SME method has been validated with full-wave FDTD simulations and a good agreement has been obtained. The whole-body SAR in a spheroid human body phantom in four different environments is examined using this fast method. We observed that the whole-body SAR in a complex environment complies with the ICNIRP basic restriction when the averaged field over the human body is equal to the ICNIRP reference level. It is also shown that the H-polarized single incident plane wave is not a worst-case exposure situation as assumed in the past. The numerical method is also applied to investigate thoroughly the whole-body SAR in the 6-year-old boy of the Virtual Family exposed to the GSM downlink frequency of 950 MHz for several realistic environments. We showed that the whole-body SAR exceeds the basic restrictions for an incident power density equal to the ICNIRP reference level for 0.26 % of the exposures at the GSM downlink frequency of 950 MHz. The whole-body SAR for realistic exposure also exceeds for 3.6 % of the exposure cases the whole-body SAR in for worst-case single plane wave exposure. Furthermore, the whole-body SAR in homogeneous spheroid human body models and for realistic multi-path exposure underestimates the whole-body SAR in heterogeneous realistic human body models. Finally, we applied the SME tool for estimating the whole-body SAR in Thelonious, the 6-year-old boy of the Virtual Family, when exposed to the the incident field values measured in Belgian and Greek indoor environments. The 95^{th} percentile of the whole-body SAR ranged from 15 μW/kg to 33 μW/kg in Belgium, and from 6 μW/kg to 92 μW/kg in Greece and were below the ICNIRP basic restricions of 0.08 W/kg for general public. We also observed that the whole-body SAR induced by indoor sources can become larger than the values induced by outdoor sources if the indoor wireless sources are approached.

Dosimeters are used in epidemiological studies to evaluate the personal exposure of a human during a certain period. A dosimeter is typically carried at the belt or in backpack where they record total field levels instead of the incident field levels, which are typically refered to as the exposure. In Chapter 7 we apply the

SME tool to evaluate the dosimeter reading when the dosimeter is worn on the human body. First, we discussed how the SME method can be used to evaluate the incident and total fields close tot the body. Next, we applied the SME method for evaluating the dosimeter reading at the GSM downlink frequency of 950 MHz when worn by Thelonious, a 6-year-old boy. On average, exposimeters worn on the body underestimate the incident field due to the shadowing of the body. The mean of the ratio of the field measured with the exposimeter (on the body) and the incident field in a realistic exposure environment varied from -3.4 dB to -0.9 dB suggesting an average underestimation of the incident field when the dosimeter is worn on-body. The maximum differences between the field measured by a exposimeter in a single position on the body and the incident field ranged from -18 dB to 3 dB for single plane wave and from -21 dB to 11 dB for multipath exposure.

8.2 Future research opportunities

In the past, exposure assessment mainly focussed on compliance testing to protect people from short-term adverse health effects from exposure to radio-frequency electromagnetic fields. In compliance testing, far-field exposure from base station antennas and near-field exposure from wireless devices operated close to the body are considered separately. But, to evaluate possible health effects from exposure, it is important to assess the combined exposure from far-field and near-field sources of the human body during a certain time period. Evaluating the total combined exposure in terms of local-averaged SAR is computationally very demanding because the location of the peak local-averaged SAR differs between exposure cases and a search is required to find peak value. A merely summation of the peak local mass-averaged values would largely overestimate the real value. The easiest way to assess the total combined SAR in a human body is by using the whole-body absorption. A drawback of using the whole-body absorption is that it might be difficult to relate possible health effects in organs to a whole-body averaged SAR. This could be solved by evaluating the SAR averaged over a certain region of the body (e.g., organ or a functional region). In this perspective, the research on the walkie-talkie (actually, any other device) could be extended by assessing the whole-body and partial-body absorption in realistic exposure scenarios.

The SMEtool as developed in this dissertation aims at assessing quickly the whole-body averaged SAR and also allows the evaluation of the influence of the body on the dosimeter reading. The SME tool can be extended in several ways to assist in future investigations. As mentioned before, current research in dosimetry aims at assessing total combined whole-body and partial-body absorption. To evaluate partial-body absorptions, the SME tool could be extended to evaluate quickly the SAR averaged over body regions, such as the local-averaged SAR in 1 g and 10 g and the organ-specific SAR, when exposed in realistic environments.

As opposed to the whole-body averaged SAR, this requires the evaluation of the electric fields induced in the human body and the implementation of routines for performing spatial averaging of the SAR. This demands a lot more processing power. Fortunately, the problem can be parallelized. The SME tool assumes plane wave exposure and, thus, is only applicable at large distances of the transmitting antenna. In an outdoor environment, this assumption holds for nearly all locations. However, in an indoor environment pico-cell antennas or access points for wireless local area networks can be easily approached. At short distances from the antenna the far-field assumption becomes invalid. The SME tool could be extended to be used with spherical or cilindrical waves for evaluating the absorption closer to the antenna.

On the application side of the SME tool, future research can include the evaluation of the whole-body and partial-body absorptions in different human body models as a function of frequency. Not only the influence of the size of the body but also the influence of the posture of the body or even the dynamic influence of movements of the body can be investigated for multipath exposure conditions.

The study on the exposimeters showed that dosimeters worn on the body underestimate the exposure. The SME tool can assist in the calibration of exposimeters to correct for the underestimation as well as in the design of future dosimeters to take better into account the influence of the body on the dosimeter reading.